IMPROVING PATIENT DOSIMETRY UNDER NON-REFERENCE CONDITIONS FOR PROTON BEAMS

JANA KRETSCHMER

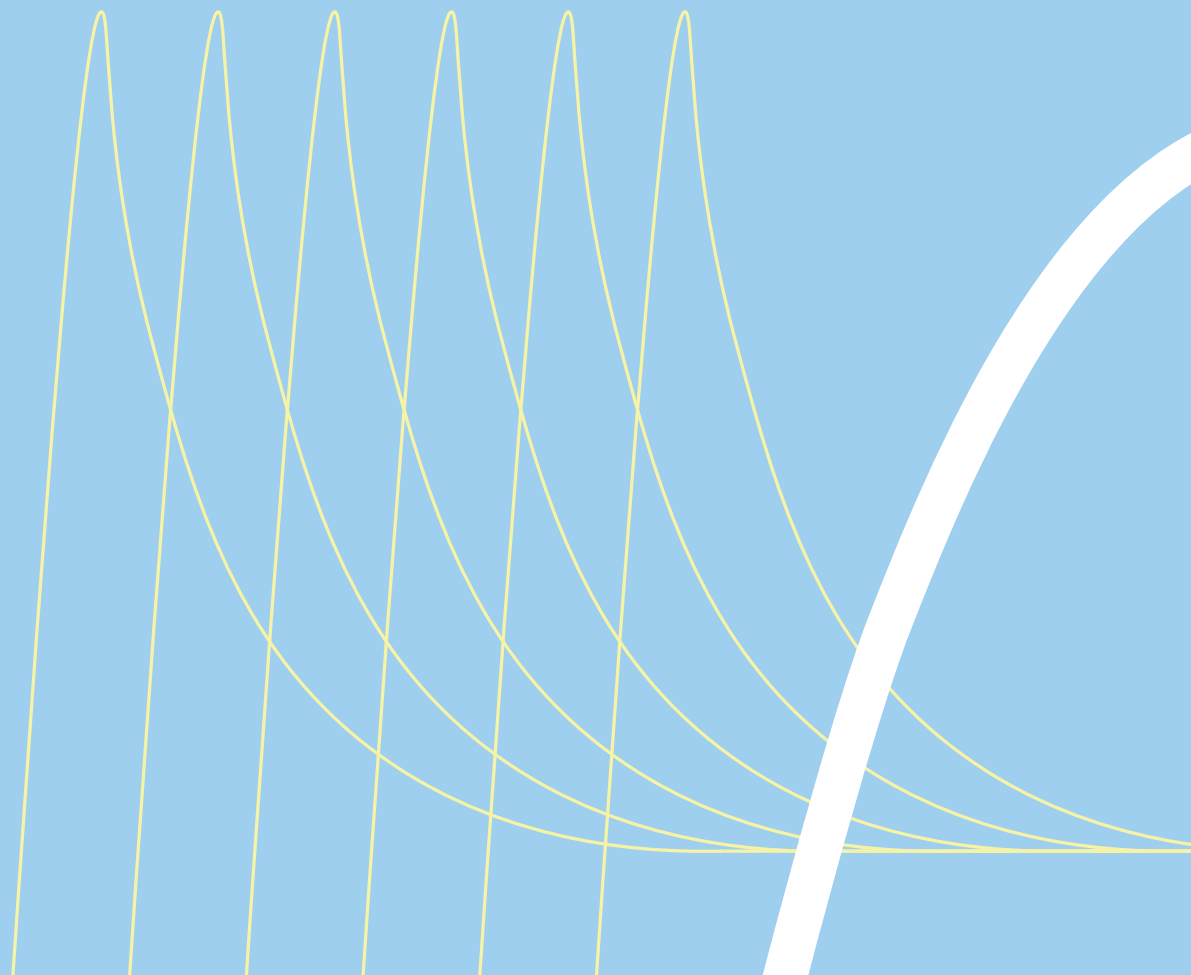

Improving patient dosimetry under non-reference conditions for proton beams

Jana Kretschmer

Cover design: Cerrin Schröer
Printing: Ridderprint | www.ridderprint.nl
The printing of this thesis was financially supported by the University Library and the Graduate School of Medical Sciences, University of Groningen, The Netherlands.

The work described in this thesis was carried out within a joint PhD programme by the University of Groningen and the Carl von Ossietzky University Oldenburg. Parts of the research were performed at the Particle Therapy Research Center (PARTREC) Accelerator Facility of the University Medical Center Groningen, University of Groningen. Beam time was partly funded by the EU Horizon 2020 project ENSAR2 (contract no. 654002). Monte Carlo simulations presented in this thesis were performed on the HPC Cluster CARL funded by the DFG under INST 184/157-1 FUGG.

university of groningen

Carl von Ossietzky Universität Oldenburg

Improving patient dosimetry under non-reference conditions for proton beams

PhD thesis

to obtain the joint degree of PhD of the
University of Groningen and the Carl von Ossietzky University of Oldenburg

on the authority of the
Rector Magnificus of the University of Groningen
Prof. J.M.A. Scherpen

and the Dean of the Faculty of Medicine and Health Sciences of the
Carl von Ossietzky University of Oldenburg
Prof. H.G. Nothwang

and in accordance with
the decision by the College of Deans of the University of Groningen.

This thesis will be defended in public on

Monday 10 November 2025 at 16:15 hours

by

Jana Kretschmer

born on 24 September 1992
in Oldenburg, Germany

Supervisors

Prof. S. Brandenburg
Prof. B. Poppe

Assessment Committee

Prof. D. Georg
Prof. F. Verhaegen
Prof. S. van de Par
Prof. J.M. Schippers

Improving patient dosimetry under non-reference conditions for proton beams

Von der Fakultät für Medizin und Gesundheitswissenschaften der Carl von Ossietzky Universität Oldenburg zur Erlangung des Grades und Titels einer

Doktorin der Naturwissenschaften (Dr. rer. nat.)

angenommene Dissertation

von Frau

Jana Kretschmer

geboren am 24.09.1992 in Oldenburg

Gutachter:
Prof. Dr. Dietmar Georg
Prof. Dr. Frank Verhaegen

Tag der Disputation:
10. November 2025

Contents

1 Introduction

Although the development in cancer treatment, as well as the implementation of early detection and prevention measures, have led to decreasing mortality rates from cancer in high-income countries, cancer is still the second main cause of death worldwide [1]. The general treatment approaches to cure cancer are surgery, systemic therapy, and radiation therapy [2, 3]. Patients are often treated by a combination of these approaches, and approximately 50% receive radiation therapy [4, 1]. The underlying principle of radiation therapy is to deliver a high radiation dose to the tumor while minimizing the dose in healthy tissue. Thereby, the cancer cells are destroyed, and the healthy organs are preserved by limiting their radiation induced side reactions and the probability of secondary malignancies [4]. Because of its superior dose deposition conformity, proton radiation therapy is expected to be advantageous over photon therapy in terms of normal tissue sparing [5, 6]. However, the quality of proton radiation therapy depends on the accuracy of the treatment, which is influenced by various uncertainties in the treatment process. While one of the major uncertainty components in proton therapy is related to the position of the proton beam distal edge in the patient [7, 8, 9], uncertainties in the calibrated output of the treatment machine, and in the characterization of the delivered dose distribution by the proton beam, further impact treatment accuracy [10, 11]. Therefore, high accuracy in clinical dosimetry is desired to warrant the best possible clinical outcome. For this purpose, different detectors are used to perform various dosimetry tasks comprising absolute dose determination under reference conditions, high-resolution dose profile acquisition in different spatial directions, and verification measurements of calculated patient treatment plans [11]. However, the non-water-equivalent components and the extended volumes of dosimetric detectors can lead to signal perturbations affecting the measurement results [12, 11, 13]. Depending on the measurement task and the detector type, detector-specific correction strategies must be developed to correct these perturbations. While extensive studies were dedicated to investigate conventional photon beams, studies on proton beam dosimetry are still comparably scarce. Therefore, proton dosimetry is associated with a higher uncertainty [14, 15, 16, 17].

1.1 Proton radiation therapy

Different radiation modalities can be used for cancer treatment comprising photons and electrons delivered by linear accelerators, radioactive sources, as well as high energy charged particles. While photon therapy is the most commonly used modality by far, some patients receive radiation therapy with charged particles such as protons or carbon ions [18]. At the time of writing, more than 7000 radiation therapy centers exist worldwide [19]. Among these centers, approximately 194 are particle therapy facilities either under operation, construction, or in planning [20]. Although the number of particle therapy facilities and patients treated with particles is increasing [18], still less than 1% of all radiation therapy patients undergo treatment with protons or heavier ions [7].

One of the main advantages of charged particles is the associated dose deposition distribution in the patient [5, 6]. The depth dose curve of a proton beam is characterized by a low entrance dose followed by a rapid dose increase leading to the so-called Bragg peak at the end of the particle range and a subsequent sharp dose fall-off, after which essentially no dose is deposited [7]. The range of the proton beam and, hence, the location of the Bragg peak depends on the initial proton energy [21]. Because the proton beam stops in the patient, it offers better sparing of the healthy tissues beyond its path. This is superior to photon therapy, where the beams penetrate the patient's body completely so that a complete sparing of healthy tissue posterior to the tumor in the beam direction is not feasible. Because proton therapy offers to deliver a lower integral dose, the probability of potential side effects such as second malignancies, cardiovascular disease, and other late effects [6] may be reduced.

To deliver a proton beam with high conformality to the tumor, different delivery techniques can be used to shape the dose distribution. The two main approaches are passive scattering and active beam scanning [21].

In passive scattering systems, proton fields are delivered by scattering techniques using a single-field uniform dose approach. Thereby, a mono-energetic narrow proton beam is spread in its energy distribution, i.e., in its penetration depth, as well as in the lateral direction, so that a homogenous dose is achieved for a specific volume. This is realized using a modulator wheel for energy modulation, a scattering system, and a collimator to define the lateral field shape, as well as a two-dimensionally shaped range compensator to modify the penetration depth locally. The modulator wheel, collimator, and range compensator are specifically made for each radiation field of each individual patient to optimize the conformity of the dose distribution with the tumor volume and to minimize the radiation dose to surrounding organs at risk [2, 9].

Nowadays, proton beam delivery machines mostly employ proton pencil beam scanning (PBS) [5], where a narrow pencil beam is steered to scan across the tumor. To do so, magnetic fields are used to direct the single Bragg peaks with Gaussian shaped lateral distributions of a few mm sigma in air to various positions in the tumor until the desired dose distribution is achieved [2], while the energy for each individual Bragg peak is produced using an energy degrader and selection system at the accelerator exit. Consequently, in contrast to passive scattering techniques, with PBS, inhomogeneous or complex shape dose distributions can be created [2]. Other advantages of PBS compared to passive scattering are that there is no need for patient-specific beam shaping devices [22, 5, 2], as well as that PBS offers intensity modulation, faster delivery, and higher beam efficiency [5].

1.2 Dosimetry

To ensure accurate and safe patient treatment, comprehensive quality assurance procedures have to be implemented [23]. These checks encompass the complete treatment chain, including the correct functioning of the accelerator, validation of the commissioning data used to set up the treatment planning system, as well as individual patient plan verification [5]. One of the important responsibilities of clinical medical physicists is to ensure the correctness of dosimetry and, therefore, the prescribed dose delivered to the patient. Accurate dosimetry is essential to guarantee the consistency of treatments so that treatment outcomes are comparable across different radiotherapy units [24, 11].

As previously described, the overall goal of radiation therapy is to deliver the intended radiation dose to the tumor that warrants the destruction of as many cancer cells as possible while keeping the damage to healthy tissue at an acceptable level [4]. The model that describes the relationship between tumor control probability (TCP) and normal tissue complication probability (NTCP) can be used to illustrate the impact of dose uncertainty on both probabilities, as depicted in Figure 1.1. While a high radiation dose offers a higher chance for tumor control, it is also associated with a higher probability of normal tissue damage. On the contrary, a low radiation dose is associated with a lower side reaction probability but also with the risk of an ineffective treatment. Therefore, the principle of radiation therapy relies on delivering the radiation dose that offers the optimal balance between TCP and NTCP [4]. Because TCP, NTCP, and hence treatment outcomes are influenced by inaccuracies in the delivered dose [25, 24], any uncertainties in the delivered proton radiation dose and, consequently, also in proton dosimetry should be minimized.

Dosimetry tasks are generally performed in water phantoms because water with reproducible properties is widely available and interacts similarly with radiation as soft tissues [26]. Dose measurements can be differentiated into two main categories: the first is dosimetry under well-defined reference conditions for the direct absorbed dose-to-water determination, and the second is dosimetry under non-reference conditions [10, 11], such as relative dosimetry measurements of lateral or depth dose distributions, output factors, as well as patient plan verifications.

Various detectors can be used, including radiation sensitive film, scintillators, ionization chambers, diamond detectors, and semi-conductor diodes [24, 11]. Depending on the measurement conditions and detector type, the detector reading may need to be corrected to provide accurate information on the actual dose deposition. Consequently, various correction strategies have been developed for reference and non-reference dosimetry. The approaches considered in this thesis will be presented below.

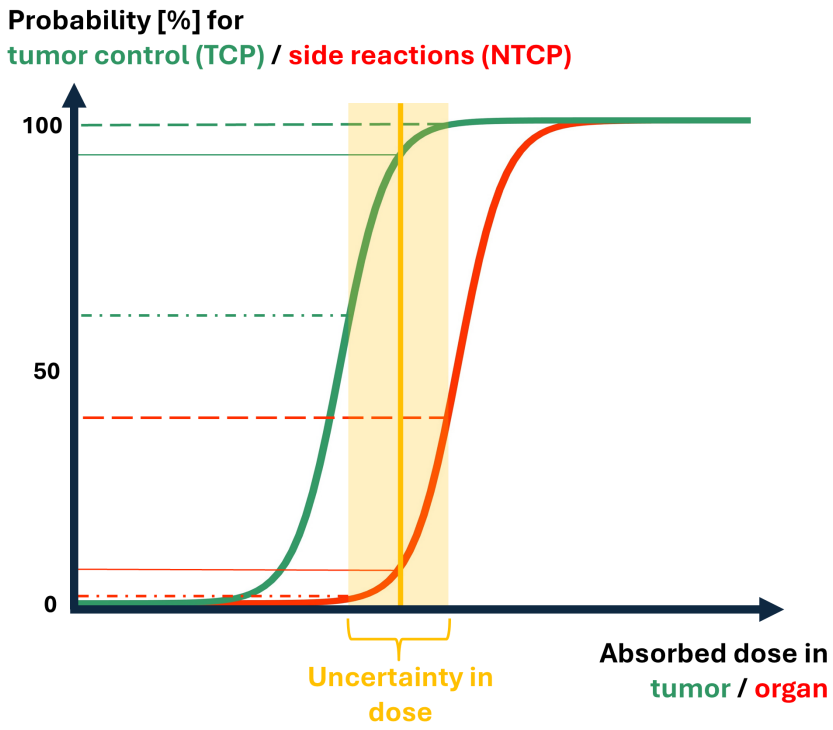

Figure 1.1. Illustration of TCP (green line) and NTCP (red line) as a function of the delivered dose. The yellow solid line shows the best compromise in the delivered dose, leading to high TCP and low NTCP (compare horizontal solid green and red lines). The yellow window illustrates the consequences of a dose uncertainty and its associated effects on TCP and NTCP (compare dashed lines): While a low dose results in low NTCP, it also leads to low TCP, whereas a high dose warrants tumor control but also increases the NTCP.

1.2.1 Reference dosimetry

Reference dosimetry is performed to calibrate the treatment machine by relating the machine output to a measured absorbed dose [5] determined with a detector in a water phantom. The so-called reference conditions, prescribing the measurement conditions, are defined in national or international codes of practice, such as the IAEA TRS-398 or the German DIN 6801 [14, 27, 28].

Equation 1.1 shows the formula for deriving the absorbed dose-to-water $D_{W,Q}$ from an ionization chamber measurement M_Q at beam quality Q [14, 28, 9, 29].

$$D_{W,Q} = M_Q \cdot N_{D_W,Q_0} \cdot k_{Q,Q0} \tag{1.1}$$

Note that the M_Q in equation 1.1 represents the ionization chamber signal in the unit of charge (Coulomb) corrected for influences such as air temperature and pressure, electrometer calibration, polarity effect as well as ion recombination, except for the beam quality [14, 28]. The calibration factor N_{D_W,Q_0} relates the chamber signal to dose with the unit Gray based on a calibration performed at a standard laboratory in a reference beam with beam quality Q_0, usually gamma radiation from a Cobalt 60 ($^{60}\mathrm{Co}$) source [14, 28, 30, 29]. Whenever the beam quality Q is different from the calibration beam quality Q_0, a beam quality correction factor $k_{Q,Q0}$ must be applied [29], which is usually abbreviated as k_Q [14]. Consequently, these chamber-specific k_Q factors are needed when a chamber is used for absolute dose measurements in proton beams.

Values for k_Q are provided in codes of practice like the international code for absorbed dose determination IAEA TRS-398 [14], which has been recently updated [31, 32, 28, 30]. However, when the first version of the TRS-398 code was published in 2000, ionization chamber-specific information for calculating k_Q in proton beams was scarce [30] and consequently the k_Q factors listed were approximated by assuming the chamber-specific perturbation factors p_Q, being one contributor to k_Q, to be unity [15]. As a consequence, the listed k_Q values for scattered proton beams were associated with an uncertainty of 1.7% for cylindrical and 2.1% for plane-parallel ionization chambers, which is high in comparison to the corresponding uncertainty in photon beams of 1% [14, 15]. Another limitation of the 2000 version of TRS-398 is that the reference conditions were only defined for passive scattering and not for the nowadays more widely adopted PBS [30], which might further increase the uncertainty of the protocol if applied to PBS. According to the 2000 version of TRS-398, the combined standard uncertainty in the determination of $D_{W,Q}$ for proton beams is estimated by 2.0% and 2.3% for cylindrical and plane-parallel chambers respectively [14]. Considering the facts that the

total uncertainty for the dose delivered to the patient should remain smaller than at least 5% [14, 33, 34, 9] and that the uncertainty for absorbed dose measurements should not exceed 1% [24, 9], a reduction of the existing uncertainties of up to 2.3% would allow a higher accuracy and motivates more detailed investigation of proton reference dosimetry and beam quality correction factors in proton beams.

1.2.2 Dosimetry under non-reference conditions

While reference dosimetry is carried out under well-defined conditions, dosimetry under non-reference conditions is performed to measure more diverse and complex dose distributions [10, 35]. Such measurements include the acquisition of lateral dose profiles, depth-dose distributions, output factors, and measurements in non-water phantoms for patient treatment plan verifications, beam commissioning or quality assurance purposes [24]. Depending on the type of measurement, various detectors can be used. While large plane-parallel ionization chambers are the typical detector type for determining the depth dose distributions of proton beams [11], lateral dose profiles are acquired with radiochromic films, luminescence detectors, two-dimensional (2D) detector arrays or point detectors [10, 36, 24]. Point-like detectors are commonly used to measure output factors or scan-field factors [16], that is the output as a function of the field size [37, 36, 16, 13]. Patient-specific radiation plan verification is commonly performed with 2D detector arrays, film, scintillation screens, three-dimensional (3D) scintillator detector systems or a 3D detector block containing multiple ionization chambers [23, 38, 35, 10, 39, 36, 24, 11, 40].

Non-reference dosimetry measurements, such as profile acquisition of narrow proton fields, are subject to charged particle disequilibrium and associated perturbations caused by the detector [13]. Since these perturbations depend on the construction of the detector, it is crucial to characterize and understand its behavior when irradiating the detector with proton beams. One of the most dominant perturbations of point detectors is the so-called detector volume effect comprising, on the one hand, a geometrical-averaging effect from the non-zero detector dimensions and, on the other hand, a density perturbation resulting from the non-water-equivalent detector components [41, 42, 43].

When a 2D dose distribution $D(x, y)$ is measured with a detector with non-negligible volume effect, the measured signal distribution $M(x, y)$ will exhibit a larger 80% to 20% lateral dose fall-off (penumbra), $d_{80/20}$ than the undisturbed $D(x, y)$ [12, 44]. In narrow fields, the volume effect can additionally lead to a reduction of the signal at the

maximum [12, 44]. A correction strategy for volume effect perturbations based on the convolution theorem is shown in equation (1.2):

$$M(x, y) = D(x, y) * K(x, y) \tag{1.2}$$

where $K(x, y)$ is the so-called detector-specific lateral dose response function which acts as the convolution kernel transforming $D(x, y)$ into $M(x, y)$ [12, 45, 46, 41, 42, 43]. The convolution theorem allows the correction of perturbations associated with the volume effect when $K(x, y)$ is known for the used detector. In other words, the actual dose distribution can be derived from the measured profile via deconvolution [44].

Dosimetry of small radiation fields is particularly influenced by the volume effect when the delivered dose changes substantially over the area of the detector [16, 13] and the lateral charged particle equilibrium is disturbed [13]. For proton therapy, the use of steep penumbras and small fields has gained increased attention in the past years. As the depth of the distal dose fall-off is very sensitive to uncertainties [9], the lateral dose fall-off is often used to spare organs at risk [47, 48, 49]. Consequently, a steep lateral dose fall-off, i.e., small penumbra, is desired [17, 49]. However, when a proton beam penetrates through the patient, the scattering of protons from atomic electrons and nuclei, and nuclear fragmentation lead to a broadening of the beam in the lateral direction, which increases with the depth [5, 6].

Because of the previously mentioned advantages, most proton therapy centers today utilize PBS [30], where the final lateral dose distribution is limited by the shape of the single pencil beams and may be larger for PBS than for passive scattering delivery techniques [50, 47]. To improve the penumbra in PBS, several authors investigated methods to reduce the lateral penumbra of proton pencil beams. These approaches include the use of apertures or collimators together with PBS [51, 22, 52, 53, 54, 17, 49], rearrangement or adjustment of components in the beam line [17, 47, 55], the use of apertures in combination with higher doses at the field edges (edge enhancement) [17, 56], performing minibeam proton therapy [50], or optimization of the position of single pencil beams such that they follow the contour of the target (contour scanning) [57, 48].

Besides delivery techniques aiming at reducing the lateral penumbra, some treatment techniques additionally involve or necessitate small irradiation fields. Proton beam applications making use of small fields are for example ocular melanoma treatments [58, 59, 60, 61, 62], stereotactic irradiations [51, 9, 63], treatments of pediatric patients, grid-

or microbeam therapy irradiations [64, 17] and small animal irradiations for radiation biology research [65, 66, 67, 68, 64, 69].

While many studies investigated dosimetry in high dose gradient regions and in small photon fields, for which international codes of practice with a focus on small fields have been published for photon therapy [70, 25], research on small proton beam dosimetry essential for standardization is still scarce [16]. The growing interest in reducing penumbras and employing small fields in proton radiation therapy justifies an investigation of detector responses and the associated perturbations under these challenging conditions, as well as the development of suitable correction strategies in clinical dosimetry.

1.3 Objectives of this thesis

As outlined above, dosimetry in proton therapy is associated with higher uncertainty in comparison to photon therapy [14, 71, 17]. This work aims at reducing the uncertainties associated with reference and non-reference dosimetry of proton beams.

Chapter 2 deals with the inaccuracies in proton reference dosimetry using ionization chambers. In this work, k_Q factors were determined for monoenergetic proton beams with the help of Monte Carlo simulations for various ionization chambers and beam energies. In addition, the chapter presents perturbation correction factors attributed to individual ionization chamber components. These findings can be used to reduce the uncertainty of the currently approximated k_Q factors for ionization chambers in monoenergetic proton fields.

Chapters 3 and 4 comprise the investigations of point detector measurements under non-reference conditions with a focus on dose profiles and output factor measurements in small proton fields. By adopting the correction strategy established in photon dosimetry, **Chapter 3** presents the determination and characterization of lateral dose response functions $K(x, y)$ for a set of point detectors in proton beams. Within a convolution model, the functions can be used to correct for perturbations of point detectors in beam profile measurements allowing to derive unperturbed dose profiles from the perturbed measured profiles. These functions were determined experimentally and by Monte Carlo simulations. A potential energy dependence was examined, and the impact of detector components was analyzed. In **Chapter 4**, the detector-specific lateral dose response functions were then applied in small proton fields resulting from different proton delivery techniques, including PBS, collimated PBS, and passive scattered collimated proton

beams. Perturbations in lateral dose profiles and output factor measurements were investigated and quantified. The results provide an overview of the detector perturbations encountered in different delivery techniques that are helpful to guide detector selection for non-reference dosimetry measurements in small proton fields.

References

[1] Wild, C. P., Weiderpass, E., Stewart, B. W., and editiors. "World Cancer Report: Cancer Research for Cancer Prevention." 2020. DOI: http://publications.iarc.fr/586.Licence:CCBY-NC-ND3.0IGO.

[2] Paganetti, H. *Proton Beam Therapy*. IOP Publishing. 2016. DOI: 10.1088/978-0-7503-1370-4.

[3] Stephens, F. O. and Aigner, K. R. *Basics of Oncology*. Springer International Publishing. Cham. 2016. DOI: 10.1007/978-3-319-23368-0.

[4] Beyzadeoglu, M., Ozyigit, G., and Ebruli, C. *Basic Radiation Oncology*. Springer International Publishing. 2022. DOI: 10.1007/978-3-030-87308-0.

[5] Durante, M. and Paganetti, H. "Nuclear physics in particle therapy: a review". *Rep Prog Phys*, 2016, 79:9, 096702 (59pp). DOI: 10.1088/0034-4885/79/9/096702.

[6] Newhauser, W. D. and Zhang, R. "The physics of proton therapy". *Phys Med Biol*, 2015, 60:8, R155–R209. DOI: 10.1088/0031-9155/60/8/R155.

[7] Mohan, R. "A review of proton therapy – Current status and future directions". *Precis Radiat Oncol*, 2022, 6:2, pp. 164–176. DOI: 10.1002/pro6.1149.

[8] Paganetti, H. "Range uncertainties in proton therapy and the role of Monte Carlo simulations". *Phys Med Biol*, 2012, 57:11, R99–R117. DOI: 10.1088/0031-9155/57/11/R99.

[9] Paganetti, H. *Proton Therapy Physics*. CRC Press. 2011. DOI: 10.1201/b11448.

[10] Giordanengo, S., Manganaro, L., and Vignati, A. "Review of technologies and procedures of clinical dosimetry for scanned ion beam radiotherapy". *Phys Med*, 2017, 43, pp. 79–99. DOI: 10.1016/j.ejmp.2017.10.013.

[11] Sahoo, N., Sawakuchi, G. O., Gillin, M. T., and Zhu, X. R. "Radiation Dosimetry of Proton Beams". In: A. K. Rath and N. Sahoo (eds.): *Particle Radiotherapy*. New Delhi, Springer India, 2016, pp. 77–94. DOI: 10.1007/978-81-322-2622-2.

[12] Brodbek, L., Kretschmer, J., Willborn, K., Meijers, A., Both, S., Langendijk, J. A., Knopf, A.-C., Looe, H. K., and Poppe, B. "Analysis of the applicability of two-dimensional detector arrays in terms of sampling rate and detector size to verify scanned intensity-modulated proton therapy plans". *Med Phys*, 2020, 47:9, pp. 4589–4601. DOI: 10.1002/mp.14346.

[13] Vatnitsky, S. M., Miller, D. W., Moyers, M. F., Levy, R. P., Schulte, R. W., Slater, J. D., and Slater, J. M. "Dosimetry techniques for narrow proton beam radiosurgery". *Phys Med Biol*, 1999, 44:11, pp. 2789–2801. DOI: 10.1088/0031-9155/44/11/308.

[14] Andreo, P., Burns, D. T., Hohlfeld, K., Huq, M. S., Kanai, T., Laitano, F., Smythe, V. G., and Vynckier, S. *Absorbed dose determination in external beam radiotherapy: an international code of practice for dosimetry based on standards of absorbed dose to water. Technical Reports Series No. 398.* International Atomic Energy Agency. Vienna. 2000.

[15] Gomà, C., Andreo, P., and Sempau, J. "Monte Carlo calculation of beam quality correction factors in proton beams using detailed simulation of ionization chambers". *Phys Med Biol*, 2016, 61:6, pp. 2389–2406. DOI: 10.1088/0031-9155/61/6/2389.

[16] Kugel, F. et al. "Validating a double Gaussian source model for small proton fields in a commercial Monte-Carlo dose calculation engine". *Z Med Phys*, 2022, 33:4, pp. 529–541. DOI: 10.1016/j.zemedi.2022.11.011.

[17] Lomax, A. "What will the medical physics of proton therapy look like 10 yr from now? A personal view". *Med Phys*, 2018, 45:11, e984–e993. DOI: 10.1002/mp.13206.

[18] Chandra, R. A., Keane, F. K., Voncken, F. E. M., and Thomas, C. R. "Contemporary radiotherapy: present and future". *Lancet*, 2021, 398:10295, pp. 171–184. DOI: 10.1016/S0140-6736(21)00233-6.

[19] *The IAEA Directory of Radiotherapy Centres (DIRAC)*. 2024. URL: https://dirac.iaea.org/ (accessed on 16/09/2024).

[20] *PTCOG*. 2024. URL: https://www.ptcog.site/ (accessed on 16/09/2024).

[21] Schardt, D., Elsässer, T., and Schulz-Ertner, D. "Heavy-ion tumor therapy: Physical and radiobiological benefits". *Rev Mod Phys*, 2010, 82:1, pp. 383–425. DOI: 10.1103/RevModPhys.82.383.

[22] Bäumer, C., Janson, M., Timmermann, B., and Wulff, J. "Collimated proton pencil-beam scanning for superficial targets: impact of the order of range shifter and aperture". *Phys Med Biol*, 2018, 63:8, p. 085020. DOI: 10.1088/1361-6560/aab79c.

[23] Arjomandy, B. et al. "AAPM task group 224: Comprehensive proton therapy machine quality assurance". *Med Phys*, 2019, 46:8, e678–e705. DOI: 10.1002/mp.13622.

[24] Karger, C. P., Jäkel, O., Palmans, H., and Kanai, T. "Dosimetry for ion beam radiotherapy". *Phys Med Biol*, 2010, 55:21, R193–R234. DOI: 10.1088/0031-9155/55/21/R01.

[25] INTERNATIONAL ATOMIC ENERGY AGENCY. *Dosimetry of Small Static Fields Used in External Beam Radiotherapy, Technical Reports Series No. 483*. IAEA. Vienna. 2017.

[26] Khan, F. M. *The physics of radiation therapy*. Lippincott Williams & Wilkins. Philadelphia. 2003.

[27] *DIN 6801-1:2019-09 Dosismessverfahren nach der Sondenmethode für Protonen- und Ionenstrahlung - Teil 1: Ionisationskammern*, 2019. DOI: https://dx.doi.org/10.31030/3038366.

[28] INTERNATIONAL ATOMIC ENERGY AGENCY. *Absorbed Dose Determination in External Beam Radiotherapy, Technical Reports Series No. 398 (Rev. 1)*. IAEA. Vienna. 2024. DOI: 10.61092/iaea.ve7q-y94k.

[29] Vedelago, J., Karger, C. P., and Jäkel, O. "A review on reference dosimetry in radiation therapy with proton and light ion beams: status and impact of new developments". *Radiat Meas*, 2022, 157, p. 106844. DOI: 10.1016/j.radmeas.2022.106844.

[30] Palmans, H., Lourenço, A., Medin, J., Vatnitsky, S., and Andreo, P. "Current best estimates of beam quality correction factors for reference dosimetry of clinical proton beams". *Phys Med Biol*, 2022, 67:19, p. 195012. DOI: 10.1088/1361-6560/ac9172.

[31] Andreo, P. et al. "Determination of consensus k_Q values for megavoltage photon beams for the update of IAEA TRS-398". *Phys Med Biol*, 2020, 65:9, p. 095011. DOI: 10.1088/1361-6560/ab807b.

[32] Baumann, K.-S., Kaupa, S., Bach, C., Engenhart-Cabillic, R., and Zink, K. "Monte Carlo calculation of beam quality correction factors in proton beams using TOPAS/GEANT4". *Phys Med Biol*, 2020, 65:5, p. 055015. DOI: 10.1088/1361-6560/ab6e53.

[33] "ICRU Report No 78 Prescribing, Recording, and Reporting Proton-Beam Therapy". *JICRU*, 2007, 7:2. DOI: 10.1093/jicru_ndm021.

[34] INTERNATIONAL ATOMIC ENERGY AGENCY. *Accuracy Requirements and Uncertainties in Radiotherapy, IAEA Human Health Series No. 31*. IAEA. Vienna. 2016.

[35] Giordanengo, S. and Palmans, H. "Dose detectors, sensors, and their applications". *Med Phys*, 2018, 45:11, e1051–e1072. DOI: 10.1002/mp.13089.

[36] Grevillot, L., Stock, M., Palmans, H., Osorio Moreno, J., Letellier, V., Dreindl, R., Elia, A., Fuchs, H., Carlino, A., and Vatnitsky, S. "Implementation of dosimetry equipment and phantoms at the MedAustron light ion beam therapy facility". *Med Phys*, 2018, 45:1, pp. 352–369. DOI: 10.1002/mp.12653.

[37] Daartz, J., Engelsman, M., Paganetti, H., and Bussière, M. R. "Field size dependence of the output factor in passively scattered proton therapy: Influence of range, modulation, air gap, and machine settings: Field size dependence of output in proton therapy". *Med Phys*, 2009, 36:7, pp. 3205–3210. DOI: 10.1118/1.3152111.

[38] Darne, C. D., Alsanea, F., Robertson, D. G., Sahoo, N., and Beddar, S. "Performance characterization of a 3D liquid scintillation detector for discrete spot scanning proton beam systems". *Phys Med Biol*, 2017, 62:14, pp. 5652–5667. DOI: 10.1088/1361-6560/aa780b.

[39] Grevillot, L. et al. "Clinical implementation and commissioning of the MedAustron Particle Therapy Accelerator for non-isocentric scanned proton beam treatments". *Med Phys*, 2020, 47:2, pp. 380–392. DOI: 10.1002/mp.13928.

[40] Schwaab, J., Brons, S., Fieres, J., and Parodi, K. "Experimental characterization of lateral profiles of scanned proton and carbon ion pencil beams for improved beam models in ion therapy treatment planning". *Phys Med Biol*, 2011, 56:24, pp. 7813–7827. DOI: 10.1088/0031-9155/56/24/009.

[41] Looe, H. K., Harder, D., and Poppe, B. "Understanding the lateral dose response functions of high-resolution photon detectors by reverse Monte Carlo and deconvolution analysis". *Phys Med Biol*, 2015, 60:16, pp. 6585–6607. DOI: 10.1088/0031-9155/60/16/6585.

[42] Looe, H. K., Stelljes, T. S., Foschepoth, S., Harder, D., Willborn, K., and Poppe, B. "The dose response functions of ionization chambers in photon dosimetry – Gaussian or non-Gaussian?" *Z Med Phys*, 2013, 23:2, pp. 129–143. DOI: 10.1016/j.zemedi.2012.12.010.

[43] Poppinga, D., Meyners, J., Delfs, B., Muru, A., Harder, D., Poppe, B., and Looe, H. "Experimental determination of the lateral dose response functions of detectors to be applied in the measurement of narrow photon-beam dose profiles". *Phys Med Biol*, 2015, 60:24, pp. 9421–9436. DOI: 10.1088/0031-9155/60/24/9421.

[44] Laub, W. U. and Wong, T. "The volume effect of detectors in the dosimetry of small fields used in IMRT". *Med Phys*, 2003, 30:3, pp. 341–347. DOI: 10.1118/1.1544678.

[45] Harder, D., Looe, H., and Poppe, B. "Convolutions and Deconvolutions in Radiation Dosimetry". In: *Comprehensive Biomedical Physics*. Elsevier, 2014, pp. 249–269. DOI: 10.1016/B978-0-444-53632-7.00913-8.

[46] Looe, H. K., Delfs, B., Poppinga, D., Jiang, P., Harder, D., and Poppe, B. "The 'cutting away' of potential secondary electron tracks explains the effects of beam size and detector wall density in small-field photon dosimetry". *Phys Med Biol*, 2017, 63:1, p. 015001. DOI: 10.1088/1361-6560/aa9b46.

[47] Safai, S., Bortfeld, T., and Engelsman, M. "Comparison between the lateral penumbra of a collimated double-scattered beam and uncollimated scanning beam in proton radiotherapy". *Phys Med Biol*, 2008, 53:6, pp. 1729–1750. DOI: 10.1088/0031-9155/53/6/016.

[48] Winterhalter, C., Meier, G., Oxley, D., Weber, D., Lomax, A., and Safai, S. "Contour scanning, multi-leaf collimation and the combination thereof for proton pencil beam scanning". *Phys Med Biol*, 2018, 64:1, p. 015002. DOI: 10.1088/1361-6560/aaf2e8.

[49] Winterhalter, Lomax, A., Oxley, D., Weber, D. C., and Safai, S. "A study of lateral fall-off (penumbra) optimisation for pencil beam scanning (PBS) proton therapy". *Phys Med Biol*, 2018, 63:2, p. 025022. DOI: 10.1088/1361-6560/aaa2ad.

[50] Farr, J. B., Moskvin, V., Lukose, R. C., Tuomanen, S., Tsiamas, P., and Yao, W. "Development, commissioning, and evaluation of a new intensity modulated minibeam proton therapy system". *Med Phys*, 2018, 45:9, pp. 4227–4237. DOI: 10.1002/mp.13093.

[51] Bäumer, C., Fuentes, C., Janson, M., Matic, A., Timmermann, B., and Wulff, J. "Stereotactical fields applied in proton spot scanning mode with range shifter and collimating aperture". *Phys Med Biol*, 2019, 64:15, p. 155003. DOI: 10.1088/1361-6560/ab2ae7.

[52] Gelover, E., Wang, D., Hill, P. M., Flynn, R. T., Gao, M., Laub, S., Pankuch, M., and Hyer, D. E. "A method for modeling laterally asymmetric proton beamlets resulting from collimation: Asymmetric proton beamlet modeling". *Med Phys*, 2015, 42:3, pp. 1321–1334. DOI: 10.1118/1.4907965.

[53] Hyer, D. E., Hill, P. M., Wang, D., Smith, B. R., and Flynn, R. T. "A dynamic collimation system for penumbra reduction in spot-scanning proton therapy: Proof of concept: Penumbra trimmer for spot scanning". *Med Phys*, 2014, 41:9, p. 091701. DOI: 10.1118/1.4837155.

[54] Hyer, D. E., Hill, P. M., Wang, D., Smith, B. R., and Flynn, R. T. "Effects of spot size and spot spacing on lateral penumbra reduction when using a dynamic collimation system for spot scanning proton therapy". *Phys Med Biol*, 2014, 59:22, N187–N196. DOI: 10.1088/0031-9155/59/22/N187.

[55] Titt, U., Mirkovic, D., Sawakuchi, G. O., Perles, L. A., Newhauser, W. D., Taddei, P. J., and Mohan, R. "Adjustment of the lateral and longitudinal size of scanned proton beam spots using a pre-absorber to optimize penumbrae and delivery efficiency". *Phys Med Biol*, 2010, 55:23, pp. 7097–7106. DOI: 10.1088/0031-9155/55/23/S10.

[56] Pedroni, E. et al. "The 200-MeV proton therapy project at the Paul Scherrer Institute: Conceptual design and practical realization". *Med Phys*, 1995, 22:1, pp. 37–53. DOI: 10.1118/1.597522.

[57] Meier, G., Leiser, D., Besson, R., Mayor, A., Safai, S., Weber, D. C., and Lomax, A. J. "Contour scanning for penumbra improvement in pencil beam scanned proton therapy". *Phys Med Biol*, 2017, 62:6, pp. 2398–2416. DOI: 10.1088/1361-6560/aa5dde.

[58] Ciocca, M. et al. "Design and commissioning of the non-dedicated scanning proton beamline for ocular treatment at the synchrotron-based CNAO facility". *Med Phys*, 2019, 46:4, pp. 1852–1862. DOI: 10.1002/mp.13389.

[59] Fleury, E. et al. "Characterization of the HollandPTC proton therapy beamline dedicated to uveal melanoma treatment and an interinstitutional comparison". *Med Phys*, 2021, 48:8, pp. 4506–4522. DOI: 10.1002/mp.15024.

[60] Saini, J., Maes, D., Regmi, R., Fung, A., Bloch, C., Schwarz, M., Stacey, A., Chen, J., Rengan, R., and Halasz, L. "Improved lateral penumbra for proton ocular treatments on a general-purpose spot scanning beamline". *Phys Med*, 2023, 107, p. 102551. DOI: 10.1016/j.ejmp.2023.102551.

[61] Slopsema, R. L., Mamalui, M., Zhao, T., Yeung, D., Malyapa, R., and Li, Z. "Dosimetric properties of a proton beamline dedicated to the treatment of ocular disease: Dosimetry of a proton eyeline". *Med Phys*, 2013, 41:1, p. 011707. DOI: 10.1118/1.4842455.

[62] Wulff, J., Koska, B., Janson, M., Bäumer, C., Denker, A., Geismar, D., Gollrad, J., Timmermann, B., and Heufelder, J. "Technical note: Impact of beam properties for uveal melanoma proton therapy—An in silico planning study". *Med Phys*, 2022, 49:5, pp. 3481–3488. DOI: 10.1002/mp.15573.

[63] Wang, D., Dirksen, B., Hyer, D., Buatti, J. M., Sheybani, A., Dinges, E., Felderman, N., TenNapel, M., Bayouth, J. E., and Flynn, R. "Impact of spot size on plan quality of spot scanning proton radiosurgery for peripheral brain lesions". *Med Phys*, 2014, 41:12, p. 121750. DOI: 10.1118/1.4901260.

[64] Lee, E., Meyer, J., and Sandison, G. “Collimator design for spatially-fractionated proton beams for radiobiology research”. *Phys Med Biol*, 2016, 61:14, pp. 5378–5389. DOI: 10.1088/0031-9155/61/14/5378.

[65] Barazzuol, L., Coppes, R. P., and Van Luijk, P. “Prevention and treatment of radiotherapy-induced side effects”. *Mol Oncol*, 2020, 14:7, pp. 1538–1554. DOI: 10.1002/1878-0261.12750.

[66] Biltekin, F., Bäumer, C., Esser, J., Ghanem, O., Ozyigit, G., and Timmermann, B. “Preclinical Dosimetry for Small Animal Radiation Research in Proton Therapy: A Feasibility Study”. *Int J Part Ther*, 2023, 10:1, pp. 13–22. DOI: 10.14338/IJPT-22-00035.1.

[67] Clausen, M., Ruangchan, S., Sotoudegan, A., Resch, A. F., Knäusl, B., Palmans, H., and Georg, D. “Small field proton irradiation for in vivo studies: Potential and limitations when adapting clinical infrastructure”. *Z Med Phys*, 2023, 33:4, pp. 542–551. DOI: 10.1016/j.zemedi.2022.10.002.

[68] Gerlach, S. et al. “Beam characterization and feasibility study for a small animal irradiation platform at clinical proton therapy facilities”. *Phys Med Biol*, 2020, 65:24, p. 245045. DOI: 10.1088/1361-6560/abc832.

[69] Urago, Y., Sakama, M., Sakata, D., Fukuda, S., Katayose, T., and Chang, W. “Monte Carlo-calculated beam quality and perturbation correction factors validated against experiments for Farmer and Markus type ionization chambers in therapeutic carbon-ion beams”. *Phys Med Biol*, 2023, 68:18, p. 185013. DOI: 10.1088/1361-6560/acf024.

[70] Das, I. J. et al. “Report of AAPM Task Group 155: Megavoltage photon beam dosimetry in small fields and non-equilibrium conditions”. *Med Phys*, 2021, 48:10, e886–e921. DOI: 10.1002/mp.15030.

[71] Baumann, K.-S., Kaupa, S., Bach, C., Engenhart-Cabillic, R., and Zink, K. “Monte Carlo calculation of perturbation correction factors for air-filled ionization chambers in clinical proton beams using TOPAS/GEANT”. *Z Med Phys*, 2021, 31:2, pp. 175–191. DOI: 10.1016/j.zemedi.2020.08.004.

2

Monte Carlo simulated beam quality and perturbation correction factors for ionization chambers in monoenergetic proton beams

This Chapter is published as: **Kretschmer, J.**, Dulkys, A., Brodbek, L., Stelljes, T.S., Looe, H.K., and Poppe, B. "Monte Carlo simulated beam quality and perturbation correction factors for ionization chambers in monoenergetic proton beams." *Med Phys*, 2020, 47:11, pp. 5890-5905. DOI: https://doi.org/10.1002/mp.14499

The Chapter is identical in content to the publication. However, due to a technical error by the publisher during the production process, a table in the article was incomplete. The missing part was added in this chapter and highlighted in light blue according to this sentence. The correction was published as: "Erratum: "Monte Carlo simulated beam quality and perturbation correction factors for ionization chambers in monoenergetic proton beams" [Med. Phys. 47, 5890–5905 (2020)]." *Med Phys*, 2021, 48:6, pp. 3284-3284, DOI: https://doi.org/10.1002/mp.14773

The author contributions are listed in Appendix A in the "Statement on own contributions".

Abstract

Purpose: Beam quality correction factors provided in current codes of practice for proton beams are approximated using the water-to-air mass stopping power ratio and by assuming the proton beam quality related perturbation correction factors to be unity. The aim of this work is to use Monte Carlo simulations to calculate energy dependent beam quality and perturbation correction factors for a set of nine ionization chambers in proton beams.
Methods: The Monte Carlo code EGSnrc was used to determine the ratio of the absorbed dose to water and the absorbed dose to the sensitive air volume of ionization chambers f_{Q_0} related to the reference photon beam quality ($^{60}\mathrm{Co}$). For proton beams, the quantity f_Q was simulated with GATE/Geant4 for five monoenergetic beam energies between 70 MeV and 250 MeV. The perturbation correction factors for the air cavity, chamber wall, chamber stem, central electrode and displacement effect in proton radiation were investigated separately. Additionally, the correction factors of cylindrical chambers were investigated with and without consideration of the effective point of measurement.
Results: The perturbation factors p_Q were shown to deviate from unity for the investigated chambers, contradicting the assumptions made in dosimetry protocols. The beam quality correction factors for both plane-parallel and cylindrical chambers positioned with the effective point of measurement at the measurement depth were constant within 0.8%. An increase of the beam quality correction factors determined for cylindrical ionization chambers placed with their reference point at the measurement depth with decreasing energy is attributed to the displacement perturbation correction factors p_{dis}, which were up to 1.045 ± 0.1% for the lowest energy and 1.005 ± 0.1% for the highest energy investigated. Besides p_{dis}, the largest perturbation was found for the chamber wall where the smallest p_{wall} determined was 0.981 ± 0.3%.
Conclusions: Beam quality correction factors applied in dosimetry with cylindrical chambers in monoenergetic proton beams strongly depend on the positioning method used. We found perturbation correction factors different from unity. Consequently, the approximation of ionization chamber perturbations in proton beams by the respective water-to-air mass stopping power ratio shall be revised.

Keywords: correction factors, effective point of measurement, EGSnrc, GATE/Geant4, proton dosimetry

2.1 Introduction

Ionization chambers used in radiation therapy are generally calibrated under $^{60}\mathrm{Co}$ radiation with beam quality Q_0. The measurement with such a calibrated chamber in a monoenergetic proton field having a different beam quality Q leads to a change in the chambers' dose response so that a correction with a beam quality correction factor k_{Q,Q_0} is required [1]. Note that this factor is referred to as k_Q whenever the reference beam quality is $^{60}\mathrm{Co}$ radiation [1]. k_Q inherits the beam quality related changes in the mean energy needed to produce an ion pair in air W_a, the water-to-air mass stopping-power ratio $s_{w,a}$, and the ionization chamber specific perturbation correction p [1]. k_Q depends on the chamber type and can be determined either experimentally [2, 3, 4, 5] or using Monte Carlo simulations by calculating the ratio of the absorbed dose to water D_{w} and the absorbed dose to the sensitive air volume of the ionization chamber D_{Cham} at both beam qualities [6, 7, 8]. Depending on the respective beam quality, this ratio is referred to as f_Q or f_{Q_0} and can also be described by the product of $(s_{\mathrm{w,a}})_{Q/Q_0}$ and p_{Q/Q_0} [7, 8, 6, 9].

Current dosimetry protocols, like the IAEA TRS-398 [1] and the German DIN6801-1 [10] assume that the perturbation correction factor p_Q can be approximated as unity for proton beams such that f_Q is described solely by $(s_{\mathrm{w,a}})_Q$ and the ionization chamber specific perturbations are only considered by a relatively large uncertainty for f_Q of up to 1.3% [1]. The German code of practice DIN6801-1 [10] states that the uncertainty in assuming p_Q being equal to unity is 0.1%. Together with the uncertainty for $(s_{\mathrm{w,a}})_Q$, this leads to an uncertainty for f_Q of 1.5%. Moreover, DIN6801-1 suggests a constant f_Q and k_Q for monoenergetic proton beams with residual ranges larger than 1.5 cm by arguing that the variance in k_Q is 0.2% [10]. The assumptions in the dosimetry protocols were questioned in the past. With the motivation to reduce the uncertainty of p_Q, f_Q and k_Q for ionization chamber measurements in monoenergetic proton beams, several Monte Carlo based studies were carried out in recent years [6, 7, 8, 11, 9]. Monte Carlo simulated f_Q and/or k_Q factors for monoenergetic proton beams were calculated by Gomà *et al.* [7], Wulff *et al.* [9], Gomà and Sterpin [8] and Baumann *et al.* [6] for several ionization chambers under consideration of the latest ICRU Report 90 [12]. In these studies, all factors were determined for various incident proton energies. Furthermore, the perturbation correction factors p_Q were individually investigated by Lourenço *et al.* [11] and Baumann *et al.* [6].

Gomà *et al.* [7] determined k_Q for a set of three cylindrical and nine plane-parallel ionization chambers with the Monte Carlo Code PENH [13] in combination with GAMOS [14], which is based on Geant4 [15]. Wulff *et al.* [9] investigated ionization chamber

calculations in proton beams with the Monte Carlo Code TOPASv3.1.p1 [16] based on GEANT4.10.3.p1 [15] and determined f_Q factors for a Farmer type and a plane-parallel ionization chamber. Lourenço *et al.* [11] used the Monte Carlo Code FLUKA [17] and determined p_Q for three plane-parallel ionization chambers, which deviate from unity by up to 1%. Gomà and Sterpin [8] presented k_Q factors for fifteen ionization chambers, which were also determined with the Monte Carlo code PENH [13]. More recently, Baumann *et al.* [6] presented k_Q factors for six plane-parallel and four cylindrical ionization chambers that were simulated with TOPASv3.1.p1/Geant4.10.03.p01 [16, 15]. Comparing their f_Q to literature, Baumann *et al.* found differences to Gomà *et al.* [7] of up to 0.9%, differences to Wulff *et al.* [9] of 0.5% and differences to the study by Gomà and Sterpin [8] of up to 1.2%, which were predominantly found for high proton energies. In addition, Baumann *et al.* simulated perturbation correction factors for the individual chamber parts of one cylindrical ionization chamber and found an overall value of p_Q = 0.987 ± 0.7%, where the perturbation from the chamber wall had the largest contribution by 1.5% [6]. Compared to photon beam dosimetry, there is still a strong deficiency of chamber specific correction factors in the literature valid for proton beams.

In this work, the beam quality correction factors k_Q and perturbation correction factors p_Q were calculated for nine ionization chambers in monoenergetic proton beams with incident energies between 70 MeV and 250 MeV using Monte Carlo simulations. Three of the chambers investigated were cylindrical ionization chambers for which to our knowledge k_Q or p_Q factors have not been determined so far for proton fields. While the absorbed dose to water and the absorbed dose to the sensitive air volume in the $^{60}\mathrm{Co}$ field were calculated with the EGSnrc code system (Version 2019a) [18, 19], the proton radiation related quantities were determined in GATE V8.0/Geant4 10.04.p01 [20, 15]. In contrast to the publications in the literature, f_Q and k_Q for cylindrical chambers were not only determined for the positioning with their reference points placed at the measurement depth, but also under the consideration of the chambers' effective point of measurement (EPOM). In addition, the perturbation correction factors p_Q for the ionization chambers were analyzed with respect to the contributions from the individual chamber components comprising the perturbation by the air cavity, chamber wall, chamber stem, central electrode and the displacement effect.

2.2 Materials and Methods

2.2.1 Calculated quantities

The beam quality correction factor k_Q calculated for various ionization chambers is defined as follows:

$$k_Q = \frac{\left(\frac{D_\mathrm{w}}{D_\mathrm{Cham}}\right)_Q}{\left(\frac{D_\mathrm{w}}{D_\mathrm{Cham}}\right)_{Q_0}} \cdot \frac{(W_\mathrm{a})_Q}{(W_\mathrm{a})_{Q_0}} = \frac{f_Q}{f_{Q_0}} \cdot \frac{(W_\mathrm{a})_Q}{(W_\mathrm{a})_{Q_0}} \tag{2.1}$$

where $\left(\frac{D_\mathrm{w}}{D_\mathrm{Cham}}\right)_{Q/Q_0}$ is the ratio of the absorbed dose to water D_w and the absorbed dose to the chamber's sensitive air volume D_Cham at the proton beam quality Q or reference beam quality Q_0, and $(W_a)_{Q/Q_0}$ is the mean energy needed to produce an ion pair in air at the respective beam quality [7]. The ratio $\frac{(W_\mathrm{a})_Q}{(W_\mathrm{a})_{Q_0}}$ is provided in ICRU Report 90 [12]. The ratios $\left(\frac{D_\mathrm{w}}{D_\mathrm{Cham}}\right)_Q$ and $\left(\frac{D_\mathrm{w}}{D_\mathrm{Cham}}\right)_{Q_0}$ are also referred to as the so-called f_Q and f_{Q_0} factors, respectively [6, 7, 8, 9]. In this case the proton beam specific factor f_Q is defined by:

$$f_Q = \left(s_\mathrm{w,a}\right)_Q \cdot p_Q \tag{2.2}$$

where $\left(s_\mathrm{w,a}\right)_Q$ is the stopping power ratio of water and air at the measurement point in the beam quality Q and p_Q is the perturbation correction factor that accounts for the perturbation by the individual components of the ionization chamber causing the deviation from ideal Bragg-Gray detector conditions [1, 10]. For cylindrical ionization chambers p_Q is given by:

$$p_Q = p_\mathrm{cav} \cdot p_\mathrm{dis} \cdot p_\mathrm{cel} \cdot p_\mathrm{wall} \cdot p_\mathrm{stem} \tag{2.3}$$

where p_cav corrects for the perturbation from the extended air cavity, p_dis is the correction factor for the displacement effect, p_cel is central electrode correction, p_wall is the outer electrode or wall material correction, and p_stem is the chamber stem correction [21]. For plane-parallel ionization chambers the equation reduces to [1, 22]:

$$p_Q = p_\mathrm{wall} \cdot p_\mathrm{cav} \tag{2.4}$$

The factors f_{Q_0}, f_Q, k_Q and p_Q, were investigated individually for various cylindrical and plane-parallel ionization chambers.

2.2.2 Monte Carlo simulation of f_{Q_0}

The f_{Q_0} factor was determined with Monte Carlo simulations in egs_chamber/EGSnrc (version 2019a) [18, 19, 23]. This code has been shown to pass the fano cavity test with 0.1% accuracy [24] and is suitable for ionization chamber simulations in photon fields. To simulate the ratio f_{Q_0}, the definition of the calibration conditions in IAEA TRS-398 [1] and DIN6801-1 [10] are adopted. The absorbed dose to the ionization chamber D_{Cham,Q_0} was scored by placing the investigated chamber with its reference point at a depth z_{Q_0} of 5 cm in a 30 x 30 x 30 cm^3 water phantom irradiated with a 10 x 10 cm^2 field of ^{60}Co radiation. For the determination of D_{w,Q_0}, a cylinder with a radius of 1 cm and a thickness of 250 µm was used as scoring volume and positioned with its center at the measurement depth z_{Q_0} [6, 7, 8]. The source was defined as parallel beam using the ^{60}Co spectrum from Mora *et al.* [25] An overview on the simulation settings used in EGSnrc is provided in Table 2.1 according to recommendations of Sechopoulos *et al.* [26].

Table 2.1. Simulation settings in EGSnrc used to determine the f_{Q_0} factors for various ionization chambers.

Item name	Description	References
Code, version, release	egs_chamber/EGSnrc (version 2019a), released on May 8, 2019	Kawrakow [18] Kawrakow *et al.* [19] Wulff *et al.* [23]
Validation	Fano cavity test passed with 0.1% accuracy	Kawrakow [24]
Source description	10x10 cm^2 parallel beam with ^{60}Co spectrum	Mora *et al.* [25]
Cross-Sections and transport parameters		
Brems cross sections	BH	
Photon cross sections	xcom	
Radiative Compton corrections	Off	
Compton cross sections	default	
Photonuclear cross sections	default	
Pair cross sections	BH	
Spin effects	On	
Brems angular sampling	KM	
Electron Impact Ionization	Off	
Triplet production	Off	
Bound Compton scattering	norej	
Pair angular sampling	Simple	
Photoelectron angular sampling	On	
Rayleigh scattering	On	
Atomic relaxations	On	
Photonuclear attenuation	Off	
Boundary crossing algorithm	Exact	
Electron-step algorithm	EGSnrc	
Global Ecut	0.512 MeV	
Global Pcut	0.001 MeV	
Global Smax	1.00E+10	
ESTEPE	0.25	
Ximax	0.5	
Skin depth for BCA	3	

Table 2.1. Simulation settings in EGSnrc used to determine the f_{Q_0} factors for various ionization chambers. (continued)

Item name	Description	References
Variance reduction techniques		
photon cross-section enhancement	XCSE enhancement factor = 512 within a region surrounding the scoring geometry of 1 cm	
Russian Roulette	Rejection factor = 512, Esave = 521 keV	
Scored quantities	Dose in sensitive volume	
# histories/statistical uncertainty	20 single batches on a cluster were used with 1E9 or 1E8 histories each	
Timing	The equivalent total simulation time for one point on a single CPU was up to 320 hours	
Statistical methods	batch method	Seco and Verhaegen [27]
Postprocessing	Dose from the output file is extracted with MATLAB R2019b [28]	

2.2.3 Monte Carlo simulations of p_Q and f_Q

At the time of writing the definition of reference conditions for monoenergetic proton beams differs between the German code of practice DIN6801-1 [10] and the international IAEA TRS-398 [1] code of practice. An overview of the definitions is shown in Table 2.2. While both protocols state that reference dosimetry should be performed in water and for a field size of 10 x 10 cm^2, the recommendations for the positioning of ionization chambers and the measurement depth differ. According to DIN6801-1, ionization chambers shall be positioned at a measurement depth of 3 cm for monoenergetic proton fields with $E \geq 100$ MeV while the measurement depth for lower proton energies is to be decided depending on energy. For the positioning of cylindrical ionization chambers, DIN6801-1 states that the chamber specific EPOM should be considered. This is done by placing the

reference point or central axis of the cylindrical chamber by a shift Δz_Q further down in the water phantom. This shift Δz_Q needs to be determined for each chamber individually and can be approximated by 0.75 times the radius of the sensitive air volume of the chamber [10]. IAEA TRS-398 only explicitly defines reference conditions for energy modulated beams and comments that in the case of monoenergetic proton beams, reference dosimetry shall be performed in the plateau region at 3 cm depth. It is suggested to only use plane-parallel chambers for residual ranges $R_{\text{res}} < 0.5$ g/cm^2 and to position ionization chambers with their reference points at the measurement depth [1]. It should be mentioned that the IAEA TRS-398 is currently being updated [8].

In this work, f_Q and p_Q were determined at a depth z_Q of 2 cm in a 40 x 40 x 40 cm^3 water phantom. The depth was chosen to slightly differ from the recommendations in the two mentioned codes of practice because this allows a comparison to f_Q and k_Q determined in the literature [6, 7, 8, 11, 9]. Simulations were performed for incident proton energies between 70 MeV ($R_{\text{res}} = 2.18$ cm) and 250 MeV ($R_{\text{res}} = 36.69$ cm). The influence of the positioning method of cylindrical ionization chambers was investigated by simulating the f_Q factors under consideration of the EPOM (reference point at depth $z_Q + \Delta z_Q$) as well as by placing the chambers with their reference points at the measurement depth z_Q.

The Monte Carlo simulations for f_Q and p_Q in proton beams were performed with the code GATE V8.0/Geant4 10.04.p01 [20, 15]. The physics parameter settings in GATE/Geant4 were chosen under consideration of a publication by Wulff *et al.* [9], who investigated the configuration of ionization chamber simulations in proton beams in TOPAS/Geant4.10.03.p1 [16, 15]. Wulff *et al.* showed that with an appropriate physics parameter setting in Geant4, a fano cavity test for protons was passed at a 0.1% level and that f_Q factors determined for two detailed ionization chamber models agreed with those presented by Gomà *et al.* [7] showing maximum deviations of 0.6% at the highest energy. While Wulff *et al.* determined f_Q factors for two different physics lists varying in the hadronic interaction models, this work will focus on one of those physics lists by using the binary cascade model (BIC) of Geant4 to simulate the nuclear interactions. Wulff *et al.* showed that the differences between the two models lead to a maximum deviation of 0.3% ± 0.1% at the highest energy [9]. Hence, simulations were performed with physics list QGSP_BIC in combination with EMStandardOpt4 as defined in Geant4.10.04.p1. Within the chamber geometry and a 5 mm margin around it, the production cuts for electrons, positrons, protons and photons were limited to 1 µm and the maximum step size in this region was set to 1 mm. For electron transport, the Goudsmit-Saunderson MSC model was used together with the fUseSafetyPlus as G4MscStepLimitType. Moreover, the following settings were used for electrons: range factor of 0.2, finalRange of 0.01 mm and dRoverRange of 0.2. Simiele and DeWerd [29] investigated various Geant4

parameters for electron transport and showed that if the Goudsmit-Saunderson MSC model is used with the UseSafetyPlus MSC step limitation in GEANT4 v10.04.p01, which is the case for this work, agreement with theory within 0.5% can be obtained without large step size restrictions. For proton transport a dRoverRange of 0.1, a finalRange of 10 µm and fUseMinimal as the G4MscStepLimitType were used following the study by Wulff *et al.* [9], who found that an additional reduction of dRoverRange to 0.05, a limitation of the maximum step size to 1 mm and changing the G4MscStepLimitType to fUseDistanceToBoundary for protons did not lead to differences in f_Q outside of the statistical uncertainty for one test simulation for a plane-parallel IBA NACP-02 ionization chamber. A summary of the chosen settings for the simulation in GATE/Geant4 is given in Table 2.3 following recommendations by Sechopoulos *et al.* [26].

The absorbed dose to water $D_{\mathrm{w},Q}$ was calculated in a cylinder with a radius of 1 cm and a thickness of 250 µm [6, 7, 8, 9]. All ionization chambers were positioned with their reference points at the measurement depth z_Q to simulate the absorbed dose to the ionization chambers' sensitive volumes $D^{\mathrm{Ref}}_{\mathrm{Cham},Q}$. Additionally, to investigate the influence of the displacement effect on the measurement with cylindrical ionization chambers, the absorbed dose $D^{\mathrm{EPOM}}_{\mathrm{Cham},Q}$ were simulated by placing the chambers with their EPOM at the measurement depth. The ratio $\frac{D_{\mathrm{w},Q}}{D^{\mathrm{Ref}}_{\mathrm{Cham},Q}}$ will then give the f^{Ref}_Q factor for the reference point positioning and the ratio $\frac{D_{\mathrm{w},Q}}{D^{\mathrm{EPOM}}_{\mathrm{Cham},Q}}$ defines f^{EPOM}_Q for cylindrical chambers positioned under consideration of their EPOM.

The approaches to determine p_Q factors have been presented in various studies [6, 11, 21, 22]. The simulated absorbed dose values that were determined to calculate the various p_Q for cylindrical chambers are illustrated in Figure 2.1. $D_{\mathrm{w},Q}$ was simulated as described above. In a next step, the absorbed dose to the chamber cavity $D_{\mathrm{cav},Q}$ was scored with the central axis, or reference point, of the cavity positioned at the measurement depth z_Q. The ratio $\frac{D_{\mathrm{w},Q}}{D_{\mathrm{cav},Q}}$ inherits two perturbation correction factors, namely p_{cav} and p_{dis}, and the water-to-air stopping power ratio $(s_{\mathrm{w,a}})_Q$. Under consideration of $(s_{\mathrm{w,a}})_Q$ calculated with PENH [13] in Gomà and Sterpin [8] based on the mean excitation energies recommended for water and air in the latest ICRU Report 90 $p_{\mathrm{cav}} \cdot p_{\mathrm{dis}}$ were separated from the ratio. Because Gomà and Sterpin [8] found an agreement within 0.1% to the $(s_{\mathrm{w,a}})_Q$ by Gomà *et al.* [30] determined in GAMOS/Geant4 [15, 14] an uncertainty of 0.1% for the $(s_{\mathrm{w,a}})_Q$ by Gomà and Sterpin [8] was assumed in this work. The perturbation factors p_{cel}, p_{wall} and p_{stem} are calculated with simulations, in which the individual chamber parts were added successively, and again by determining the ratio of the corresponding absorbed dose values. Finally, to isolate p_{cav} from p_{dis}, the perturbation correction factor compensating for the displacement effect p_{dis} is determined by calculating the ratio $\frac{D^{\mathrm{Ref}}_{\mathrm{Cham},Q}}{D^{\mathrm{EPOM}}_{\mathrm{Cham},Q}}$.

For cylindrical ionization chambers, the overall perturbation correction factors p_Q were determined under consideration of the two different positioning approaches. For the reference point positioning, p_Q^{Ref} was determined by the product of all individual factors p_{cel}, p_{wall}, p_{stem}, p_{cav}, p_{dis}. In contrast, when positioning the ionization chamber with its EPOM at the measurement depth, p_{dis} was already corrected for by shifting the chamber by Δz_Q further down in the water phantom during the simulations, such that p_Q^{EPOM} resulted from the product of p_{cel}, p_{wall}, p_{stem} and p_{cav} only. The simulations performed for plane-parallel ionization chambers only consisted of the determination of $D_{\text{cav},Q}$ and $D_{\text{Cham},Q}^{\text{Ref}}$ because p_Q for plane-parallel chambers is defined by the product of p_{cav} and p_{wall} [1, 22], where the EPOM is considered to lie at the chamber's reference point.

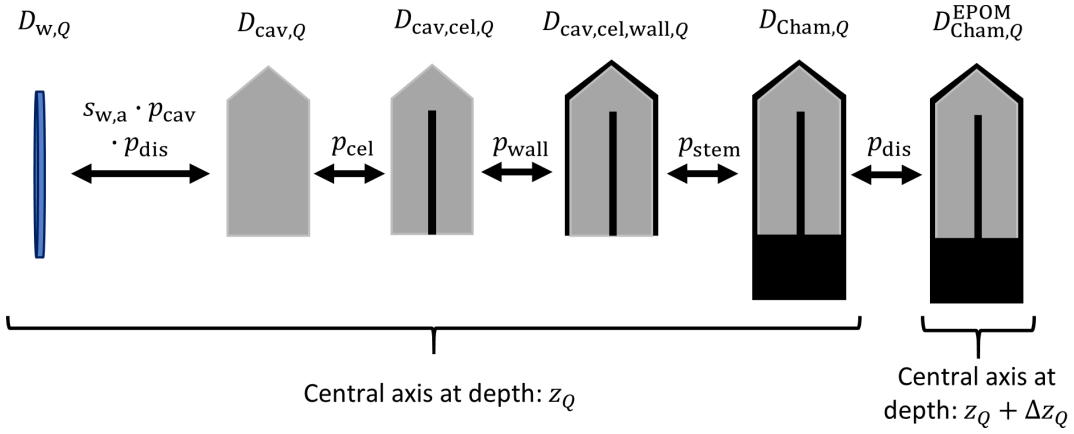

Figure 2.1. Illustration of simulated quantities to determine the individual perturbation correction factors for cylindrical ionization chambers.

Table 2.2. Comparison of the definition of reference conditions for monoenergetic proton beams between DIN6801-1 [10] and IAEA TRS-398 [1].

	DIN6801-1	**IAEA TRS-398**
Phantom material	Water	Water
Field size	10 x 10 cm^2	10 x 10 cm^2
Depth *z*	>100 MeV: 3 cm <100 MeV: depending on energy	3 cm
Chamber type	R_{res} ≥ 1.5 cm: Compact chambers R_{res} <1.5 cm: suitable, small plane-parallel chambers or suitable, small compact chambers	R_{res} ≥ 0.5 g/cm^2: cylindrical and plane-parallel R_{res} <0.5 g/cm^2: plane-parallel
Chamber positioning	Effective point of measurement	Reference point

Table 2.3. Simulation settings in GATE/Geant4 used to determine the f_Q factors for various ionization chambers.

Item name	Description	References
Code, version, release date	GATE V8.0 released April 20, 2017 and Geant4 10.04.p01 released on February 28, 2018	Agostinelli *et al.* [15], Jan *et al.* [20]
Validation	Proton transport: Fano cavity test was passed at a 0.1% level; Electron transport: Agreement with theory within 0.5%	Wulff *et al.* [9]; Simiele and DeWerd [29]
Source description	10x10 cm^2 parallel beam of monoenergetic protons with incident energies of 70 MeV, 100 MeV, 150 MeV, 200 MeV, and 250 MeV	
Physics list	QGSP_BIC_EMZ (EMstandardOpt4)	
Electron transport		
MSC model	Goudsmit-Saunderson (E <100 MeV), WentzelIV (E >100 MeV)	
MSC range factor	0.2	
MSC step limitation	fUseSafetyPlus	
skin	3	
e–/e+ ionization model	Penelope Ionisation (E <1 MeV), Moller Bhaba (E >1 MeV)	
dRoverRange	0.2	
final range	10 µm	
Production cut	1 µm (scoring volume + 5 mm margin), 1 mm (water phantom)	
Maximum step size	1 mm (scoring volume + 5 mm margin)	

Table 2.3. Simulation settings in GATE/Geant4 used to determine the f_Q factors for various ionization chambers. (continued)

Item name	Description	References
Proton transport		
MSC model	WentzelVI Model	
MSC range factor	0.2	
MSC step limitation	fMinimal	
Hadron ionization model	Bragg (E <2 MeV), Bethe-Bloch Formula (E >2 MeV)	
dRoverRange	0.1	
final range	10 μm	
Production cut	1 μm (scoring volume + 5 mm margin), 1 mm (water phantom)	
Maximum step size	1 mm (scoring volume + 5 mm margin)	
Variance reduction techniques	-	
Scored quantities	Energy deposited in sensitive volume	
# histories/statistical uncertainty	200 single batches on a cluster were used with 1E7 and 8E7 primary particles	
Timing	The equivalent total simulation time for one point on a single CPU corresponds to up to 800 days	
Statistical methods	batch method	Seco and Verhaegen [27]
Postprocessing	The scored energy deposited from the output files was extracted with MATLAB R2019b [28] and divided by the density and volume of the sensitive volume	

2.2.4 Investigated ionization chambers

Four plane-parallel and five cylindrical ionization chambers were investigated in this work. Chamber geometries were implemented in the two Monte Carlo codes EGSnrc [18, 19] and GATE V8.0/Geant4 [15, 20] based on construction drawings. The plane-parallel ionization chambers were the NACP-02 (IBA Dosimetry, Schwarzenbruck, Germany), Markus 23343 (PTW Freiburg, Germany), Advanced Markus 34045 (PTW Freiburg, Germany), and Roos 34001 (PTW Freiburg, Germany). As cylindrical chambers, the Farmer chamber NE 2571, Farmer 30013 (PTW Freiburg, Germany), PinPoint 31014 (PTW Freiburg, Germany), Semiflex 3D 31021 (PTW Freiburg, Germany) and PinPoint 3D 31022 (PTW Freiburg, Germany) were studied. Detailed construction drawings of all PTW ionization chambers were provided by the manufacturer. The geometry information for the Farmer chamber NE 2571 was partly taken from Wulff *et al.* [21] and partly taken from the Phoenix Dosimetry website [31]. The IBA NACP-02 model was based on the one in Wulff *et al.* [9]. The geometries of all cylindrical chambers are illustrated in Figure 2.2. Table 2.4 provides information on the plane-parallel chambers. In both Monte Carlo codes, the materials water, air and graphite were generated by assigning the mean excitation energies $I_{\text{water}} = 78$ eV, $I_{\text{air}} = 85.7$ eV and $I_{\text{graphite}} = 81$ eV following the recommendations of ICRU Report 90 [12]. A ratio of $\frac{(W_{\text{a}})_Q}{(W_{\text{a}})_{Q_0}} = 1.014 \pm 0.4\%$ is used to calculate k_Q with $(W_{\text{a}})_Q = 34.44$ eV and $(W_{\text{a}})_{Q_0} = 33.97$ eV also according to ICRU Report 90 [12].

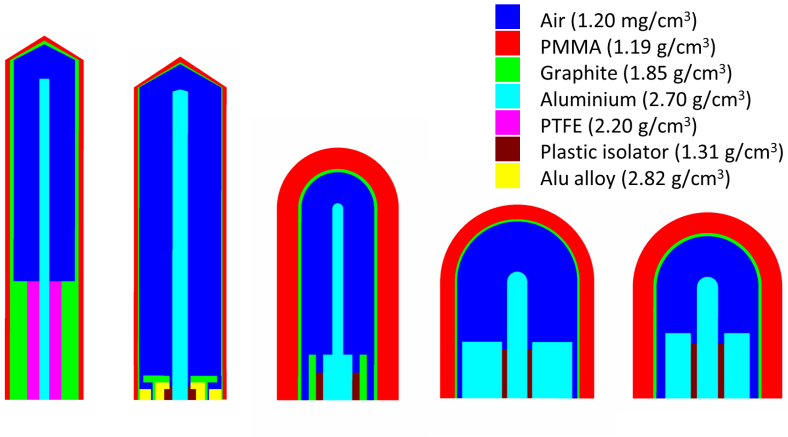

Figure 2.2. Geometries (not true to scale) and materials with density given in parenthesis of all cylindrical chambers investigated in this study visualized with egs_view from EGSnrc [18, 19]. Geometries from left to right: Farmer chamber NE 2571, PTW Farmer chamber 30013, PTW PinPoint 31014, PTW Semiflex 3D 31021 and PTW PinPoint 3D 31022.

Table 2.4. Geometry and material description of all plane-parallel chambers investigated in this work.

Ionization chamber	Composition and thickness of entrance window	Electrode spacing [mm]	Collecting electrode thickness	Radius of sensitive volume [mm]	Thickness of guard ring [mm]
IBA NACP-02	0.1 mm mylar (1.39 g/cm^3) 0.5 mm graphite (1.85 g/cm^3)	2	0.05 mm graphite (0.92 g/cm^3) 0.25 mm rexolite (1.05 g/cm^3)	5	3.25
PTW Markus	0.87 mm PMMA (1.19 g/cm3) 0.4 mm air (1.20 mg/cm^3) 0.03 mm PE (0.92 g/cm^3)	2.01	0.03 mm graphite (0.44 g/cm^3)	2.65	0.27
PTW Advanced Markus	0.87 mm PMMA (1.19 g/cm^3) 0.4 mm air (1.20 mg/cm^3) 0.03 mm PE (0.92 g/cm^3)	1	0.03 mm graphite (0.44 g/cm^3)	2.5	2
PTW Roos	1.01 mm PMMA (1.19 g/cm^3) 0.02 mm graphite (0.82 g/cm^3) 0.1 mm PMMA (1.19 g/cm^3)	2.01	0.03 mm graphite (0.44 g/cm^3)	7.8	4

2.3 Results

2.3.1 Monte Carlo simulated f_{Q_0}

The simulated f_{Q_0} factors determined in EGSnrc within this work are presented in Figure 2.3 in comparison to f_{Q_0} factors from literature that were simulated under consideration of the latest ICRU Report 90 recommendations [12].

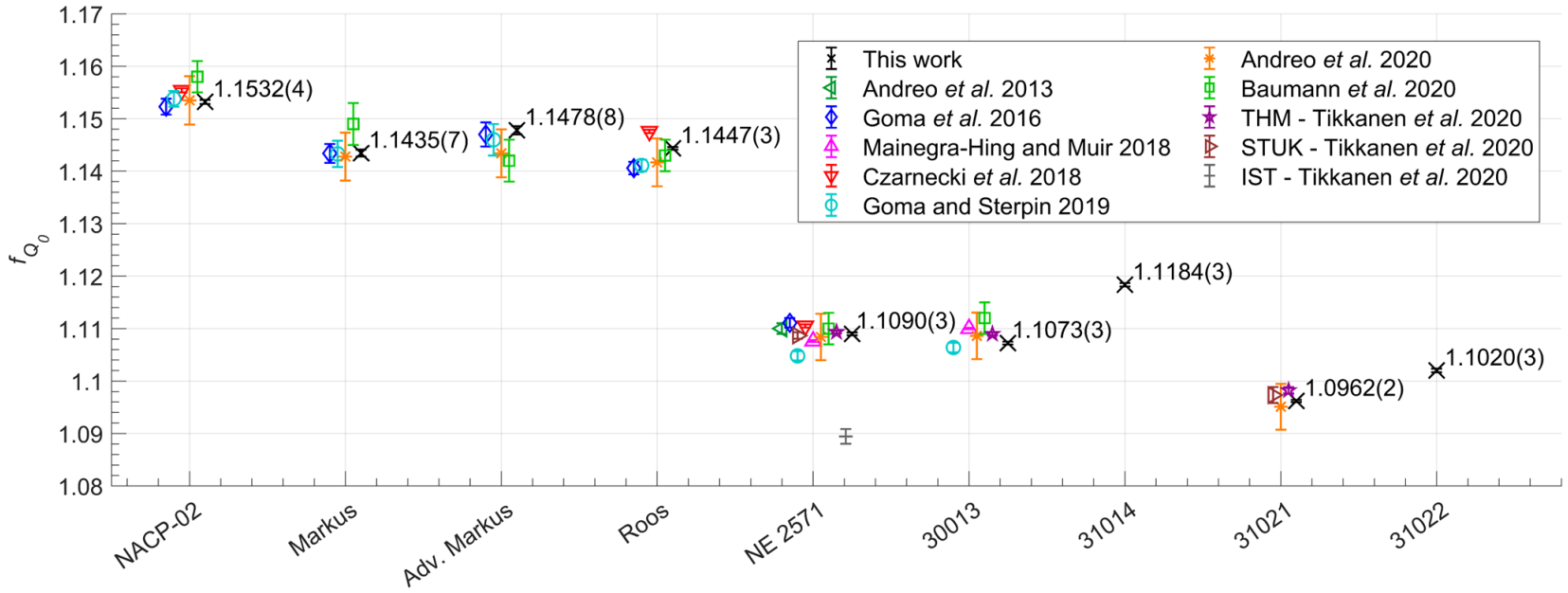

Figure 2.3. f_{Q_0} factors simulated with EGSnrc within this work in comparison to values determined based on the ICRU Report 90 [12] recommendations presented in literature [32, 33, 6, 34, 7, 8, 35, 36]. The f_{Q_0} factors determined in this work are listed next to the corresponding data point. The value within parenthesis corresponds to one standard deviation of the mean with respect to the last digit.

2.3.2 Monte Carlo simulated f_Q

Simulated f_Q ratios for all ionization chambers investigated are listed in Table 2.5. For each cylindrical chamber, two values are presented that were determined for the two positioning approaches. Figures 2.4 and 2.5 show f_Q for two cylindrical farmer type chambers and those of plane-parallel chambers, respectively, in comparison to literature.

The values of f_Q^{Ref} for cylindrical chambers placed with their reference points at the measurement depth increase with decreasing energy. This increase is most pronounced for large cylindrical chambers like the two Farmer chambers NE 2571 and PTW 30013, where the f_Q^{Ref} between 70 MeV and 250 MeV differ by 4.5%.

The positioning of cylindrical chambers with their EPOM at the measurement depth of 2 cm leads to a reduced energy dependence and nearly constant f_Q^{EPOM} with a maximum variation of 0.6% seen for the PTW Farmer chamber 30013. When comparing the f_Q^{EPOM} and f_Q^{Ref} for individual cylindrical chambers, the difference between both factors decreases with increasing energy. The largest difference between f_Q^{EPOM} and f_Q^{Ref} amounts to 4.5% at 70 MeV for the NE 2571 and still amounts to 0.5% at 250 MeV for both Farmer type chambers.

The f_Q determined for plane-parallel ionization chambers as shown in Figure 2.5 are nearly constant over the considered energy range with a maximum difference of 0.8% for the f_Q of the PTW Markus chamber.

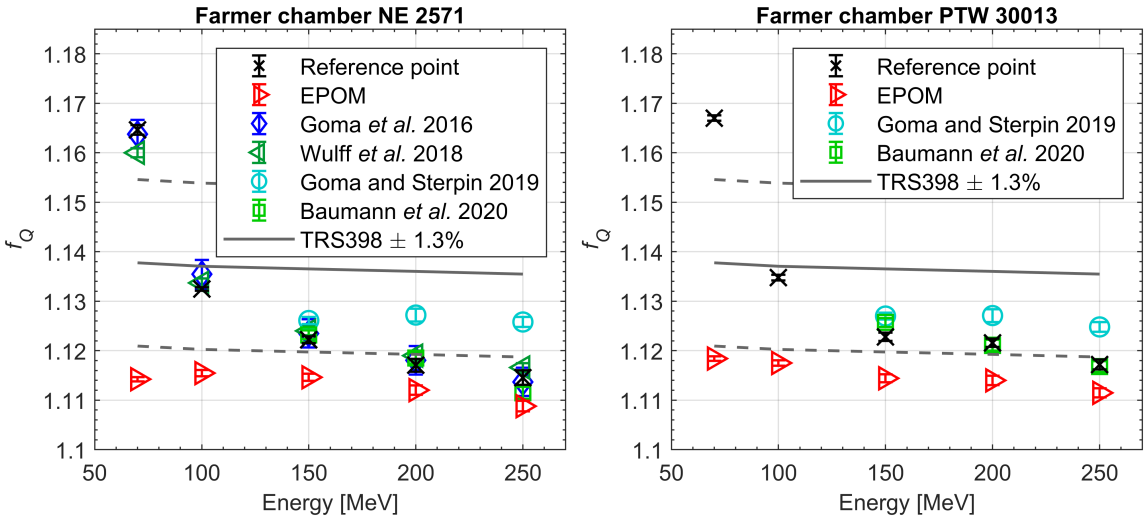

Figure 2.4. Monte Carlo simulated f_Q factors for the two positioning approaches (Reference point and EPOM) determined in this work for Farmer type cylindrical ionization chambers in comparison to literature [1, 6, 7, 8, 9].

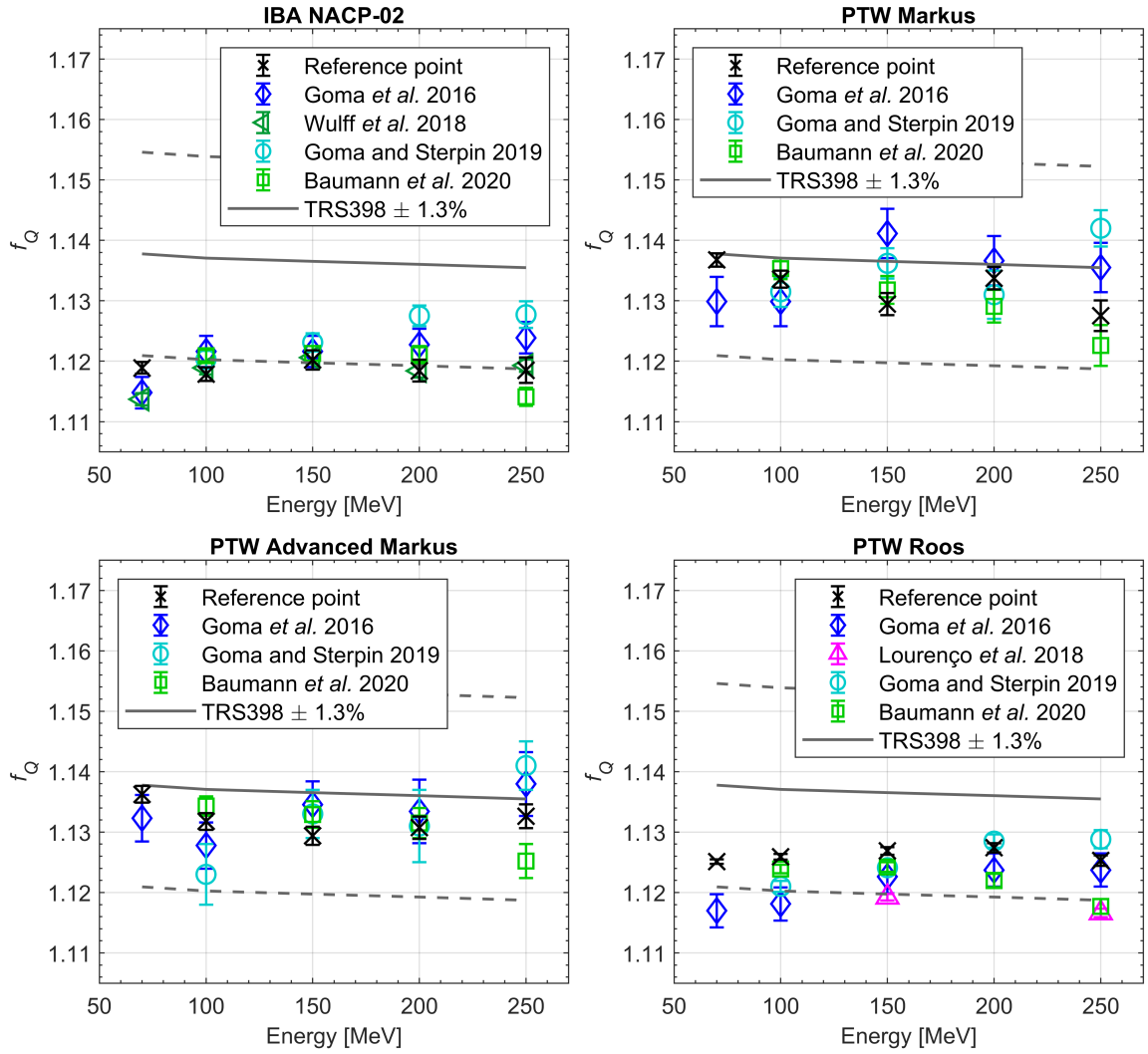

Figure 2.5. Monte Carlo simulated f_Q factors of plane-parallel ionization chambers determined in this work (Reference point) in comparison to literature [1, 6, 7, 11, 9].

Table 2.5. Monte Carlo simulated f_Q factors for various ionization chambers and incident proton energies. The value(s) given in parenthesis indicate the standard deviation of the mean with respect to the last digit(s). Note that values for cylindrical chambers are presented for two different positioning approaches.

Chamber and positioning type	Ionization chamber	Energy [MeV] 70	100	150	200	250
f_Q Plane-parallel: Reference point = EPOM	IBA NACP-02	1.1189(9)	1.1179(11)	1.1202(16)	1.1184(18)	1.1185(21)
	PTW Markus	1.1368(11)	1.1336(14)	1.1294(18)	1.1337(19)	1.1275(25)
	PTW Adv. Markus	1.1362(14)	1.1318(14)	1.1294(15)	1.1307(19)	1.1326(20)
	PTW Roos	1.1251(4)	1.1259(5)	1.1269(6)	1.1274(8)	1.1253(9)
f_Q^{Ref} Cylindrical: Reference point	NE 2571	1.1646(10)	1.1325(3)	1.1222(7)	1.1171(13)	1.1146(15)
	PTW 30013	1.1670(5)	1.1348(5)	1.1228(8)	1.1216(8)	1.1172(10)
	PTW 31014	1.1345(9)	1.1231(13)	1.1169(12)	1.1151(24)	1.1148(27)
	PTW 31021	1.1515(9)	1.1269(9)	1.1166(13)	1.1129(16)	1.1098(17)
	PTW 31022	1.1368(13)	1.1207(17)	1.1120(12)	1.1127(16)	1.1079(29)
f_Q^{EPOM} Cylindrical: EPOM	NE 2571	1.1142(4)	1.1155(6)	1.1146(7)	1.1120(9)	1.1088(11)
	PTW 30013	1.1184(5)	1.1175(6)	1.1144(8)	1.1140(9)	1.1115(9)
	PTW 31014	1.1170(10)	1.1148(11)	1.1144(15)	1.1148(16)	1.1139(17)
	PTW 31021	1.1136(6)	1.1129(8)	1.1123(9)	1.1102(12)	1.1078(12)
	PTW 31022	1.1134(9)	1.1120(11)	1.1107(14)	1.1108(18)	1.1096(19)

2.3.3 Monte Carlo simulated perturbation correction factors p_Q

Figures 2.6 and 2.7 show the simulated perturbation correction factors for the investigated cylindrical and plane-parallel ionization chambers, respectively. The perturbation correction factors for the PTW Roos chamber are compared to a study by Lourenço *et al.* [11].

Of all the perturbation factors p_{dis} shows the greatest deviation from unity. Figure 2.6 shows an increase in p_{dis} towards low proton energies for cylindrical ionization chambers. This increase is most pronounced for large cylindrical chambers with an extended air cavity, like the Farmer chambers NE 2571 and PTW 30013, for which the p_{dis} vary from 1.005 ± 0.2% up to 1.045 ± 0.1%. The smallest variation over the energy range of 1.5% is determined for the p_{dis} of the PTW PinPoint 31014. The other individual perturbation correction factors of both chamber types are relatively constant over the considered energy range. The most pronounced perturbation among the chamber components is caused by the chamber wall, where the largest correction was found for the PTW PinPoint 3D with p_{wall} = 0.981 ± 0.3% at 250 MeV. The maximum variation within the energy range can be seen for the p_{wall} of the PTW Markus chamber with a maximum difference of 1.5%. The mean value of p_{stem} considering all cylindrical chambers and energies, is 0.996 with a maximum variation of 1.2%. Correspondingly, the mean value of p_{cel} is determined as 0.997 with a maximum variation of 1.3%. The mean perturbation correction factor for the chambers' air cavity p_{cav} was found to be 1.005 with a maximum variation of 0.8% considering both plane-parallel and cylindrical chambers.

For cylindrical ionization chambers, the two different positioning approaches recommended in IAEA TRS-398 [1] (reference point) and DIN6801-1 [10] (EPOM) resulted in two distinct total perturbation correction factors p_Q^{Ref} and p_Q^{EPOM}. While p_Q^{Ref} increases with decreasing energy with a maximum difference of 4.4% for the Farmer chamber NE 2571, the p_Q^{EPOM} are relatively constant over the considered energy range within 0.7% for the two Farmer chambers, 0.2% for the PTW PinPoint 31014, 0.6% for the PTW Semiflex 3D 31021, and 0.3% for the PTW PinPoint 3D. The total p_Q determined for plane-parallel chambers are also constant in the energy range within 0.3% for the IBA NACP-02 and PTW Roos chamber, 0.7% for the PTW Markus chamber, and 0.5% for the PTW Advanced Markus.

2.3.4 Beam quality correction factor k_{Q,Q_0}

Figures 2.8 and 2.9 show the k_Q for cylindrical and plane-parallel chambers, respectively, in comparison to literature [1, 6, 7, 8]. The corresponding values are shown in Table 2.6, where two f_Q factors for cylindrical ionization chambers resulting from the EPOM- and reference point positioning approaches, k_Q^{EPOM} and k_Q^{Ref} , are presented. Because f_{Q_0} for each chamber is constant over the considered energy range, the same observations described above for the f_Q factors also apply for k_Q.

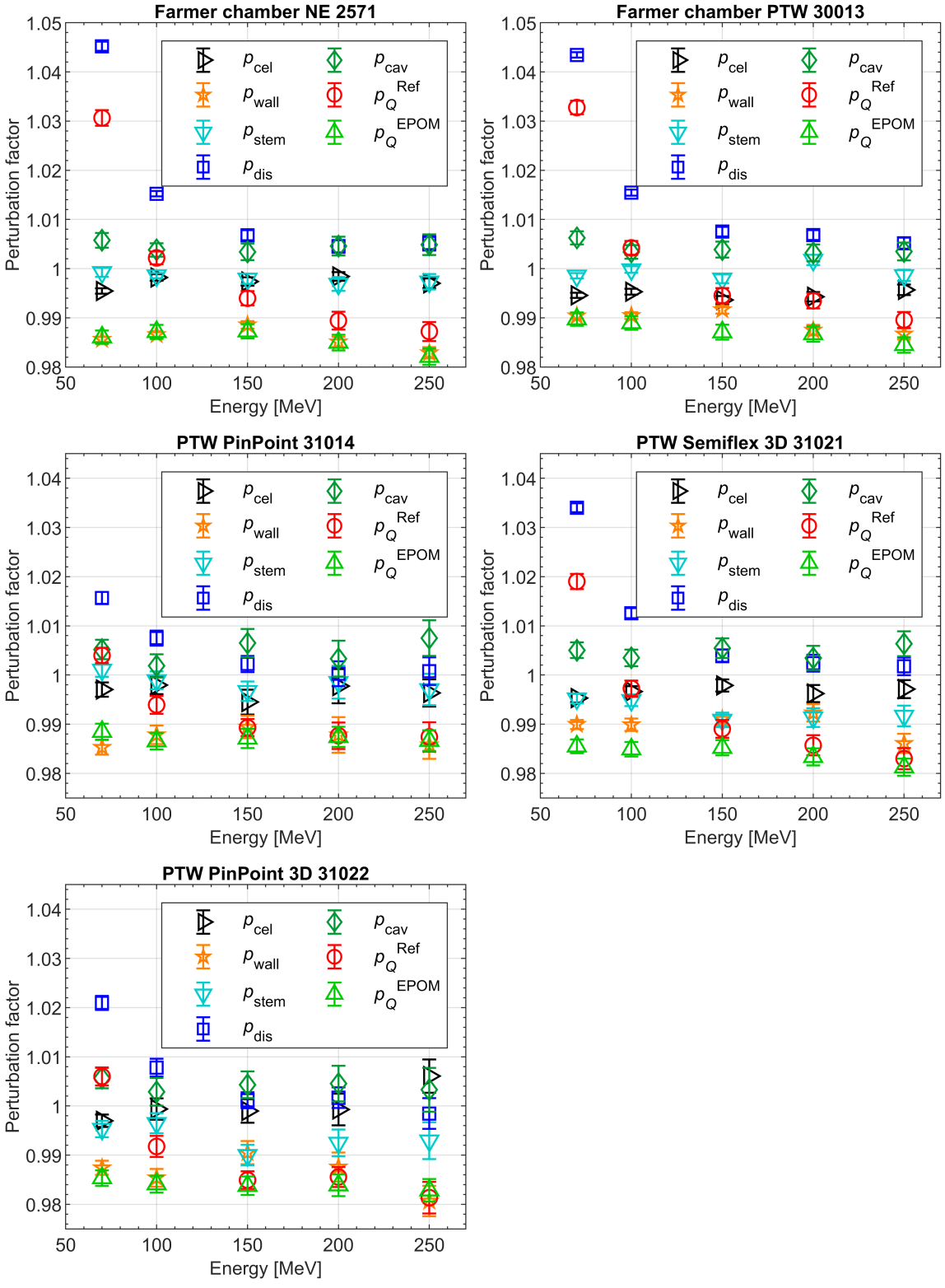

Figure 2.6. Monte Carlo simulated perturbation correction factors of cylindrical ionization chambers. Note that the total perturbation correction factors p_Q^{Ref} for the reference point positioning are obtained by the product of p_{cel}, p_{wall}, p_{stem}, p_{dis}, and p_{cav}. In contrast, when positioning the ionization chamber with its EPOM at the measurement depth, p_{dis} is already corrected so that p_Q^{EPOM} results from the product of p_{cel}, p_{wall}, p_{stem} and p_{cav}.

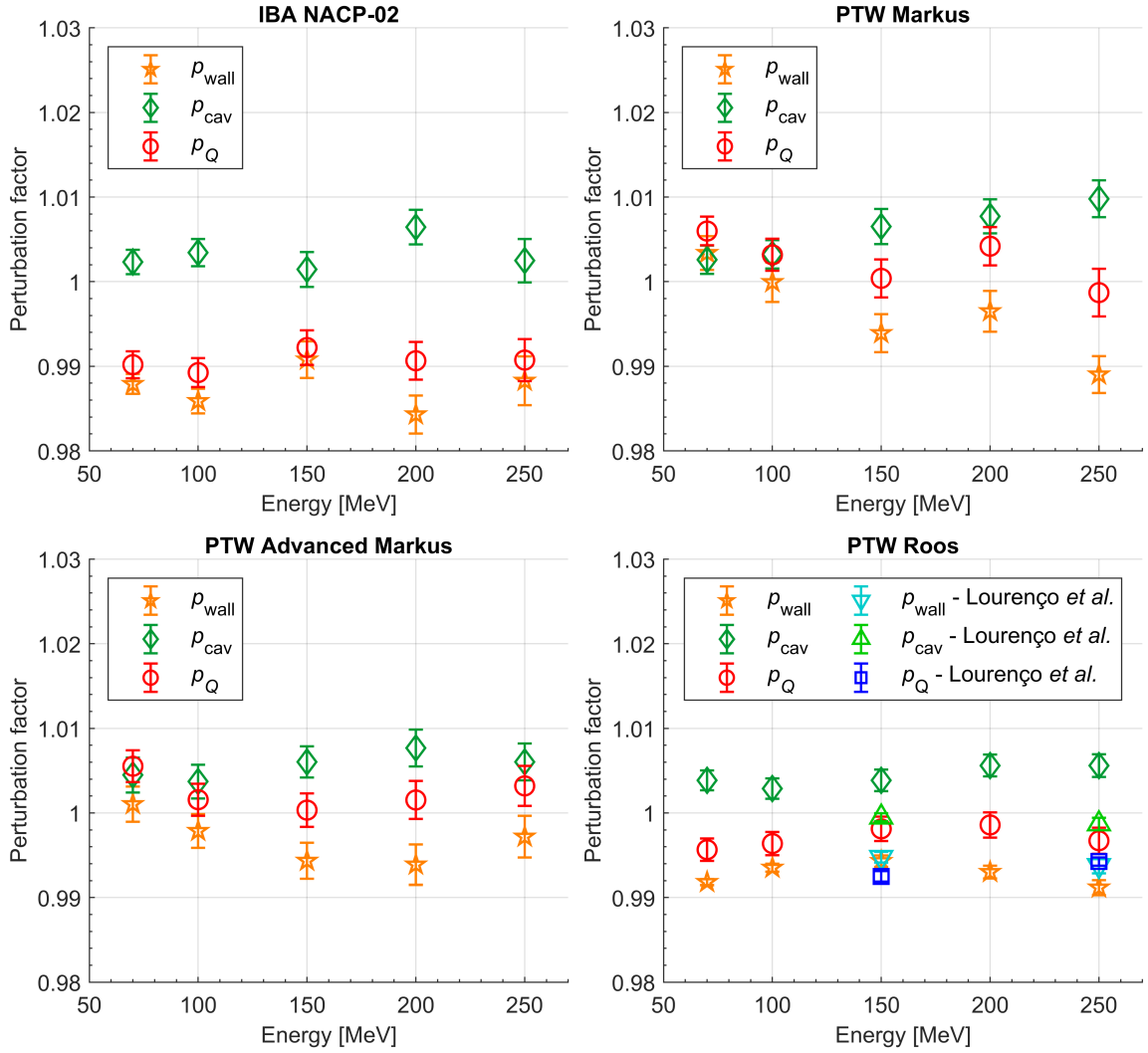

Figure 2.7. Monte Carlo simulated perturbation correction factors of plane-parallel ionization chambers. p_Q is obtained by the product of p_{wall} and p_{cel}. The perturbation correction factors determined for the PTW Roos chamber are compared to those determined by Lourenço *et al.* [11].

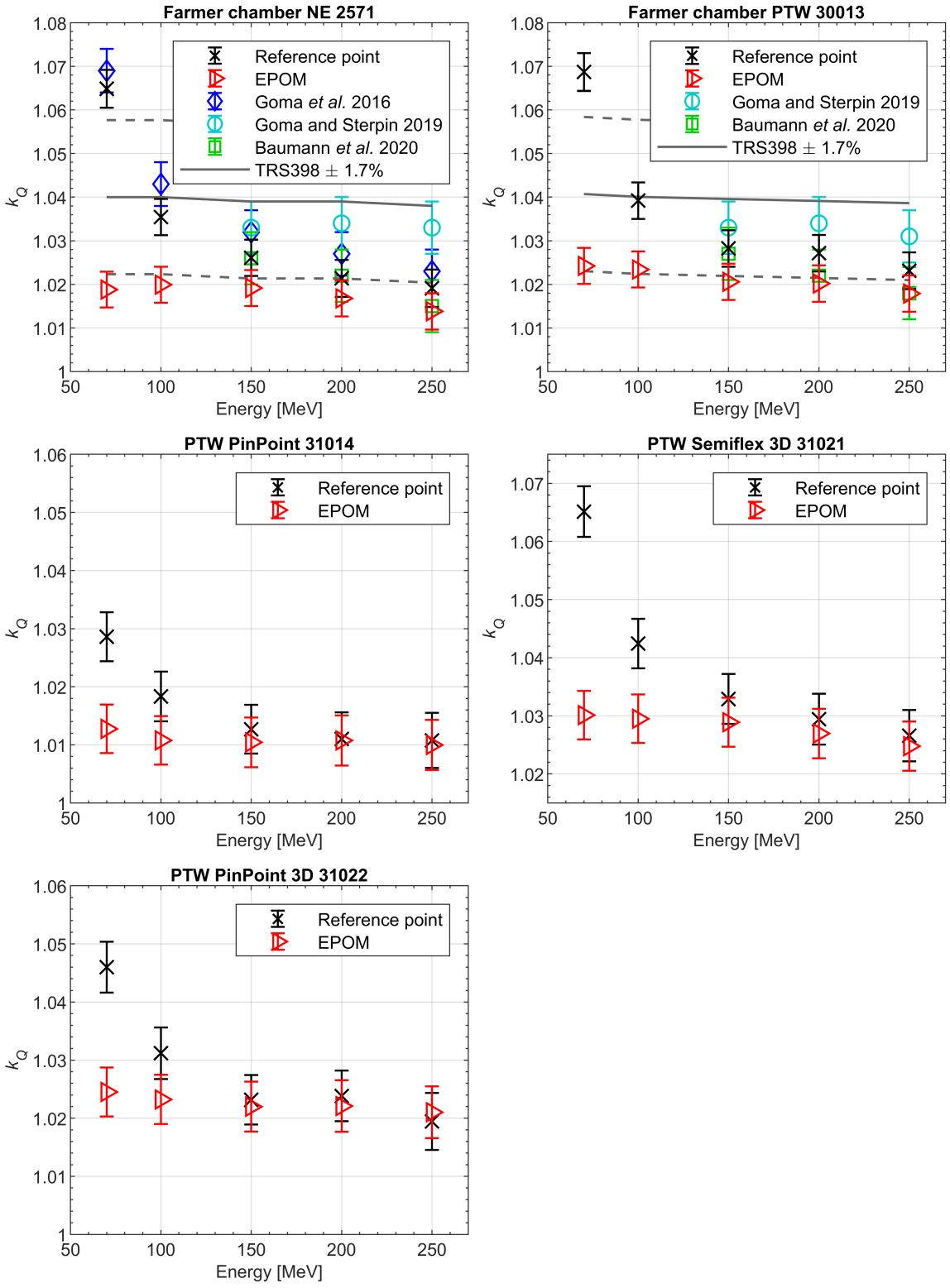

Figure 2.8. Monte Carlo simulated k_Q factors for the two positioning approaches (Reference point and EPOM) determined in this work for cylindrical ionization chambers in comparison to literature [1, 6, 7, 8].

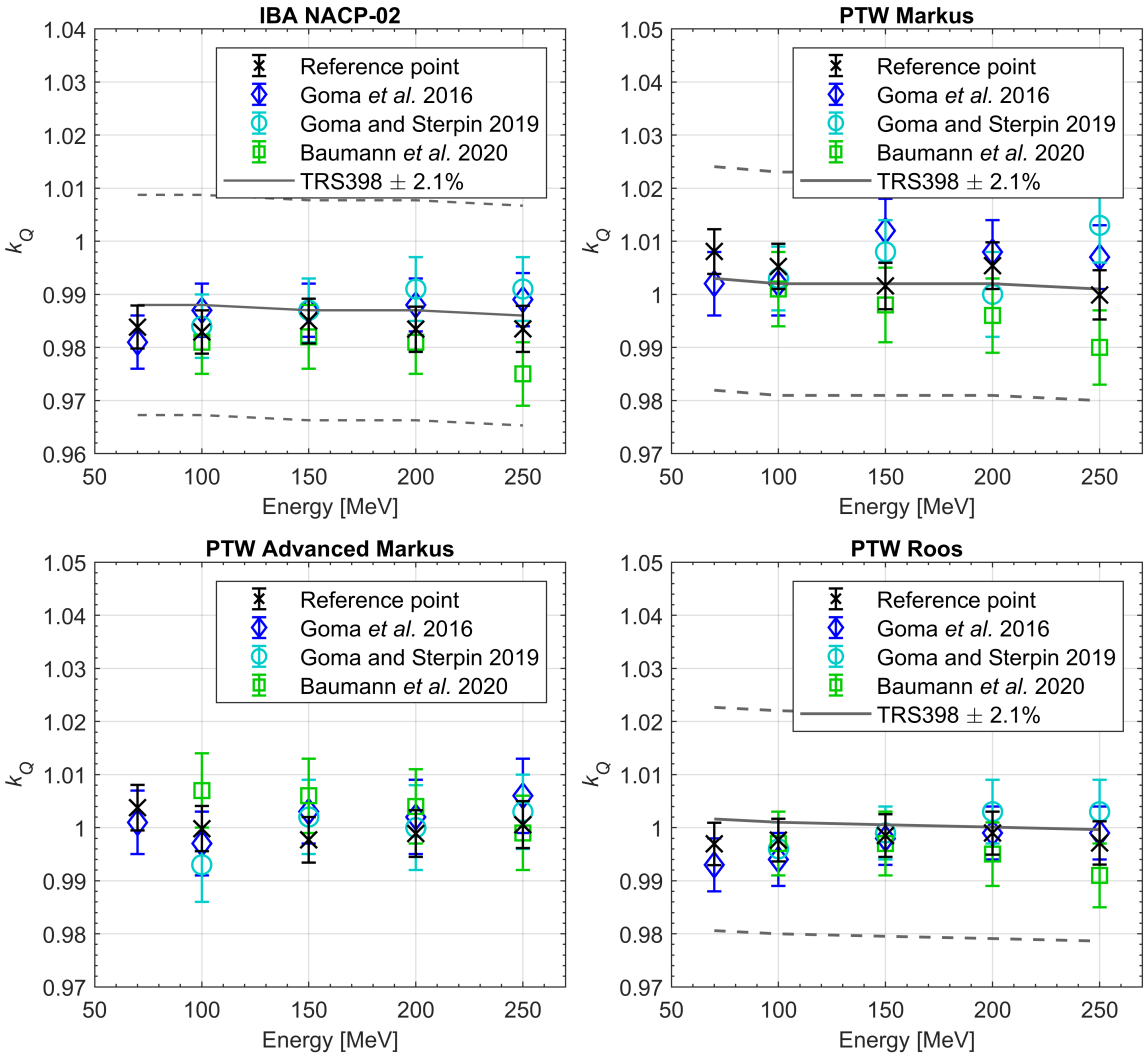

Figure 2.9. Monte Carlo simulated k_Q factors of plane-parallel ionization chambers determined in this work (Reference point) in comparison to literature [1, 6, 7, 8].

Table 2.6. Monte Carlo simulated beam quality correction factors k_Q for various ionization chambers and incident proton energies. The value within parenthesis corresponds to one standard deviation of the mean with respect to the last digit(s). Note that k_Q for the cylindrical chambers are presented for two different positioning approaches.

Chamber and positioning type	Ionization chamber	Energy [MeV] 70	100	150	200	250
k_Q Plane-parallel: Reference point = EPOM	IBA NACP-02	0.9838(40)	0.9829(41)	0.9850(42)	0.9834(43)	0.9835(44)
	PTW Markus	1.0081(42)	1.0052(43)	1.0016(44)	1.0054(44)	0.9999(46)
	PTW Adv. Markus	1.0038(43)	0.9998(43)	0.9977(43)	0.9989(44)	1.0006(44)
	PTW Roos	0.9969(40)	0.9977(40)	0.9985(40)	0.9990(41)	0.9971(41)
k_Q^{Ref} Cylindrical: Reference point	NE 2571	1.0649(44)	1.0355(42)	1.0261(42)	1.0214(43)	1.0191(43)
	PTW 30013	1.0687(43)	1.0392(42)	1.0282(42)	1.0271(42)	1.0231(42)
	PTW 31014	1.0286(42)	1.0183(43)	1.0127(42)	1.0110(46)	1.0108(47)
	PTW 31021	1.0651(43)	1.0424(43)	1.0329(43)	1.0294(44)	1.0266(44)
	PTW 31022	1.0460(44)	1.0312(44)	1.0232(43)	1.0238(44)	1.0194(49)
k_Q^{EPOM} Cylindrical: EPOM	NE 2571	1.0188(41)	1.0199(41)	1.0191(41)	1.0168(42)	1.0138(42)
	PTW 30013	1.0242(41)	1.0234(41)	1.0206(42)	1.0202(42)	1.0179(42)
	PTW 31014	1.0127(42)	1.0108(42)	1.0104(43)	1.0108(43)	1.0100(43)
	PTW 31021	1.0301(42)	1.0295(42)	1.0289(42)	1.0270(43)	1.0248(42)
	PTW 31022	1.0245(42)	1.0232(42)	1.0220(43)	1.0221(44)	1.0210(45)

2.4 Discussion

2.4.1 Monte Carlo simulated f_{Q_0}

f_{Q_0} factors determined in this work are in good agreement with the literature (Figure 2.3), where the values of f_{Q_0} have been calculated with different Monte Carlo codes considering ICRU Report 90 [12].

Figure 2.3 shows that the f_{Q_0} factors determined within this work for the plane-parallel chambers agree with those from literature with a maximum difference of 0.5% from the f_{Q_0} for the PTW Advanced Markus chamber calculated by Baumann *et al.* with TOPAS/Geant4 [6]. Considering the f_{Q_0} of the NE 2571, all factors agree within 0.6% when disregarding the outlier from Tikkanen *et al.* [36] (IST research group), which differs by 1.8% from the result determined in this work. The f_{Q_0} simulated for PTW Farmer chamber 30013 shows a maximum difference of 0.4% to the work by Baumann *et al.* [6]. The f_{Q_0} determined for the PTW Semiflex 3D 31021 chamber in this work agrees within 0.2% with the value presented by Tikkanen *et al.* [36] (THM research group).

2.4.2 Monte Carlo simulated p_Q

p_{dis} determined for cylindrical chambers were found to have the greatest contributions to p_Q^{Ref} of up to 1.045 ± 0.1% for large cylindrical ionization chambers at low proton energies. This is a result of the reference point positioning in combination with the dose gradient present at the measurement depth [7, 4, 37]. It is remarkable that p_{dis} of up to 1.005 are also found at the highest energies for large Farmer chambers. To further examine this finding, the p_{dis} determined for the PTW Farmer chamber 30013 of 1.045 ± 0.1% at 70 MeV and of 1.005 ± 0.1% at 250 MeV were compared to the ratio $\frac{D_{\text{w}}(z_Q)}{D_{\text{w}}(z_Q-\Delta z_Q)}$, which was found to be 1.0439 ± 0.03% at 70 MeV and 1.0049 ± 0.06% at 250 MeV. The good agreement further elucidates the origin of p_{dis} that is directly related to the gradient effect caused by the non-vanishing gradient in the depth dose curve despite the measurement in the plateau region. Therefore, measurement values of a cylindrical ionization chamber placed with its reference point at the measurement depth should be corrected by the displacement correction factors, [38, 39] which are dependent on energy. It is noteworthy that p_{dis} is part of the k_Q^{Ref} and f_Q^{Ref} presented in this work such that the application of these factors leads to a correction of the reference point positioning for the depth and energies considered in this study.

The relatively constant p_Q^{EPOM} over the considered energy range indicate that the recommended EPOM of 0.75 times the radius of the sensitive volume of the ionization chambers as provided in DIN6801-1 [10] for proton beams is a good estimate for the ionization chambers investigated in this work. This agrees with the observation made by Palmans and Verhaegen [39] and Palmans [40] for most ionization chambers.

The p_{cel} presented in this work for the NE 2571, which are on average 0.997, agree with the experimental values determined by Medin *et al.* [41] and Palmans *et al.* [38] of 0.997 ± 0.004 in a 170 MeV proton beam and 0.997 ± 0.002 in a 75 MeV proton beam, respectively. Considering secondary electron perturbations only, Palmans [42] presents Monte Carlo calculated p_{wall} and p_{cel} for the NE 2571, which saturate at around 0.985 and 0.998, respectively. Those factors are comparable to the average p_{wall} of 0.986 and p_{cel} of 0.997 determined in this work. Palmans *et al.* [43] determined ratios of p_Q in a 75 MeV proton beam at a depth corresponding to an R_{res} of 2.65 cm using the Farmer chamber NE 2571 as the reference such that a comparison to p_Q ratios determined in this work for the 70 MeV proton beam (R_{res} = 2.18 cm) was possible as shown in Table 2.7. Because Palmans *et al.* [43] corrected for gradient perturbations, the $p_Q^{\text{EPOM,NE 2571}}$ were used to determine the ratios for this work. A maximum difference of 1.8% was found for the ratio $p_Q^{\text{Markus}}/p_Q^{\text{EPOM,NE 2571}}$.

Lourenço *et al.* [11] determined p_Q of the PTW Roos chamber using the Monte Carlo code FLUKA [17] as shown in Figure 2.7. While p_{wall} of this work agree with those by Lourenço *et al.* within 0.3%, the p_{cav} determined by Lourenço *et al.* are closer to unity with a maximum difference to the p_{cav} determined in this work of 0.6%. Recently, Baumann *et al.* [6] used the Monte Carlo code TOPASv3.1.p1 [16] together with GEANT4.10.03.p1 [15] to calculate k_Q factors in monoenergetic proton fields and exemplarily simulated perturbation correction factors in a 250 MeV proton beam for the individual chamber parts of the cylindrical ionization chamber Extradin A1SL. They found a total p_Q^{Ref} of 0.987(7), where the perturbation from the chamber wall had the largest contribution of 1.5% [6]. This finding is in accordance with this work where the same conclusion for the most pronounced perturbation of all ionization chamber components being the chamber wall can be drawn.

The results in the recent literature and of this work show that the chambers' perturbation correction factors may differ from unity. Consequently, the approximation of $p_Q = 1$ assumed in the dosimetry protocols IAEA TRS-398 [1] and DIN6801-1 [10] should be revised.

Table 2.7. $p_Q/p_Q^{\text{EPOM,NE 2571}}$ ratios as determined experimentally by Palmans *et al.* [43] in comparison to the corresponding ratios determined in this study. The value within parenthesis corresponds to the standard uncertainty in the last digit(s).

	Palmans *et al.* (R_{res} = 2.65 cm)	This work (R_{res} = 2.18 cm)	Difference [%]
$p_Q^{\text{NACP-02}}/p_Q^{\text{EPOM,NE 2571}}$	1.006(6)	1.004(2)	-0.2
$p_Q^{\text{Markus}}/p_Q^{\text{EPOM,NE 2571}}$	1.002(5)	1.020(2)	1.8
$p_Q^{\text{Roos}}/p_Q^{\text{EPOM,NE 2571}}$	1.000(3)	1.010(2)	1.0

2.4.3 Monte Carlo simulated f_Q

Considering the two Farmer chambers NE 2571 and PTW 30013, an agreement within 0.4% between the f_Q^{Ref} determined in this work and the f_Q determined by Gomà *et al.* [7], Wulff *et al.* [9] and Baumann *et al.* [6] is found as depicted in Figure 2.4. Although Wulff *et al.* investigated two different physics lists for simulating the hadronic interactions, for better visibility, Figures 2.4 and 2.5 only include their results for the QGSP_BIC physics list. The influence from the two physics lists was found to be less than 0.3% ± 0.1% [9].

The increase in f_Q^{Ref} of the NE 2571 at low proton energies agrees with that described by Gomà *et al.* [7] and Wulff *et al.* [9]. Baumann *et al.* only determined f_Q for cylindrical chambers for energies E ≥ 150 MeV [6]. The increase of f_Q^{Ref} at low energies is a result of the gradient effect as discussed above. Differences of up to 1% are observed when comparing the f_Q^{Ref} of the Farmer chambers to those calculated by Gomà and Sterpin [8], which are most pronounced at the high proton energies. In contrast to Gomà *et al.* [7], this more recent study included the simulation of nuclear interactions and prompt-gamma emission, which was implemented by Sterpin *et al.* [44].

The f_Q^{EPOM} of cylindrical chambers are nearly constant over the energy range considered. This shows that the positioning of cylindrical chambers with the EPOM at the measurement depth leads to an adequate compensation of the displacement effect. When comparing the f_Q^{EPOM} and f_Q^{Ref} for the chambers in Figure 2.4, it can be seen that the factors not only differ at low proton energies, where a comparably steep gradient is present at the measurement depth and a large displacement effect is expected, but also at the highest proton energies where the measurement depth of 2 cm lies in the plateau of the depth dose curve as previously explained for the total perturbation factor p_Q.

The f_Q for plane-parallel chambers in Figure 2.5 from the different studies are all relatively constant over the energy range studied. The f_Q determined in this work for the IBA NACP-02 agrees with a maximum difference of 0.5% with the data presented by Wulff *et al.* [9] at 70 MeV. The maximum difference of f_Q for plane-parallel chambers in this work to Baumann *et al.* [6] is 0.7% for the PTW Roos chamber at 250 MeV. While the f_Q for the PTW Markus and PTW Advanced Markus chamber agree quite well with the f_Q from IAEA TRS-398 [12], the f_Q of the IBA NACP-02 and PTW Roos chamber are up to 1.7% and 1.1% smaller, respectively. Larger deviations are also found at higher energies when compared to the recent publication by Gomà and Sterpin [8], who claimed nuclear interactions are only considered in the Monte Carlo code PENH used in this more recent study. Baumann *et al.* [6] further investigated this argument by comparing f_Q simulations in TOPAS/Geant4 where nuclear interactions were either switched off or on and found that the f_Q factors without nuclear interaction simulation were 1.5% higher than those determined with the corresponding physics switched on [6]. Similar conclusions can be drawn from the work by Lourenço *et al.* [11] who determined p_Q in FLUKA and investigated the impact of nuclear interaction simulation. Lourenço *et al.* found that p_Q increases when nuclear interactions are disregarded [11]. The findings by Baumann *et al.* and Lourenço *et al.* therefore contradict the results by Gomà and Sterpin that indicate that nuclear interaction simulation leads to larger f_Q at high energies [6, 8, 11].

2.4.4 Monte Carlo simulated k_Q

The beam quality correction factors have been determined for four plane-parallel and five cylindrical ionization chambers in this work. A distinction between two positioning approaches has been made resulting in k_Q^{Ref} and k_Q^{EPOM} for each cylindrical chamber. Despite the scarce data available in the literature for comparisons, where mostly only k_Q^{Ref} have been presented, the values obtained in this work for cylindrical chambers differ from those presented by Gomà *et al.* [7] and Baumann *et al.* [6] by a maximum of 0.7%. Gomà and Sterpin [8] and Baumann *et al.* [6] have only calculated k_Q^{Ref} factors for cylindrical chambers for proton energies E ≥ 150 MeV, where the impact from the gradient effect is assumed to be less pronounced. Larger differences are found in comparison to the k_Q factors by Gomà and Sterpin [8] with a maximum difference of 1.4% for the Farmer chamber NE 2571 at the highest energy of 250 MeV.

The k_Q^{EPOM} determined in this work for the Farmer chamber NE 2571 can be compared to experimental values obtained by Medin *et al.* [2]. Using water calorimetry as the reference, they determined a k_Q^{EPOM} for the NE 2571 of 1.021 ± 0.7% in a 175 MeV

monoenergetic proton beam with R_{res} = 14.7 cm. This value differs from the k_Q^{EPOM} obtained here for the 150 MeV proton field with comparable R_{res} = 14.12 cm by 0.2%. Medin [3] presents a k_Q of 1.032 ± 0.013 for the NE 2571 determined using water calorimetry in a 180 MeV scanned pulsed proton beam with R_{res} = 16.5 cm. No remarks concerning the consideration of the effective measurement depth are made. The k_Q^{Ref} and k_Q^{EPOM} determined in this work at 150 MeV (R_{res} = 14.12 cm) for the NE 2571 are both within the uncertainty of the value by Medin [3] with a difference of 0.6% and 1.3%, respectively.

For the plane-parallel chambers IBA NACP-02, PTW Advanced Markus and PTW Roos, a maximum difference of 0.6% was found comparing to the work by Gomà *et al.* [7], whereas the maximum difference from the studies by Gomà and Sterpin [8] and Baumann *et al.* [6] is 0.8% and 0.9%, respectively. The largest differences can be asserted for the PTW Markus chamber, with a maximum difference of 1.3% from the literature.

k_Q/k_Q^{Markus} ratios were determined experimentally by Gomà *et al.* [4] in a pseudo-monoenergetic field of 174 MeV protons at 15 g/cm^2 depth at R_{res} = 5.93 cm allowing for a comparison to ratios of this work presented in Table 2.8. Table 2.8 reveals a maximum difference to the work by Gomà *et al.* [4] of 1.7% in the ratio of $k_Q^{30013}/k_Q^{\text{Markus}}$.

In line with previous studies, the data determined in this work show discrepancies of up to 2.6% for k_Q^{Ref} and 2.4% for k_Q^{EPOM} for cylindrical chambers and a maximum difference of 0.6% for plane-parallel chambers from the values recommended in IAEA TRS-398 [1]. The large difference between the k_Q^{Ref} and k_Q^{EPOM} for cylindrical chambers shows that reference dosimetry in steep dose gradients should be carried out with caution. Several studies [7, 4, 37, 45] suggested to only perform reference dosimetry with plane-parallel ionization chambers or under consideration of the EPOM if a cylindrical chamber is used. Similar recommendations are provided in the German protocol for proton and light ion dosimetry DIN6801-1 [10] by stating that suitable small compact chambers or plane-parallel chambers should be used for reference dosimetry at residual ranges smaller than 1.5 cm and that the EPOM should be considered. The relatively constant k_Q^{EPOM} for cylindrical and k_Q for plane-parallel chambers indicates that positioning according to the EPOM may allow the use of energy-independent beam quality correction factors, which in these cases appear to be more practicable and less prone to errors. DIN6801-1 proposes such constant k_Q^{EPOM} for monoenergetic proton beams with residual ranges larger than 1.5 cm arguing that the variance is 0.2%, although this work shows that the associated variations can be up to 0.8%. It is also noteworthy that while IAEA TRS-398 suggests considering the EPOM in carbon ion fields, this approach is currently not recommended for proton fields [1].

Table 2.8. k_Q/k_Q^{Markus} ratios as determined experimentally by Gomà *et al.* [4] in comparison to the corresponding ratios determined in this study. The value within parenthesis corresponds to the standard uncertainty in the last digit(s).

	Gomà *et al.* 2015 (R_{res} = 5.93 cm)	This work (R_{res} = 5.9 cm)	Difference [%]
$k_Q^{30013}/k_Q^{\text{Markus}}$	1.051(8)	1.0338(59)	-1.7
$k_Q^{\text{NACP-02}}/k_Q^{\text{Markus}}$	0.989(8)	0.9778(59)	-1.1
$k_Q^{\text{Roos}}/k_Q^{\text{Markus}}$	1.007(8)	0.9924(58)	-1.4
$k_Q^{\text{Adv. Markus}}/k_Q^{\text{Markus}}$	0.996(8)	0.9946(60)	-0.1

The k_Q^{Ref} presented here are listed with a combined type A uncertainty for f_{Q_0} and f_Q determined in this work and the type B uncertainty for the W_{a} ratio. Type B uncertainties for f_Q/f_{Q_0} ratios of at least 0.3% were estimated in Wulff *et al.* [9] and Baumann *et al.* [6], where the same underlying code (Geant4) has been used for the calculations of both factors. In this work, the f_{Q_0} factors have been calculated using the well benchmarked code EGSnrc for photon beams, which is more efficient, and allows for better comparability to the literature, whereas the factors f_Q were simulated using GATE/Geant4. Therefore, the Type B uncertainty associated with the f_Q/f_{Q_0} ratios presented here may differ from the estimation in Wulff *et al.* [9] and Baumann *et al.* [6] due to differences in the cross-section data and particle transport of the codes. Baumann *et al.* [46] investigated the impact of combining a f_Q factor determined in TOPAS/Geant4 and a f_{Q_0} calculated in EGSnrc and found that the resulting difference from using the same code for both factors is (0.3 ± 0.2)%.

The new mean excitation energies for water, air and graphite as recommended in the ICRU Report 90 have been considered in both Monte Carlo codes by using user-generated materials instead of the standard material database. Direct comparisons between the stopping powers of the materials used in this work to the tabulated values in ICRU Report 90 have been performed exemplarily for 50 MeV, 100 MeV, 150 MeV and 200 MeV protons. The electronic stopping powers agree within 0.15% for water and air and within 0.33% for graphite and are consequently well within the uncertainty listed in the ICRU Report 90. It is noteworthy that the ICRU 90 stopping powers for protons have been directly implemented in Geant4 recently.

2.5 Conclusions

k_Q and p_Q were determined for five cylindrical and four plane-parallel ionization chambers in monoenergetic proton beams. To the best of our knowledge, k_Q for the three cylindrical ionization chambers, PTW Semiflex 31021, PTW PinPoint 31014 and PTW PinPoint 3D 31022, have not been determined so far for monoenergetic proton fields. For cylindrical ionization chambers, the influence on k_Q from the two commonly used positioning procedures, reference point and EPOM, has been investigated over the energy range from 70 MeV to 250 MeV, within which the respective values have been compared. The difference in k_Q from the two positioning approaches amounts up to 4.5% at 70 MeV and still half a percent at the highest proton energy investigated, 250 MeV, showing that the positioning is critical even at higher energies.

The chamber's perturbation correction factors have been found to differ from unity, underlining the findings from recent publications [6, 7, 8, 11, 9] and providing more rationale for revising the approximation of p_Q being unity currently made in IAEA TRS-398 [1] and DIN6801-1 [10]. Among these perturbation factors, the energy dependent displacement effect correction factors p_{dis} for cylindrical ionization chambers contribute the greatest to p_Q, whereas the chamber wall causes the largest perturbation among the individual chamber components.

Acknowledgements

The authors would like to thank Jörg Wulff for fruitful discussions, providing the TOPAS/Geant4 input file of the plane-parallel chamber IBA NACP-02 and the f_Q factors determined in their work in private communication. Moreover, we would like to thank Kilian Baumann, Ana Lourenço and Joonas Tikkannen for providing the numerical values of their results. We thank Sytze Brandenburg and Emiel van der Graaf from the KVI-Center for Advanced Radiation Technology Groningen for fruitful discussions on the presented results. The authors would like to thank PTW-Freiburg for providing the construction drawings of detectors investigated in this work.

Conflict of interest

The authors have no conflicts to disclose.

References

[1] Andreo, P., Burns, D. T., Hohlfeld, K., Huq, M. S., Kanai, T., Laitano, F., Smythe, V. G., and Vynckier, S. *Absorbed dose determination in external beam radiotherapy: an international code of practice for dosimetry based on standards of absorbed dose to water. Technical Reports Series No. 398.* International Atomic Energy Agency. Vienna. 2000.

[2] Medin, J., Ross, C. K., Klassen, N. V., Palmans, H., Grusell, E., and Grindborg, J.-E. "Experimental determination of beam quality factors, k_Q, for two types of Farmer chamber in a 10 MV photon and a 175 MeV proton beam". *Phys Med Biol*, 2006, 51:6, pp. 1503–1521. DOI: 10.1088/0031-9155/51/6/010.

[3] Medin, J. "Implementation of water calorimetry in a 180 MeV scanned pulsed proton beam including an experimental determination of k_Q for a Farmer chamber". *Phys Med Biol*, 2010, 55:12, pp. 3287–3298. DOI: 10.1088/0031-9155/55/12/002.

[4] Gomà, C., Hofstetter-Boillat, B., Safai, S., and Vörös, S. "Experimental validation of beam quality correction factors for proton beams". *Phys Med Biol*, 2015, 60:8, pp. 3207–3216. DOI: 10.1088/0031-9155/60/8/3207.

[5] Vatnitsky, S. M., Siebers, J. V., and Miller, D. W. "k_Q factors for ionization chamber dosimetry in clinical proton beams". *Med Phys*, 1996, 23:1, pp. 25–31. DOI: 10.1118/1.597768.

[6] Baumann, K.-S., Kaupa, S., Bach, C., Engenhart-Cabillic, R., and Zink, K. "Monte Carlo calculation of beam quality correction factors in proton beams using TOPAS/GEANT4". *Phys Med Biol*, 2020, 65:5, p. 055015. DOI: 10.1088/1361-6560/ab6e53.

[7] Gomà, C., Andreo, P., and Sempau, J. "Monte Carlo calculation of beam quality correction factors in proton beams using detailed simulation of ionization chambers". *Phys Med Biol*, 2016, 61:6, pp. 2389–2406. DOI: 10.1088/0031-9155/61/6/2389.

[8] Gomà, C. and Sterpin, E. "Monte Carlo calculation of beam quality correction factors in proton beams using PENH". *Phys Med Biol*, 2019, 64:18, p. 185009. DOI: 10.1088/1361-6560/ab3b94.

[9] Wulff, J., Baumann, K.-S., Verbeek, N., Bäumer, C., Timmermann, B., and Zink, K. "TOPAS/ Geant4 configuration for ionization chamber calculations in proton beams". *Phys Med Biol*, 2018, 63:11, p. 115013. DOI: 10.1088/1361-6560/aac30e.

[10] *DIN 6801-1:2019-09 Dosismessverfahren nach der Sondenmethode für Protonen- und Ionenstrahlung - Teil 1: Ionisationskammern*, 2019. DOI: https://dx.doi.org/10.31030/3038366.

[11] Lourenço, A., Bouchard, H., Galer, S., Royle, G., and Palmans, H. "The influence of nuclear interactions on ionization chamber perturbation factors in proton beams: FLUKA simulations supported by a Fano test". *Med Phys*, 2018, 46:2, pp. 885–891. DOI: 10.1002/mp.13281.

[12] Seltzer, S. M., Fernández-Varea, J. M., Andreo, P., Bergstrom, P. M., Burns, D. T., Krajear Bronié, I., Ross, C. K., and Salvat, F. "Key data for ionizing radiation dosimetry: measurement standards and applications. ICRU Report 90". *J ICRU*, 2016, 14, pp. 1–110.

[13] Salvat, F. "A generic algorithm for Monte Carlo simulation of proton transport". *Nucl Instrum Methods Phys Res Sect B Beam Interact Mater At*, 2013, 316, pp. 144–159. DOI: 10.1016/j.nimb.2013.08.035.

[14] Arce, P. et al. "Gamos: A framework to do Geant4 simulations in different physics fields with an user-friendly interface". *Nuclear Instruments and Methods in Physics Research Section A: Accelerators, Spectrometers, Detectors and Associated Equipment*, 2014, 735, pp. 304–313. DOI: 10.1016/j.nima.2013.09.036.

[15] Agostinelli, S. et al. "Geant4 - a simulation toolkit". *Nucl Instrum Methods Phys Res Sect Accel Spectrom Detect Assoc Equip*, 2003, 506:3, pp. 250–303. DOI: 10.1016/S0168-9002(03)01368-8.

[16] Perl, J., Shin, J., Schümann, J., Faddegon, B., and Paganetti, H. "TOPAS: An innovative proton Monte Carlo platform for research and clinical applications: TOPAS: An innovative proton Monte Carlo platform". *Med Phys*, 2012, 39:11, pp. 6818–6837. DOI: 10.1118/1.4758060.

[17] Ferrari, A., Sala, P., Fasso, A., and Ranft, J. *FLUKA: A Multi-Particle Transport Code. Report No. SLAC-R-773*. Cern, 2005. DOI: 10.2172/877507.

[18] Kawrakow, I. "Accurate condensed history Monte Carlo simulation of electron transport. I. EGSnrc, the new EGS4 version". *Med Phys*, 2000, 27:3, pp. 485–498. DOI: 10.1118/1.598917.

[19] Kawrakow, I., Mainegra-Hing, E., Rogers, D. W. O., Tessier, F., and Walters, B. R. B. "The EGSnrc Code System: Monte Carlo Simulation of Electron and Photon Transport. Technical Report PIRS-701". *National Research Council of Canada*, 2017.

[20] Jan, S. et al. "GATE V6: a major enhancement of the GATE simulation platform enabling modelling of CT and radiotherapy". *Phys Med Biol*, 2011, 56:4, pp. 881–901. DOI: 10.1088/0031-9155/56/4/001.

[21] Wulff, J., Heverhagen, J. T., and Zink, K. "Monte-Carlo-based perturbation and beam quality correction factors for thimble ionization chambers in high-energy photon beams". *Phys Med Biol*, 2008, 53:11, pp. 2823–2836. DOI: 10.1088/0031-9155/53/11/005.

[22] Zink, K. and Wulff, J. "Beam quality corrections for parallel-plate ion chambers in electron reference dosimetry". *Phys Med Biol*, 2012, 57:7, pp. 1831–1854. DOI: 10.1088/0031-9155/57/7/1831.

[23] Wulff, J., Zink, K., and Kawrakow, I. "Efficiency improvements for ion chamber calculations in high energy photon beams". *Med Phys*, 2008, 35:4, pp. 1328–1336. DOI: 10.1118/1.2874554.

[24] Kawrakow, I. "Accurate condensed history Monte Carlo simulation of electron transport. II. Application to ion chamber response simulations". *Med Phys*, 2000, 27:3, pp. 499–513. DOI: 10.1118/1.598918.

[25] Mora, G. M., Maio, A., and Rogers, D. W. O. "Monte Carlo simulation of a typical ^{60}Co therapy source". *Med Phys*, 1999, 26:11, pp. 2494–2502. DOI: 10.1118/1.598770.

[26] Sechopoulos, I., Rogers, D. W. O., Bazalova-Carter, M., Bolch, W. E., Heath, E. C., McNitt-Gray, M. F., Sempau, J., and Williamson, J. F. "RECORDS: improved Reporting of montE CarlO RaDiation transport Studies: Report of the AAPM Research Committee Task Group 268". *Med Phys*, 2018, 45:1, e1–e5. DOI: 10.1002/mp.12702.

[27] Seco, J. and Verhaegen, F. *Monte Carlo techniques in radiation therapy*. CRC/Taylor & Francis. Boca Raton. 2013. DOI: https://doi.org/10.1201/b13961.

[28] MATLAB. *version 9.7.0.1190202 (R2019b)*. The MathWorks Inc. Natick, Massachusetts. 2019.

[29] Simiele, E. and DeWerd, L. "On the accuracy and efficiency of condensed history transport in magnetic fields in GEANT4". *Phys Med Biol*, 2018, 63:23, p. 235012. DOI: 10.1088/1361-6560/aaedc9.

[30] Gomà, C., Andreo, P., and Sempau, J. "Spencer–Attix water/medium stopping-power ratios for the dosimetry of proton pencil beams". *Phys Med Biol*, 2013, 58:8, pp. 2509–2522. DOI: 10.1088/0031-9155/58/8/2509.

[31] *Ionisation Chambers – Phoenix Dosimetry*. 2020. URL: https://phoenix-dosimetry.co.uk/ionisation-chambers/ (accessed on 22/04/2022).

[32] Andreo, P. et al. "Determination of consensus k_Q values for megavoltage photon beams for the update of IAEA TRS-398". *Phys Med Biol*, 2020, 65:9, p. 095011. DOI: 10.1088/1361-6560/ab807b.

[33] Andreo, P., Wulff, J., Burns, D. T., and Palmans, H. "Consistency in reference radiotherapy dosimetry: resolution of an apparent conundrum when ^{60}Co is the reference quality for charged-particle and photon beams". *Phys Med Biol*, 2013, 58:19, pp. 6593–6621. DOI: 10.1088/0031-9155/58/19/6593.

[34] Czarnecki, D., Poppe, B., and Zink, K. "Impact of new ICRU Report 90 recommendations on calculated correction factors for reference dosimetry". *Phys Med Biol*, 2018, 63:15, p. 155015. DOI: 10.1088/1361-6560/aad148.

[35] Mainegra-Hing, E. and Muir, B. R. "On the impact of ICRU report 90 recommendations on k_Q factors for high-energy photon beams". *Med Phys*, 2018, 45:8, pp. 3904–3908. DOI: 10.1002/mp.13027.

[36] Tikkanen, J., Zink, K., Pimpinella, M., Teles, P., Borbinha, J., Ojala, J., Siiskonen, T., Gomà, C., and Pinto, M. "Calculated beam quality correction factors for ionization chambers in MV photon beams". *Phys Med Biol*, 2020, 65:7, p. 075003. DOI: 10.1088/1361-6560/ab7107.

[37] Gomà, C., Lorentini, S., Meer, D., and Safai, S. "Proton beam monitor chamber calibration". *Phys Med Biol*, 2014, 59:17, pp. 4961–4971. DOI: 10.1088/0031-9155/59/17/4961.

[38] Palmans, H., Verhaegen, F., Denis, J.-M., Vynckier, S., and Thierens, H. "Experimental p_{wall} and p_{cel} correction factors for ionization chambers in low-energy clinical proton beams". *Phys Med Biol*, 2001, 46:4, pp. 1187–1204. DOI: 10.1088/0031-9155/46/4/319.

[39] Palmans, H. and Verhaegen, F. "On the effective point of measurement of cylindrical ionization chambers for proton beams and other heavy charged particle beams". *Phys Med Biol*, 2000, 45:8, pp. L20–L22. DOI: 10.1088/0031-9155/45/8/103.

[40] Palmans, H. "Perturbation factors for cylindrical ionization chambers in proton beams. Part I: corrections for gradients". *Phys Med Biol*, 2006, 51:14, pp. 3483–3501. DOI: 10.1088/0031-9155/51/14/014.

[41] Medin, J., Andreo, P., Grusell, E., Mattsson, O., Montelius, A., and Roos, M. "Ionization chamber dosimetry of proton beams using cylindrical and plane parallel chambers. N_w versus N_K ion chamber calibrations". *Phys Med Biol*, 1995, 40:7, pp. 1161–1176. DOI: 10.1088/0031-9155/40/7/002.

[42] Palmans, H. "Secondary electron perturbations in farmer type ion chambers for clinical proton beams." In: *Standards, applications and quality assurance in medical radiation dosimetry (IDOS): proceedings of an international symposium*. Vienna, IAEA, 2010, pp. 309–310.

[43] Palmans, H., Verhaegen, F., Denis, J.-M., and Vynckier, S. “Dosimetry using plane-parallel ionization chambers in a 75 MeV clinical proton beam”. *Phys Med Biol*, 2002, 47:16, pp. 2895–2905. DOI: 10.1088/0031-9155/47/16/305.

[44] Sterpin, E., Sorriaux, J., Souris, K., Vynckier, S., and Bouchard, H. “A Fano cavity test for Monte Carlo proton transport algorithms: Fano cavity test for MC simulations of protons”. *Med Phys*, 2013, 41:1, p. 011706. DOI: 10.1118/1.4835475.

[45] Palmans, H. and Vatnitsky, S. M. “Comment on ‘Proton beam monitor chamber calibration’” *Phys Med Biol*, 2016, 61:17, pp. 6585–6593. DOI: 10.1088/0031-9155/61/17/6585.

[46] Baumann, K.-S., Horst, F., Zink, K., and Gomà, C. “Comparison of PENH, FLUKA, and GEANT4/TOPAS for absorbed dose calculations in air cavities representing ionization chambers in high-energy photon and proton beams”. *Med Phys*, 2019, 46:10, pp. 4639–4653. DOI: 10.1002/mp.13737.

3

Investigating the lateral dose response functions of point detectors in proton beams

This Chapter is published as: **Kretschmer, J.**, Brodbek, L., Looe, H.K., van der Graaf, E., van Goethem, M.J., Kiewiet, H., Olivari, F., Meyer, C., Poppe, B. and Brandenburg, S. "Investigating the lateral dose response functions of point detectors in proton beams." *Phys Med Biol*, 2022, 67:14, p. 145003. DOI: doi:10.1088/1361-6560/ac783c

The Chapter is identical in content to the publication. The author contributions are listed in Appendix A in the "Statement on own contributions".

Abstract

Objective. Point detector measurements in proton fields are perturbed by the volume effect originating from geometrical volume-averaging within the extended detector's sensitive volume and density perturbations by non-water equivalent detector components. Detector specific lateral dose response functions $K(x)$ can be used to characterize the volume effect within the framework of a mathematical convolution model, where $K(x)$ is the convolution kernel transforming the true dose profile $D(x)$ into the measured signal profile of a detector $M(x)$. The aim of this work is to investigate $K(x)$ for detectors in proton beams.
Approach. The $K(x)$ for five detectors were determined by iterative deconvolution of measurements of $D(x)$ and $M(x)$ profiles at 2 cm water equivalent depth of a narrow 150 MeV proton beam. Monte Carlo simulations were carried out for two selected detectors to investigate a potential energy dependence, and to study the contribution of volume-averaging and density perturbation to the volume effect.
Main results. The Monte Carlo simulated and experimentally determined $K(x)$ agree within 2.1% of the maximum value. Further simulations demonstrate that the main contribution to the volume effect is volume-averaging. The results indicate that an energy or depth dependence of $K(x)$ is almost negligible in proton beams. While the signal reduction from a Semiflex 3D ionization chamber in the center of a gaussian shaped field with 2 mm sigma is 32% for photons, it is 15% for protons. When measuring the field with a microDiamond the trend is less pronounced and reversed with a signal reduction for protons of 3.9% and photons of 1.9%.
Significance. The determined $K(x)$ can be applied to characterize the influence of the volume effect on detectors measured signal profiles at all clinical proton energies and measurement depths. The functions can be used to derive the actual dose distribution from point detector measurements.

Keywords: volume effect, lateral dose response function, proton beams, small fields, dosimetry

3.1 Introduction

While modern proton pencil beam scanning (PBS) with almost vanishing dose at positions beyond the Bragg-peak allows for effective sparing of healthy tissue in beam direction, the lateral dose fall-off (penumbra) of such intensity-modulated proton beams is limited by the penumbra of the single pencil beams. In the past few years, irradiation techniques have been investigated and implemented, which aim to steepen the lateral penumbra of proton beams to better spare adjacent organs-at-risk or to better conform the radiation beam to small lesions. These techniques comprise PBS in combination with collimating apertures or a dynamic collimation system, PBS with a reduced air gap between nozzle and patient, or combined with edge-enhanced collimation [1, 2, 3, 4]

For general PBS with gaussian shaped pencil beams, previous studies indicate that the volume effect of detectors, which comprises the volume-averaging and density effects, does not or only slightly influence the measurement process [5, 6, 7, 8, 9]. In contrast, insight into the performance of point detectors in proton beams with reduced penumbrae is scarce. While McAuley *et al.* [10] found no significant difference between the profiles of a scattered collimated proton beam measured with high resolution film and a diode detector, Hoehr *et al.* [11] identified differences in output factor measurements for collimated 74 MeV scattered proton fields down to 5 mm diameter measured with a diode detector. Lomax [12] predicts that developments in proton therapy comprise a trend towards reduced penumbras and (very) small field dosimetry. For both steep penumbras and small fields, i.e. wherever the spatial dose distribution exhibits strongly varying gradients, special care must be taken to mitigate perturbations due to the volume effect of point detectors.

Describing the measurement process with a convolution model, the volume effect of a detector can be characterized by its lateral dose response function $K(x, y)$ that encompasses two contributing mechanisms: the volume-averaging within the extended sensitive volume and the density perturbation that results from the disturbance of the charged particle fluence by non-water-equivalent detector components [13, 14, 15]. The function $K(x, y)$ acts as the convolution kernel transforming the undisturbed dose distribution $D(x, y)$ into the measured signal distribution $M(x, y)$ [13, 16, 14, 15, 17, 5]:

$$M\left(x,y\right) = \; K\left(x,y\right) * D\left(x,y\right) = \int_{-\infty}^{\infty}\int_{-\infty}^{\infty} K\left(x-u,y-v\right) D\left(u,v\right) \; du\, dv \qquad (3.1)$$

When $K(x,y)$ is known for a certain detector, the dose profiles $D(x,y)$ can be recovered from the measured profiles $M(x,y)$ by deconvolution [18]. $K(x,y)$ for photon fields have been derived experimentally and/or by Monte Carlo simulations [19, 13, 14, 15, 17, 20]. To do so, $D(x,y)$ and $M(x,y)$ profiles of a narrow slit beam or pencil beam were obtained such that $K(x,y)$ could be derived from the relationship in Equation 3.1 for a large set of detectors [19, 13, 15, 14, 17, 20]. Considering the shorter average secondary electron range in proton beams as compared to photons [5] the influence of the density perturbation is anticipated to be smaller in proton beams, while the volume-averaging component remains the same. Therefore, the lateral dose response functions of detectors for proton beams are expected to differ from that for photon beams and to the best of our knowledge have not yet been studied.

The aim of this work is to experimentally determine one-dimensional $K(x)$ of a number of detectors in proton beams, that can be transformed to two-dimensional functions by considering the detectors' rotational symmetry. The lateral profiles $D(x)$ and $M(x)$ of a scattered 150 MeV proton beam collimated by a 0.5 mm wide slit collimator were measured at 2 cm water equivalent depth with EBT3 film and point detectors, respectively. Using the previously described convolution model (Equation 3.1), $K(x)$ was determined for three ionization chambers, a silicon diode and a diamond detector. The depth dependence of $K(x)$ was investigated by applying the $K(x)$ derived at 2 cm depth to profiles measured at larger depths. In addition, Monte Carlo simulations to elucidate the contributions of volume-averaging and density perturbation to the total volume effect of the detectors in clinical proton beams were performed and simulations for 60 MeV and 240 MeV protons were used to study a potential energy dependence.

3.2 Method

3.2.1 Determination of $K(x)$

Setup

Experiments were performed at the PARTREC Accelerator Facility (University Medical Center Groningen, University of Groningen) using a dedicated narrow proton beam geometry. A 150 MeV proton beam was scattered by a 1.44 mm Pb foil, located 3.03 m upstream from a 50 mm diameter, 45 mm thick circular brass collimator. Prior to the actual measurements the flatness of the 50 mm diameter field was checked using a

Table 3.1. Diameters of the detectors including wall material and of the detectors sensitive area for all investigated point detectors as well as the sensitive detector volumes in mm^3 as calculated from finite-element methods taken from (Tekin *et al.* [21]) (*) or calculated using data given in (Tekin *et al.* [22]) (**).

Detector	Outer detector diameter in mm	Diameter of sensitive area in mm	Sensitive volume in mm^3
microSilicon 60023 (PTW)	6.9	1.5	0.03(*)
microDiamond 60019 (PTW)	6.9	2.2	0.004(*)
CC01G Razor (IBA)	3.0	2.0	9.185
PinPoint 3D 31022 (PTW)	4.3	2.9	13.1(**)
Semiflex 3D 31021 (PTW)	6.1	4.8	52.5(**)

CCD/scintillator system (scintillator: Kodak LANEX Fine®; camera: Apogee ALTA® E1, CCD: Kodak Blue Plus® full frame sensor; 768x512 pixels of 9x9 μm^2). Subsequently the proton beam was further collimated to create the desired narrow beam profile. Preliminary experiments showed that the narrow dose distribution needed to derive $K(x)$ can be obtained by using a 104 mm thick slit collimator and a slit width of 0.5 mm. During the experiments, the slit collimator was placed at approximately 3.1 m from the scatter foil on a translation (Newport M-443) and rotation stage (Newport URS 100BC) to align the slit collimator with the beam by optimizing the slit output at the center and the symmetry of the measured profile.

Dose profiles $D(x)$

The $D(x)$ profiles of the slit beam were measured with Gafchromic EBT3 films in a 250 mm (x) x 258 mm (y) x 554 mm (z) water phantom with a 2.9 mm thick polycarbonate entrance window located 43 mm from the slit collimator exit. The film response was calibrated in a 50 mm diameter 150 MeV proton beam against the dose measured with a PTW Markus chamber type 23343 (0, 0.02, 0.05, 0.1, 0.21, 0.42, 0.84, 1.1, 1.7 and 4.2 Gy) at 2 cm depth in a polystyrene phantom. The calibration was performed following the procedure described in Brodbek *et al.* [5] but using two third-degree polynomial fit functions, one for the low and another for the high dose range, to improve the goodness of the fit over the entire dose range. To warrant an overall smooth calibration curve the two ranges had an overlap of three measurement points. Using the calibrated films $D(x)$ profiles were acquired at 2, 8 and 13 cm water equivalent depth at corresponding residual ranges of approximately 12.2, 6.2 and 1.2 cm. The films were scanned with an Epson 10000XL flatbed scanner (Seiko Epson Corp., Suwa, Japan) at a resolution of 600 dpi and 48 bit. The $D(x)$ profile of each film was obtained from the average of 71 pixel

rows (3 mm) across the measured profile. For each individual film, the background was estimated by averaging the dose in 3x3 mm^2 regions in the four corners of the film (see section 3.4.2). The $D(x)$ profiles were determined as the mean of three independent background-corrected film measurements.

Signal profiles $M(x)$

The corresponding $M(x)$ profiles were acquired using three ionization chambers (a Semiflex 3D 31021 and a PinPoint 3D 31022 from PTW Freiburg, Germany and a CC01G Razor chamber from IBA Dosimetry, Schwarzenbruck, Germany), as well as a microSilicon diode 60023 and a microDiamond detector 60019 (both from PTW Freiburg, Germany). Geometrical information on the sensitive volumes of all five investigated detectors is given in Table 3.1. All detectors were positioned with the detector axis parallel to the beam axis. $M(x)$ profiles were acquired at 2, 8 and 13 cm water equivalent depth taking into account the effective points of measurement. The detector signal was read out with an UNIDOS electrometer type 10001 (PTW Freiburg, Germany) as a function of lateral position across the profile in the water phantom. The detectors were moved using a translation stage (Thorlabs NRT100/M) with 0.015 mm accuracy and variable step sizes (between 0.1 and 0.5 mm) chosen according to the profile shape and dose gradient. A fixed number of Monitor Units (MU) was delivered for all points in one profile.

The detector specific $K(x)$ were derived according to Equation 3.1 from the measured $D(x)$ and $M(x)$ using the iterative van Cittert [23] deconvolution method as described in Looe *et al.* [14]. The number of iterations was limited to five to suppress the unavoidable noise amplification during the iteration process. Prior to deconvolution, the measured $M(x)$ and $D(x)$ were pre-processed by first interpolating them using a cubic spline interpolation in MATLAB R2019b [24] and subsequently taking the average of the left- and right side of the profiles.

3.2.2 Monte Carlo simulations

Validation of $K(x)$ by Monte Carlo simulations

Monte Carlo simulations in GATEV9.0/Geant4.10.06.p03 were performed to further investigate the experimentally determined $K(x)$. The complete beam line model of the PARTREC Irradiation Facility as described by Mulder [25] was implemented and adapted to correspond to the actual setup described in section 3.2.1. The simulations are

performed completely independent from the measurements. In the first step, a proton phase space file was generated directly behind the exit plane of the slit collimator using the PhaseSpaceActor. Subsequently, the $D(x)$ profile was scored at 2 cm depth in a water phantom using a 0.1 mm (x) x 20 mm (y) x 0.1 mm (z) water voxel. $M(x)$ profiles of the Semiflex 3D chamber and microDiamond were simulated at the same depth using a step size of 0.1 mm within the central area of the slit beam and a step size of 0.5 mm in the outer region. Detailed models of the detectors were built based on constructional drawings provided by the manufacturers. Figure 3.1 shows the geometry details and material information of the two detectors as implemented in the Monte Carlo code. The sensitive volume of the Semiflex 3D chamber derived using finite-element methods as described in Delfs *et al.* [26] was implemented. In addition to the 150 MeV protons as used during the experiments, the simulations were also done for incident proton energies of 60 and 240 MeV.

Contribution of the volume-averaging and the density perturbation

To investigate the contribution of the volume-averaging and the density perturbation on the detector's volume effect in proton beams, $K(x)$ were determined from $M(x)$ simulations performed as described above using a modified detector geometry instead of the complete detector models. In the first modification, $M_{\text{sens}}(x)$ profiles were simulated by replacing all detector components with water, except the sensitive volume. By comparing $M_{\text{sens}}(x)$ and $M(x)$ the perturbation caused by the presence of the non-water equivalent components surrounding the sensitive volume was established. In a second step, all detector component materials, including the sensitive detector volume, were replaced by water to obtain the profiles $M_{\text{water}}(x)$ representing the contribution from only the volume-averaging.

Monte Carlo simulation settings

The physics parameters in GATE/Geant4 used in this work were selected based on previous publications [27, 28, 29]. The settings are summarized in the table S3.1 provided as supplementary material following the Monte Carlo reporting recommendations by Sechopoulos *et al.* [30]. The stopping power tables for G4_AIR and G4_WATER based on the ICRU Report 90 [31] were used for the simulations by setting the corresponding command in GATE (/gate/physics/setUseICRU90DataFlag true). The mean excitation energy of graphite used was 81 eV, in agreement with the recent ICRU recommendation [31].

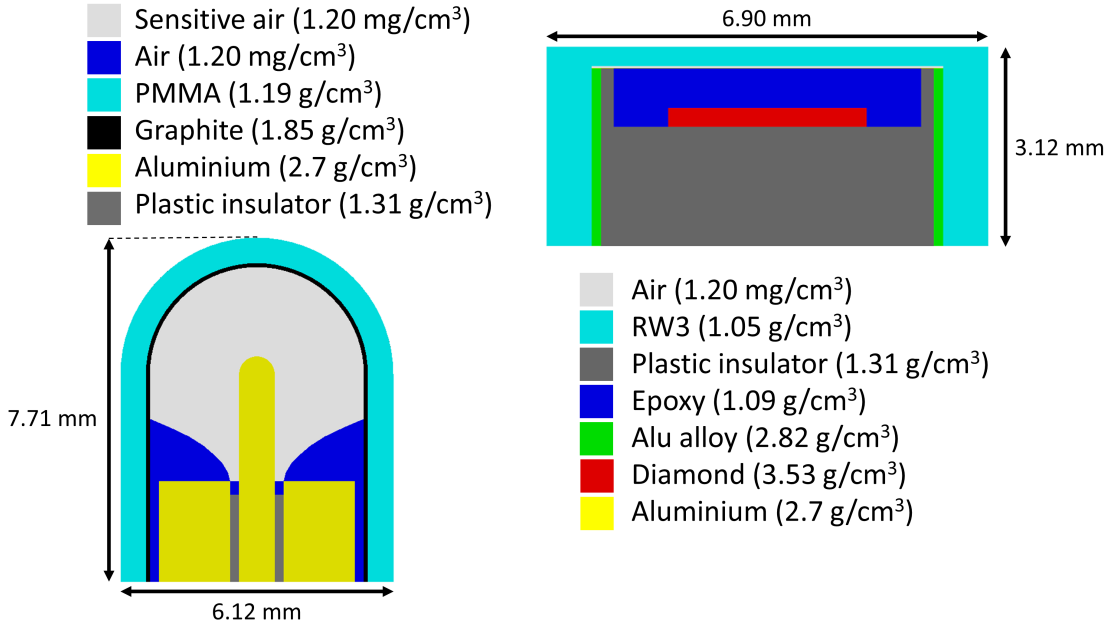

Figure 3.1. Geometries (not true to scale) and materials with density given in parenthesis of the PTW Semiflex 3D 31021 chamber (left, material information above) and the microDiamond 60019 detector (right, material information below) as implemented in the Monte Carlo code GATE. The air and aluminum part of the microDiamond below the RW3 layer are too thin to be visible.

3.3 Results

3.3.1 Measured $D(x)$ and $M(x)$

The experimentally determined $D(x)$ and $M(x)$ profiles of the optimized narrow slit beam geometry at 2, 8 and 13 cm water equivalent depth with corresponding residual ranges in water of approximately 12.2, 6.2 and 1.2 cm are shown in figure 3.2. Note that all profiles are normalized to their maxima. A constant background of approximately 0.02 Gy was subtracted from the $D(x)$ profiles, which have peak dose values of at least 1 Gy. Table 3.2 lists the corresponding FWHM and $d_{80/20}$. The tabulated $d_{80/20}$ values were computed as the average $d_{80/20}$ values of the left and right profile sides. At 2 cm depth, all $M(x)$ profiles have a larger $d_{80/20}$ than the $D(x)$ profile. While the FWHM of the $D(x)$ profile is 0.7 mm, the $M(x)$ profile of the microSilicon and Semiflex 3D have a FWHM of 1.3 mm and 3.9 mm, respectively.

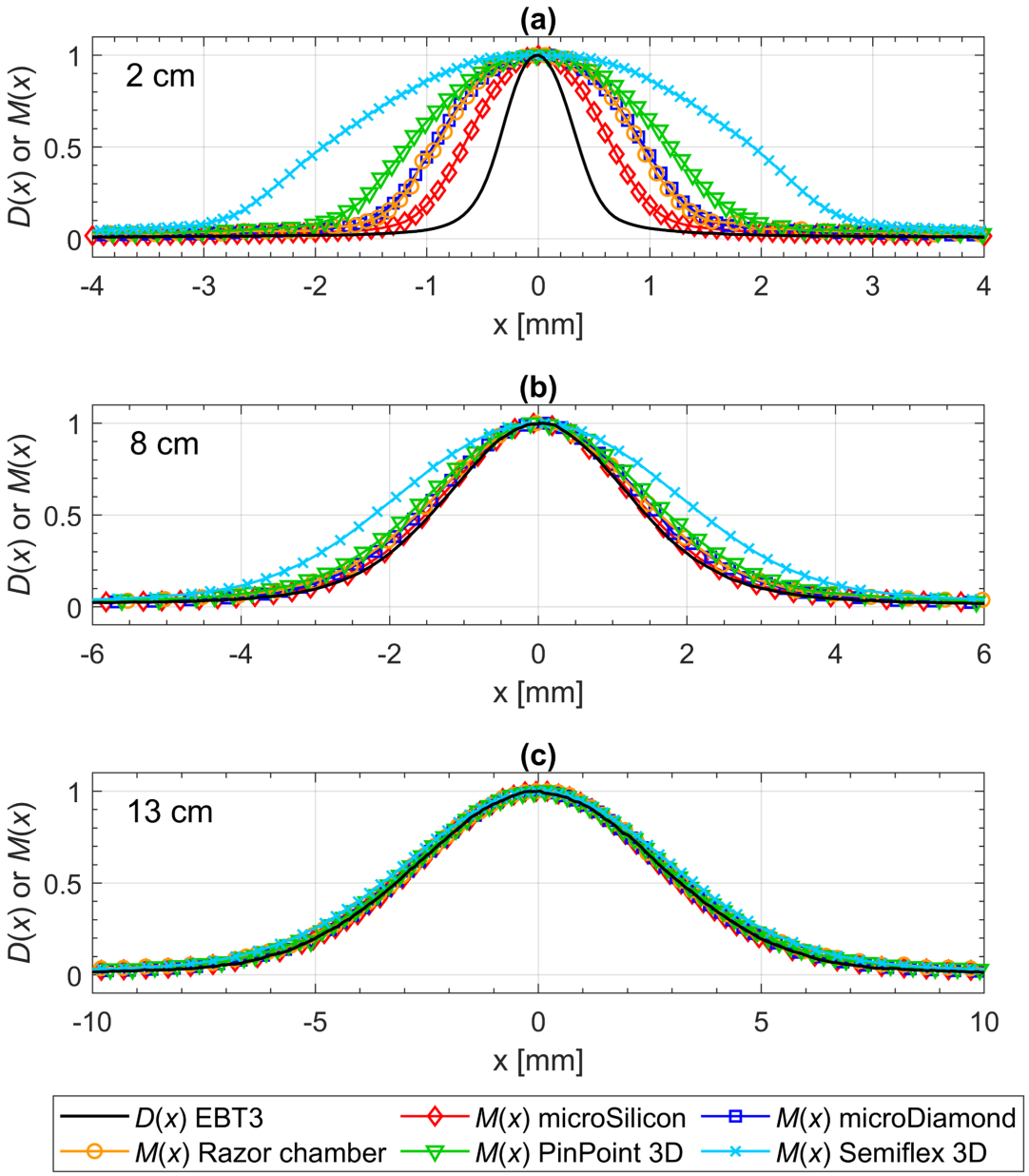

Figure 3.2. Measured profiles $M(x)$ in comparison to $D(x)$ determined with EBT3 film at (a) 2 cm, (b) 8 cm and (c) 13 cm depth in water for all investigated detectors. All profiles have been normalized to their respective maximum. Note the difference in the x-scales.

Table 3.2. FWHM and $d_{80/20}$ of experimentally determined $D(x)$ and $M(x)$ profiles shown in figure 3.2. The uncertainty of the values is estimated as half the distance between two measurement points, which is 0.02 mm for the $D(x)$ profile and 0.05 mm for the $M(x)$ profiles.

Depth	2 cm		8 cm		13 cm	
	$d_{80/20}$ [mm]	FWHM [mm]	$d_{80/20}$ [mm]	FWHM [mm]	$d_{80/20}$ [mm]	FWHM [mm]
$D(x)$ - Film	0.35	0.73	1.58	2.92	3.30	6.44
$M(x)$ - microSilicon	0.57	1.34	1.59	3.05	3.19	6.34
$M(x)$ - microDiamond	0.68	1.90	1.68	3.24	3.25	6.45
$M(x)$ - Razor chamber	0.65	1.84	1.70	3.27	3.36	6.49
$M(x)$ - PinPoint 3D	0.87	2.37	1.80	3.50	3.27	6.58
$M(x)$ - Semiflex 3D	1.33	3.86	2.10	4.43	3.51	7.00

3.3.2 Experimentally determined $K(x)$

The $K(x)$ derived from the 2 cm depth measurements, normalized to their respective maximum are presented in figure 3.3. Please note that during convolutions, the $K(x)$ are area-normalized. All $K(x)$ show almost vanishing values beyond the borders of the detector's sensitive volume. However small oscillations can be observed at the borders of the detectors, especially for the diode type detectors. The origin of these oscillations will be analyzed in the discussion.

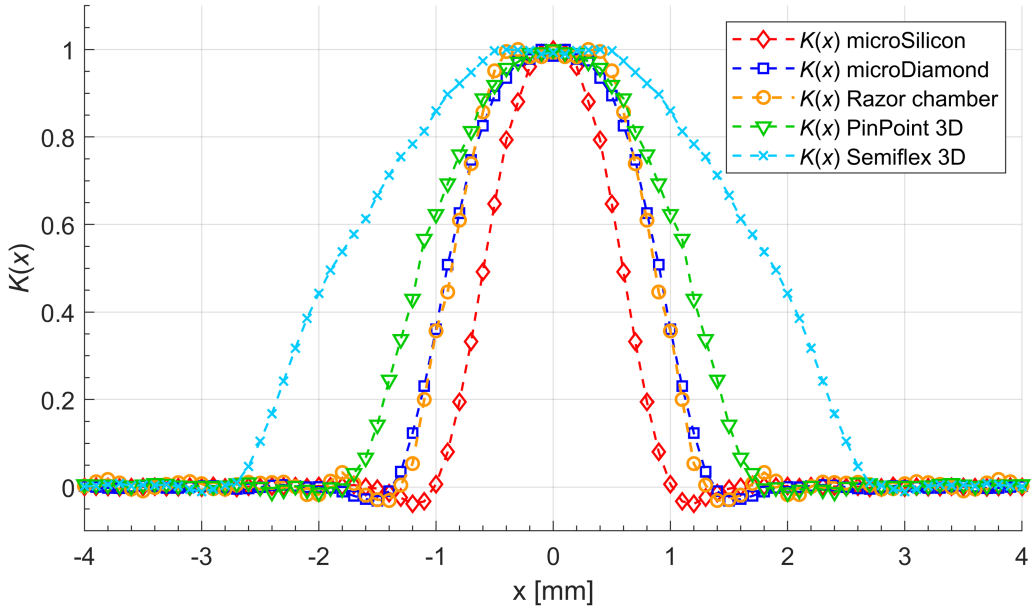

Figure 3.3. Comparison of experimentally derived lateral dose response functions $K(x)$ determined based on measurements of $D(x)$ and $M(x)$ at 2 cm depth in water. All curves are normalized to their respective maximum.

3.3.3 Validation of $K(x)$ at larger depths

To investigate the applicability of the $K(x)$ determined at 2 cm depth at larger measurement depths, the measured $D(x)$ profiles at 8 and 13 cm depth were convolved with the $K(x)$ shown in figure 3.3 ($K_{2\text{cm}}(x) * D_{8\text{cm/13cm}}(x)$) and compared to actual measurements of $M_{8\text{cm/13cm}}(x)$ performed with the Semiflex 3D chamber and microDiamond. The comparison shown in figure 3.4 reveals that the convolution products $K_{2\text{cm}}(x) * D_{8\text{cm/13cm}}(x)$ and the measured $M_{8\text{cm/13cm}}(x)$ agree well for both measurement depths and detectors.

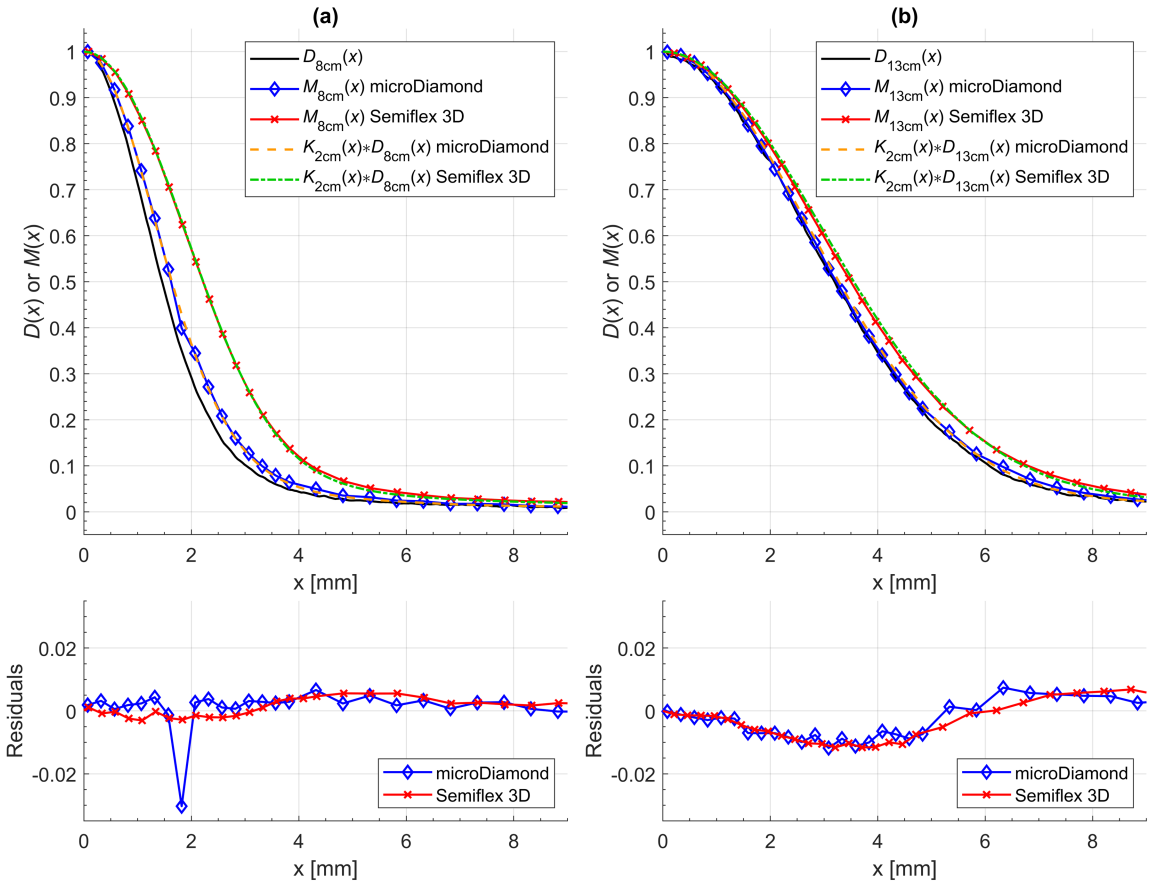

Figure 3.4. Measured profiles $M_{8\text{cm}/13\text{cm}}(x)$ in comparison to $K_{2\text{cm}}(x) * D_{8\text{cm}/13\text{cm}}(x)$ for the Semiflex 3D and microDiamond at (a) 8 cm and (b) 13 cm depth in water. All profiles have been normalized to their respective maximum. The residuals represent the difference between the normalized profiles associated with each detector.

3.3.4 Comparison between experiment and Monte Carlo simulations

Figure 3.5 shows a comparison of the experimentally and Monte Carlo simulated $K(x)$ derived for the Semiflex 3D and microDiamond using a 150 MeV proton slit beam at 2 cm depth. The comparison reveals that the maximum-normalized $K(x)$ agree within ±0.03 for both detectors. A comparison of the corresponding $D(x)$ and $M(x)$ profiles is provided as supplementary material (figures S3.1 and S3.2).

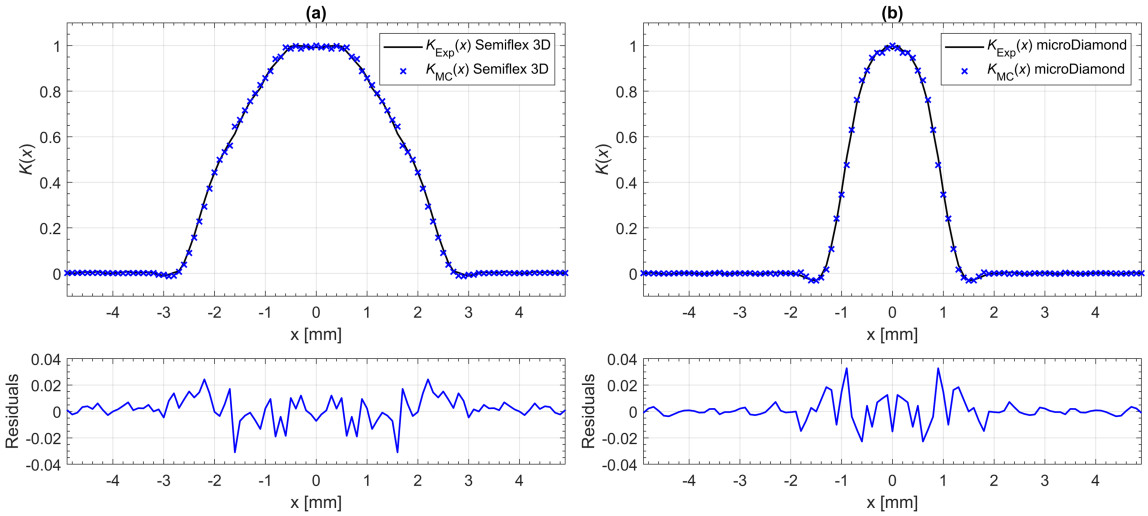

Figure 3.5. Comparison of the lateral dose response functions $K(x)$ determined experimentally (Exp) and by Monte Carlo simulations (MC) for the Semiflex 3D (a) and microDiamond (b) at 2 cm depth in water. All profiles are normalized to their respective maximum. The residuals represent the difference between the measurement and simulation.

3.3.5 Influence of detector components on $K(x)$

Figure 3.6 shows the comparison of $K(x)$, $K_{\text{sens}}(x)$ and $K_{\text{water}}(x)$ for the Semiflex 3D (a) and microDiamond detector (b). The functions were determined by deconvolution of the $M(x)$, $M_{\text{sens}}(x)$ and $M_{\text{water}}(x)$, respectively, with $D(x)$. The $M(x)$ profiles were simulated using the modified detector geometries of the Semiflex 3D chamber and the microDiamond detector and are provided as supplementary material (figure S3.3). For the Semiflex 3D chamber, the $K(x)$ and $K_{\text{sens}}(x)$ functions are the same within the uncertainty of the simulations while a 0.2 mm difference in FWHM between $K(x)$ and $K_{\text{water}}(x)$ can be observed. In contrast, all three functions associated with the microDiamond detector are the same within the uncertainty of the simulations.

3.3.6 Dependence of $K(x)$ on incident proton energy

The $K(x)$ functions derived for the Semiflex 3D and microDiamond detector at three different energies are presented in figure 3.7 (a) and (b). The corresponding simulated $D(x)$ and $M(x)$ profiles as well as associated FWHM and $d_{80/20}$ are provided as supplementary material (figures S3.4 and S3.5, table S3.2). Both the $K_{150\text{MeV}}(x)$ and $K_{240\text{MeV}}(x)$ are very similar while the $K_{60\text{MeV}}(x)$ shows a penumbra that is less steep.

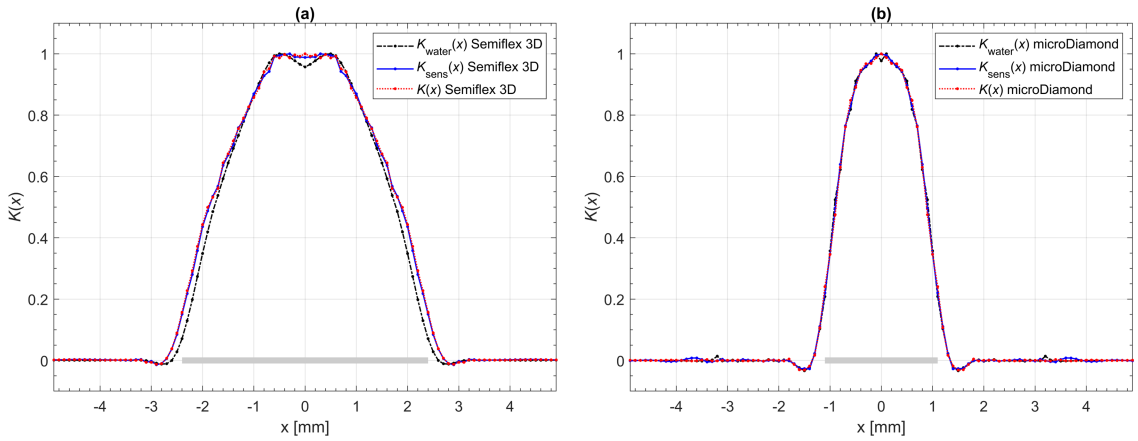

Figure 3.6. Maximum-normalized lateral dose response functions $K(x)$ for the Semiflex 3D chamber (a) and microDiamond (b) derived from Monte Carlo simulations of $D(x)$ and $M(x)$ for modified detector geometries. The red line shows the function obtained by modelling the whole detector, the blue line the function resulting if only the sensitive detector volume is implemented in the simulation. The black line shows the function obtained if all detector materials are replaced by water. The grey area indicates the width of the sensitive volume.

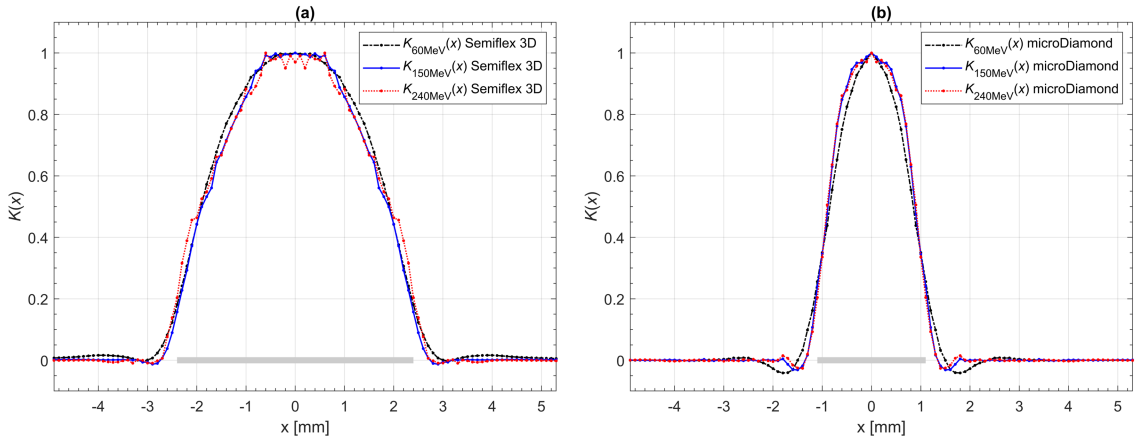

Figure 3.7. Maximum-normalized lateral dose response functions $K(x)$ for the Semiflex 3D (a) and microDiamond (b) derived from Monte Carlo simulated $D(x)$ and $M(x)$ at incident proton energies of 60, 150 and 240 MeV at 2 cm depth in water. The grey area indicates the width of the sensitive volume area.

The clinical significance of this energy dependence observed in the $K(x)$ has been investigated in figure 3.8 showing a comparison of the convolution of $D(x)$ at 60 and 240 MeV with the simulated $K_{150\text{MeV}}(x)$ and the corresponding signal profiles $M(x)$ obtained at 60 and 240 MeV, respectively. A discussion is provided in section 4.3.

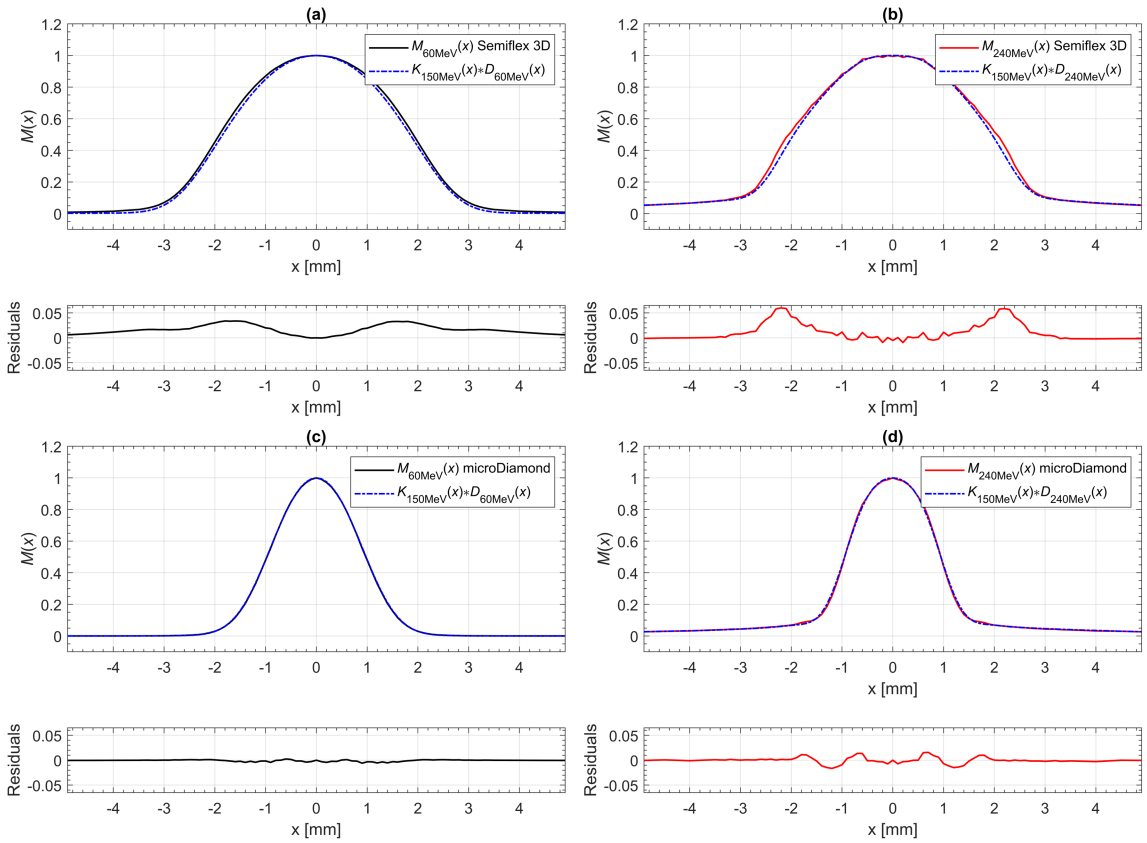

Figure 3.8. Simulated measured signal profiles $M(x)$ of the Semiflex 3D ((a) and (b)) and microDiamond ((c) and (d)) for 60 and 240 MeV in comparison to the convolutions $K_{150\text{MeV}}(x) * D_{60\text{MeV}}(x)$ ((a) and (c)) and $K_{150\text{MeV}}(x) * D_{240\text{MeV}}(x)$ ((b) and (d)). All profiles have been normalized to their respective maximum. The residuals represent the difference between the normalized profiles.

3.4 Discussion

3.4.1 Volume effect in proton beams

Lateral dose response functions $K(x)$ have been experimentally determined for five point detectors at 2 cm depth in water using a 150 MeV proton slit beam. The profiles $M(x)$ measured with various detectors reveal a volume effect for all investigated detectors. The FWHM and $d_{80/20}$ values of both $D(x)$ and $M(x)$ increase with the measurement depth due to beam broadening from multiple coulomb scattering and nuclear interactions. As a result, the differences between the $D(x)$ and $M(x)$ profiles become smaller with the depth.

The residuals of the experimentally and Monte Carlo simulated $K(x)$ for the Semiflex 3D chamber and microDiamond agree within 0.03. This good agreement allowed further investigations of the underlying mechanisms of the observed volume effect in proton beams. Detailed Monte Carlo simulations were performed to separately study the volume-averaging and the density perturbation caused by non-water equivalent detector components.

For the Semiflex 3D chamber, the $K_{\text{water}}(x)$ that solely represents the volume-averaging of the chamber is narrower than the $K_{\text{sens}}(x)$, where the sensitive volume consists of air. This difference indicates a disturbance of the particle fluence by the air cavity of the chamber due to its much lower density. The same effect has been reported for air-filled chambers in photon fields [14] as caused by an increased signal contribution from inward-directed transport of secondary electrons. The difference observed here is much less prominent than in photon fields, which is explained by the much shorter range of the secondary electrons in proton beams causing most of the dose to be deposited close to the track of the primary protons [5]. The presence of not water-equivalent components such as the aluminum central electrode or graphite and PMMA wall does not perturb the measurements as is shown by very small differences between $K_{\text{sens}}(x)$ and $K(x)$ (residuals of maximum normalized distributions within 0.02).

As shown in figure 3.6, the differences between $K(x)$, $K_{\text{sens}}(x)$ and $K_{\text{water}}(x)$ of the microDiamond detector can be considered negligible (residuals within 0.05). The results show that the thin (in the range of micrometers) sensitive volume of diode-type detectors and their surrounding materials are not causing any significant fluence perturbation. In other words, the volume effect of diode-type detectors can be solely attributed to averaging over sensitive volume of the detector. This agrees with findings by Moignier *et al.* [7], who studied diamond detector design and performed Monte Carlo simulations mimicking the measurement process of a 100 MeV proton pencil beam profile. They used a water voxel, diamond voxels of various size (widths between 0.25 mm and 4 mm) and a complete detector geometry. The profiles obtained with the water voxel, with the complete detector and a diamond voxel having the same size as the other two scoring volumes differed by less than 1%. Based on these results, it is noteworthy that detector over-response along the beam's axis and profile steepening at the beam penumbra associated to the density perturbation of diode-type detectors, as frequently reported for photon fields [32, 14, 15], are expected to be much less prominent in proton beams because of the much lower secondary electron energy.

To estimate the contributions of the geometrical volume-averaging effect and the density perturbation to the overall detector's volume effect and to provide a comparison between photons and protons, calculations based on equation 3.1 have been performed for a

small exemplary field. The results of the investigation are shown in figure 3.9. As the volume effect is most pronounced in small fields, the dose profile $D(x)$ used for the calculations was created by a gaussian function with a sigma of 2 mm representing the lower limit of the clinical field sizes used in most state-of-the-art delivery techniques. The presented perturbed $M(x)$ profiles were derived by applying equation 1 in the one-dimensional case such that $D(x)$ was convolved with the lateral dose response functions $K(x)$ of the Semiflex 3D chamber and the microDiamond detector as presented in figure 3.2. Thereby, the contribution from the overall volume effect in protons $M_{\text{proton}}(x) = D(x) * K(x)$ was estimated. For photons, the corresponding $K_{\text{6MV}}(x)$ of both detectors, valid for 6 MV photons, as previously published by Delfs *et al.* [20] were used to derive the overall volume effect in photons $M_{\text{photon}}(x) = D(x) * K_{\text{6MV}}(x)$. Additionally, the $K_{\text{water}}(x)$ that characterizes solely the volume-averaging effect in proton fields, which is independent of the beam quality [14], were used for both detectors to determine perturbed measured signal profiles resulting from solely the volume-averaging effect $M_{\text{water}}(x) = D(x) * K_{\text{water}}(x)$. For the Semiflex 3D chamber, the comparison shows that a perturbation for the exemplary field would be larger in photons than in protons with corresponding signal reductions at the field center (output) of 32% for photons and 15% for protons. In contrast, the signal reduction with a microDiamond is larger for protons by 3.9% in comparison to a photon field with a reduction of 1.9% as the density perturbation in the latter caused by the higher density detector components results in an overresponse [14, 15]. The difference between $M_{\text{water}}(0)$ and $M_{\text{proton}}(0)$ that can be attributed to the density perturbation amounts to 2% for the Semiflex 3D and is negligible (0.1%) for the microDiamond.

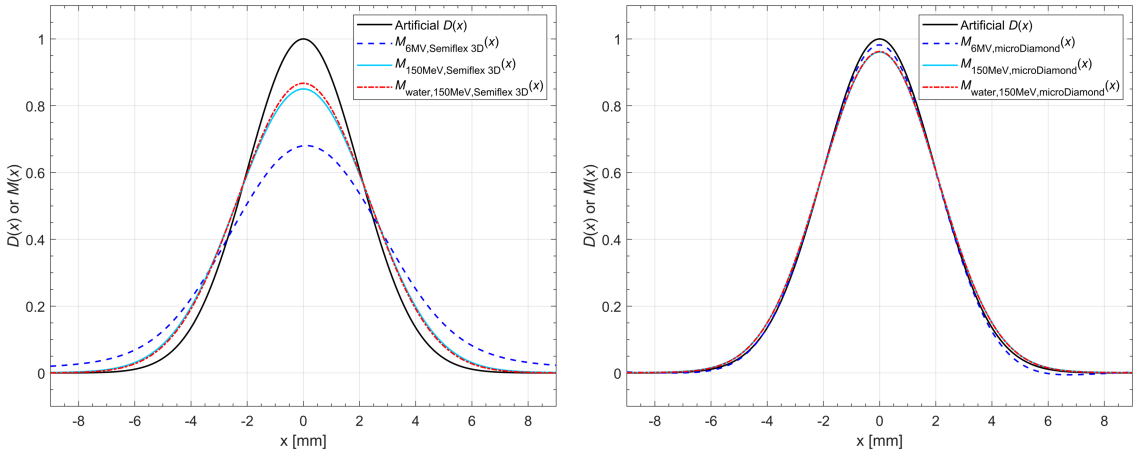

Figure 3.9. Estimation of the contributions of the geometrical volume-averaging effect and the density perturbation to the overall detector's volume effect as well as a comparison between proton and photon beam for an exemplary small field. See text for details.

The derived $K(x)$ for the diode-type detector show small oscillations at the detector edges. In photon beam dosimetry, the $K(x)$ of diode detectors also exhibit such negative values at the detector borders, which in that case are due to the perturbation of the secondary electron transport by the presence of higher density detector components [14]. However, the magnitude of these negative values is usually much larger in photon fields than that observed in this work. Furthermore, the $K_{\text{water}}(x)$ determined for the microDiamond derived without any detector components also shows the same oscillations. Thus, the oscillations cannot be attributed to the perturbation of the particle fluence by non-water equivalent detector components like in photon beams. Further evidence for this is found in figure 3.7, which shows that the $K_{60\text{MeV}}(x)$ calculated from the lowest energy simulations exhibits the strongest oscillations. This observation contradicts a potential origin of the oscillations from secondary electron transport because electrons from higher energy protons have larger ranges. Based on these observations we conclude that the small negative values of $K(x)$ of diode-type detectors are caused by a previously described artifact often observed in the iterative deconvolution process at sharp edges that is referred to as edge or ringing artifact [33]. Possible methods to suppress these artefacts in $K(x)$ of solid state detectors are to either introduce a negativity constraint or by a geometrical weighting function to compensate for volume averaging as suggested also for photon fields in TRS-483 [34].

3.4.2 Influence of the incident proton energy and measurement depth

Both the spectral and scattering angle distributions of the primary and secondary particles are expected to change as a function of measurement depth and incident proton energy. In photon fields, the functions $K(x)$ have been shown to depend on the nominal photon energy due to the associated range of the secondary electrons, but can be considered depth independent for the same incident photon beam quality [17]. Since volume-averaging was found to be the main contribution to the resulting volume effect in proton beams, the energy dependence of $K(x)$ is expected to be much smaller than in photon fields. In fact, the $K(x)$ functions derived in this work using three incident proton energies of 60, 150 and 240 MeV were found to be very similar (compare figure 3.7 ((a) and (b))).

Therefore, the question arises whether it is sufficient to characterize the detector's volume effect in proton beams by using only one detector specific $K(x)$ determined at a single proton energy and depth, as was done experimentally in this study. This was investigated

by considering profiles for various incident proton energies and measurement depths. For the former, $K_{150\text{MeV}}(x)$ was convolved with the simulated $D_{60\text{MeV}}(x)$ or $K_{240\text{MeV}}(x)$ and compared to the simulated $M_{60\text{MeV}}(x)$ or $K_{240\text{MeV}}(x)$ (compare figure 3.8). For the latter, $K_{150\text{MeV}}(x)$ determined at 2 cm depth was applied to larger measurement depths of 8 cm and 13 cm, where its applicability was studied by comparing the convolution products $K_{2\text{cm}}(x) * D_{8\text{cm}}(x)$ and $K_{2\text{cm}}(x) * D_{13\text{cm}}(x)$ with the actual measurements of $M_{8\text{cm}}(x)$ or $M_{13\text{cm}}(x)$, respectively (compare figure 43.4). In both cases, good agreement was found with a maximum difference of 0.06.

3.4.3 $K(x)$ in the context of clinical proton dosimetry

The results from this study demonstrate that the volume-averaging within the extended sensitive detector volume dominates the volume effect in proton beams. For air-filled ionization chambers, the low-density air cavity is shown to cause further fluence perturbations. However, this is not the case for diode-type detectors, where both the semiconductor chips and other housing materials are not causing observable perturbation effects apart from the volume-averaging.

Furthermore, due to the broadening of the dose profile with increasing depth, the influence of the detector's volume effect also becomes less prominent at larger depths. This underlines the conclusion from previous studies that measurements of pencil beams or PBS treatment plans, which generally have relatively large penumbras, can be characterized correctly with the detectors studied in these works [8, 35, 9, 6, 5]. Nevertheless, the selection of the detector used for profile measurements may be more important in the future as recent works have described attempts to reduce the penumbra in proton therapy [1, 12, 2, 3, 4].

The results presented here show that such sharp penumbra fields cannot be measured accurately even when using small point-like ionization chambers unless the data are corrected for the spatial response of the detector. Currently such chambers are listed as suitable detectors for measuring scattered and scanned beam profiles in the Task group 224 report on proton therapy machine QA [36] and were also recommended for measurements in dose gradients in a review of clinical dosimetry in scanned ion beam dosimetry [37]. Rath and Sahoo [38] state that small-volume ionization chambers can be used for lateral profile measurements but point out that such measurements may need a correction for the detector size. The findings of this work can guide the choice of detectors for characterizing complex protons fields. In addition, the $K(x)$ determined in this work can be used in conjunction with the convolution model to derive field size

dependent correction factors [14, 15, 39] or to recover the dose profiles from the detector signal profiles perturbed by the volume effect [9, 5].

3.5 Conclusion

The volume effect of a detector perturbs the measurement process of small fields and lateral dose profiles. This perturbation can be characterized using the associated lateral dose response function $K(x, y)$ within the framework of an established convolution model. While $K(x)$ were investigated in various studies for photon fields, these functions are presented for the first time for proton beams for three ionization chambers, a diode and a diamond detector. Contrary to photon fields, the density perturbation caused by the non-water equivalent materials is small in proton beams and the volume-averaging from the extended sensitive volume is the main determinant of the volume effect. $K(x)$ determined at 150 MeV and 2 cm depth were used at different incident energies and depths to estimate potential errors. Considering the associated results, we could conclude that the $K(x)$ can be considered energy and depth independent, so that the $K(x)$ determined with an incident proton energy of 150 MeV and at a measurement depth of 2 cm in this work can be applied to describe the distortion of measured lateral profiles for all depth positions up to the Bragg-peak and for incident energies between 60 and 240 MeV. For an exemplary gaussian shaped field with a sigma of 2 mm, the signal reduction at the field center as a result of the volume effect was calculated to be 17% smaller for protons compared to photons for a Semiflex 3D ionization chamber, whereas the measured output is 2% larger for protons than for photons when using a microDiamond detector. The determined $K(x)$ functions can be used to correct for volume effect perturbations and to derive small field correction factors that are especially important for measurements in small proton beams or collimated proton beams with sharp lateral dose profiles.

Acknowledgement

The authors thank PTW Freiburg and IBA Dosimetry for providing the detectors investigated in this study. Experiments were performed at the PARTREC Accelerator Facility of the University Medical Center Groningen, University of Groningen. Beam time was partly funded by the EU Horizon 2020 project ENSAR2 (contract no. 654002). Monte

Carlo simulations were performed on the HPC Cluster CARL funded by the DFG under INST 184/157-1 FUGG.

Supplementary material

Table S3.1. Simulation settings in GATE/Geant4 used in this work.

Item name	Description	References
Code, version, release date	GATEV9.0 released March 2020 and Geant4.10.06.p03 released on November 6, 2020	Agostinelli *et al.* [40]; Jan *et al.* [41]
Validation	Proton transport: Fano cavity test was passed at a 0.1% level Electron transport: Agreement with theory within 0.5%	Wulff *et al.* [27] Simiele and DeWerd [28]
Source description	A proton phase space was generated directly behind the slit collimator. The whole beam line shaping the 60 MeV, 150 MeV or 240 MeV proton field was modeled to generate the phase space.	Beam line model provided by Mulder [25]
Physics list	QGSP_BIC_EMZ (EMstandardOpt4) setUseICRU90DataFlag true	
Electron transport		
MSC model	Goudsmit-Saunderson (E <100 MeV), WentzelIV (E >100 MeV)	
MSC range factor	0.08	
MSC step limitation	fUseSafetyPlus	
skin	3	
e–/e+ ionization model	LowEnergyIoni (E <100 keV), Moller Bhabha (E >100 keV)	
dRoverRange	0.2	
final range	10 µm	
Production cut	1 µm (scoring volume + at least 5 mm margin), 0.02 mm (world)	
Maximum step size	1 mm (scoring volume + at least 5 mm margin)	

Table S3.1. Simulation settings in GATE/Geant4 used in this work. (continued)

Item name	Description	References
Proton transport		
MSC model	WentzelVI Model	
MSC range factor	0.2	
MSC step limitation	fMinimal	
Hadron ionization model	Bragg (E <2 MeV), Bethe-Bloch Formula (E >2 MeV)	
dRoverRange	0.1	
final range	20 µm	
Production cut	1 µm (scoring volume + at least 5 mm margin), 0.02 mm (world)	
Maximum step size	1 mm (scoring volume + at least 5 mm margin)	
Variance reduction techniques	-	
Scored quantities	Energy deposited in sensitive volume	
# histories/ statistical uncertainty	Each phase space was generated using between 300 and 500 single batches with 5E7 primary particles resulting in approximately 1E6 protons (60 MeV), 8E6 protons (150 MeV), 35E6 protons (240 MeV) recorded in the phase space. The simulation of the D(x) profile was performed with the respective phase space using 200 single batches with 5E5 initial particles each.	

Table S3.1. Simulation settings in GATE/Geant4 used in this work. (continued)

Item name	Description	References
	The simulation of each point for the M(x) profile was performed with the respective phase space using between 10 and 30 single batches on a cluster with 3E6 (Semiflex 3D) and 5E6 (microDiamond) primary particles.	
Timing	Simulations were performed on the HPC Cluster CARL, University of Oldenburg The equivalent total simulation time to generate the phase space on a single Intel Xeon 2.2GHz CPU corresponds to approximately 1900 days (60 MeV), 870 days (150 MeV), 1400 days (240 MeV). The equivalent total simulation time for one D(x) profile on a single Intel Xeon 2.2GHz CPU corresponds to between 28 and 800 days. The equivalent total simulation time for one M(x) profile on a single Intel Xeon 2.2GHz CPU corresponds to approximately 9.5 days per point (Semiflex 3D) and 17 days per point (microDiamond).	
Statistical methods	batch method All simulations were performed to reach a statistical uncertainty below 1% at the dose maximum.	Seco and Verhaegen [42]
Postprocessing	The scored energy deposited from the output files was extracted with MATLAB R2019b	MATLAB [24]

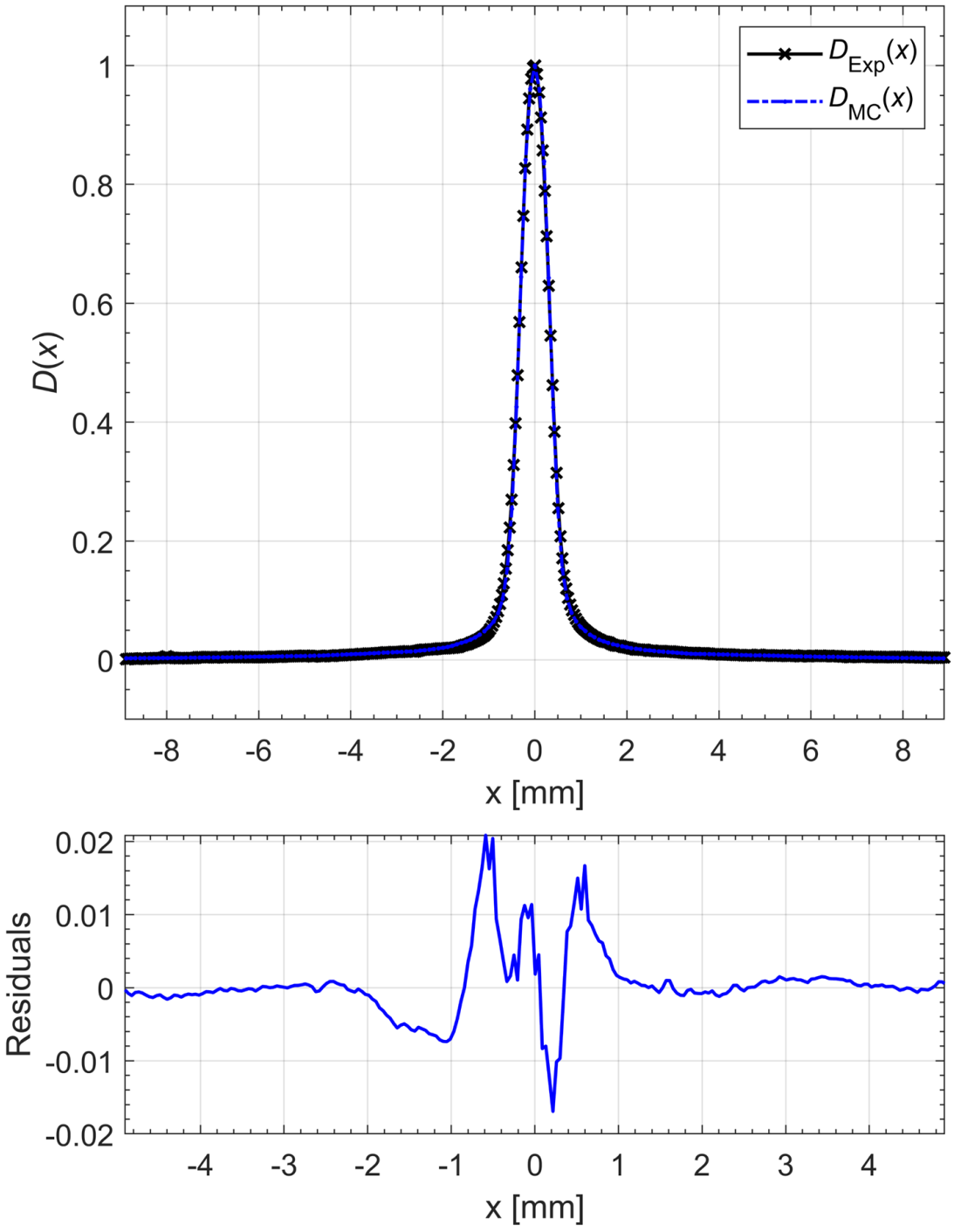

Figure S3.1. Comparison of the EBT3 film (Exp) measured and Monte Carlo simulated (MC) narrow proton dose profiles $D(x)$ at 2 cm depth in water. Both profiles have been normalized to their respective maximum. The residuals represent the difference between the normalized profiles.

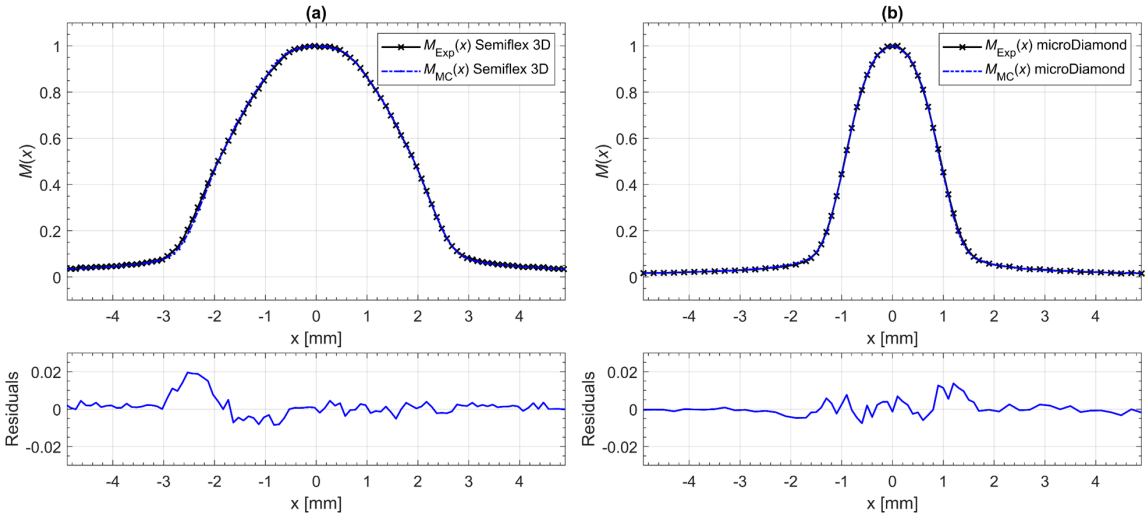

Figure S3.2. Comparison of the measured (Exp) and Monte Carlo simulated (MC) maximum-normalized signal profiles $M(x)$ determined for the Semiflex 3D (a) and microDiamond (b) at 2 cm depth in water. The residuals represent the difference between the normalized profiles.

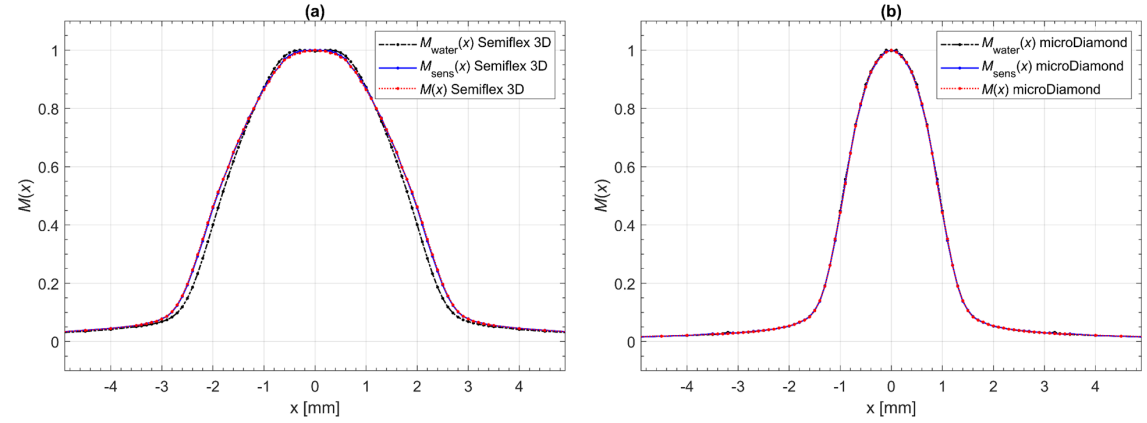

Figure S3.3. Monte Carlo simulated signal profiles $M(x)$ for the Semiflex 3D chamber (a) and microDiamond (b) at 2 cm depth in water. The red line shows the function obtained by modelling the whole detector, the blue line the function resulting if only the sensitive detector volume is implemented in the simulation. The black line shows the function obtained if all detector materials are replaced by water.

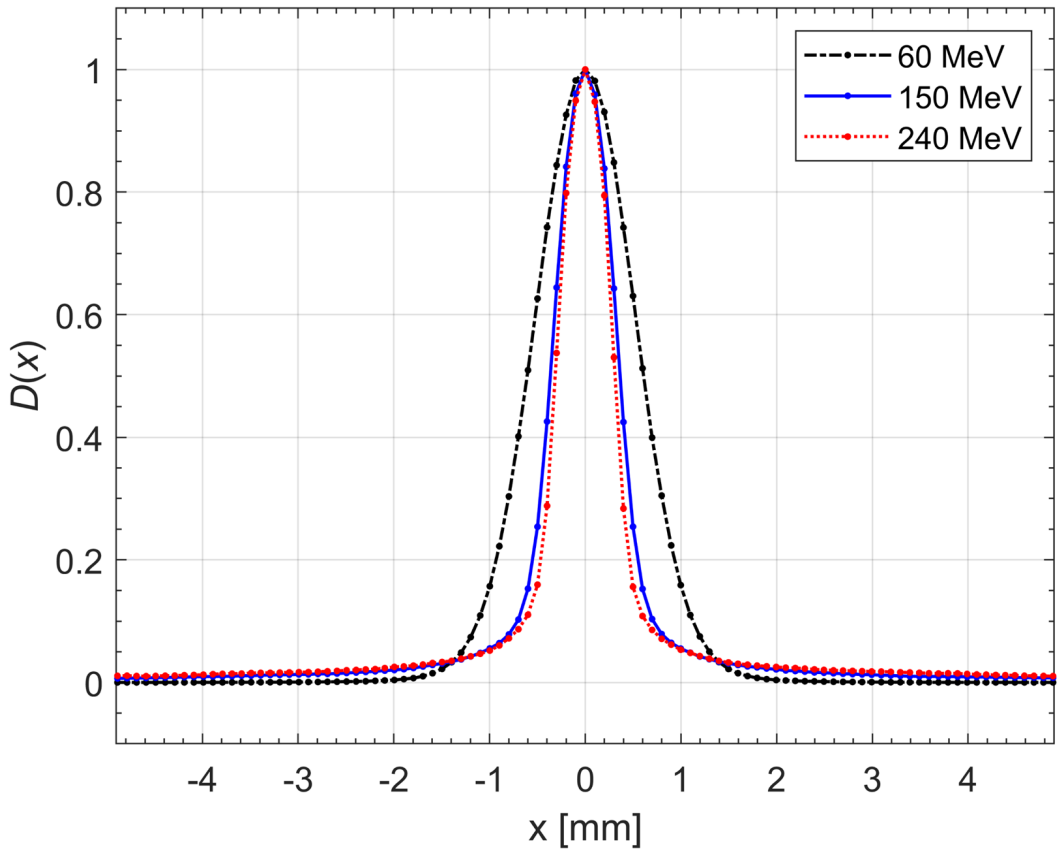

Figure S3.4. Maximum-normalized Monte Carlo simulated dose profiles D(x) for incident proton energies of 60 MeV, 150 MeV and 240 MeV at 2 cm depth in water.

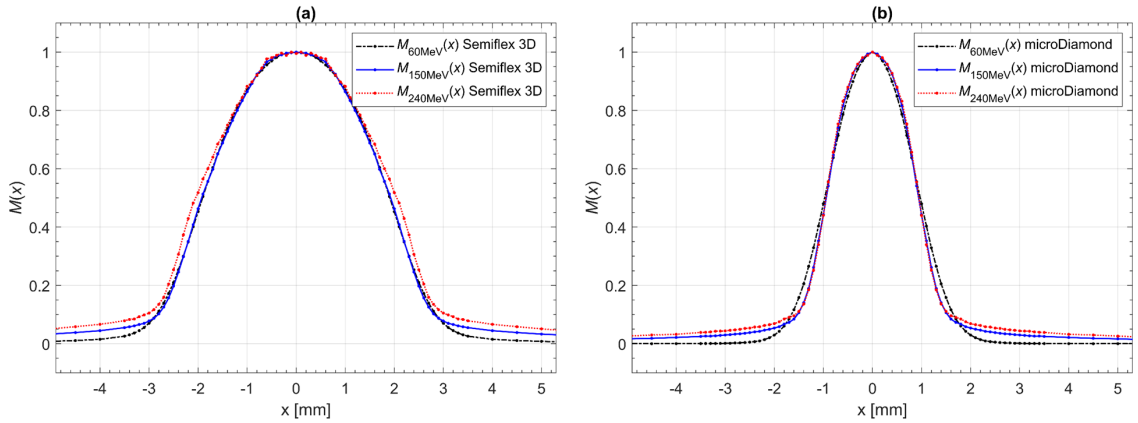

Figure S3.5. Maximum-normalized Monte Carlo simulated measured signal profiles $M(x)$ for the Semiflex 3D (a) and microDiamond (b) and for incident proton energies of 60 MeV, 150 MeV and 240 MeV at 2 cm depth in water. The grey area indicates the width of the sensitive volume area (the complete simulation geometries are shown in figure 3.2 in the article file).

Table S3.2. FWHM and $d_{80/20}$ of the Monte Carlo simulated $D(x)$ and $M(x)$ profiles in dependence of the proton energy. The uncertainty of the values is estimated as half the distance between two simulation points, which is 0.05 mm.

	$D(x)$ - Film		$M(x)$ - microDiamond		$M(x)$ - Semiflex 3D	
Proton energy	$d_{80/20}$ [mm]	FWHM [mm]	$d_{80/20}$ [mm]	FWHM [mm]	$d_{80/20}$ [mm]	FWHM [mm]
60 MeV	0.58	1.22	0.83	1.95	1.30	3.82
150 MeV	0.32	0.73	0.66	1.88	1.29	3.85
240 MeV	0.26	0.62	0.63	1.90	1.35	4.10

References

[1] Hyer, D. E., Hill, P. M., Wang, D., Smith, B. R., and Flynn, R. T. "A dynamic collimation system for penumbra reduction in spot-scanning proton therapy: Proof of concept: Penumbra trimmer for spot scanning". *Med Phys*, 2014, 41:9, p. 091701. DOI: 10.1118/1.4837155.

[2] Winterhalter, Lomax, A., Oxley, D., Weber, D. C., and Safai, S. "A study of lateral fall-off (penumbra) optimisation for pencil beam scanning (PBS) proton therapy". *Phys Med Biol*, 2018, 63:2, p. 025022. DOI: 10.1088/1361-6560/aaa2ad.

[3] Ciocca, M. et al. "Design and commissioning of the non-dedicated scanning proton beamline for ocular treatment at the synchrotron-based CNAO facility". *Med Phys*, 2019, 46:4, pp. 1852–1862. DOI: 10.1002/mp.13389.

[4] Grevillot, L. et al. "Clinical implementation and commissioning of the MedAustron Particle Therapy Accelerator for non-isocentric scanned proton beam treatments". *Med Phys*, 2020, 47:2, pp. 380–392. DOI: 10.1002/mp.13928.

[5] Brodbek, L., Kretschmer, J., Willborn, K., Meijers, A., Both, S., Langendijk, J. A., Knopf, A.-C., Looe, H. K., and Poppe, B. "Analysis of the applicability of two-dimensional detector arrays in terms of sampling rate and detector size to verify scanned intensity-modulated proton therapy plans". *Med Phys*, 2020, 47:9, pp. 4589–4601. DOI: 10.1002/mp.14346.

[6] Furukawa, T., Inaniwa, T., Hara, Y., Mizushima, K., Shirai, T., and Noda, K. "Patient-specific QA and delivery verification of scanned ion beam at NIRS-HIMAC: QA and verification for scanning delivery". *Med Phys*, 2013, 40:12, p. 121707. DOI: 10.1118/1.4828845.

[7] Moignier, C. et al. "Development of a synthetic single crystal diamond dosimeter for dose measurement of clinical proton beams". *Phys Med Biol*, 2017, 62:13, pp. 5417–5439. DOI: 10.1088/1361-6560/aa70cf.

[8] Sahoo, N., Ciangaru, G., Sawakuchi, G., Anand, A., Poenisch, F., Suzuki, K., Mohan, R., Gillin, M., and Zhu, X. "SU-GG-T-463: Study of the Magnitude of Detector Size Effect in the Measured Lateral Profiles of Proton Pencil Beam Spots". *Med Phys*, 2010, 37:6, pp. 3293–3293. DOI: 10.1118/1.3468861.

[9] Schwaab, J., Brons, S., Fieres, J., and Parodi, K. "Experimental characterization of lateral profiles of scanned proton and carbon ion pencil beams for improved beam models in ion therapy treatment planning". *Phys Med Biol*, 2011, 56:24, pp. 7813–7827. DOI: 10.1088/0031-9155/56/24/009.

[10] McAuley, G. A., Teran, A. V., Slater, J. D., Slater, J. M., and Wroe, A. J. "Evaluation of the dosimetric properties of a diode detector for small field proton radiosurgery". *J Appl Clin Med Phys*, 2015, 16:6, pp. 51–64. DOI: 10.1120/jacmp.v16i6.5391.

[11] Hoehr, C., Lindsay, C., Beaudry, J., Penner, C., Strgar, V., Lee, R., and Duzenli, C. "Characterization of the exradin W1 plastic scintillation detector for small field applications in proton therapy". *Phys Med Biol*, 2018, 63:9, p. 095016. DOI: 10.1088/1361-6560/aabd2d.

[12] Lomax, A. "What will the medical physics of proton therapy look like 10 yr from now? A personal view". *Med Phys*, 2018, 45:11, e984–e993. DOI: 10.1002/mp.13206.

[13] Looe, H. K., Stelljes, T. S., Foschepoth, S., Harder, D., Willborn, K., and Poppe, B. "The dose response functions of ionization chambers in photon dosimetry – Gaussian or non-Gaussian?" *Z Med Phys*, 2013, 23:2, pp. 129–143. DOI: 10.1016/j.zemedi.2012.12.010.

[14] Looe, H. K., Harder, D., and Poppe, B. "Understanding the lateral dose response functions of high-resolution photon detectors by reverse Monte Carlo and deconvolution analysis". *Phys Med Biol*, 2015, 60:16, pp. 6585–6607. DOI: 10.1088/0031-9155/60/16/6585.

[15] Poppinga, D., Meyners, J., Delfs, B., Muru, A., Harder, D., Poppe, B., and Looe, H. "Experimental determination of the lateral dose response functions of detectors to be applied in the measurement of narrow photon-beam dose profiles". *Phys Med Biol*, 2015, 60:24, pp. 9421–9436. DOI: 10.1088/0031-9155/60/24/9421.

[16] Harder, D., Looe, H., and Poppe, B. "Convolutions and Deconvolutions in Radiation Dosimetry". In: *Comprehensive Biomedical Physics*. Elsevier, 2014, pp. 249–269. DOI: 10.1016/B978-0-444-53632-7.00913-8.

[17] Looe, H. K., Harder, D., and Poppe, B. "The energy dependence of the lateral dose response functions of detectors with various densities in photon-beam dosimetry". *Phys Med Biol*, 2017, 62:3, N32–N44. DOI: 10.1088/1361-6560/aa54aa.

[18] Laub, W. U. and Wong, T. "The volume effect of detectors in the dosimetry of small fields used in IMRT". *Med Phys*, 2003, 30:3, pp. 341–347. DOI: 10.1118/1.1544678.

[19] Gago-Arias, A., Brualla-González, L., González-Castaño, D. M., Gómez, F., García, M. S., Vega, V. L., Sueiro, J. M., and Pardo-Montero, J. "Evaluation of chamber response function influence on IMRT verification using 2D commercial detector arrays". *Phys Med Biol*, 2012, 57:7, pp. 2005–2020. DOI: 10.1088/0031-9155/57/7/2005.

[20] Delfs, B., Poppinga, D., Ulrichs, A.-B., Kapsch, R.-P., Harder, D., Poppe, B., and Looe, H. K. "The 1D lateral dose response functions of photon-dosimetry detectors in magnetic fields—measurement and Monte-Carlo simulation". *Phys Med Biol*, 2018, 63:19, p. 195002. DOI: 10.1088/1361-6560/aadd3d.

[21] Tekin, T., Blum, I., Delfs, B., Schönfeld, A.-B., Kapsch, R.-P., Poppe, B., and Looe, H. K. "The dose response of high-resolution diode-type detectors and the role of their structural components in strong magnetic field". *Med Phys*, 2020, 47:12, pp. 6509–6518. DOI: 10.1002/mp.14535.

[22] Tekin, T., Blum, I., Delfs, B., Schönfeld, A.-B., Poppe, B., and Looe, H. K. "The magnetic field dependent displacement effect and its correction in reference and relative dosimetry". *Phys Med Biol*, 2022, 67:4, p. 045004. DOI: 10.1088/1361-6560/ac4a41.

[23] Cittert, P. H. van. "Zum Einfluß der Spaltbreite auf die Intensitätsverteilung in Spektrallinien. II". *Z. Physik*, 1931, 69:5, pp. 298–308. DOI: 10.1007/BF01391351.

[24] MATLAB. *version 9.7.0.1190202 (R2019b)*. The MathWorks Inc. Natick, Massachusetts. 2019.

[25] Mulder, J. "Water calorimetry for proton therapy: implementing a primary dose measurement standard". 2017. PhD Thesis, University of Groningen, Groningen.

[26] Delfs, B. et al. "The role of the construction and sensitive volume of compact ionization chambers on the magnetic field-dependent dose response". *Med Phys*, 2021, 48:8, pp. 4572–4585. DOI: 10.1002/mp.14994.

[27] Wulff, J., Baumann, K.-S., Verbeek, N., Bäumer, C., Timmermann, B., and Zink, K. "TOPAS/ Geant4 configuration for ionization chamber calculations in proton beams". *Phys Med Biol*, 2018, 63:11, p. 115013. DOI: 10.1088/1361-6560/aac30e.

[28] Simiele, E. and DeWerd, L. "On the accuracy and efficiency of condensed history transport in magnetic fields in GEANT4". *Phys Med Biol*, 2018, 63:23, p. 235012. DOI: 10.1088/1361-6560/aaedc9.

[29] Kretschmer, J., Dulkys, A., Brodbek, L., Stelljes, T. S., Looe, H. K., and Poppe, B. "Monte Carlo simulated beam quality and perturbation correction factors for ionization chambers in monoenergetic proton beams". *Med Phys*, 2020, 47:11, pp. 5890–5905. DOI: 10.1002/mp.14499.

[30] Sechopoulos, I., Rogers, D. W. O., Bazalova-Carter, M., Bolch, W. E., Heath, E. C., McNitt-Gray, M. F., Sempau, J., and Williamson, J. F. "RECORDS: improved Reporting of montE CarlO RaDiation transport Studies: Report of the AAPM Research Committee Task Group 268". *Med Phys*, 2018, 45:1, e1–e5. DOI: 10.1002/mp.12702.

[31] Seltzer, S. M., Fernández-Varea, J. M., Andreo, P., Bergstrom, P. M., Burns, D. T., Krajear Bronié, I., Ross, C. K., and Salvat, F. "Key data for ionizing radiation dosimetry: measurement standards and applications. ICRU Report 90". *J ICRU*, 2016, 14, pp. 1–110.

[32] Francescon, P., Beddar, S., Satariano, N., and Das, I. J. "Variation of $k_{Qclin,Qmsr}^{fclin,fmsr}$ for the small-field dosimetric parameters percentage depth dose, tissue-maximum ratio, and off-axis ratio". *Med Phys*, 2014, 41:10, p. 101708. DOI: 10.1118/1.4895978.

[33] Xiong, R., Ding, W., Ma, S., and Gao, W. "A new image deblurring algorithm with less ringing artifacts via error variance estimation and soft decision". In: *18th IEEE International Conference on Image, Processing*. Brussels, Belgium, IEEE, 2011, pp. 701–704. DOI: 10.1109/ICIP.2011.6116650.

[34] INTERNATIONAL ATOMIC ENERGY AGENCY. *Dosimetry of Small Static Fields Used in External Beam Radiotherapy, Technical Reports Series No. 483*. IAEA. Vienna. 2017.

[35] Sawakuchi, G. O., Zhu, X. R., Poenisch, F., Suzuki, K., Ciangaru, G., Titt, U., Anand, A., Mohan, R., Gillin, M. T., and Sahoo, N. "Experimental characterization of the low-dose envelope of spot scanning proton beams". *Phys Med Biol*, 2010, 55:12, pp. 3467–3478. DOI: 10.1088/0031-9155/55/12/013.

[36] Arjomandy, B. et al. "AAPM task group 224: Comprehensive proton therapy machine quality assurance". *Med Phys*, 2019, 46:8, e678–e705. DOI: 10.1002/mp.13622.

[37] Giordanengo, S., Manganaro, L., and Vignati, A. "Review of technologies and procedures of clinical dosimetry for scanned ion beam radiotherapy". *Phys Med*, 2017, 43, pp. 79–99. DOI: 10.1016/j.ejmp.2017.10.013.

[38] Sahoo, N., Sawakuchi, G. O., Gillin, M. T., and Zhu, X. R. "Radiation Dosimetry of Proton Beams". In: A. K. Rath and N. Sahoo (eds.): *Particle Radiotherapy*. New Delhi, Springer India, 2016, pp. 77–94. DOI: 10.1007/978-81-322-2622-2.

[39] Poppinga, D., Delfs, B., Meyners, J., Harder, D., Poppe, B., and Looe, H. K. "The output factor correction as function of the photon beam field size – direct measurement and calculation from the lateral dose response functions of gas-filled and solid detectors". *Z Med Phys*, 2018, 28:3, pp. 224–235. DOI: 10.1016/j.zemedi.2017.07.006.

[40] Agostinelli, S. et al. "Geant4 - a simulation toolkit". *Nucl Instrum Methods Phys Res Sect Accel Spectrom Detect Assoc Equip*, 2003, 506:3, pp. 250–303. DOI: 10.1016/S0168-9002(03)01368-8.

[41] Jan, S. et al. “GATE V6: a major enhancement of the GATE simulation platform enabling modelling of CT and radiotherapy”. *Phys Med Biol*, 2011, 56:4, pp. 881–901. DOI: 10.1088/0031-9155/56/4/001.

[42] Seco, J. and Verhaegen, F. *Monte Carlo techniques in radiation therapy*. CRC/Taylor & Francis. Boca Raton. 2013. DOI: https://doi.org/10.1201/b13961.

4

Comprehensive investigation of lateral dose profile and output factor measurements in small proton fields from different delivery techniques

This Chapter is published as: **Kretschmer, J.**, Brodbek, L., Behrends, C., Kugel, F., Koska, B., Bäumer, C., Wulff., J., Timmermann, B., Poppe, B. and Looe, H.K. "Comprehensive investigation of lateral dose profile and output factor measurements in small proton fields from different delivery techniques." *Med Phys*, 2023, 50:7, pp. 4546-4561. DOI: https://doi.org/10.1002/mp.16357

The Chapter is identical in content to the publication. The author contributions are listed in Appendix A in the "Statement on own contributions".

Abstract

Background and purpose: As part of the commissioning and quality assurance in proton beam therapy, lateral dose profiles and output factors have to be acquired. Such measurements can be performed with point detectors and are especially challenging in small fields or steep lateral penumbra regions as the detector's volume effect may lead to perturbations. To address this issue, this work aims to quantify and correct for such perturbations of six point detectors in small proton fields created via three different delivery techniques.
Methods: Lateral dose profile and output measurements of three proton beam delivery techniques (pencil beam scanning, pencil beam scanning combined with collimators, passive scattering with collimators) were performed using high-resolution EBT3 films, a PinPoint 3D 31022 ionization chamber, a microSilicon diode 60023 and a microDiamond detector 60019 (all PTW Freiburg, Germany). Detector specific lateral dose response functions $K(x, y)$ acting as the convolution kernel transforming the undisturbed dose distribution $D(x, y)$ into the measured signal profiles $M(x, y)$ were applied to quantify perturbations of the six investigated detectors in the proton fields and correct the measurements. A signal theoretical analysis in Fourier space of the dose distributions and detector's $K(x, y)$ was performed to aid the understanding of the measurement process with regard to the combination of detector choice and delivery technique.
Results: Quantification of the lateral penumbra broadening and signal reduction at the fields center revealed that measurements in the pencil beam scanning fields are only compromised slightly even by large volume ionization chambers with maximum differences in the lateral penumbra of 0.25 mm and 4% signal reduction at the field center. In contrast, radiation techniques with collimation are not accurately represented by the investigated detectors as indicated by a penumbra broadening up to 1.6 mm for passive scattering with collimators and 2.2 mm for pencil beam scanning with collimators. For a 3 mm diameter collimator field, a signal reduction at field center between 7.6% and 60.7% was asserted. Lateral dose profile measurements have been corrected via deconvolution with the corresponding $K(x, y)$ to obtain the undisturbed $D(x, y)$. Corrected output ratios of the passively scattered collimated fields obtained for the microDiamond, microSilicon and PinPoint 3D show agreement better than 0.9% (one standard deviation) for the smallest field size of 3 mm.
Conclusion: Point detector perturbations in small proton fields created with three delivery techniques were quantified and found to be especially pronounced for collimated small proton fields with steep dose gradients. Among all investigated detectors, the microSilicon diode showed the smallest perturbations. The correction strategies based on detector's $K(x, y)$ were found suitable for obtaining unperturbed lateral dose profiles and

output factors. Approximation of $K(x, y)$ by considering only the geometrical averaging effect has been shown to provide reasonable prediction of the detector's volume effect. The findings of this work may be used to guide the choice of point detectors in various proton fields and to contribute towards the development of a code of practice for small field proton dosimetry.

Keywords: lateral penumbra, output factors, proton fields, small field dosimetry, volume effect

4.1 Introduction

Dosimetry of small or steep radiation fields can be challenging and recent works have emphasized the need for higher spatial accuracy of detectors in proton therapy [1] as well as investigations of small proton field dosimetry [2, 3, 4]. While the dosimetry of small photon fields has been studied intensively in the past and international guidelines were published as a report by the AAPM Task Group 155 [5] and as TRS 483 by the IAEA [6], there are no national or international standards for dosimetry of small proton fields which may require a separate treatment due to the different nature of dose deposition processes of protons from that of photons.

Nevertheless, the commissioning and quality assurance tasks involved are similar to photon beams including measurements of lateral dose profiles and output or field size factors, i.e. the change of the dose per monitor unit as a function of field size [7, 8, 9]. Such measurements are usually acquired using point detectors with extended sensitive volume that may be subject to perturbations [10, 11, 2, 1, 12] related to the so-called volume effect [13, 14]. Although several studies found that the detector's volume effect does not noteworthy perturb measurements of proton fields with Gaussian shaped profiles or large fields with broad lateral penumbra as for example occurring in pencil beam scanning (PBS) fields [15, 16, 17, 13], volume effect perturbations have been identified in some studies and especially for proton beam delivery techniques leading to reduced penumbras [10, 2, 1, 12]. While small proton fields are used in ocular treatments, treatments of pediatric patients, minibeam irradiations or stereotactic treatments [4, 10, 18, 19, 20],the smallest possible lateral penumbra is generally desired as this allows for better sparing of adjacent organs at risk [21, 22, 20, 23]. As a consequence, several studies presented novel proton irradiation techniques utilizing small proton fields with reduced lateral penumbras [24, 22, 25, 26, 27, 9, 28].

The anticipated increasing use of small and collimated proton fields motivates further investigations of the performance of detectors under these conditions. The detector's volume effect, being dominant in small fields, may lead to a broadening of the measured lateral penumbra or, during output factor measurements, to a reduction of the measured signal at the field center [13].

Therefore, correction strategies may be needed for these measurements [29]. One of these is based on the mathematical model in equation 4.1, where the volume effect is characterized by the detector specific lateral dose response function $K(x, y)$, which acts as the convolution kernel transforming the undisturbed dose distribution $D(x, y)$ into

the measured dose distribution $M(x, y)$ representing the distribution of the background-subtracted electrical signal measured with a detector [30, 31, 32, 13].

$$M(x, y) \; = \; D(x, y) \; * \; K(x, y) \tag{4.1}$$

Equation 4.1 also shows that the knowledge of detector specific $K(x, y)$ allows the correction of the measurements performed with the detector, i.e. the detector signal with respect to position, $M(x, y)$, to obtain the unperturbed dose distributions $D(x, y)$ by deconvolution. The function $K(x, y)$ encompasses the detector perturbation due to geometrical volume averaging and disturbances of the local particle fluence by non-water equivalent detector components, where the latter is often called the density perturbation in the literature [14, 30, 32, 33]. In the following, the combined effect is referred to as the volume effect.

Recently, Kretschmer *et al.* [14] investigated the volume effect of point detectors in proton fields and presented one-dimensional $K(x)$ measured in a 150 MeV proton slit beam for various detectors, including ionization chambers and diode-type detectors. The results indicated that $K(x)$ in proton fields can be generally considered as energy and depth independent. Using the knowledge of the detector specific $K(x, y)$, volume effect perturbation at each position (x, y) in the measured lateral profiles $M(x, y)$ can be quantified according to equation 4.1 and corrected to obtain the undisturbed dose profiles $D(x, y)$ by deconvolution techniques [34]. Furthermore, field size dependent output correction factors can be derived [35].

The aim of this work is to provide insights on small field proton dosimetry by investigating perturbation effects of point detectors with regard to various proton beam delivery techniques. To do so, measurements have been performed with proton fields created via *PBS*, PBS combined with collimators (*collimated PBS*) and passive scattering with collimators (*passively scattered collimated*) using high-resolution EBT3 films, a small volume ionization chamber, a diode, and a diamond detector. Based on the mathematical convolution model (equation 4.1) and two-dimensional $K(x, y)$, perturbation effects in the studied proton fields have been quantified separately for each delivery technique. Additionally, signal theoretical analysis has been carried out to compare the undisturbed dose distributions delivered by the three techniques. The differences are discussed in conjunction with the detector specific $K(x, y)$ with regard to the magnitude of perturbations or potential errors, from which the suitability of a detector used for the characterization of small proton fields in each investigated case will be examined.

4.2 Materials & Methods

4.2.1 Beam delivery techniques for small proton fields

The perturbation of point detectors was studied in small proton fields delivered with the three techniques *PBS*, *collimated PBS* and *passively scattered collimated* (see section 4.1). All fields were provided using an IBA ProteusPlus system (IBA, Louvain-la-Neuve/Belgium) at the West German Proton Therapy Centre Essen (WPE). In the following, the technical details of each beam delivery technique in conjunction to the measurements performed are elaborated.

Pencil beam scanning

For the *PBS* delivery technique, monoenergetic proton pencil beams of 160 MeV protons with constant spot weight and 2.5 mm spot spacing were used to generate 10 mm x 10 mm and 20 mm x 20 mm square fields. The underlying pencil beam has a Gaussian distribution free in air at isocenter defined by a standard deviation of 5.1 mm. No range shifters were used. The two-dimensional dose distributions $D(x, y)$ of the fields were measured with Gafchromic EBT3 films (Ashland Speciality Ingredients G.P., Bridgewater, NJ, USA), which have been calibrated following the methods described in Brodbek *et al.* [13]. For each field size, three films were positioned in an RW3 solid water phantom (SP34 phantom, IBA Dosimetry, Schwarzenbruck) at 3 cm water equivalent depth at isocenter and irradiated simultaneously. The films were scanned with an Epson 10000XL flatbed scanner (Seiko Epson Corp., Suwa, Japan) at a resolution of 600 dpi and 48 bit. Each film scan was post-processed by applying a 2 mm x 2 mm median filter in MATLAB R2019b [36]. Subsequently, all three films for each field size were aligned and the average was computed.

Collimated PBS proton fields

For the *collimated PBS* technique, PBS fields were collimated allowing for steeper lateral dose fall-offs. Measurements were performed using a monoenergetic 160 MeV proton field collimated by 6.6 cm thick circular brass collimators of 5, 10 and 15 mm diameter. The PBS fields were delivered without a range shifter. Two-dimensional $D(x, y)$ profiles were determined from EBT3 film measurements using the same methodology as described in section 4.2.1 with a 0.3 mm x 0.3 mm median filter.

Passively scattered collimated proton fields

Measurements in *passively scattered collimated* proton fields were carried out at the WPE eye treatment nozzle. An 82.5 MeV proton beam is scattered laterally by tantalum foils and modulated in depth with a spinning modulator wheel. The basic design of the eye nozzle has been described in Slopsema *et al.* [37]. A spread-out-Bragg peak with 25 mm range and 20 mm modulation was selected for measurements, representing a typical radiation field in ocular proton therapy.

Measurements were performed for 12 mm thick collimators with opening diameters of 3, 5, 10, 15, 20 and 30 mm. Lateral profiles $M(x, y = 0)$ and $M(x = 0, y)$ of these fields were measured with a microSilicon diode 60023 and a PinPoint 3D 31022 chamber. In addition, the field outputs at the field center, i.e. $M(x = 0, y = 0)$, were measured using the microSilicon, PinPoint 3D and microDiamond 60019. The detectors were connected to a TANDEM electrometer (PTW Freiburg, Germany) and positioned axially under consideration of their effective point of measurement at 15 mm depth in a MP3XS phantom (PTW Freiburg, Germany) with a modified thin entrance window. The phantom's surface was positioned at the isocenter. Lateral profiles of the 5 mm field were scanned along the crossplane (x) and inplane (y) direction to center the detectors for output measurements.

4.2.2 Derivation of two-dimensional lateral dose response functions $K(x, y)$

The one-dimensional $K(x)$ for three ionization chambers: a Semiflex 3D 31021 and a PinPoint 3D 31022 (PTW Freiburg, Germany), and a CC01G Razor chamber (IBA Dosimetry, Schwarzenbruck, Germany), a microSilicon diode 60023 and a microDiamond detector 60019 (PTW Freiburg, Germany) have been previously reported in Kretschmer *et al.* [14] for the axial orientation, i.e. the detector's axis is parallel to the beam's axis. Additionally, Monte Carlo simulations in GATE9.0/Geant4.10.06.p03 [38, 39] were performed in this work according to the methods reported in Kretschmer *et al.* [14] to determine $K(x)$ for an Advanced Markus 34045 ionization chamber (PTW Freiburg, Germany) not included in the previous work. These functions derived using a narrow slit beam geometry are also referred to as the line spread function. The sought two-dimensional function $K(x, y)$ in Equation 4.1 or the point spread function is related to the one-dimensional $K(x)$ according to the integral Equation:

$$K(x) = \int_{-\infty}^{+\infty} K(x,y)\ dy \tag{4.2}$$

By utilizing the rotational symmetry of all investigated detectors around the detector's axis, the corresponding rotational symmetric point spread functions $K(r)$ were calculated from the one-dimensional $K(x)$ by solving an integral equation, as proposed by Marchand [40] where $r = (x^2 + y^2)^{1/2}$ is the radial distance with origin at the detector's center, i.e. point of symmetry. Subsequently, the two-dimensional $K(x, y)$ function was generated with 0.1 mm resolution for each detector from the derived $K(r)$.

4.2.3 Application of $K(x, y)$ functions

According to Equation 4.1, the $K(x, y)$ determined according to the methods presented in Section 4.2.2 can be used to retrieve the unperturbed dose profile $D(x, y)$ from the measured profile $M(x, y)$ by deconvolution or vice versa by convolution. Since it has been shown that the underlying $K(x)$ are depth and energy independent [14], the functions are regarded to be shift-invariant and therefore applicable at all previously described radiation fields.

For the *PBS* and *collimated PBS* fields, the undisturbed dose distributions $D(x, y)$ acquired using EBT3 films were compared to the detector signal profiles $M(x, y)$ representing the expected distribution of the background-subtracted electrical signal measured with a detector. The latter was computed from the $D(x, y)$ by application of equation 4.1 using the corresponding detector specific $K(x, y)$. The detector's volume effect perturbation was quantified in terms of lateral penumbra broadening and the reduction of the measured signal at the field center with respect to the actual dose at the field center $D(x, y)$. The broadening was defined as the change in the 80%-20% lateral dose fall-off, $\Delta d_{80/20} = d_{80/20,M(x)} - d_{80/20,D(x)}$ [8]. The reduction of the measured signal at the field center, also referred to as difference at $(0, 0)$ in percent in the following, is defined as $(M(0, 0) - D(0, 0)) \cdot 100$.

For the *passively scattered collimated* proton fields, the undisturbed dose profile $D(x, y)$ was derived from the measured signal profiles $M(x, y)$ acquired with a microSilicon detector and a PinPoint 3D chamber by deconvolution (Equation 4.1) utilizing the known detector specific $K(x, y)$. To do so, two-dimensional $M(x, y)$ distributions were computed from the measured profiles along the x- and y-axis, $M(x, y = 0)$ and $M(x = 0, y)$, respectively, acquired with step sizes in the range of 0.2-0.3 mm. Both profiles were then interpolated to 0.1 mm resolution using a spline interpolation in MATLAB R2019b [36].

A radial symmetrical profile $M_{\text{sym}}(r)$ was determined by averaging the four half measured profiles centered at $x = 0$ and $y = 0$. Finally, a two-dimensional $M(x, y)$ distribution with 0.1 mm resolution was generated from the $M_{\text{sym}}(r)$. The deconvolution of $M(x, y)$ was performed in two-dimensional space according to an iterative deconvolution approach [41] as described in Looe *et al.* [33] using the two-dimensional lateral dose response functions $K(x, y)$ to obtain the $D(x, y)$ profiles. The iteration was terminated after five iteration cycles to suppress noise amplification.

Furthermore, the detector specific field output correction factors k were calculated according to equation 4.3 [35] from the measured $M(x = 0, y = 0)$ and the derived $D(x = 0, y = 0)$ of the *passively scattered collimated* fields. The detector output ratio measurements acquired with the microSilicon, PinPoint 3D and microDiamond 60019 were then corrected by multiplication with the derived k factors to obtain the field output factors, i.e., the unperturbed relative dose at the field center.

$$k = \frac{D(x = 0, y = 0)}{M(x = 0, y = 0)} \tag{4.3}$$

4.2.4 Application of approximated $K_{\text{area}}(x, y)$

As pointed out in Kretschmer *et al.* [14], the dominant detector perturbation in small proton fields is attributed to the geometrical volume averaging. Therefore, it is worthwhile to investigate the suitability to approximate the lateral dose response function by a geometrical weighting function as suggested for small photon fields in TRS-483 [6] or by a Gaussian or parabolic function as performed in previous studies to correct proton PBS measurements [15, 16]. This has been performed using the smallest fields of the three delivery techniques as examples. The rotational symmetrical approximations $K_{\text{area}}(r)$ were defined according to a Heaviside function under consideration of the radius of the sensitive area $r_{\text{sensitiveArea}}$ (equation 4.4). The $d_{80/20}$ and the signal reduction at the maximum have been calculated using $K_{\text{area}}(x, y)$ and were compared to the corresponding results obtained from $K(x, y)$.

$$K_{\text{area}}(r) = \begin{cases} 1, & \text{for } r \leq r_{\text{sensitiveArea}} \\ 0, & \text{for } r > r_{\text{sensitiveArea}} \end{cases} \tag{4.4}$$

4.2.5 Signal theoretical analysis

The convolution operation described in equation 4.1 can be expressed in the Fourier space as multiplication according to equation 4.5.

$$FT[M\,(x,y)] = FT[D\,(x,y)] \cdot FT[K\,(x,y)] \tag{4.5}$$

Based on this relationship, the suitability of a detector associated with a lateral dose response function $K(x,y)$ to characterize an underlying dose distribution $D(x,y)$ can be further evaluated by examining the frequency components in $D(x,y)$ and $K(x,y)$ [42, 43, 30, 13]. To do so, the Fourier transform of the narrowest dose profile, i.e. the dose profile with smallest lateral width, $FT[D\,(x,y)]$, from each delivery technique was computed and compared to $FT\,[K\,(x,y)]$ of four selected detectors (microSilicon, PinPoint 3D, Semiflex 3D and Advanced Markus).

4.2.6 Influence of detector positioning errors

In addition to perturbations from the detector's volume effect, the detector positioning also plays an important role during output measurements in small fields [4, 10, 44]. The $M(x,y)$ and $D(x,y)$ determined for the various delivery techniques allow to estimate the impact due to uncertainties in detector positioning. To do so, a selection of proton fields from the investigated delivery techniques: 3 mm, 5 mm and 10 mm *passively scattered collimated* fields, 5 mm and 10 mm *collimated PBS* fields and a 10 mm x 10 mm *PBS* field, were analyzed exemplarily by simulating positioning errors up to 1.5 mm. Thereby, the percentage signal reduction in the $M(x, y=0)$ with respect to the corresponding $M(0,0)$ was determined as the values $\left(1 - \frac{M(x,y=0)}{M(x=0,y=0)}\right) \cdot 100$ at different off-axis positions x.

4.3 Results

4.3.1 Two-dimensional lateral dose response functions

Figure 4.1 shows the rotational symmetrical $K(r)$ for the six point detectors derived from the corresponding $K(x)$ determined experimentally in Kretschmer *et al.* [14] or simulated in this work (Advanced Markus chamber). The width of $K(r)$ increases with

increasing diameter of the sensitive volume such that the Advanced Markus chamber has the broadest function, while the $K(r)$ of the smallest microSilicon diode is the narrowest among the investigated detectors.

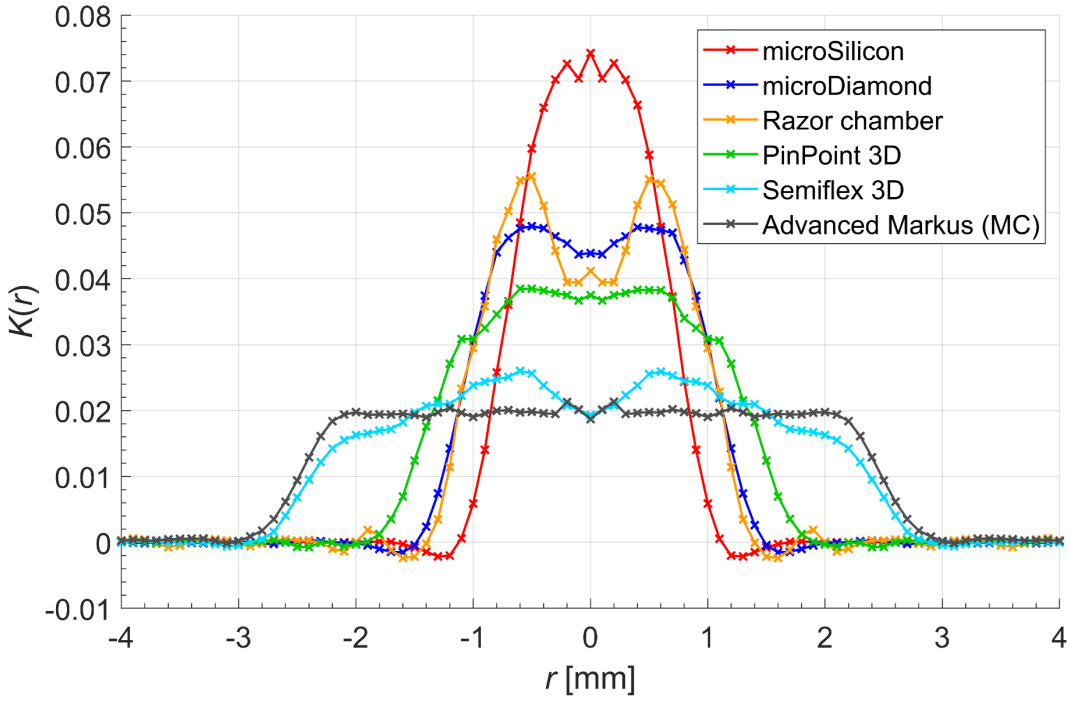

Figure 4.1. Rotationally symmetrical area normalized $K(r)$ of the six investigated point detectors.

4.3.2 Pencil beam scanning

Figure 4.2 shows the measured lateral dose profiles along the x-axis $D(x, y = 0)$ as determined from film measurements of the two PBS fields with square field sizes of 10 mm (left) and 20 mm (right) side length. The average $d_{80/20}$ of the fields are 6.9 and 8.7 mm, for the 10 mm x 10 mm and 20 mm x 20 mm, respectively. In addition to the $D(x, y = 0)$, figure 4.2 shows the calculated signal profiles $M(x, y = 0)$ for various detectors from the two-dimensional convolution of $D(x, y)$ with the $K(x, y)$ according to equation 4.1. For the 10 mm x 10 mm field (left panel), a reduction of the signal maximum of 2.9% (Semiflex 3D) and 4% (Advanced Markus) can be observed. For the 20 mm x 20 mm field (right panel in figure 4.2), the $D(x, y = 0)$ and all $M(x, y = 0)$, show minimal differences along the whole profile. Even for the Advanced Markus chamber the signal reduction at the field center is well below 1.5%. The differences in $d_{80/20}$ of the $M(x, y = 0)$ as well as the percentage signal reduction at the field center in the

measurements $M(0,0)$ with respect to the undisturbed dose profiles are listed in table 4.1.

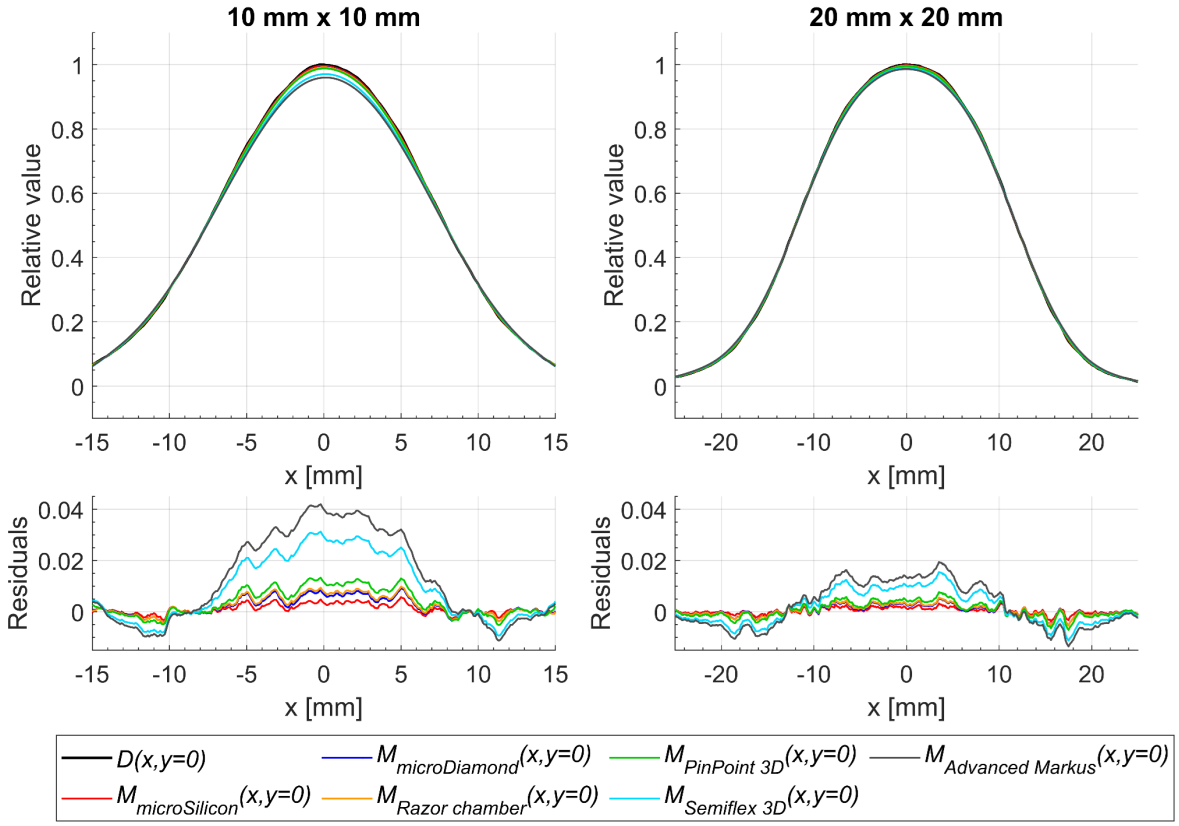

Figure 4.2. EBT3 film measured lateral dose profiles $D(x, y = 0)$ of square *PBS* fields with side lengths of 10 mm (left) and 20 mm (right) as well as the corresponding measured dose profiles $M(x, y = 0)$ obtained from the two-dimensional convolution of $D(x, y)$ and $K(x, y)$ for various point detectors. The relative values correspond to the profile values normalized to $D(x = 0, y = 0)$. The residuals represent the difference between the normalized $D(x, y = 0)$ and $M(x, y = 0)$ determined for each detector.

Table 4.1. Penumbra broadening ($\Delta d_{80/20}$) and reduction of the signal at the field center $(0, 0)$ for point detectors in dependence of the field size and investigated delivery technique. $\Delta d_{80/20}$ represents the increase in lateral penumbra calculated as the difference between the $d_{80/20}$ of $M(x, y = 0)$ and that of the corresponding $D(x, y = 0)$. The difference at $(0, 0)$ is the percentage signal reduction between the respective $M(0, 0)$ and $D(0, 0)$. The dose profiles used to retrieve the data are shown in figure 4.2 (*PBS*), figure 4.3 (*collimated PBS*) and figure 4.6 (*passively scattered collimated*). $\Delta d_{80/20}$ are associated with an uncertainty of 0.2 mm and the uncertainty for the difference at $(0, 0)$ was estimated to be 2%, 1%, 0.5% and 0.2% for field sizes with side legths or diameters of 3, 5, 10 mm or larger, respectively.

	PBS - Square field side length [mm]					
	3	**5**	**10**		**15**	**20**	
Detector			$\Delta d_{80/20}$ **[mm]**	**Diff. at** $(0, 0)$ **[%]**		$\Delta d_{80/20}$ **[mm]**	**Diff. at** $(0, 0)$ **[%]**
microSilicon			0.03	-0.34		0.02	-0.13
microDiamond			0.06	-0.68		0.04	-0.27
Razor chamber			0.06	-0.78		0.04	-0.29
PinPoint 3D			0.10	-1.15		0.06	-0.43
Semiflex 3D			0.20	-2.93		0.15	-1.01
Adv. Markus			0.25	-4.00		0.22	-1.34

Table 4.1 continued from previous page

Detector	Collimated PBS - Aperture diameter [mm]							
	3		5		10		15	20
			$\Delta d_{80/20}$ [mm]	Diff. at $(0,0)$ [%]	$\Delta d_{80/20}$ [mm]	Diff. at $(0,0)$ [%]	$\Delta d_{80/20}$ [mm]	Diff. at $(0,0)$ [%]	
microSilicon			0.30	0.27	0.35	0.15	0.34	-0.98	
microDiamond			0.58	0.12	0.65	0.17	0.62	-1.03	
Razor chamber			0.55	-0.48	0.62	0.07	0.60	-1.02	
PinPoint 3D			0.86	-0.42	0.95	0.15	0.91	-1.10	
Semiflex 3D			1.64	-8.66	1.83	-0.04	1.78	-1.24	
Adv. Markus			1.88	-15.67	2.16	-0.35	2.10	-1.28	
Detector	**Passively scattered collimated - Aperture diameter [mm]**							
	3		5		10		15	20
	$\Delta d_{80/20}$ [mm]	Diff. at $(0,0)$ [%]	$\Delta d_{80/20}$ [mm]	Diff. at $(0,0)$ [%]	$\Delta d_{80/20}$ [mm]	Diff. at $(0,0)$ [%]	$\Delta d_{80/20}$ [mm]	Diff. at $(0,0)$ [%]	
microSilicon	0.10	-7.55	0.17	-0.47	0.17	-0.42	0.19	-0.13	
microDiamond	0.20	-15.79	0.35	-1.31	0.36	-0.26	0.38	-0.20	
Razor chamber	0.19	-15.41	0.33	-1.81	0.35	-0.50	0.37	-0.22	
PinPoint 3D	0.32	-25.36	0.54	-3.37	0.58	-0.24	0.59	-0.20	
Semiflex 3D	0.68	-52.95	1.06	-17.01	1.31	-0.45	1.31	-0.19	
Adv. Markus	0.77	-60.68	1.24	-24.34	1.59	-1.03	1.59	-0.23	

4.3.3 Collimated pencil beam scanning

Figure 4.3 shows the measured lateral dose profiles along the x-axis $D(x, y = 0)$ as determined from the film measurements of the collimated PBS fields with collimator diameters of 5, 10 and 15 mm. All fields show comparable $d_{80/20}$ between 0.7 and 0.8 mm, which are achieved by collimating PBS fields created without a range shifter. The corresponding computed signal profiles $M(x, y = 0)$ for various detectors from the convolution are presented alongside. The differences between $d_{80/20}$ values of the $M(x, y = 0)$ and that of the dose profiles as well as the signal reduction at the maximum are listed in table 4.1. For all field sizes, the $M(x, y = 0)$ profiles show broader lateral penumbras than the $D(x, y = 0)$. This penumbra broadening is most pronounced for the Advanced Markus chamber ($\Delta d_{80/20}$ up to 2.2 mm) and least present in the $M(x, y = 0)$ of the microSilicon diode ($\Delta d_{80/20}$ up to 0.4 mm). For the smallest aperture diameter (5 mm), a reduction of the signal at the maximum of 8.7% (Semiflex 3D) and 15.7% (Advanced Markus) can also be observed.

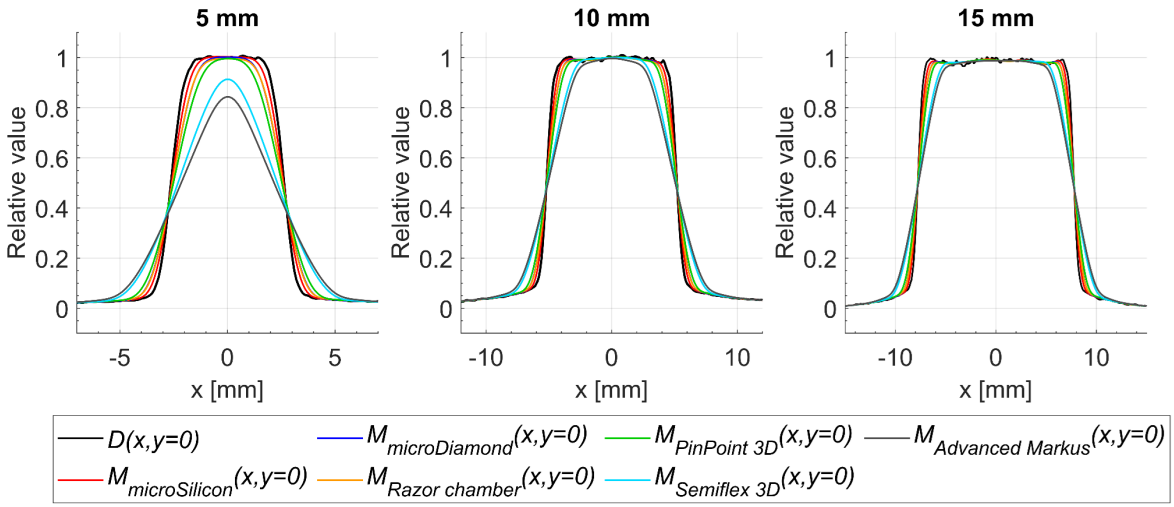

Figure 4.3. Lateral dose profiles $D(x, y = 0)$ of collimated PBS fields with circular collimators with opening diameters of 5 mm (left), 10 mm (middle) and 15 mm (right) as well as the corresponding signal profiles $M(x, y = 0)$ as obtained from the two-dimensional convolution of $D(x, y)$ and $K(x, y)$ for various point detectors. The relative values correspond to the profile values normalized to $D(x = 0, y = 0)$.

4.3.4 Passively scattered collimated proton fields

Figure 4.4 exemplarily shows the centered $M(x, y = 0)$ and $M(x = 0, y)$ of the *passively scattered* proton beam collimated by a 3 mm diameter aperture as measured with a

microSilicon detector and a PinPoint 3D chamber along the x- and y-axis, respectively. In addition, the rotational symmetrical profile $M_{sym}(x, y = 0)$, which was derived from averaging the four half profile sides is shown. The comparison between the individual points of the half profiles and $M_{sym}(x, y = 0)$ for which all profiles were normalized to the maximum of $M_{sym}(0, 0)$ resulted in a maximum difference of 1.8% of the maximum.

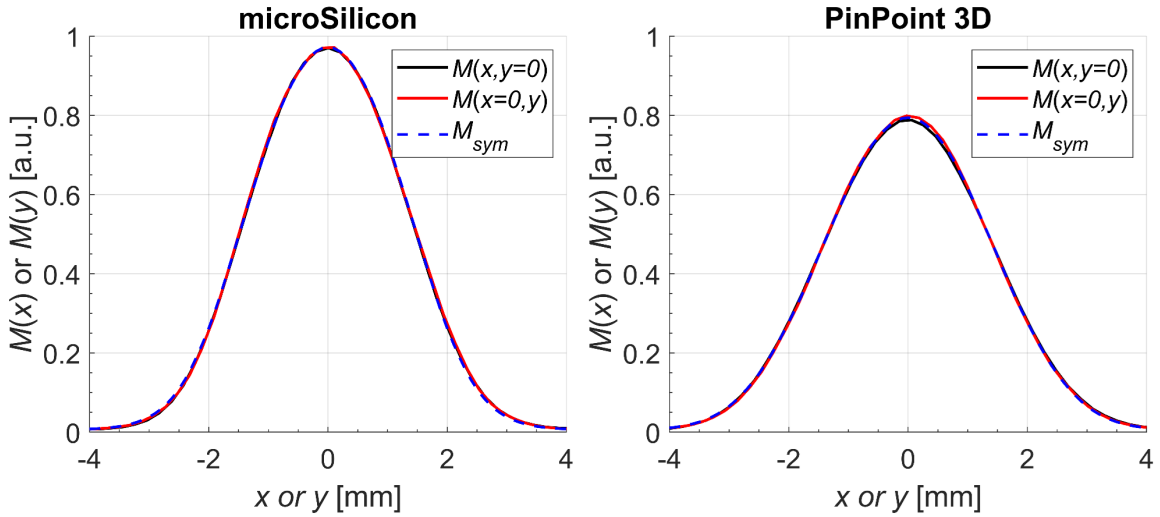

Figure 4.4. Centered signal profiles $M(x, y = 0)$ and $M(x = 0, y)$ of the 3 mm circular field measured with the microSilicon (left) and PinPoint 3D (right) as well as the corresponding rotational symmetrical profiles $M_{sym}(x, y = 0)$, which were determined by averaging the four half profiles.

Figure 4.5 shows the dose profiles $D_{\text{PinPoint3D}}(x, y = 0)$ and $D_{\text{microSilicon}}(x, y = 0)$ derived from the deconvolution in comparison to the measured $M_{Sym,\text{PinPoint3D}}(x, y = 0)$ and $M_{Sym,\text{microSilicon}}(x, y = 0)$ for the aperture diameters 3, 5, 10 and 15 mm. For ease of comparison, the profiles measured with the PinPoint 3D were multiplied by a cross-calibration factor determined as the ratio $\frac{M_{\text{microSilicon}}(x=0,y=0)}{M_{\text{PinPoint3D}}(x=0,y=0)}$ from a 30 mm diameter field. The $d_{80/20}$ values of the derived $D_{\text{PinPoint3D}}(x, y = 0)$ and $D_{\text{microSilicon}}(x, y = 0)$ are given in table 4.2 showing an agreement within 0.13 mm. Based on these results the uncertainty for calculating $\Delta d_{80/20}$ with the convolution model approach was estimated as 0.2 mm (table 4.1).

When comparing the $M(x, y = 0)$ with the deconvolved $D(x, y = 0)$ profiles, the perturbation of the volume effect of the PinPoint 3D chamber can be identified for all four field sizes in terms of penumbra broadening. In addition, a reduction of the signal at the maximum of 23.5% and 3.7% can be seen for the PinPoint 3D chamber in the two smallest field sizes, 3 and 5 mm. The perturbation of the microSilicon diode, having a much smaller sensitive volume and narrower $K(x, y)$, is less pronounced and can only

Table 4.2. $d_{80/20}$ and difference in $d_{80/20}$ between $D_{\text{PinPoint3D}}(x, y = 0)$ and $D_{\text{microSilicon}}(x, y = 0)$ derived from the corresponding measured signal profiles $M_{Sym,\text{PinPoint3D}}(x, y = 0)$ and $M_{Sym,\text{microSilicon}}(x, y = 0)$ by iterative deconvolution with $K(x, y)$ of the PinPoint 3D and microSilicon in dependence of the aperture diameter of the *passively scattered collimated fields*.

	Aperture diameter [mm]			
	3	5	10	15
$d_{80/20}$ of $D_{\text{microSilicon}}(x, y = 0)$ [mm]	1.22	1.28	1.25	1.25
$d_{80/20}$ of $D_{\text{PinPoint3D}}(x, y = 0)$ [mm]	1.32	1.33	1.38	1.37
$\Delta d_{80/20}$ [mm]	-0.10	-0.05	-0.13	-0.12

be seen in the 3 and 5 mm fields in terms of penumbra broadening and in the smallest field also in terms of a reduction of the signal at the maximum (7.0%).

To examine the influence of other detectors in the *passively scattered collimated* fields, detector signal profiles $M(x, y)$ were calculated from the convolution of $D_{\text{microSilicon}}(x, y)$ and the presented $K(x, y)$ of point detectors in Figure 4.1. Figure 4.6 shows the $M(x, y = 0)$ in comparison to $D_{\text{microSilicon}}(x, y = 0)$. Table 4.1 lists the increase in $d_{80/20}$ between the profiles as well as the percentage difference between the signal at position $(0, 0)$ with respect to $D_{\text{microSilicon}}(0, 0)$.

Figure 4.6 and table 4.1 show that measurements of the *passively scattered collimated* fields with the point detectors investigated in this work would all suffer from a broadening of the penumbra, which would be most pronounced for the Advanced Markus chamber ($\Delta d_{80/20}$ up to 1.6 mm) and least pronounced for the microSilicon diode ($\Delta d_{80/20}$ up to 0.2 mm). All $M(x, y = 0)$ of the 3 mm diameter field show a reduction of the signal at the maximum from 7.6% (microSilicon) to 60% (Advanced Markus). For the 5 mm diameter field the reduction of the signal at the maximum lies within the uncertainty for the microSilicon diode but can still be identified for all other detectors, varying between 1.3% (microDiamond) and 24.3% (Advanced Markus). In the 10 mm diameter field, a reduction of the signal at the maximum of 1% is only determined for the Advanced Markus chamber. No reduction was observed for all detectors in the 15 mm diameter field.

The left panel of figure 4.7 shows the measured output ratios normalized to the 20 mm diameter field $\frac{M(x=0,y=0)}{M_{20\text{mm}}(x=0,y=0)}$ using the microSilicon, PinPoint 3D and microDiamond. The uncertainty for the output ratios considers the machine reproducibility of 1% (2σ) as specified by the manufacturer and the signal deviation resulted from a 0.2 mm positioning uncertainty based on the detailed analysis in section 4.3.7. A value of 0.2 mm was chosen taking into account the PTW specification for the geometrical uncertainty

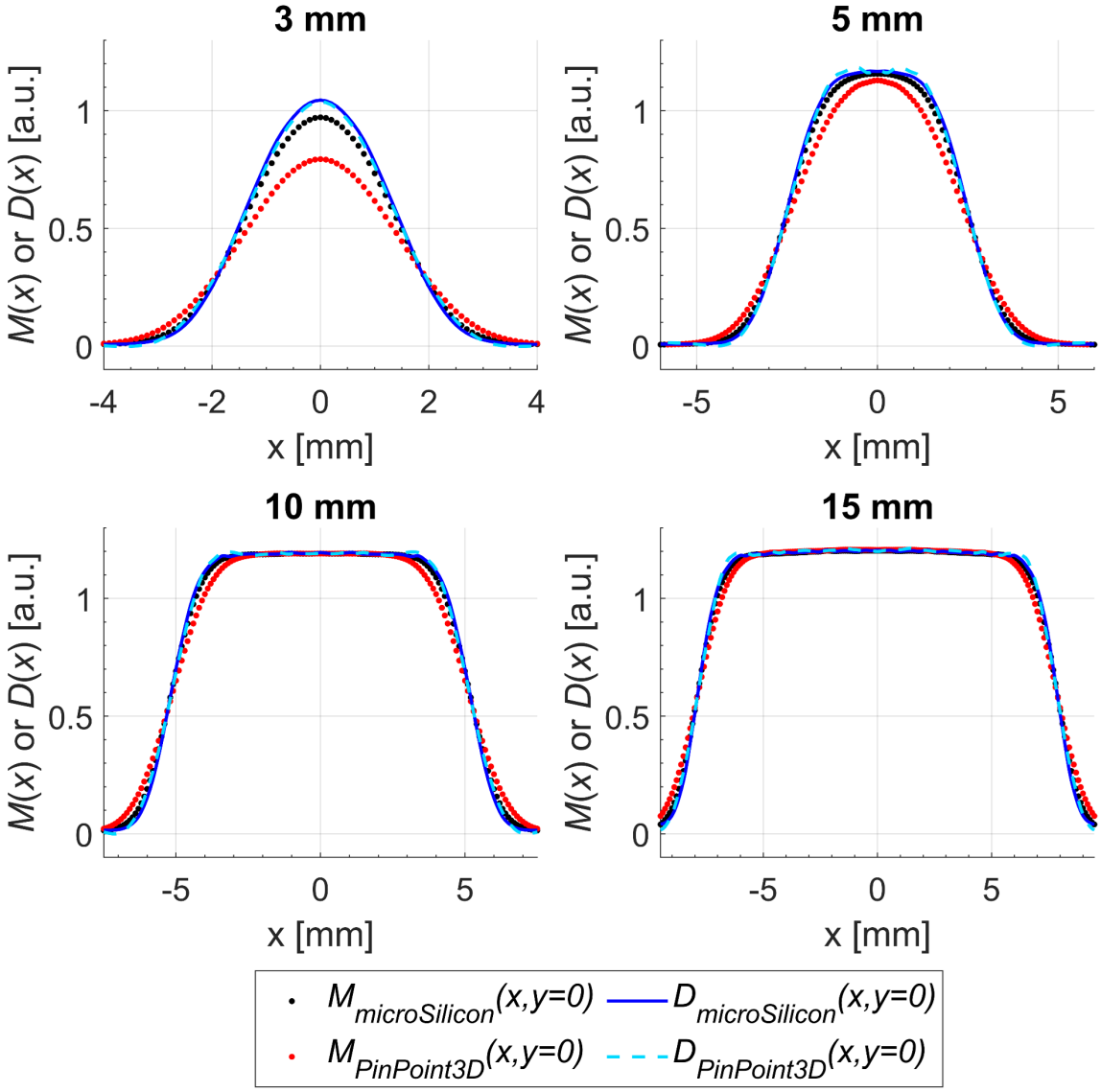

Figure 4.5. Dose profiles $D_{\text{PinPoint3D}}(x, y = 0)$ and $D_{\text{microSilicon}}(x, y = 0)$ from deconvolution in comparison to the corresponding $M_{\text{PinPoint3D}}(x, y = 0)$ and $M_{\text{microSilicon}}(x, y = 0)$ for the four smallest field sizes (3 mm, 5 mm, 10 mm and 15 mm) investigated for the *passively scattered collimated* proton beam delivery technique. The $M_{\text{PinPoint3D}}(x, y = 0)$ profiles were scaled by a cross-calibration factor to be comparable to the $M_{\text{microSilicon}}(x, y = 0)$ (compare text). The corresponding $D(x, y = 0)$ were obtained from deconvolving the presented $M(x, y = 0)$.

of $\pm$ 0.1 mm for the used phantom and the chosen step size (0.2 mm) of the profile measurements to center the detector.

The detector specific output correction factors k were derived from the ratio $\frac{D(x=0,y=0)/D_{20\text{mm}}(x=0,y=0)}{M(x=0,y=0)/M_{20\text{mm}}(x=0,y=0)}$ at the field center, where the dose profiles derived from the microSilicon measurements $D_{\text{microSilicon}}(x, y)$ were used in the numerator. Table 4.3 sum-

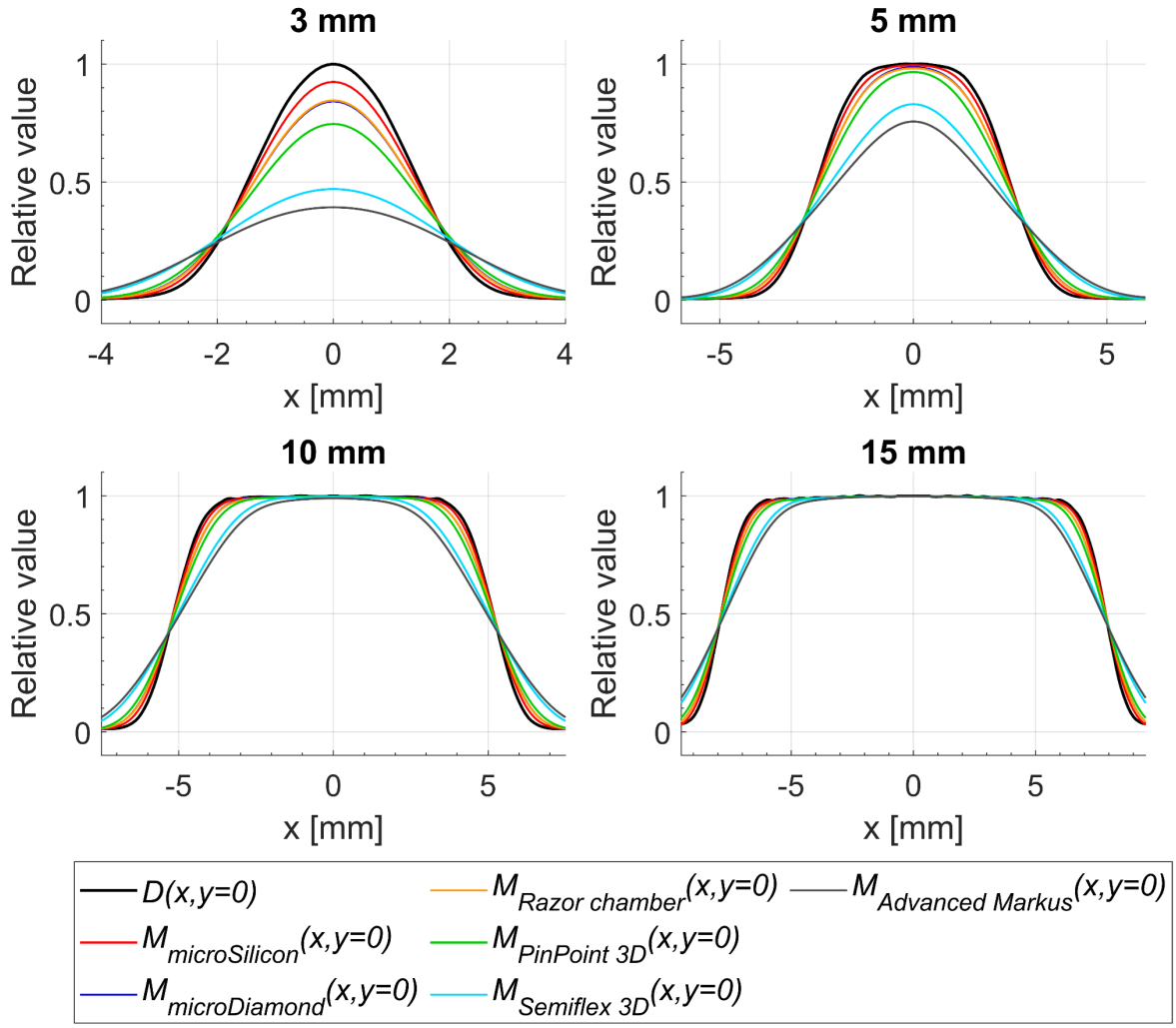

Figure 4.6. Lateral dose profiles $D_{\text{microSilicon}}(x, y)$ of *passively scattered collimated* fields using circular apertures with opening diameters of 3 mm (upper left), 5 mm (upper right), 10 mm (lower left) and 15 mm (lower right) as well as the corresponding measured dose profiles obtained from the convolution of $D_{\text{microSilicon}}(x, y)$ and $K(x, y)$ of the corresponding detectors. The relative values correspond to the profile values normalized to $D(x = 0, y = 0)$.

marizes the resulting detector and field size specific output correction factors k by adopting the same consideration as above for the uncertainty estimation. The right panel of figure 4.7 shows the corrected field output factors $\frac{D(x=0,y=0)}{D_{20\text{mm}}(x=0,y=0)}$ determined by multiplying $\frac{M(x=0,y=0)}{M_{20\text{mm}}(x=0,y=0)}$ with the corresponding k factor in table 4.3. The sought average field output factors were calculated as the mean values of the three corrected detector measurements (diamonds in figure 4.7, right panel). The percentage standard deviations of the average field output factors considering all three detectors were smaller than 0.5% for all field sizes except for the smallest 3 mm diameter field with a percentage standard deviation of 0.9%.

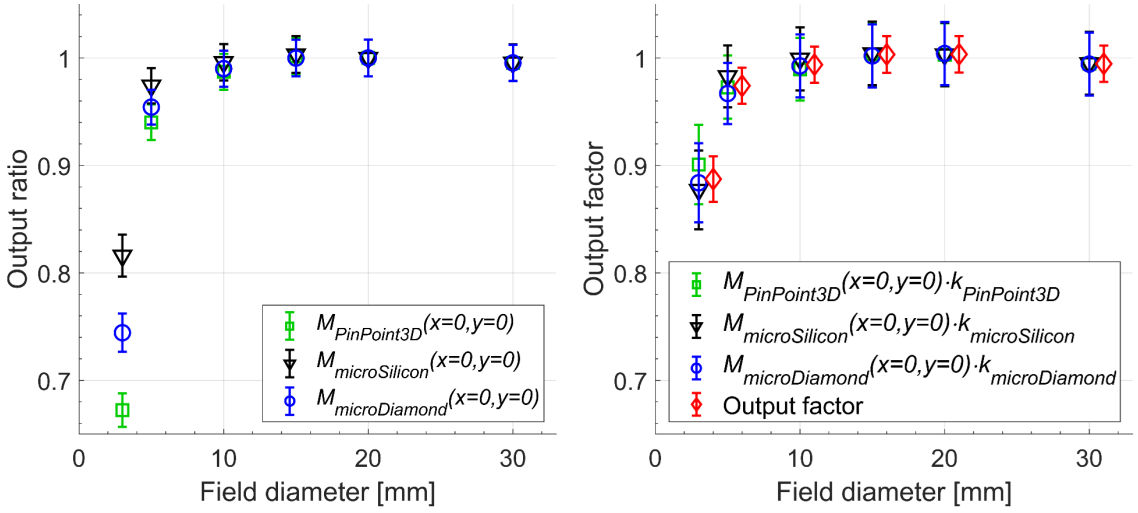

Figure 4.7. Output ratios $\frac{M(x=0,y=0)}{M_{20\text{mm}}(x=0,y=0)}$ (left) measured with the PinPoint 3D, microSilicon and microDiamond in *passively scattered collimated* proton fields and corrected output factors determined after application of the correction factors k (see table 4.3) $\frac{D(x=0,y=0)}{D_{20\text{mm}}(x=0,y=0)}$ from which an average output factor (red diamonds given a shift of 1 mm for better visibility) was calculated (right). The errorbar for the average output factor (red diamonds) corresponds to the standard error of the mean.

Table 4.3. Output correction factors k and corrected output factors determined for the detectors PinPoint 3D, microSilicon and microDiamond for *passively scattered collimated* proton fields with aperture diameters from 3 to 30 mm. The value within parenthesis corresponds to the uncertainty in the last digit(s).

Aperture	Correction factor k			Corrected output factors		
diameter [mm]	PinPoint 3D	microSilicon	microDiamond	PinPoint 3D	microSilicon	microDiamond
3	1.340(45)	1.082(37)	1.187(40)	0.901(37)	0.877(37)	0.884(37)
5	1.035(25)	1.005(24)	1.013(24)	0.973(29)	0.983(29)	0.967(28)
10	1.002(24)	1.004(24)	1.003(24)	0.989(29)	0.999(29)	0.993(29)
15	1.002(24)	1.001(24)	1.002(24)	1.004(30)	1.004(30)	1.002(30)
20	1.003(24)	1.005(24)	1.004(24)	1.003(30)	1.003(30)	1.004(30)
30	0.999(24)	0.999(24)	0.999(24)	0.995(29)	0.995(29)	0.994(29)

4.3.5 Application of approximated $K_{\text{area}}(x, y)$

To estimate the impact of using an approximated convolution kernel based on the sensitive area of the detectors $K_{\text{area}}(x, y)$, table 4.4 shows the difference in $d_{80/20}$ and in the signal reduction at the maximum of the corresponding $M(x, y = 0)$ profiles and those obtained from using the $K(x, y)$ shown in figure 4.1. Table 4.4 reveals differences in $d_{80/20}$ up to 0.13 mm (Semiflex 3D in the 5 mm *collimated PBS* field). The percentage point difference of the signal reduction at the maximum is less than 1% for the diode type detectors and most chamber-field size combinations, but becomes larger for ionization chambers with greater signal reductions at the maximum.

Table 4.4. Difference in determined penumbra ($d_{80/20}$) and percentage point difference of the signal reduction at the field center $(0, 0)$ between measured signal profiles as predicted for point detectors by the convolution of $D(x, y)$ with the detectors lateral dose response function $K(x, y)$ or an approximated convolution kernel $K_{\text{area}}(x, y)$ exemplarily for the three smallest fields of investigated techniques, the 10 x 10 mm^2 *PBS*, 5 mm *collimated PBS* and 3 mm *passively scattered collimated* field.

	10 x 10 mm^2 *PBS*		5 mm *collimated PBS*		3 mm *passively scattered collimated*	
	Difference in $d_{80/20}$ [mm]	Percentage point difference at $(0, 0)$	Difference in $d_{80/20}$ [mm]	Percentage point difference at $(0, 0)$	Difference in $d_{80/20}$ [mm]	Percentage point difference at $(0, 0)$
microSilicon	0.00	0.04	0.00	0.04	0.00	-0.04
microDiamond	0.00	0.03	0.00	0.13	0.00	0.04
Razor chamber	0.01	0.24	0.05	0.76	0.02	2.27
PinPoint 3D	0.00	0.03	-0.04	0.39	-0.02	-0.65
Semiflex 3D	-0.01	-0.09	-0.13	0.44	0.00	-2.99
Adv. Markus	0.03	0.74	0.04	5.22	0.07	2.02

4.3.6 Signal theoretical analysis

The left panel in figure 4.8 shows the Fourier transform of the dose profiles with the smallest lateral width FT[$D(x, y = 0)$] for each delivery technique investigated in this work (10 mm x 10 mm *PBS* field, 5 mm diameter *collimated PBS* field, 3 mm diameter *passively scattered collimated* field). The 3 mm diameter *passively scattered collimated* field exhibits the highest frequency components followed by the 5 mm diameter *collimated PBS* field and the 10 mm x 10 mm *PBS* field.

The Fourier transforms of the lateral dose response functions of microSilicon, PinPoint 3D, Semiflex 3D and Advanced Markus FT[$K(x, y = 0)$] are shown in the right panel of figure 4.8. All lateral response functions presented in the right panel of figure 4.8 serve as low-pass filter during the measurement process attenuating high-frequency components present in the dose profiles according to equation 4.5. The cutoff frequency of these functions defined at FT[$K(x, y = 0)$]=0.5 [43] corresponds to 0.41, 0.22, 0.13 and 0.12 mm^{-1} for the microSilicon, PinPoint 3D, Semiflex 3D and Advanced Markus, respectively. In other words, the smaller the dimensions of the detector, the higher is the cutoff frequency.

Considering their low-pass filter property, the suitability of the detector can be evaluated by comparing the maximum frequency components present in the dose profiles and the cutoff frequency associated with the detectors. For example, the maximum frequency component of the 10 mm x 10 mm *PBS* field is approximately 0.1 mm^{-1} which is less than the cutoff frequencies of all the detectors including the Advanced Markus chamber. As a consequence, measurements of the 10 mm x 10 mm *PBS* profile are not largely perturbed by these detectors resulting in the good agreement between $M(x, y = 0)$ and $D(x, y = 0)$ as presented in figure 4.2. In contrast, the maximum frequencies of the 5 mm diameter *collimated PBS* field and 3 mm diameter *passively scattered collimated* field exceed the cutoff frequencies of the PinPoint 3D, Semiflex 3D and Advanced Markus that would result in the strong perturbation demonstrated in figures 4.3 and 4.6.

4.3.7 Influence of detector positioning errors

Figure 4.9 shows the percentage signal reductions in the $M(x, y = 0)$ at different off-axis x-positions that could be resulted from positioning error. Note that, the values $(1 - \frac{M(x,y=0)}{M(x=0,y=0)}) \cdot 100$ presented in figure 4.9 correspond to the signal reduction due to positioning errors only and the perturbation due to the volume effect, that is, the difference between $M(x = 0, y = 0)$ and $D(x = 0, y = 0)$, must be additionally considered

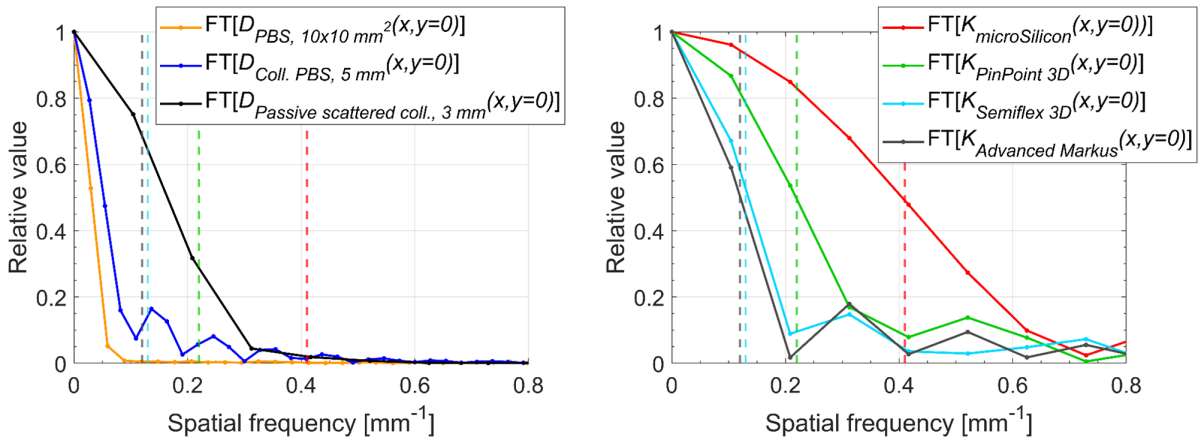

Figure 4.8. Left: FT[$D(x, y = 0)$] of dose profiles of the smallest proton fields investigated in this work (10 mm x 10 mm *PBS* field, 5 mm diameter *collimated PBS* field, 3 mm diameter *passively scattered collimated* field). Right: FT[$K(x, y = 0)$] of the $K(x, y = 0)$ of selected point detectors (microSilicon, PinPoint 3D, Semiflex 3D and Advanced Markus). The vertical dashed lines indicate the cutoff frequencies at FT[$K(x, y = 0)$]=0.5 of the point detectors. All profiles are maximum normalized.

to estimate the overall error. Figure 4.9 shows that the smallest fields are influenced the strongest by positioning errors. For the smallest 3 mm *passively scattered collimated* field, the largest signal reduction due to a 0.5 mm positioning error can be observed for the microSilicon that amounts to 6.6%. In contrast, the impact of positioning errors in larger collimated fields, such as a 5 mm diameter field, becomes less prominent for small detectors. Of all 10 mm fields (right column in figure 4.9) the 10 mm x 10 mm *PBS* field is most sensitive to detector positioning errors but shows a similar signal reduction in dependence of the off-axis position for all detectors. The 10 mm diameter collimated fields are more robust to positioning errors with positioning errors up to 1.5 mm leading to signal reductions withtin 0.5% for all detectors, except for the Advanced Markus chamber for which the signal reduction is up to 1.2%.

4.4 Discussion

4.4.1 Detector choice based on delivery techniques

The comparison between the dose distributions of small clinical proton fields delivered using three different techniques and the corresponding detector measurements presented in this work have clearly demonstrated the challenges associated with the correct dosimetric characterization of these fields. More importantly, the results reveal

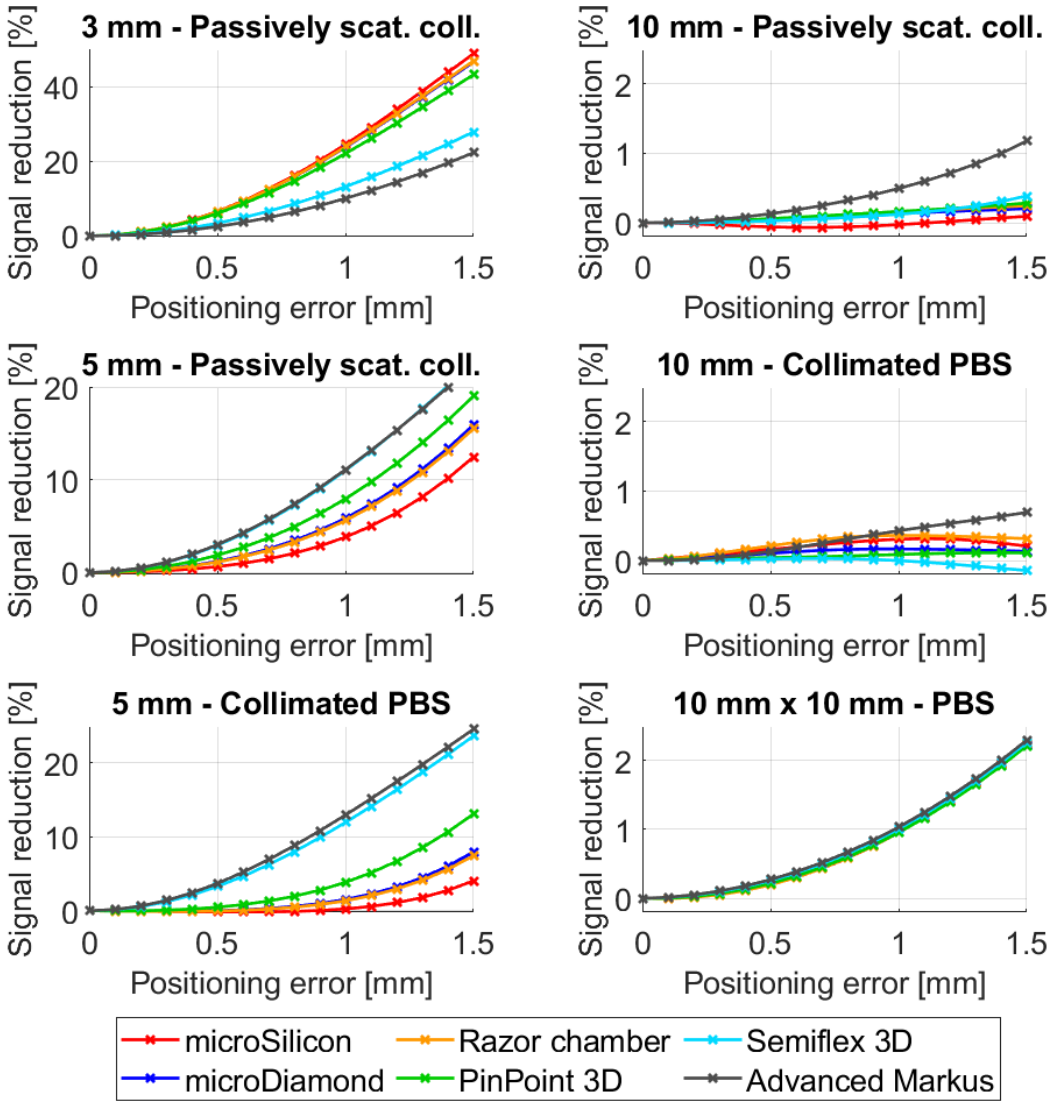

Figure 4.9. Percentage signal reduction in the $M(x, y = 0)$ with respect to the corresponding $M(0, 0)$ in dependence of a positioning error for selected fields from the three delivery techniques.

that the suitability of point detectors depends on the delivery technique, field size, beam collimation and detector's lateral dose response function. Based on these results, the clinical recommendations presented in the following sections can be derived. It should be mentioned that the fields investigated in this work serve as examples for the considered techniques. Nonetheless, other parameters like incident energies or measurement depths can lead to different lateral penumbras or field shape. Consequently, individual measurement conditions require separate considerations to conclude on the suitability of the detector's choice.

Pencil beam scanning fields

The $d_{80/20}$ of the 10 mm x 10 mm and 20 mm x 20 mm PBS proton fields studied in this work were 6.9 mm and 8.7 mm, respectively. The achievable steepness of PBS fields, including the small fields investigated in this study, is limited by that of the single pencil beams so that the lateral penumbra widths of *PBS* fields are generally larger than those of an individual pencil beam.

As shown in figure 4.8, the frequency analysis of the smallest *PBS* field (10 mm x 10 mm) showed frequency components below approximately 0.1 mm^{-1}, which is in accordance with a previously performed frequency analysis of intensity modulated proton therapy treatment plans [13]. Since the cutoff frequencies of all investigated detectors are larger than the frequencies associated with *PBS*, the Gaussian shaped *PBS* fields are not expected to suffer from detector's volume effect perturbations. Therefore, the predicted $M(x, y)$ derived by convolution of film measured $D(x, y)$ with $K(x, y)$ only showed differences in $d_{80/20}$ smaller than 0.25 mm for all investigated detectors and both field sizes.

For some detectors in PBS fields, similar findings were presented in the past [15, 45, 17, 29, 46, 13]. Schwaab *et al.* [16], Sahoo *et al.* [15] and Sawakuchi *et al.* [45] measured proton and/or carbon ion pencil beam profiles with ionization chambers and concluded that the effect of detector size can be neglected for the Gussian like lateral profiles in scanned fields [15, 45, 16, 29]. Furukawa *et al.* and Brodbek *et al.* [13] showed that the volume effect of ionization chambers of 2D arrays only has a minor or even negligible impact on the plan verification process of the intensity modulated carbon ion or proton therapy fields studied [13, 17]. Moignier *et al.* [46] simulated profiles of a 100 MeV proton pencil beam with a full width at half maximum (FWHM) of 5 mm using sensitive diamond crystal volumes of widths between 0.25 and 4 mm. Their results also showed no volume averaging effect for detector widths of 1 mm or less. However, they found an increased measured lateral penumbra for detectors with larger active surface at this small field size [46]. Grevillot *et al.* [47] investigated several detectors and phantoms for commissioning a light ion beam facility. A comparison of lateral profiles measured with a PinPoint chamber and microDiamond detector revealed a constant underestimation of the fields FWHM measured with the microDiamond, which Grevillot *et al.* attribute to the PinPoints larger cavity diameter [47]. In the Task group 224 report on proton therapy machine QA [8], small point-like ionization chambers are listed as suitable detectors for measuring scanned beam profiles, which can be confirmed by the results presented in our work. According to a review of clinical dosimetry in scanned ion beam dosimetry, PinPoint type ionization chambers with radii smaller 1.5 mm should be used for point dose measurements in gradient regions [48], which is supported by

the negligible increase in $d_{80/20}$ of *PBS* fields found in this work. For lateral dose profile acquisition, Giordanengo, Manganaro and Vignati [48] list films, scintillation screens and diodes as detectors for commissioning in scanned ion beams and add ministrips ionization chambers as suitable detector for quality assurance measurements [48].

In this work, the signal reduction at the maximum in the smallest *PBS* field (10mm x 10 mm) was estimated to be 2.9% and 4% for the two largest detectors used, Semiflex 3D and Advanced Markus, and between 1.2% and 0.8% for smaller ionization chambers like the Razor chamber and PinPoint 3D, respectively. Harms *et al.* measured output in 70 MeV PBS fields with a CC04 ionization chamber, films and a scintillation screen and determined differences of the chamber's signal of 3.6% and 0.8% in the smallest field size of 20 mm width from the film and scintillator measurements, respectively [49]. Recently, Kugel *et al.* estimated the standard uncertainty from disregarding volume averaging in dependence of the PBS field size and incident proton energy for a CC01 ionization chamber (IBA Dosimetry, Schwarzenbruck, Germany) having the same inner diameter as the Razor chamber [4]. In that work the uncertainty of measuring a small 160 MeV 10 mm x 10 mm proton field with the CC01 was determined to be approximately 0.9% [4]. Following the same methodology as described in the paper, the authors also investigated other detectors and provided the corresponding uncertainties for the microSilicon detector and PinPoint 3D chamber of 0.2% and 1%, respectively, in private communication. Their results are in good agreement with the reduction of the signal at the maximum calculated in this work for the investigated dectectors (0.8% for Razor chamber, 0.3% for microSilicon and 1.2% for PinPoint 3D).

Proton fields combined with collimators

In comparison to PBS fields, lateral penumbras of collimated proton fields are greatly reduced. The $d_{80/20}$ values of the dose profiles are 0.8 mm for all three collimated PBS fields with diameters between 5 mm and 15 mm, while the $d_{80/20}$ of the *passively scattered collimated* fields for which no range shifter was used are around 1.3 mm for all aperture diameters between 3 mm and 20 mm (table 4.2). Due to the use of apertures in combination with the thereby smaller field sizes achievable, the frequency components of these collimated fields are higher than in PBS fields as shown in figure 4.8, where the frequency components in the 5 mm diameter *collimated PBS* field and the 3 mm diameter *passively scattered collimated* field exceed the cutoff frequencies of the ionization chambers. This implies that measurements with such chambers in collimated proton fields will be perturbed, which can also be seen in figures 4.3 and 4.6.

For the *collimated PBS* fields, the computed $\Delta d_{80/20}$ values reveal a broadening of the measured lateral penumbra by all investigated detectors. As the $d_{80/20}$ of the dose profiles for these fields are approximately the same (between 0.7 and 0.8 mm), the magnitudes of penumbra broadening, $\Delta d_{80/20}$, caused by each detector are also comparable among the field sizes between 5 and 15 mm with values up to 0.35 mm for the microSilicon, 0.65 mm for the microDiamond, 0.62 mm for the Razor chamber, 0.95 mm for the PinPoint 3D, 1.84 mm for the Semiflex 3D, and 2.16 mm for the Advanced Markus.

The same can also be observed for the *passively scattered collimated* fields, whereas the penumbra broadening, $\Delta d_{80/20}$, are slightly smaller than that experienced in *collimated PBS* fields. This can be partly attributed to the larger $d_{80/20}$ of the dose profiles (1.3 mm) as lower proton energies and more scatterers are used in these ocular treatment fields.

Several studies have also investigated potential perturbations from detectors in lateral profile measurements of collimated proton fields. For example, McAuley *et al.* [50] found only small difference between the collimated scattered profiles measured with high resolution film and a diode detector operated in radial orientation having an especially small cross-sectional width of 20 μm [50]. Marsolat *et al.* [1] investigated microDiamond detectors in a passively scattered collimated proton beam with an energy of 138 MeV and found increased penumbras by approximately 0.3 mm in comparison to penumbra measured with an SFD diode. In addition, they operated the detectors oriented perpendicular to the beam by which they were able to obtain even lower penumbras than those measured with the SFD diode indicating a much better resolution due to the small thickness of the diamond in that orientation (1 μm) [1]. Recently, spectral fiber dosimetry using beryllium oxide as radioluminescent material with high spatial resolution has been applied to acquire proton beam profiles and depth dose distributions [51].

In addition to films and scintillation screens, Task group 224 report [8] lists small point-like ionization chambers as suitable for scanned and scattered beam profile measurements. Although the maximum penumbra increase identified with such small ionization chambers in this work of 0.62 mm (Razor chamber) and 0.94 mm (PinPoint 3D) is within the tolerances for $d_{80/20}$ suggested in the Task group 224 report of $\pm$2 mm, this penumbra increase is still quite large with respect to the small field sizes investigated in this work. As a consequence, the recommendations may need to be adapted to lateral profile measurements of such small fields. As shown in this study, higher accuracy can be achieved in these cases either by using detectors like the microSilicon diode or by correcting the measurements acquired using ionization chambers as demonstrated in this work. For passive scattering proton beam dosimetry under non-reference conditions, Rath and Sahoo mention several detectors as suitable for lateral profile measurements including

small-volume ionization chambers and point out that such measurements may need a correction for the detector size effect [29] which is supported by our results.

A strong reduction of the signal at the maximum was found for the small collimated fields studied in this work. When measuring the 5 mm *collimated PBS* field using the two detectors with the largest sensitive area, a reduction of the signal at the maximum of 8.7% and 15.7% was determined for the Semiflex 3D and Advanced Markus, respectively. In the 3 mm diameter *passively scattered collimated* field this reduction was even larger of up to 52.9% (Semiflex 3D) and 60.7% (Advanced Markus).

Perturbations in output factor measurements of collimated fields have already been described in the past. Andersen *et al.* [2] measured dose output in proton beams collimated with apertures between 5 mm and 100 mm using radiochromic film and a microDiamond detector, and found differences between both detectors of up to 70% [2]. Hoehr *et al.* [12] identified differences in output factor measurements for collimated 74 MeV scattered proton fields down to 5 mm diameter. Their investigation included a scintillation detector, a diamond detector oriented perpendicular to the beam direction and a silicon diode detector, of which the latter had the largest cross-sectional area of 2.65 mm x 2.65 mm and showed a relative signal difference of 2% for the smallest field size, which the authors attributed to larger volume averaging [12]. Fleury *et al.* [20] measured output ratios for *passively scattered collimated* fields dedicated for eye treatments with an Advanced Markus chamber having a comparably large sensitive area but found no remarkable change in the Dose/MU ratios in dependence of the field size for field sizes between 10 and 35 mm diameter [20]. This is in agreement with our prediction for the measurement with the Advanced Markus chamber of 10 mm diameter fields for which we estimated the signal reduction caused by the Advanced Markus chamber to be only 0.4% (*collimated PBS*) and 1% (*passively scattered collimated*). Fleury *et al.* emphasized that for fields smaller than 10 mm diameter, proper considerations of small field dosimetry should be made. This statement is supported by our investigation of fields with smaller diameter for which the volume effect of the Advanced Markus chamber leads to a noteworthy reduction of the signal at the maximum of up to 60.7% (3 mm diameter *passively scattered collimated* field) indicating that a higher resolution detector would be necessary to accurately measure the dose in these smaller field sizes [20]. Vatnitsky *et al.* [10] investigated dosimetry techniques for stereotactic proton fields and measured output factors for two scattered proton beams of 127 MeV or 155 MeV collimated with collimators between 2 and 30 mm diameter. Vatnitsky *et al.* considered a large set of detectors and concluded that the investigated point detectors may only be used for measurements in collimated fields with diameters greater than 8 mm. While they list a diode and a TLD detector to be suitable for characterizing the 8 mm field, they

stated that a PinPoint ionization chamber and diamond detector should only be used for collimators of 10 mm diameter or larger, and even larger detectors (Extradin T1 and PTW Markus chamber) are only considered accurate for collimators of 20 mm diameter or larger [10].

4.4.2 Correction strategies with lateral dose response functions

In this work, rotational symmetrical $K(r)$ were determined from experimentally derived or Monte Carlo simulated $K(x)$ for six detectors in proton fields that can be used to correct the perturbations of point detectors in lateral dose profile or output factor measurements. This has been demonstrated for measurements of *passively scattered collimated* proton fields, where the undisturbed $D(x, y)$ have been derived from the deconvolution of $M(x, y)$ measured using a microSilicon detector and PinPoint 3D chamber with the respective $K(x, y)$. The comparison of the resulting dose profiles $D_{\text{PinPoint3D}}(x, y = 0)$ and $D_{\text{microSilicon}}(x, y = 0)$ showed an overall good agreement with maximum differences in the $d_{80/20}$ of 0.13 mm (table 4.2).

Output measurements in *passively scattered collimated* proton fields were performed with a microSilicon, microDiamond and PinPoint 3D and corrected with output correction factors k in table 4.3. After the corrections, the percentage standard deviation of the average field output factors considering all three detectors was within 1% indicating the suitability of the proposed correction strategy based on the detector $K(x, y)$. It is noteworthy that the magnitude of k depends strongly on the shape of the underlying dose profiles and the correction factors in table 4.3 should be validated before they can be applied for other small proton fields. Despite the good consistency of the corrected output factors as presented in the right panel of figure 4.7, one should avoid using detectors that require large corrections [6] such as the PinPoint 3D chamber or microDiamond with k = 1.340 and 1.187 for the 3 mm field size, respectively. The most suitable detector in this case is in fact the microSilicon with the smallest sensitive area. Nevertheless, the numerical values in table 4.3 could still be helpful to guide the detector choice and estimate the measurement uncertainty.

The investigation of using an approximated convolution kernel based on the detectors sensitive areas (compare table 4.4) shows differences in $d_{80/20}$, as predicted from using the two convolution kernels, $K(x, y)$ and $K_{\text{area}}(x, y)$, up to 0.13 mm and percentage point differences of the signal reduction at the maximum below 1% for the diode type detectors

and most chamber-field size combinations, but becomes larger for ionization chambers. For example, the signal reduction from using the Advanced Markus chamber in the 5 mm *collimated PBS* field is estimated to be 16% using $K(x, y)$ and 11% using $K_{\text{area}}(x, y)$. Similar differences can be observed in the 3 mm *passively scattered collimated* field, where the ionization chambers Razor chamber, Semiflex 3D and Advanced Markus also show some higher percentage point differences up to 3%. The larger difference observed for the ionization chambers can be partly attributed to the negligence of the density perturbation caused by the low density air volume when using $K_{\text{area}}(r)$. Furthermore, the approximation of the sensitive volume by considering solely the detector radius may cause additional discrepancy as the geometry of their sensitive volume is more complex due to the spherical chamber tip and the presence of nonsensitive air volume adjacent to the chamber's stem [52].

4.4.3 Detector positioning

To estimate the role of an accurate positioning of the detectors in the fields center during output measurements in small fields, positioning errors were simulated for selected $M(x, y)$. The results in figure 4.9 show that the smallest fields are influenced the strongest by errors in positioning. For the smallest 3 mm *passively scattered collimated* field, the signal reduction due to a 0.5 mm positioning error was found for the microSilicon of up to 6.6%. Considering that the microSilicon is the detector with the smallest sensitive volume this observation may be surprising at first but this is a result of the steep $M(x, y = 0)$ profile (compare figure 4.6) measured with the microSilicon that resembles closest the $D(x, y = 0)$ making it much more sensitive to changes in position. For the larger chambers, such as the Advanced Markus chamber, the steepness of the measured $M(x, y = 0)$ has been strongly reduced by the volume effect so that it is less sensitive to detector positioning errors.

In contrast, the impact of positioning errors in larger collimated fields becomes less prominent for small detectors as the profiles feature a plateau region that is least affected by the volume effect associated with small detectors. However, as demonstrated previously in figures 4.3 and 4.6, this plateau region vanishes when measured with large detectors, so that $M(x, y = 0)$ profiles become steeper around the maximum and therefore more susceptible to positioning errors.

The comparison of the results of the 10 mm x 10 mm *PBS* field and 10 mm diamater collimated fields (right panels in figure 4.9) shows that, on the one hand, the *PBS* field is more sensitive to positioning errors due to the non-vanishing dose gradient around

its maximum. On the other hand, the collimated fields associated with a relatively homogenous plateau are more robust to positioning errors such that the percentage signal reduction associated with positioning errors up to 1.5 mm of all detectors, except for the Advanced Markus chamber, is within 0.5%.

4.5 Conclusion

Point detector measurements in small fields can be challenging because the extended detector volume can perturb the measurements leading to inadequate representation of the actual dose distributions. To address this issue, we investigated the suitability and accuracy of six clinical point detectors for lateral dose profile and output measurements in small proton fields. Generic correction strategies based on a convolution model in combination with detector specific lateral dose response functions $K(x, y)$ were used to estimate or to correct for perturbations in these fields created via *PBS*, *collimated PBS* and a *passively scattered collimated* proton therapy delivery techniques. While the difference between $D(x, y)$ and $M(x, y)$ of *PBS* fields was generally small, stronger detector perturbations were identified in collimated proton fields associated with a steep lateral penumbra. The findings of this work can guide the detector selection for lateral dose profile and output factor measurements in small proton fields with regard to the different delivery techniques. The results can contribute to the development of a code of practice for small field proton dosimetry in the future.

Acknowledgement

The authors would like to thank Sytze Brandenburg and Emiel van der Graaf for fruitful discussions on the presented results. Monte Carlo simulations were performed on the HPC Cluster CARL funded by the DFG under INST 184/157-1 FUGG.

Conflict of interest statement

The authors have no relevant conflicts of interest to disclose.

References

[1] Marsolat, F., De Marzi, L., Patriarca, A., Nauraye, C., Moignier, C., Pomorski, M., Moignau, F., Heinrich, S., Tromson, D., and Mazal, A. "Dosimetric characteristics of four PTW microDiamond detectors in high-energy proton beams". *Phys Med Biol*, 2016, 61:17, pp. 6413–6429. DOI: 10.1088/0031-9155/61/17/6413.

[2] Andersen, A., Coutinho, L., and Das, I. "SU-D-304-03: Small Field Proton Dosimetry Using MicroDiamond and Gafchromic Film". *Med Phys*, 2015, 42:6, pp. 3208–3208. DOI: 10.1118/1.4923862.

[3] Lomax, A. "What will the medical physics of proton therapy look like 10 yr from now? A personal view". *Med Phys*, 2018, 45:11, e984–e993. DOI: 10.1002/mp.13206.

[4] Kugel, F. et al. "Validating a double Gaussian source model for small proton fields in a commercial Monte-Carlo dose calculation engine". *Z Med Phys*, 2022, 33:4, pp. 529–541. DOI: 10.1016/j.zemedi.2022.11.011.

[5] Das, I. J. et al. "Report of AAPM Task Group 155: Megavoltage photon beam dosimetry in small fields and non-equilibrium conditions". *Med Phys*, 2021, 48:10, e886–e921. DOI: 10.1002/mp.15030.

[6] INTERNATIONAL ATOMIC ENERGY AGENCY. *Dosimetry of Small Static Fields Used in External Beam Radiotherapy, Technical Reports Series No. 483*. IAEA. Vienna. 2017.

[7] Sahoo, N., Zhu, X. R., Arjomandy, B., Ciangaru, G., Lii, M., Amos, R., Wu, R., and Gillin, M. T. "A procedure for calculation of monitor units for passively scattered proton radiotherapy beams: MU calculation for passively scattered proton therapy beams". *Med Phys*, 2008, 35:11, pp. 5088–5097. DOI: 10.1118/1.2992055.

[8] Arjomandy, B. et al. "AAPM task group 224: Comprehensive proton therapy machine quality assurance". *Med Phys*, 2019, 46:8, e678–e705. DOI: 10.1002/mp.13622.

[9] Grevillot, L. et al. "Clinical implementation and commissioning of the MedAustron Particle Therapy Accelerator for non-isocentric scanned proton beam treatments". *Med Phys*, 2020, 47:2, pp. 380–392. DOI: 10.1002/mp.13928.

[10] Vatnitsky, S. M., Miller, D. W., Moyers, M. F., Levy, R. P., Schulte, R. W., Slater, J. D., and Slater, J. M. "Dosimetry techniques for narrow proton beam radiosurgery". *Phys Med Biol*, 1999, 44:11, pp. 2789–2801. DOI: 10.1088/0031-9155/44/11/308.

[11] Karger, C. P., Jäkel, O., Palmans, H., and Kanai, T. "Dosimetry for ion beam radiotherapy". *Phys Med Biol*, 2010, 55:21, R193–R234. DOI: 10.1088/0031-9155/55/21/R01.

[12] Hoehr, C., Lindsay, C., Beaudry, J., Penner, C., Strgar, V., Lee, R., and Duzenli, C. "Characterization of the exradin W1 plastic scintillation detector for small field applications in proton therapy". *Phys Med Biol*, 2018, 63:9, p. 095016. DOI: 10.1088/1361-6560/aabd2d.

[13] Brodbek, L., Kretschmer, J., Willborn, K., Meijers, A., Both, S., Langendijk, J. A., Knopf, A.-C., Looe, H. K., and Poppe, B. "Analysis of the applicability of two-dimensional detector arrays in terms of sampling rate and detector size to verify scanned intensity-modulated proton therapy plans". *Med Phys*, 2020, 47:9, pp. 4589–4601. DOI: 10.1002/mp.14346.

[14] Kretschmer, J., Brodbek, L., Looe, H. K., Graaf, E. van der, Jan van Goethem, M., Kiewiet, H., Olivari, F., Meyer, C., Poppe, B., and Brandenburg, S. "Investigating the lateral dose response functions of point detectors in proton beams". *Phys Med Biol*, 2022, 67:14, p. 145003. DOI: 10.1088/1361-6560/ac783c.

[15] Sahoo, N., Ciangaru, G., Sawakuchi, G., Anand, A., Poenisch, F., Suzuki, K., Mohan, R., Gillin, M., and Zhu, X. "SU-GG-T-463: Study of the Magnitude of Detector Size Effect in the Measured Lateral Profiles of Proton Pencil Beam Spots". *Med Phys*, 2010, 37:6, pp. 3293–3293. DOI: 10.1118/1.3468861.

[16] Schwaab, J., Brons, S., Fieres, J., and Parodi, K. "Experimental characterization of lateral profiles of scanned proton and carbon ion pencil beams for improved beam models in ion therapy treatment planning". *Phys Med Biol*, 2011, 56:24, pp. 7813–7827. DOI: 10.1088/0031-9155/56/24/009.

[17] Furukawa, T., Inaniwa, T., Hara, Y., Mizushima, K., Shirai, T., and Noda, K. "Patient-specific QA and delivery verification of scanned ion beam at NIRS-HIMAC: QA and verification for scanning delivery". *Med Phys*, 2013, 40:12, p. 121707. DOI: 10.1118/1.4828845.

[18] Peucelle, C., Nauraye, C., Patriarca, A., Hierso, E., Fournier-Bidoz, N., Martínez-Rovira, I., and Prezado, Y. "Proton minibeam radiation therapy: Experimental dosimetry evaluation: Proton minibeam radiation therapy: Experimental evaluation". *Med Phys*, 2015, 42:12, pp. 7108–7113. DOI: 10.1118/1.4935868.

[19] Vernimmen, F. "Intracranial Stereotactic Radiation Therapy With Charged Particle Beams: An Opportunity to Regain the Momentum". *IJROBP*, 2016, 95:1, pp. 52–55. DOI: 10.1016/j.ijrobp.2015.10.016.

[20] Fleury, E. et al. “Characterization of the HollandPTC proton therapy beamline dedicated to uveal melanoma treatment and an interinstitutional comparison”. *Med Phys*, 2021, 48:8, pp. 4506–4522. DOI: 10.1002/mp.15024.

[21] Safai, S., Bortfeld, T., and Engelsman, M. “Comparison between the lateral penumbra of a collimated double-scattered beam and uncollimated scanning beam in proton radiotherapy”. *Phys Med Biol*, 2008, 53:6, pp. 1729–1750. DOI: 10.1088/0031-9155/53/6/016.

[22] Winterhalter, Lomax, A., Oxley, D., Weber, D. C., and Safai, S. “A study of lateral fall-off (penumbra) optimisation for pencil beam scanning (PBS) proton therapy”. *Phys Med Biol*, 2018, 63:2, p. 025022. DOI: 10.1088/1361-6560/aaa2ad.

[23] Wulff, J., Koska, B., Janson, M., Bäumer, C., Denker, A., Geismar, D., Gollrad, J., Timmermann, B., and Heufelder, J. “Technical note: Impact of beam properties for uveal melanoma proton therapy—An in silico planning study”. *Med Phys*, 2022, 49:5, pp. 3481–3488. DOI: 10.1002/mp.15573.

[24] Hyer, D. E., Hill, P. M., Wang, D., Smith, B. R., and Flynn, R. T. “A dynamic collimation system for penumbra reduction in spot-scanning proton therapy: Proof of concept: Penumbra trimmer for spot scanning”. *Med Phys*, 2014, 41:9, p. 091701. DOI: 10.1118/1.4837155.

[25] Bäumer, C., Fuentes, C., Janson, M., Matic, A., Timmermann, B., and Wulff, J. “Stereotactical fields applied in proton spot scanning mode with range shifter and collimating aperture”. *Phys Med Biol*, 2019, 64:15, p. 155003. DOI: 10.1088/1361-6560/ab2ae7.

[26] Bäumer, C., Plaude, S., Khalil, D. A., Geismar, D., Kramer, P.-H., Kröninger, K., Nitsch, C., Wulff, J., and Timmermann, B. “Clinical Implementation of Proton Therapy Using Pencil-Beam Scanning Delivery Combined With Static Apertures”. *Front Oncol*, 2021, 11, p. 599018. DOI: 10.3389/fonc.2021.599018.

[27] Ciocca, M. et al. “Design and commissioning of the non-dedicated scanning proton beamline for ocular treatment at the synchrotron-based CNAO facility”. *Med Phys*, 2019, 46:4, pp. 1852–1862. DOI: 10.1002/mp.13389.

[28] Grewal, H. S., Ahmad, S., and Jin, H. “Characterization of penumbra sharpening and scattering by adaptive aperture for a compact pencil beam scanning proton therapy system”. *Med Phys*, 2021, 48:4, pp. 1508–1519. DOI: 10.1002/mp.14771.

[29] Sahoo, N., Sawakuchi, G. O., Gillin, M. T., and Zhu, X. R. “Radiation Dosimetry of Proton Beams”. In: A. K. Rath and N. Sahoo (eds.): *Particle Radiotherapy*. New Delhi, Springer India, 2016, pp. 77–94. DOI: 10.1007/978-81-322-2622-2.

[30] Looe, H. K., Stelljes, T. S., Foschepoth, S., Harder, D., Willborn, K., and Poppe, B. "The dose response functions of ionization chambers in photon dosimetry – Gaussian or non-Gaussian?" *Z Med Phys*, 2013, 23:2, pp. 129–143. DOI: 10.1016/j.zemedi.2012.12.010.

[31] Harder, D., Looe, H., and Poppe, B. "Convolutions and Deconvolutions in Radiation Dosimetry". In: *Comprehensive Biomedical Physics*. Elsevier, 2014, pp. 249–269. DOI: 10.1016/B978-0-444-53632-7.00913-8.

[32] Poppinga, D., Meyners, J., Delfs, B., Muru, A., Harder, D., Poppe, B., and Looe, H. "Experimental determination of the lateral dose response functions of detectors to be applied in the measurement of narrow photon-beam dose profiles". *Phys Med Biol*, 2015, 60:24, pp. 9421–9436. DOI: 10.1088/0031-9155/60/24/9421.

[33] Looe, H. K., Harder, D., and Poppe, B. "Understanding the lateral dose response functions of high-resolution photon detectors by reverse Monte Carlo and deconvolution analysis". *Phys Med Biol*, 2015, 60:16, pp. 6585–6607. DOI: 10.1088/0031-9155/60/16/6585.

[34] Laub, W. U. and Wong, T. "The volume effect of detectors in the dosimetry of small fields used in IMRT". *Med Phys*, 2003, 30:3, pp. 341–347. DOI: 10.1118/1.1544678.

[35] Poppinga, D., Delfs, B., Meyners, J., Harder, D., Poppe, B., and Looe, H. K. "The output factor correction as function of the photon beam field size – direct measurement and calculation from the lateral dose response functions of gas-filled and solid detectors". *Z Med Phys*, 2018, 28:3, pp. 224–235. DOI: 10.1016/j.zemedi.2017.07.006.

[36] MATLAB. *version 9.7.0.1190202 (R2019b)*. The MathWorks Inc. Natick, Massachusetts. 2019.

[37] Slopsema, R. L., Mamalui, M., Zhao, T., Yeung, D., Malyapa, R., and Li, Z. "Dosimetric properties of a proton beamline dedicated to the treatment of ocular disease: Dosimetry of a proton eyeline". *Med Phys*, 2013, 41:1, p. 011707. DOI: 10.1118/1.4842455.

[38] Agostinelli, S. et al. "Geant4 - a simulation toolkit". *Nucl Instrum Methods Phys Res Sect Accel Spectrom Detect Assoc Equip*, 2003, 506:3, pp. 250–303. DOI: 10.1016/S0168-9002(03)01368-8.

[39] Jan, S. et al. "GATE V6: a major enhancement of the GATE simulation platform enabling modelling of CT and radiotherapy". *Phys Med Biol*, 2011, 56:4, pp. 881–901. DOI: 10.1088/0031-9155/56/4/001.

[40] Marchand, E. W. “From Line to Point Spread Function: The General Case”. *J Opt Soc Am*, 1965, 55:4, p. 352. DOI: 10.1364/JOSA.55.000352.

[41] Cittert, P. H. van. “Zum Einfluß der Spaltbreite auf die Intensitätsverteilung in Spektrallinien. II”. *Z. Physik*, 1931, 69:5, pp. 298–308. DOI: 10.1007/BF01391351.

[42] Poppe, B., Djouguela, A., Blechschmidt, A., Willborn, K., Rühmann, A., and Harder, D. “Spatial resolution of 2D ionization chamber arrays for IMRT dose verification: single-detector size and sampling step width”. *Phys Med Biol*, 2007, 52:10, pp. 2921–2935. DOI: 10.1088/0031-9155/52/10/019.

[43] Poppe, B., Stelljes, T. S., Looe, H. K., Chofor, N., Harder, D., and Willborn, K. “Performance parameters of a liquid filled ionization chamber array: Properties of a liquid filled ionization chamber array”. *Med Phys*, 2013, 40:8, p. 082106. DOI: 10.1118/1.4816298.

[44] Lechner, W., Georg, D., and Palmans, H. “An analytical formalism for the assessment of dose uncertainties due to positioning uncertainties”. *Med Phys*, 2020, 47:3, pp. 1357–1363. DOI: 10.1002/mp.13991.

[45] Sawakuchi, G. O., Zhu, X. R., Poenisch, F., Suzuki, K., Ciangaru, G., Titt, U., Anand, A., Mohan, R., Gillin, M. T., and Sahoo, N. “Experimental characterization of the low-dose envelope of spot scanning proton beams”. *Phys Med Biol*, 2010, 55:12, pp. 3467–3478. DOI: 10.1088/0031-9155/55/12/013.

[46] Moignier, C. et al. “Development of a synthetic single crystal diamond dosimeter for dose measurement of clinical proton beams”. *Phys Med Biol*, 2017, 62:13, pp. 5417–5439. DOI: 10.1088/1361-6560/aa70cf.

[47] Grevillot, L., Stock, M., Palmans, H., Osorio Moreno, J., Letellier, V., Dreindl, R., Elia, A., Fuchs, H., Carlino, A., and Vatnitsky, S. “Implementation of dosimetry equipment and phantoms at the MedAustron light ion beam therapy facility”. *Med Phys*, 2018, 45:1, pp. 352–369. DOI: 10.1002/mp.12653.

[48] Giordanengo, S., Manganaro, L., and Vignati, A. “Review of technologies and procedures of clinical dosimetry for scanned ion beam radiotherapy”. *Phys Med*, 2017, 43, pp. 79–99. DOI: 10.1016/j.ejmp.2017.10.013.

[49] Harms, J., Chang, C.-W., Zhang, R., and Lin, L. “Nuclear halo measurements for accurate prediction of field size factor in a Varian ProBeam proton PBS system”. *J Appl Clin Med Phys*, 2020, 21:1, pp. 197–204. DOI: 10.1002/acm2.12783.

[50] McAuley, G. A., Teran, A. V., Slater, J. D., Slater, J. M., and Wroe, A. J. “Evaluation of the dosimetric properties of a diode detector for small field proton radiosurgery”. *J Appl Clin Med Phys*, 2015, 16:6, pp. 51–64. DOI: 10.1120/jacmp.v16i6.5391.

[51] Metzner, E. et al. “Spectral fiber dosimetry with beryllium oxide for quality assurance in hadron radiation therapy”. *J. Inst.* 2022, 17:2, P02009. DOI: 10.1088/1748-0221/17/02/P02009.

[52] Delfs, B. et al. “The role of the construction and sensitive volume of compact ionization chambers on the magnetic field-dependent dose response”. *Med Phys*, 2021, 48:8, pp. 4572–4585. DOI: 10.1002/mp.14994.

5

General Discussion

The number of patients suffering from cancer is increasing steadily [1], and more than half of all cancer patients receive radiation therapy [2] as part of their treatment. For an effective radiation therapy treatment, parts of the normal tissue close to the tumor are unavoidably part of the irradiation volume and even need to be included to ensure tumor coverage. Consequently, radiation therapy can lead to normal tissue complications, which depend on the delivered radiation dose. For a successful treatment with reasonably low side effects, the dose distribution is optimized such that the probability of tumor control is high while the probability of normal tissue complications remains as low as possible. However, slight differences between the planned and the actually delivered dose can impact both probabilities. In the IAEA Human Health Series report 31 [3] sources of uncertainty in photon radiation therapy were investigated in terms of their influence on TCP (tumor control probability) and NTCP (normal tissue complication probability) using a generic model: for example, the report found that delivery of 1.5% less dose can lead to a 3% loss in TCP and delivering 3% more dose can result in an increase in NTCP by 3%, which according to the authors may be the maximum clinically acceptable change in TCP or NTCP [3]. Therefore, even small dose uncertainties impact the outcome of individual patient treatments, and potential improvements in accuracy should be considered and evaluated.

Several publications propose maximum acceptable uncertainties for the difference between the prescribed and the actually delivered dose. Depending on the treatment intent, such maximum uncertainty limits vary between 3% and 5% at the 1 sigma level [4, 5, 3, 6, 7]. To fulfill the requirement for an overall uncertainty of less than 3%, the individual uncertainties contributing to the overall uncertainty need to be much smaller. Contributions include, for example, uncertainties in imaging, treatment planning, patient setup and immobilization, as well as treatment delivery [3, 7]. Among these contributions, the uncertainties in treatment planning and delivery are directly linked to the accuracy in absolute and relative dose measurements, which is why a high accuracy in dosimetry is important. Reference dosimetry using ionization chambers is essential for beam calibration. Consequently, inaccuracies in reference dosimetry directly affect the absolute dose output. Previous works showed that small offsets in beam output calibration in photon beams can lead to clinically relevant changes in TCP and NTCP [8,

9]. The required uncertainty for reference dosimetry was estimated to be approximately 1% [10, 6]. However, at the time of performing the research described in Chapter 2, the uncertainty associated with proton reference dosimetry was 2.3% [4], with the main contribution being due to approximated beam quality correction factors k_Q. Therefore, more accurate k_Q factors have been derived using Monte Carlo simulations as described in **Chapter 2**. The results contributed to an update of recommended k_Q factors for proton beams which allowed to reduce the uncertainty of proton reference dosimetry to 1.7% [5]. Non-reference dosimetry measurements are required for beam commissioning, treatment plan verification measurements, and to determine the beam model in the treatment planning system. Hence, uncertainties can propagate into patient treatment plans and influence the treatment outcome. In particular, the characterization of small fields and fields with steep dose fall-offs is known to be challenging and associated with a higher uncertainty [3, 11, 12]. While a Code of Practice (CoP) for small field photon dosimetry has recently been published [13], the research on detector performance in proton non-reference dosimetry is still scarce compared to photons. To better understand and describe proton non-reference dosimetry, point detectors have been characterized by their lateral dose response functions for proton beams in **Chapter 3**, and beam measurements with various detectors for three different proton beam delivery techniques have been investigated in **Chapter 4** of this thesis. The following sections discuss and contextualize the findings of the previous chapters. Finally, limitations and future fields of proton dosimetry research are elaborated.

5.1 Dosimetry under reference conditions

With the aim to contribute to a reduction of the uncertainty associated with proton reference dosimetry, which amounts to 2.3% according to the CoP TRS-398 published in 2000 [4], Chapter 2 presents a set of Monte Carlo simulated perturbation factors p_Q and beam quality correction factors k_Q of ionization chambers for different monoenergetic proton beam qualities. To obtain these factors, simulations for proton beams leading to f_Q factors and for photon beams to obtain f_{Q_0} factors were performed. The investigation comprises five cylindrical and four plane-parallel chambers. Since the reference conditions from the CoP available at the time of writing of Chapter 2 were uncertain, two positioning methods were investigated for cylindrical ionization chambers: (i) by positioning the chambers with their reference point, defined along the central axis of the cylindrical chamber, at the measurement depth of 2 cm to obtain the corresponding p_Q^{ref} and k_Q^{ref} factors; and (ii) by positioning the chambers according to their effective

point of measurement (EPOM), realized by shifting the reference point of the chamber by 0.75 times the respective chamber radius deeper in the water phantom, to obtain the associated p_Q^{EPOM} and k_Q^{EPOM} factors. The results presented in Chapter 2 were included in a recent publication on current best estimates of beam quality correction factors for proton reference dosimetry aiming at providing updated k_Q recommendations for ionization chambers in proton beams adopted in the update of IAEA TRS-398 [5, 14] and in a publication presenting average Monte Carlo simulated k_Q values [15].

5.1.1 Perturbation correction factors p_Q

When the CoP TRS-398 was published in 2000, ionization chamber specific information on p_Q was scarce so that p_Q factors were approximated by unity and therefore associated with a large uncertainty of 0.8% [4, 16]. The results in Chapter 2 show that the overall p_Q^{ref} for cylindrical ionization chambers are energy dependent and range from 1.033 ± 0.001 for 70 MeV protons and 0.981 ± 0.003 for 250 MeV protons. In contrast, the p_Q^{EPOM} for cylindrical ionization chambers and the p_Q for plane-parallel chambers were found to be more constant with p_Q factors for a certain chamber being constant within 0.8% over the energy range 70 MeV to 250 MeV. While p_Q^{EPOM} for cylindrical chambers showed an average deviation from unity of -1.4% and a maximum deviation of -1.9%, the p_Q of all plane-parallel chambers deviated on average by 0.4% from unity with a maximum deviation of -1.1%. Considering these deviations from unity, the p_Q factors obtained in Chapter 2 differ significantly from the approximated $p_Q = 1$ in CoP TRS-398 from 2000 and even exceed the associated uncertainty of 0.8% [4]. Hence, the results provide more accurate p_Q values with uncertainties smaller than 0.4%.

In addition to the overall perturbation factors, the perturbations caused by various chamber components were considered. For plane-parallel chambers and cylindrical chambers positioned according to their EPOM, the strongest perturbation is attributed to the chamber wall with p_{wall} of 0.981 ± 0.003, agreeing with other works [17, 18]. Wall perturbations are associated with an overresponse of the chambers due to additional dose contributions within the air cavity from low-energy electrons and secondary charged particles generated in the chamber wall by nuclear interactions [16, 18, 14, 19].

For cylindrical ionization chambers positioned with their reference point at the measurement depth, the largest contribution arises from the displacement perturbation p_{dis}, which increases with decreasing energy up to 1.045 ± 0.001 for large chambers in low-energy proton fields. Because p_{dis} is included in p_Q^{ref}, this increase in p_{dis} explains the observed increase in p_Q^{ref} towards low proton energies for cylindrical ionization chambers.

This energy dependence was found to be related to the gradient in the depth dose curve of monoenergetic proton beams at 2 cm measurement depth [14], which is larger for low-energy proton beams. In contrast, p_Q^{EPOM} in the considered energy range do not increase towards low energies for cylindrical chambers because the positioning in the EPOM accounts for this displacement effect.

Palmans *et al.* [20] investigated the gradient effects in measured depth dose distributions of scanned proton beams and developed an empirical model for displacement correction factors [14, 20]. Figure 5.1 shows a comparison of the p_{dis} determined in Chapter 2 and the p_{dis} obtained by their empirical model for several chambers at 2 cm depth. The comparison was previously performed by Palmans *et al.* [14], who concluded that the data agrees well except for the highest energy, where differences up to 0.5% can be observed. This discrepancy may arise either due to stray radiation, that is, radiation produced in the monitor chambers of the beamline because this was not considered in the Monte Carlo simulations in Chapter 2, or due to nuclear interaction modeling [16, 14]. Considering the good agreement between the investigated p_{dis}, Palmans *et al.* [14] concluded that the displacement perturbation mainly resulted from depth dose gradient effects, which agrees with the findings from Chapter 2 showing good agreement between the ratio $\frac{D_{\text{w},z_{\text{ref}}}}{D_{\text{w},z_{\text{EPOM}}}}$ and the simulated p_{dis} for a PTW 30013 ionization chamber at 70 MeV and 250 MeV. Similar to the constant p_Q^{EPOM} presented in Chapter 2 for cylindrical chambers, Palmans *et al.* also found that p_Q/p_{dis} is constant over the energy range with variations within 0.3% and 0.5% for monoenergetic and spread out Bragg Peak beams, respectively [14].

5.1.2 Chamber positioning and reference conditions

Because reference conditions were not well defined at the time of writing of Chapter 2, two positioning methods were investigated for deriving k_Q of cylindrical chambers. k_Q for cylindrical ionization chambers positioned with their reference point at the measurement depth increase with decreasing energy by up to 4.6% for large chambers, whereas k_Q^{EPOM} for cylindrical chambers positioned according to the EPOM are constant within 0.7% over the considered energy range. One purpose of updating TRS-398 was to define the reference conditions for monoenergetic scanned proton beams [21]. The reference conditions for proton beams in the updated version of TRS-398 will maintain the recommendation of positioning cylindrical chambers with their reference point at the measurement depth and limit the use of cylindrical chambers to scanned beams with $R_{\text{res}} \geq 15$ g·cm^{-2} [5, 14]. Thereby the same k_Q can be used for monoenergetic proton beams and scattered beams [14]. This limitation implies that the entire energy range in

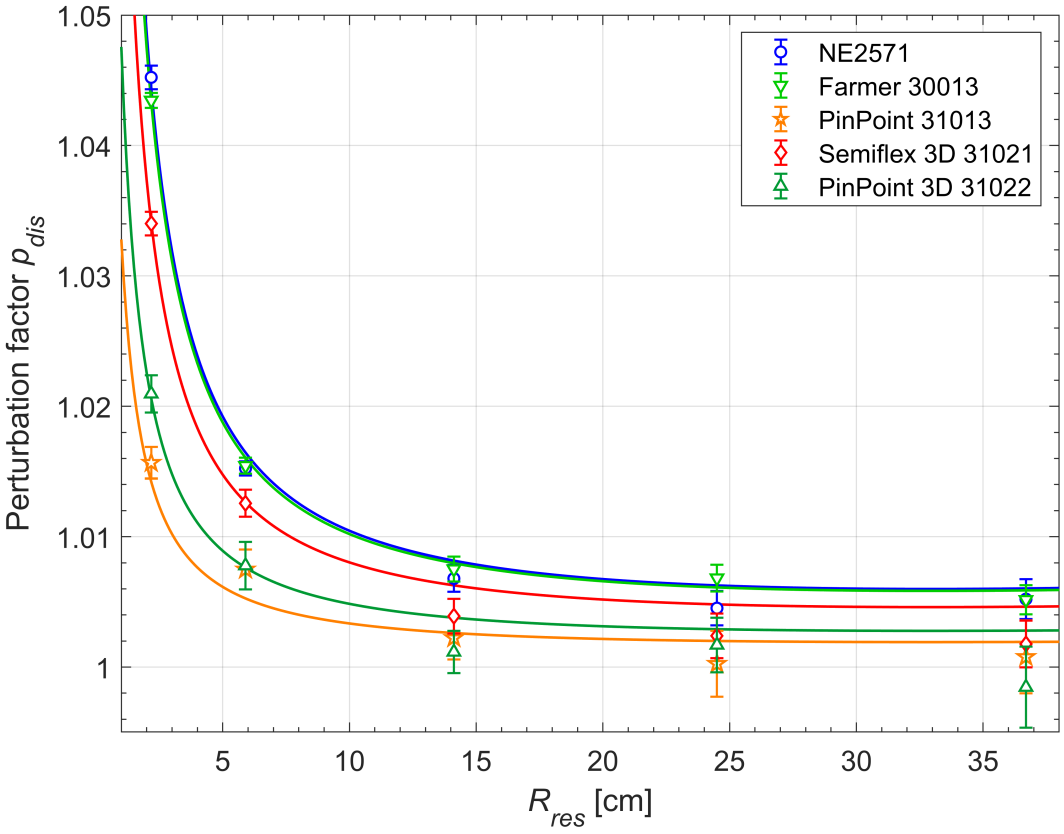

Figure 5.1. Adapted from Palmans *et al.* [14] showing the agreement between the calculations of p_{dis} presented in their work (solid lines) to the p_{dis} presented in Chapter 2 (markers).

scanned proton beam radiation therapy can not be covered with cylindrical chambers only. Consequently, cylindrical chambers will have to be used to cross-calibrate plane-parallel chambers in high energy beams [20]. Further considerations of the EPOM uncertainty associated with cylindrical chambers and the negligible ion recombination correction required for plane-parallel chambers in proton beams [22] lead to the recommendation to use plane-parallel chambers for proton reference dosimetry.

5.1.3 Updated beam quality correction factors f_Q and k_Q

As p_Q is included in f_Q and k_Q, a similar behavior as described for p_Q was observed for f_Q and k_Q in Chapter 2. That is f_Q and k_Q for plane-parallel chambers were found to be constant over the considered energy range, while f_Q^{ref} and k_Q^{ref} for cylindrical chambers were found to increase towards low energies due to the displacement effect. In contrast,

f_Q^{EPOM} and k_Q^{EPOM} for cylindrical chambers did not show an energy dependence as the displacement effect was compensated for by positioning the detectors in their EPOM.

In addition to the results presented in Chapter 2, several other studies on f_Q and k_Q factors for ionization chambers in proton reference dosimetry have been published in the past years. Most correction factors were determined with the help of Monte Carlo simulations [16, 17, 23, 24, 18, 25, 19, 26], from which average Monte Carlo calculated f_Q and k_Q for proton beams have been determined recently [15]. Moreover, correction factors were determined via relative measurements [27, 28, 29] or using calorimetry measurements [30, 31, 32, 33, 34, 35, 36]. Palmans *et al.* [14] determined correction factors k_Q for the update of IAEA TRS-398 CoP by reviewing the available data and deriving current best estimates for k_Q in energy modulated scattered proton beams and monoenergetic scanned proton beams. They considered calorimeter measurements, relative measurements, and Monte Carlo calculated correction factors, including the results presented in Chapter 2 of this thesis. The k_Q compiled by Palmans *et al.* can be used within scattered and scanned beams with a limitation for cylindrical chambers in scanned beams as their k_Q factors are valid for measurement depths with $R_{\text{res}} \geq 15$ g·cm^{-2} only.

As an example of the influence of the updated k_Q and their associated uncertainties, the k_Q of a plane-parallel Markus 23343 (PTW Freiburg, Germany) and a cylindrical Farmer NE2571 chamber derived according to Palmans *et al.* [14] are compared to k_Q determined in our work and those from the previous version of TRS-398 [4] in Figures 5.2 and 5.3, respectively.

The factors in Figures 5.2 and 5.3 show that the data determined by Palmans *et al.* agree well with the k_Q derived in Chapter 2 except for the k_Q^{ref} of the Farmer Chamber NE2571 at low proton energies which are much higher in comparison to the k_Q of Palmans *et al.* The reason for this difference is that the k_Q in Chapter 2 were determined with monoenergetic proton beams over the complete energy range, whereas the values listed in Palmans *et al.* are for the lower energies derived for spread-out Bragg peak (SOBP) conditions. As a consequence, Palmans *et al.* limit the use of their k_Q for monoenergetic proton beams to beams with $R_{\text{res}} \geq 15$ g·cm^{-2}. Therefore, their values shown for the Farmer chamber for $R_{\text{res}} \leq 15$ g·cm^{-2} correspond to measurements in scattered beams within the SOBP only, such that the factors in this range are not comparable to the k_Q^{ref} of our work.

A comparison of the updated k_Q factors to the approximated k_Q in TRS-398 from 2000 shows that the updated k_Q lead to changes of approximately 0.5% for plane-parallel chambers and up to 1.7% for cylindrical chambers [14]. The uncertainty estimates of

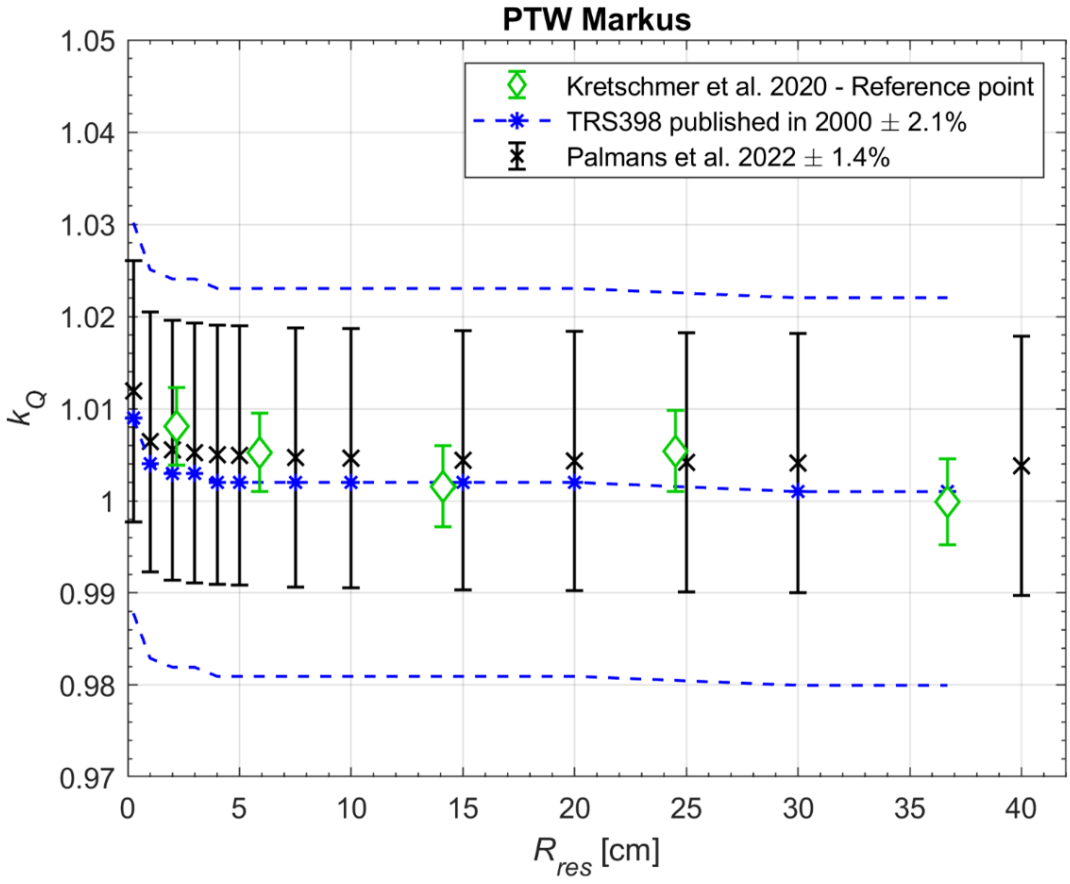

Figure 5.2. k_Q as calculated in Chapter 2 for the plane-parallel Markus chamber in comparison to the data recommended in TRS-398 from 2000 [4] and to the corresponding average k_Q to be used in the update of TRS-398 determined by Palmans *et al.* [14]

1.7% and 2.1% for k_Q of cylindrical and plane-parallel chambers, respectively, as listed in the TRS-398 from 2000, were expected to decrease when more data are considered in the compilation of k_Q for proton beams [10]. While p_Q in the TRS-398 from 2000 were approximated by unity for ionization chambers in proton beams [4], the new k_Q used for the update of TRS-398 by Palmans *et al.* were calculated under consideration of experimental results and Monte Carlo simulated data, motivating a new assessment of the associated uncertainties. However, the overall relative standard uncertainty for the newly derived k_Q could only be reduced to 1.4% for both chamber types [5, 14], which is still large compared to the estimate of the required uncertainty for reference dosimetry of 1% [10, 6]. As a consequence, the main benefit of the update of k_Q factors for proton beams is the increase in accuracy achieved by omitting approximations and using Monte Carlo simulation results instead: the effect can, for example, be seen by comparing the old TRS-398 k_Q values to the results published by Palmans *et al.* in Figure 5.3 showing

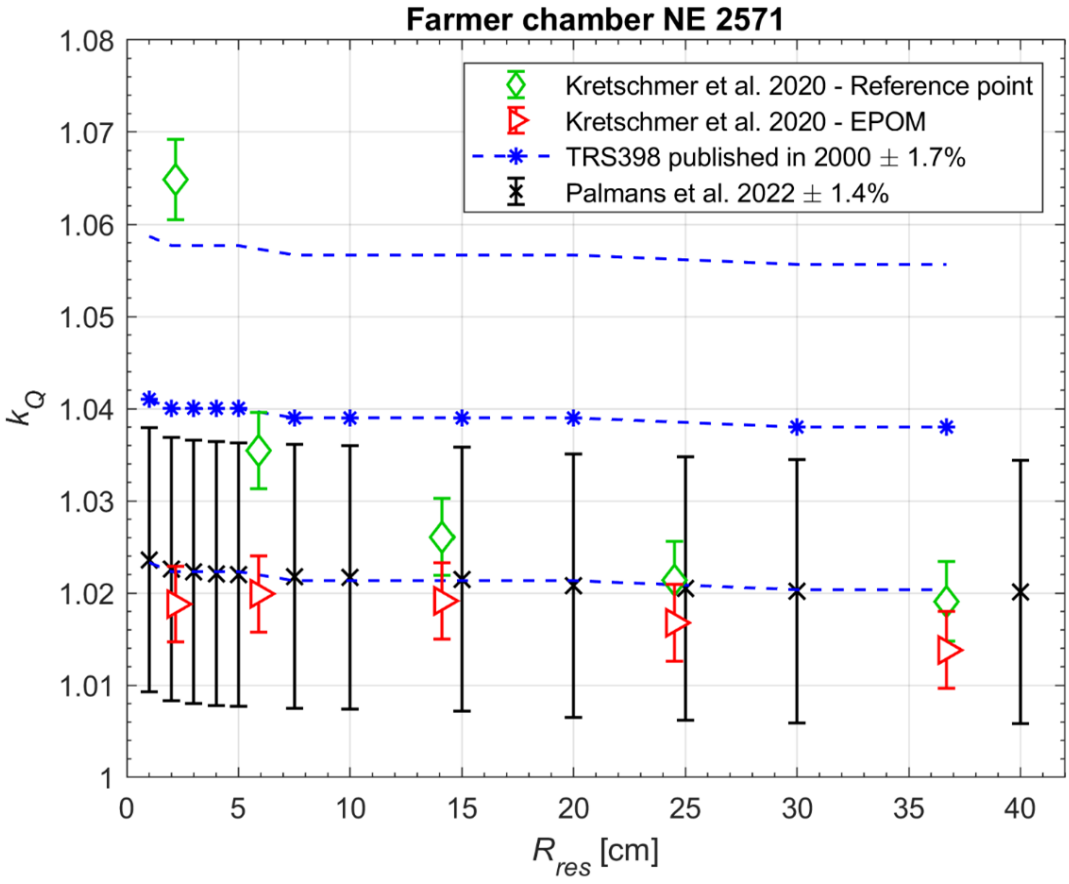

Figure 5.3. k_Q^{ref} and k_Q^{EPOM} as presented in Chapter 2 for the NE 2571 Farmer chamber in comparison to the data recommended in TRS-398 from 2000 and to the corresponding average k_Q to be used in the update of TRS-398 determined by Palmans *et al.* [14]. Note that k_Q presented by Palmans *et al.* for cylindrical chambers are valid for scanned and scattered beams with $R_{\text{res}} \geq 15$ g·cm^{-2} but k_Q for $R_{\text{res}} \leq 15$ g·cm^{-2} may only be used within SOBP measurements.

that changes of k_Q factors between the old and the new TRS-398 version are up to 1.7% [14] while the uncertainties are similar.

5.2 Dosimetry under non-reference conditions

5.2.1 Lateral dose response functions of point detectors in proton beams

Chapter 3 presents an experimental approach to derive lateral dose response functions $K(x)$ for point detectors in proton beams. Similar to an approach applied in photon beam dosimetry [37], the profile of a 150 MeV proton beam created with a narrow slit was used to derive an actual dose profile $D(x)$ from high-resolution film measurements as well as measured signal profiles $M(x)$ at 2 cm depth in water for three ionization chambers, a diode, and a diamond detector. From these profiles, the detector-specific $K(x)$ could be determined by iterative deconvolution of $D(x)$ and $M(x)$ in analogy to Looe *et al.* [38]. To further investigate the derived $K(x)$, Monte Carlo simulations were used to model the experimental setup and the measurements of $D(x)$ and $M(x)$ for a Semiflex 3D and microDiamond detector. The $K(x)$, derived from both the measured and simulated profiles, showed good agreement, thus providing a rationale for using Monte Carlo simulations in further investigations. $K(x)$ simulated with different initial proton energies revealed that $K(x)$ can be regarded as independent of proton energy in the considered energy range. Further simulations were performed for other point detectors, such as the Advanced Markus chamber, which was presented in Chapter 4. Additionally, detailed Monte Carlo simulations of the lateral dose response functions $K(x)$ were conducted with modified detector geometries in Chapter 3 to study the roles of the geometrical volume averaging and the density perturbations of detector components, which lead to the overall volume effect in proton beams as described by $K(x)$. The results presented in Figure 3.6 in Chapter 3 demonstrate that the main detector perturbation in proton fields arises from volume averaging. In contrast, the density perturbation is much less pronounced in proton fields than density perturbations observed in photon fields.

For photon radiation, the density perturbation of ionization chambers was found to be due to the low-density air cavity because fewer electrons are released in the sensitive air volume as compared to electrons that originated in other components of the chamber and surrounding medium. Therefore, the predominantly inward-directed transport of secondary electrons manifests in a $K(x)$ that is broader than the sensitive volume itself [38]. The simulations of $K(x)$ in proton fields with modified detector geometries shown in Figure 3.6 in Chapter 3 illustrate a similar effect for proton beams. However, the density perturbation of the Semiflex 3D in 150 MeV protons was found to be much smaller in comparison to the perturbation in 6 MV photons (Figure 3.9 in Chapter 3),

which can be explained by the smaller range of the secondary electrons released in proton fields compared to the range of secondary electrons in photon fields [39, 21].

In contrast to air-filled ionization chambers, the sensitive volume of diode-type detectors is composed of a higher-density material compared to water. For photon radiation, the opposite effect as described for the low-density air cavity has been reported; that is, more electrons are released in the high-density sensitive volume as compared to electrons released in the surroundings, resulting in predominantly outward-directed electron transport [38]. Consequently, the $K(x)$ of high-density detectors in photon fields show negative values [38] outside the detector's borders. However, the results showed that the density perturbation is negligible for diode-type detectors in proton beams, which can again be attributed to the much lower range of secondary electrons in proton beams compared to photon beams [39, 21].

The differences between $K(x)$ in proton and photon fields also lead to differences in effects on profile and output measurements in proton and photon fields. While the density perturbation of diode-type detectors in photon fields is associated with an overresponse in output measurements and a steepening of lateral beam profiles [40, 38, 37], proton beam measurements with diode-type detectors are expected to be perturbed by the volume averaging effect only.

The finding that detector perturbations in proton beams are dominated by volume averaging was supported by testing simplistic geometrical weighting functions $K_{\text{area}}(x, y)$ in Chapter 4. $K_{\text{area}}(x, y)$ were derived by considering the geometry of the respective detector´s sensitive volume without considering the density. The suitability of using $K_{\text{area}}(x, y)$ instead of the simulated $K(x, y)$ was investigated by convolving both functions with small beam profiles $D(x, y)$ of proton beams delivered by pencil beam scanning (PBS), collimated PBS, and collimated passive scattering. The corresponding predictions of resulting $M(x, y)$ profiles for various detectors were compared in terms of the difference in $d_{80/20}$, and the percentage point differences at the maximum. The results show that $K_{\text{area}}(x, y)$ for diode-type detectors are good approximations of the experimental and Monte Carlo simulated $K(x, y)$ in relative dosimetry measurements. For ionization chambers the application of $K_{\text{area}}(x, y)$ leads to $d_{80/20}$ comparable to those obtained with $K(x)$. The point dose differences at the maximum were within 1% for most chambers. However, point dose differences up to 3% were observed for the Semiflex 3D and up to 5.2% for the Advanced Markus chamber, which is why the approximation does not seem to be sufficient for absolute dose measurement purposes.

5.2.2 Point detectors for non-reference dosimetry in clinical proton fields

Lateral dose response functions $K(x)$ have been used within a convolution model to correct detector measurements in photon beams, such as signal profiles and output factors, for the volume effect perturbations [39, 41, 38, 42, 37, 43]. To extend these correction strategies to proton radiation and to estimate the perturbations of point detectors in non-reference proton measurements, $K(x)$ derived for proton irradiations were applied to proton beams delivered with different techniques in Chapter 4.

Lateral beam profiles of small fields delivered via PBS, collimated PBS, and collimated passively scattered techniques were measured using different ionization chamber types, a diode, and a diamond detector. The convolution model was applied to estimate the perturbations associated with the investigated point detectors in terms of penumbra broadening and signal reduction at the maximum. Our investigations showed that the perturbations were, as expected, most pronounced in collimated proton fields with steep lateral dose fall-offs and for detectors with a larger radius of the sensitive area. While PBS fields, as such, were not susceptible to perturbations from the detectors, attention to detector choice should be paid when collimated fields and fields with steep lateral dose fall-offs are measured with point detectors. Our results can be especially helpful for characterizing fields from proton delivery techniques aiming at smaller penumbras, which has been investigated in several studies [44, 45, 46, 47, 48, 49, 50, 51, 52, 53, 54, 55]. To measure profiles of such fields, we found that point detectors associated with small volume-averaging effects, like, for example, the microSilicon detector, are most suitable, although it should be noted that these detectors still suffer from perturbations in small steep gradient fields.

In addition, detector and field size specific output correction factors were derived with the help of $K(x)$ and the convolution model defined by equation 1.2 in Chapter 1. The factors were applied to correct the output ratio measurements of a PinPoint 3D ionization chamber, a microSilicon diode, and a microDiamond detector. While the relative deviation of uncorrected output ratios of all detectors is 9.7% at the smallest field size of 3 mm, the relative standard deviation of corrected output factors was smaller than 0.9% for all field sizes supporting the rationale for the applied correction approach.

Accurate detector positioning has been shown to be crucial during output ratio measurements in small radiation fields [11]. Hence, the influence of positioning uncertainties on the measured signal in proton fields was investigated for different combinations of

detectors, delivery techniques, and field sizes. The results show that even slight positioning errors of 0.5 mm can lead to signal deviations up to 6.6% and that the robustness towards positioning errors highly depends on the shape of the underlying dose profile in combination with the detector type. A frequency analysis of the smallest radiation fields of the three different delivery techniques investigated showed that collimated fields are associated with higher frequency components. Therefore, high-resolution detectors with higher cutoff frequencies are required to accurately resolve these fields.

5.3 Limitations and future research

A limitation of the k_Q factor simulations in Chapter 2 was recently pointed out by Vilches-Freixas *et al.* [56], stating that the water equivalent thickness of the entrance window was not considered for plane-parallel chambers positioned with their reference point at the measurement depth. As this was also the case for all other Monte Carlo simulations considered for the updated k_Q in TRS-398 published in 2024 [5], the k_Q presented therein may suffer from a systematic deviation [57, 56]. Baumann *et al.* [57] estimated the impact of this deviation on k_Q for plane-parallel chambers and found a maximum of 0.5%. Moreover, they found that the deviation is mainly a result of the dose gradient at the measurement depth [57] so the deviation can be corrected with the help of the water equivalent thickness (WET) and the dose distribution.

Another limitation is that the k_Q factors in Chapter 2 were derived from data simulated using two different Monte Carlo codes, which means that potential discrepancies could arise from differences in the modeling of the detectors in terms of material definitions or geometries. For the simulations, the updated I-values in ICRU 90 [58] have been used, and the simulated stopping powers for water, air, and graphite showed deviations from the tabulated stopping powers in ICRU Report 90 of approximately up to 0.3%. Therefore, it should be noted that the stopping powers, as listed in ICRU 90, are now available in Geant4 and should be used for further simulations.

The differences described in Chapter 2 for the Monte Carlo simulated correction factors at high proton energies have been investigated by several works in the past years [15, 16, 17, 59, 18] and might be attributable to the different modeling of nuclear interactions [15, 16, 17, 59, 18, 14]. Baumann *et al.* [17] showed that f_Q can differ by up to approximately 1.5% when f_Q are simulated for an ionization chamber in 250 MeV protons with and without activating nuclear interactions. Baumann *et al.* [15] reviewed available Monte Carlo data and illustrated the dependence of the standard

deviation of f_Q factors for different chamber models on the proton energy, where higher standard uncertainties were found for high proton energies. Therefore, improved nuclear interaction models based on carefully designed experiments could help to reduce the variation of Monte Carlo calculated correction factors at high energies. Palmans *et al.* [14] also observed differences at high proton energies when comparing their analytical function predictions for p_{dis} derived from experimental data to the p_{dis} presented in Chapter 2 and p_{dis} estimated from simulations by Baumann *et al.* [16]. While they also mentioned the nuclear interaction models in the Monte Carlo codes as a potential origin, they additionally pointed out that simplistic source geometries do not consider stray radiation produced in the monitor chambers [14] or other parts within the beamline and suggest performing simulations using more realistic clinical scenarios.

The limitations and suggestions mentioned above will only lead to minor improvements in the simulation accuracy and are, therefore, suggestions on what should be considered in case k_Q factors of newly available ionization chambers are to be simulated. However, for ionization chambers with k_Q listed in the updated TRS-398 well-controlled experiments are more promising to validate the existing data and to reduce the uncertainty in reference dosimetry.

Most recent data of k_Q were obtained using Monte Carlo simulations, and experimentally obtained values are still scarce [14], in particular for scanned proton beams [31]. Experimental k_Q can be derived by relative ionization chamber measurements or by calorimetry measurements [60, 61, 31, 14, 33, 56]. Although such measurements are complex and require well-defined reference conditions, they help to validate k_Q factors derived using simulations, which is important because of the previously described uncertainties or inaccuracies associated with simulations. In addition, calorimetry is currently also considered a new primary standard for proton beams offering direct determination of absorbed dose-to-water [21, 60, 61] where a CoP has recently been published by Green *et al.* [62]. Despite the complexity of calorimeter measurements [21], this approach allows for chamber calibration in proton beams instead of ^{60}Co [60, 61] such that the k_Q factors published in TRS-398 will not be needed [62]. Thereby, the uncertainty in proton reference dosimetry decreases to 1% at the one sigma level [60, 62], which is well below the uncertainty recommended in the updated TRS-398 of 1.7% [5]. While the improved uncertainty demonstrates that the methodology presented by Green *et al.* [62] should be focused on in future research, calorimetry as a primary standard is not yet broadly available such that in the near future most proton centers are still dependent on ionization chambers calibrated in ^{60}Co which require the application

of k_Q factors. Because the proposed calorimetry measurements are often combined with reference dosimetry according to TRS-398, the calorimetry based direct determination of absorbed dose-to-water allows for an experimental validation of existing beam quality correction factors k_Q [63, 64, 30, 31, 32, 65, 66, 34, 35, 67, 21]. This is still worthwhile to do as long as calorimetry is not broadly available.

The investigations performed here can be extended to other modalities, such as carbon ions which are frequently used besides protons in particle therapy. While some authors already derived k_Q or f_Q for carbon ions [63, 64, 68, 69, 65, 66, 70], the data is still very scarce [21] and the uncertainty of k_Q factors for carbon ion dosimetry of 2.4% [5] could be improved [70]. Furthermore, recent developments in MRI-guided proton therapy [71] require new dosimetry investigations as the trajectories of the charged primary and secondary particles are influenced by the Lorentz force. Therefore, the response of the used detectors may be impacted [72], as already reported in the case of MRI-guided photon therapy. Another exciting development is proton FLASH therapy, where very high dose rates are used with the potential of better sparing healthy tissues while maintaining the same tumor response. Few new studies have provided insights on the associated dosimetry aspects [73, 67, 74] that should be further investigated to ensure safe treatment delivery in the future. Under consideration of the previously mentioned benefit of calorimetry on the accuracy of reference dosimetry [62], using calorimetry measurements in the beam quality in which the chamber will be used for chamber calibration will also be beneficial for other modalities. Consequently, such approaches should be focused on and become broadly available as soon as possible. However, as this will take some time, k_Q factors in such beam qualities are still worthwhile to derive for increasing accuracy in the dosimetry with chambers calibrated in $^{60}\mathrm{Co}$.

Although the positioning according to the reference point was recommended for reference dosimetry in proton beams [5], EPOM positioning can be important for measurement tasks in non-reference dosimetry such as depth-dose measurements or absolute dose measurements. The energy independent p_Q^{EPOM} observed in Chapter 2 for cylindrical chambers indicate that the estimate of the EPOM, as 0.75 times the radius of the sensitive volume of ionization chambers, is good for proton beam dosimetry. Similar conclusions were drawn in Palmans [75] and Palmans and Verhaegen [76]. However, a recent study [77] showed that the experimentally determined EPOM of a PTW Semiflex ionization chamber type 31010 is 0.92 instead of 0.75 times the radius, hinting that the EPOMs of non-Farmer type ionization chambers may be larger. Furthermore, Palmans [75] and Vedelago *et al.* [21] discussed that the EPOM may also be dependent on the measurement depth. However, the results of Chapter 2 and those of a recent study by Baumann *et al.* [57] indicate that the impact of uncertainty in the EPOM can be

directly estimated from the dose gradient at the measurement depth. Consequently, the uncertainty from an inaccuracy in EPOM can be estimated based on the dose gradient and will, in most fields, be small, especially for small-volume detectors.

Another topic of interest in non-reference dosimetry is the use of 2D and 3D measurement devices for plan verification or other quality assurance measurements. 2D and 3D measurement devices are composed of multiple point detectors, allowing the investigation presented in Chapters 3 and 4 to be applied and extended to more dimensions to ensure the correctness of such measurements. Brodbek *et al.* [39] approximated the lateral response function of the single chambers arranged in 2D detector arrays by 2D step functions and investigated the associated perturbations in scanned intensity-modulated proton therapy plan measurements. While they found that most field measurements are not perturbed by the volume effect, the investigation did not cover small or collimated proton fields with higher gradients. A frequency analysis by Brodbek *et al.* showed that the 2D ionization chamber arrays investigated have cutoff frequencies comparable to the two largest detectors investigated in Chapter 4 where strong perturbations were observed for such detectors when used in collimated fields motivating the proposed investigation. Some studies reported the use of multiple PinPoint-type ionization chambers arranged as a 3D detector block for treatment plan quality assurance [78, 79, 43]. The results of this work have shown that ionization chambers with similar dimensions as the PinPoint chambers in the detector block can suffer from uncertainties in beam characterizations if the fields consist of steep dose gradients. Because 2D or 3D measurement devices are commonly used for commissioning, treatment plan verification, and TPS validation measurements [39, 80, 81, 82], associated inaccuracies can severely influence the treatment accuracy and consequently also the treatment outcome.

Keeping in mind that the relative dose as a function of field size is used to set up or validate the treatment planning system, the differences between the initial uncorrected output ratios and the corrected average output factor discussed in Chapter 4 could result in dose output differences of the same order in patient treatment plans if such measurements are not corrected. These differences were 8% for the microSilicon diode and 24% for the PinPoint 3D in the 3 mm field, demonstrating the importance of the presented correction strategy. However, the correction factors derived in Chapter 4 are only valid for the investigated delivery technique and cannot be applied in other proton beams or even at other proton beam energies. In contrast, output correction factors for photon beams as a function of field size have been determined for several detectors and are listed in international CoP for various photon energies and treatment machines [13]. Consideration of the number of available detectors, the proton beam energy range commonly accessible, and the number of beam delivery techniques apart from PBS

- for which output correction is especially important - shows that creating tabulated output correction factors as it was done for photons is impractical for proton beams. Our findings in Chapter 4 indicate that lateral dose response functions can be used to derive detector-, energy- and delivery-technique-specific output correction factors from profile measurements. Therefore, it could be worthwhile to further investigate the presented method for proton output measurement correction with the aim of providing a widely applicable methodology. To do so, it could be further investigated to which extent the lateral response functions based on the chamber geometry $K_{\text{area}}(x, y)$ may be used because these are much easier to derive in comparison to lateral response functions from simulations or experiments.

Estimation of overall uncertainty for proton non-reference dosimetry is difficult because uncertainties strongly depend on the measurement conditions and detectors used. In addition, non-reference dosimetry includes various measurement scenarios of which this work only covered a few. However, we showed that, for example, a 0.5 mm positioning error or disregarding a correction of output measurements may lead to differences in dose above 5%, which was estimated to be the limit for the overall uncertainty in dose delivered to a patient [4, 5, 3, 6, 7]. In addition, substantial differences in observed beam penumbra were shown to occur if using a detector that is not suitable for the profile shape. Because the described measurements are important for accurate beam commissioning, treatment planning, patient plan verification, and quality assurance, the associated accuracy should be ensured to remain small, and errors should be avoided. To do so, developing a CoP for non-reference proton dosimetry with a focus on complex measurement conditions, such as small fields or high gradient measurements, would be highly important.

5.4 Final Conclusion

Because small differences in dose can lead to clinically significant changes in TCP or NTCP, the overall uncertainty in proton dosimetry should be small. Therefore, the aim of this thesis was to improve the dosimetry in proton beams. To do so, ionization chamber specific p_Q and k_Q factors, which were previously approximated, were derived using Monte Carlo simulations, and the results were considered in an update of a CoP for proton reference dosimetry. As the derived k_Q are more accurate than the approximated factors, the simulations helped to improve the accuracy in proton reference dosimetry. However, the uncertainty associated with k_Q, according to the CoP, is still comparably large, and future research using calorimetry is expected to lead to higher accuracy in

proton reference dosimetry. To characterize point detectors in non-reference conditions, lateral dose response functions were determined and investigated for various detectors. The functions were then used to correct and explore the behavior of the detectors in dose profile and output measurements, considering three proton beam delivery techniques. The results clearly demonstrate that volume effect perturbations in proton fields can lead to substantial differences in observed beam penumbra and dose output measurements for small fields. The results can guide detector choice for various measurements and could contribute to the development of a new CoP for non-reference proton dosimetry.

References

[1] Wild, C. P., Weiderpass, E., Stewart, B. W., and editiors. "World Cancer Report: Cancer Research for Cancer Prevention." 2020. DOI: http://publications.iarc.fr/586.Licence:CCBY-NC-ND3.0IGO.

[2] WHO. *List of priority medical devices for cancer management*. World Health Organization. Geneva. 2017.

[3] INTERNATIONAL ATOMIC ENERGY AGENCY. *Accuracy Requirements and Uncertainties in Radiotherapy, IAEA Human Health Series No. 31*. IAEA. Vienna. 2016.

[4] Andreo, P., Burns, D. T., Hohlfeld, K., Huq, M. S., Kanai, T., Laitano, F., Smythe, V. G., and Vynckier, S. *Absorbed dose determination in external beam radiotherapy: an international code of practice for dosimetry based on standards of absorbed dose to water. Technical Reports Series No. 398.* International Atomic Energy Agency. Vienna. 2000.

[5] INTERNATIONAL ATOMIC ENERGY AGENCY. *Absorbed Dose Determination in External Beam Radiotherapy, Technical Reports Series No. 398 (Rev. 1)*. IAEA. Vienna. 2024. DOI: 10.61092/iaea.ve7q-y94k.

[6] Paganetti, H. *Proton Therapy Physics*. CRC Press. 2011. DOI: 10.1201/b11448.

[7] Merwe, D. van der, Van Dyk, J., Healy, B., Zubizarreta, E., Izewska, J., Mijnheer, B., and Meghzifene, A. "Accuracy requirements and uncertainties in radiotherapy: a report of the International Atomic Energy Agency". *Acta Oncol*, 2017, 56:1, pp. 1–6. DOI: 10.1080/0284186X.2016.1246801.

[8] Bentzen, S., Bernier, J., Davis, J., Horiot, J., Garavaglia, G., Chavaudra, J., Johansson, K., and Bolla, M. "Clinical impact of dosimetry quality assurance programmes assessed by radiobiological modelling of data from the thermoluminescent dosimetry study of the European Organization for Research and Treatment of Cancer". *Eur J Cancer*, 2000, 36:5, pp. 615–620. DOI: 10.1016/S0959-8049(99)00336-6.

[9] Bolt, M., Clark, C. H., Nisbet, A., and Chen, T. "Quantification of the uncertainties within the radiotherapy dosimetry chain and their impact on tumour control". *Phys. Imaging Radiat. Oncol*, 2021, 19, pp. 33–38. DOI: 10.1016/j.phro.2021.06.004.

[10] Karger, C. P., Jäkel, O., Palmans, H., and Kanai, T. "Dosimetry for ion beam radiotherapy". *Phys Med Biol*, 2010, 55:21, R193–R234. DOI: 10.1088/0031-9155/55/21/R01.

[11] Kugel, F. et al. "Validating a double Gaussian source model for small proton fields in a commercial Monte-Carlo dose calculation engine". *Z Med Phys*, 2022, 33:4, pp. 529–541. DOI: 10.1016/j.zemedi.2022.11.011.

[12] Vatnitsky, S. M., Miller, D. W., Moyers, M. F., Levy, R. P., Schulte, R. W., Slater, J. D., and Slater, J. M. "Dosimetry techniques for narrow proton beam radiosurgery". *Phys Med Biol*, 1999, 44:11, pp. 2789–2801. DOI: 10.1088/0031-9155/44/11/308.

[13] INTERNATIONAL ATOMIC ENERGY AGENCY. *Dosimetry of Small Static Fields Used in External Beam Radiotherapy, Technical Reports Series No. 483*. IAEA. Vienna. 2017.

[14] Palmans, H., Lourenço, A., Medin, J., Vatnitsky, S., and Andreo, P. "Current best estimates of beam quality correction factors for reference dosimetry of clinical proton beams". *Phys Med Biol*, 2022, 67:19, p. 195012. DOI: 10.1088/1361-6560/ac9172.

[15] Baumann, K.-S., Gomà, C., Wulff, J., Kretschmer, J., and Zink, K. "Monte Carlo calculated ionization chamber correction factors in clinical proton beams – deriving uncertainties from published data". *Phys Med*, 2023, 113, p. 102655. DOI: 10.1016/j.ejmp.2023.102655.

[16] Baumann, K.-S., Kaupa, S., Bach, C., Engenhart-Cabillic, R., and Zink, K. "Monte Carlo calculation of perturbation correction factors for air-filled ionization chambers in clinical proton beams using TOPAS/GEANT". *Z Med Phys*, 2021, 31:2, pp. 175–191. DOI: 10.1016/j.zemedi.2020.08.004.

[17] Baumann, K.-S., Kaupa, S., Bach, C., Engenhart-Cabillic, R., and Zink, K. "Monte Carlo calculation of beam quality correction factors in proton beams using TOPAS/GEANT4". *Phys Med Biol*, 2020, 65:5, p. 055015. DOI: 10.1088/1361-6560/ab6e53.

[18] Lourenço, A., Bouchard, H., Galer, S., Royle, G., and Palmans, H. "The influence of nuclear interactions on ionization chamber perturbation factors in proton beams: FLUKA simulations supported by a Fano test". *Med Phys*, 2018, 46:2, pp. 885–891. DOI: 10.1002/mp.13281.

[19] Verhaegen, F. and Palmans, H. "A systematic Monte Carlo study of secondary electron fluence perturbation in clinical proton beams (70-250 MeV) for cylindrical and spherical ion chambers". *Med Phys*, 2001, 28:10, pp. 2088–2095. DOI: 10.1118/1.1406519.

[20] Palmans, H., Medin, J., Trnková, P., and Vatnitsky, S. "Gradient corrections for reference dosimetry using Farmer-type ionization chambers in single-layer scanned proton fields". *Med Phys*, 2020, 47:12, pp. 6531–6539. DOI: 10.1002/mp.14554.

[21] Vedelago, J., Karger, C. P., and Jäkel, O. "A review on reference dosimetry in radiation therapy with proton and light ion beams: status and impact of new developments". *Radiat Meas*, 2022, 157, p. 106844. DOI: 10.1016/j.radmeas.2022.106844.

[22] Farr, J. B. et al. "Clinical commissioning of intensity-modulated proton therapy systems: Report of AAPM Task Group 185". *Med Phys*, 2021, 48:1, e1–e30. DOI: 10.1002/mp.14546.

[23] Gomà, C., Andreo, P., and Sempau, J. "Monte Carlo calculation of beam quality correction factors in proton beams using detailed simulation of ionization chambers". *Phys Med Biol*, 2016, 61:6, pp. 2389–2406. DOI: 10.1088/0031-9155/61/6/2389.

[24] Gomà, C. and Sterpin, E. "Monte Carlo calculation of beam quality correction factors in proton beams using PENH". *Phys Med Biol*, 2019, 64:18, p. 185009. DOI: 10.1088/1361-6560/ab3b94.

[25] Palmans, H. and Verhaegen, F. "Monte Carlo study of fluence perturbation effects on cavity dose response in clinical proton beams". *Phys Med Biol*, 1998, 43:1, pp. 65–89. DOI: 10.1088/0031-9155/43/1/005.

[26] Wulff, J., Baumann, K.-S., Verbeek, N., Bäumer, C., Timmermann, B., and Zink, K. "TOPAS/ Geant4 configuration for ionization chamber calculations in proton beams". *Phys Med Biol*, 2018, 63:11, p. 115013. DOI: 10.1088/1361-6560/aac30e.

[27] Gomà, C., Hofstetter-Boillat, B., Safai, S., and Vörös, S. "Experimental validation of beam quality correction factors for proton beams". *Phys Med Biol*, 2015, 60:8, pp. 3207–3216. DOI: 10.1088/0031-9155/60/8/3207.

[28] Palmans, H., Verhaegen, F., Denis, J.-M., and Vynckier, S. "Dosimetry using plane-parallel ionization chambers in a 75 MeV clinical proton beam". *Phys Med Biol*, 2002, 47:16, pp. 2895–2905. DOI: 10.1088/0031-9155/47/16/305.

[29] Palmans, H., Verhaegen, F., Denis, J.-M., Vynckier, S., and Thierens, H. "Experimental p_{wall} and p_{cel} correction factors for ionization chambers in low-energy clinical proton beams". *Phys Med Biol*, 2001, 46:4, pp. 1187–1204. DOI: 10.1088/0031-9155/46/4/319.

[30] Medin, J. "Implementation of water calorimetry in a 180 MeV scanned pulsed proton beam including an experimental determination of k_Q for a Farmer chamber". *Phys Med Biol*, 2010, 55:12, pp. 3287–3298. DOI: 10.1088/0031-9155/55/12/002.

[31] Medin, J., Andreo, P., and Palmans, H. "Experimental determination of k_Q factors for two types of ionization chambers in scanned proton beams". *Phys Med Biol*, 2022, 67:5, p. 055001. DOI: 10.1088/1361-6560/ac4efa.

[32] Medin, J., Ross, C. K., Klassen, N. V., Palmans, H., Grusell, E., and Grindborg, J.-E. "Experimental determination of beam quality factors, k_Q, for two types of Farmer chamber in a 10 MV photon and a 175 MeV proton beam". *Phys Med Biol*, 2006, 51:6, pp. 1503–1521. DOI: 10.1088/0031-9155/51/6/010.

[33] Palmans, H., Thomas, R., Simon, M., Duane, S., Kacperek, A., DuSautoy, A., and Verhaegen, F. "A small-body portable graphite calorimeter for dosimetry in low-energy clinical proton beams". *Phys Med Biol*, 2004, 49:16, pp. 3737–3749. DOI: 10.1088/0031-9155/49/16/019.

[34] Palmans, H., Seuntjens, J., Verhaegen, F., Denis, J.-M., Vynckier, S., and Thierens, H. "Water calorimetry and ionization chamber dosimetry in an 85-MeV clinical proton beam". *Med Phys*, 1996, 23:5, pp. 643–650. DOI: 10.1118/1.597700.

[35] Sarfehnia, A., Clasie, B., Chung, E., Lu, H. M., Flanz, J., Cascio, E., Engelsman, M., Paganetti, H., and Seuntjens, J. "Direct absorbed dose to water determination based on water calorimetry in scanning proton beam delivery". *Med Phys*, 2010, 37:7, pp. 3541–3550. DOI: 10.1118/1.3427317.

[36] Vatnitsky, S. M., Siebers, J. V., and Miller, D. W. "k_Q factors for ionization chamber dosimetry in clinical proton beams". *Med Phys*, 1996, 23:1, pp. 25–31. DOI: 10.1118/1.597768.

[37] Poppinga, D., Meyners, J., Delfs, B., Muru, A., Harder, D., Poppe, B., and Looe, H. "Experimental determination of the lateral dose response functions of detectors to be applied in the measurement of narrow photon-beam dose profiles". *Phys Med Biol*, 2015, 60:24, pp. 9421–9436. DOI: 10.1088/0031-9155/60/24/9421.

[38] Looe, H. K., Harder, D., and Poppe, B. "Understanding the lateral dose response functions of high-resolution photon detectors by reverse Monte Carlo and deconvolution analysis". *Phys Med Biol*, 2015, 60:16, pp. 6585–6607. DOI: 10.1088/0031-9155/60/16/6585.

[39] Brodbek, L., Kretschmer, J., Willborn, K., Meijers, A., Both, S., Langendijk, J. A., Knopf, A.-C., Looe, H. K., and Poppe, B. "Analysis of the applicability of two-dimensional detector arrays in terms of sampling rate and detector size to verify scanned intensity-modulated proton therapy plans". *Med Phys*, 2020, 47:9, pp. 4589–4601. DOI: 10.1002/mp.14346.

[40] Francescon, P., Beddar, S., Satariano, N., and Das, I. J. "Variation of $k_{Qclin,Qmsr}^{fclin,fmsr}$ for the small-field dosimetric parameters percentage depth dose, tissue-maximum ratio, and off-axis ratio". *Med Phys*, 2014, 41:10, p. 101708. DOI: 10.1118/1.4895978.

[41] Laub, W. U. and Wong, T. "The volume effect of detectors in the dosimetry of small fields used in IMRT". *Med Phys*, 2003, 30:3, pp. 341–347. DOI: 10.1118/1.1544678.

[42] Poppinga, D., Delfs, B., Meyners, J., Harder, D., Poppe, B., and Looe, H. K. "The output factor correction as function of the photon beam field size – direct measurement and calculation from the lateral dose response functions of gas-filled and solid detectors". *Z Med Phys*, 2018, 28:3, pp. 224–235. DOI: 10.1016/j.zemedi.2017.07.006.

[43] Schwaab, J., Brons, S., Fieres, J., and Parodi, K. "Experimental characterization of lateral profiles of scanned proton and carbon ion pencil beams for improved beam models in ion therapy treatment planning". *Phys Med Biol*, 2011, 56:24, pp. 7813–7827. DOI: 10.1088/0031-9155/56/24/009.

[44] Bäumer, C., Fuentes, C., Janson, M., Matic, A., Timmermann, B., and Wulff, J. "Stereotactical fields applied in proton spot scanning mode with range shifter and collimating aperture". *Phys Med Biol*, 2019, 64:15, p. 155003. DOI: 10.1088/1361-6560/ab2ae7.

[45] Bäumer, C., Janson, M., Timmermann, B., and Wulff, J. "Collimated proton pencil-beam scanning for superficial targets: impact of the order of range shifter and aperture". *Phys Med Biol*, 2018, 63:8, p. 085020. DOI: 10.1088/1361-6560/aab79c.

[46] Farr, J. B., Moskvin, V., Lukose, R. C., Tuomanen, S., Tsiamas, P., and Yao, W. "Development, commissioning, and evaluation of a new intensity modulated minibeam proton therapy system". *Med Phys*, 2018, 45:9, pp. 4227–4237. DOI: 10.1002/mp.13093.

[47] Gelover, E., Wang, D., Hill, P. M., Flynn, R. T., Gao, M., Laub, S., Pankuch, M., and Hyer, D. E. "A method for modeling laterally asymmetric proton beamlets resulting from collimation: Asymmetric proton beamlet modeling". *Med Phys*, 2015, 42:3, pp. 1321–1334. DOI: 10.1118/1.4907965.

[48] Hyer, D. E., Hill, P. M., Wang, D., Smith, B. R., and Flynn, R. T. "A dynamic collimation system for penumbra reduction in spot-scanning proton therapy: Proof of concept: Penumbra trimmer for spot scanning". *Med Phys*, 2014, 41:9, p. 091701. DOI: 10.1118/1.4837155.

[49] Hyer, D. E., Hill, P. M., Wang, D., Smith, B. R., and Flynn, R. T. "Effects of spot size and spot spacing on lateral penumbra reduction when using a dynamic collimation system for spot scanning proton therapy". *Phys Med Biol*, 2014, 59:22, N187–N196. DOI: 10.1088/0031-9155/59/22/N187.

[50] Lomax, A. “What will the medical physics of proton therapy look like 10 yr from now? A personal view”. *Med Phys*, 2018, 45:11, e984–e993. DOI: 10.1002/mp.13206.

[51] Meier, G., Leiser, D., Besson, R., Mayor, A., Safai, S., Weber, D. C., and Lomax, A. J. “Contour scanning for penumbra improvement in pencil beam scanned proton therapy”. *Phys Med Biol*, 2017, 62:6, pp. 2398–2416. DOI: 10.1088/1361-6560/aa5dde.

[52] Safai, S., Bortfeld, T., and Engelsman, M. “Comparison between the lateral penumbra of a collimated double-scattered beam and uncollimated scanning beam in proton radiotherapy”. *Phys Med Biol*, 2008, 53:6, pp. 1729–1750. DOI: 10.1088/0031-9155/53/6/016.

[53] Titt, U., Mirkovic, D., Sawakuchi, G. O., Perles, L. A., Newhauser, W. D., Taddei, P. J., and Mohan, R. “Adjustment of the lateral and longitudinal size of scanned proton beam spots using a pre-absorber to optimize penumbrae and delivery efficiency”. *Phys Med Biol*, 2010, 55:23, pp. 7097–7106. DOI: 10.1088/0031-9155/55/23/S10.

[54] Winterhalter, C., Meier, G., Oxley, D., Weber, D., Lomax, A., and Safai, S. “Contour scanning, multi-leaf collimation and the combination thereof for proton pencil beam scanning”. *Phys Med Biol*, 2018, 64:1, p. 015002. DOI: 10.1088/1361-6560/aaf2e8.

[55] Winterhalter, Lomax, A., Oxley, D., Weber, D. C., and Safai, S. “A study of lateral fall-off (penumbra) optimisation for pencil beam scanning (PBS) proton therapy”. *Phys Med Biol*, 2018, 63:2, p. 025022. DOI: 10.1088/1361-6560/aaa2ad.

[56] Vilches-Freixas, G., Bosmans, G., Douralis, A., Martens, J., Meijers, A., Rinaldi, I., Salvo, K., Thomas, R., Palmans, H., and Lourenço, A. “Experimental comparison of cylindrical and plane parallel ionization chambers for reference dosimetry in continuous and pulsed scanned proton beams”. *Phys Med Biol*, 2024, 69:10, p. 105021. DOI: 10.1088/1361-6560/ad40f9.

[57] Baumann, K.-S., Lourenço, A., Wulff, J., Vilches-Freixas, G., and Palmans, H. “Investigating the impact of the effective point of measurement for plane-parallel ionization chambers in clinical proton beams”. *Phys Med Biol*, 2025, 70:1, p. 015014. DOI: 10.1088/1361-6560/ad9e7c.

[58] Seltzer, S. M., Fernández-Varea, J. M., Andreo, P., Bergstrom, P. M., Burns, D. T., Krajear Bronié, I., Ross, C. K., and Salvat, F. “Key data for ionizing radiation dosimetry: measurement standards and applications. ICRU Report 90”. *J ICRU*, 2016, 14, pp. 1–110.

[59] Baumann, K.-S., Horst, F., Zink, K., and Gomà, C. "Comparison of PENH, FLUKA, and GEANT4/TOPAS for absorbed dose calculations in air cavities representing ionization chambers in high-energy photon and proton beams". *Med Phys*, 2019, 46:10, pp. 4639–4653. DOI: 10.1002/mp.13737.

[60] Lourenço, A. et al. "A portable primary-standard level graphite calorimeter for absolute dosimetry in clinical pencil beam scanning proton beams". *Phys Med Biol*, 2023, 68:17, p. 175005. DOI: 10.1088/1361-6560/ace50f.

[61] Lourenço, A., Lee, N., Shipley, D., Romano, F., Kacperek, A., Duane, S., Cashmore, M., Bass, G., Palmans, H., and Thomas, R. "Application of a portable primary standard level graphite calorimeter for absolute dosimetry in a clinical low-energy passively scattered proton beam". *Phys Med Biol*, 2022, 67:22, p. 225021. DOI: 10.1088/1361-6560/ac95f6.

[62] Green, S. et al. "IPEM code of practice for proton therapy dosimetry based on the NPL primary standard proton calorimeter calibration service". *Phys Med Biol*, 2025, 70:6, p. 065016. DOI: 10.1088/1361-6560/adad2e.

[63] Holm, K. M., Jäkel, O., and Krauss, A. "Direct determination of k_Q for Farmer-type ionization chambers in a clinical scanned carbon-ion beam using water calorimetry". *Phys Med Biol*, 2022, 67:4, p. 049401. DOI: 10.1088/1361-6560/ac4fa0.

[64] Holm, K. M., Jäkel, O., and Krauss, A. "Water calorimetry-based k_Q factors for Farmer-type ionization chambers in the SOBP of a carbon-ion beam". *Phys Med Biol*, 2021, 66:14, p. 145012. DOI: 10.1088/1361-6560/ac0d0d.

[65] Osinga-Blättermann, J.-M., Brons, S., Greilich, S., Jäkel, O., and Krauss, A. "Direct determination of k_Q for Farmer-type ionization chambers in a clinical scanned carbon ion beam using water calorimetry". *Phys Med Biol*, 2017, 62:6, pp. 2033–2054. DOI: 10.1088/1361-6560/aa5bac.

[66] Osinga-Blättermann, J.-M. and Krauss, A. "Determination of k_Q factors for cylindrical and plane-parallel ionization chambers in a scanned carbon ion beam by means of cross calibration". *Phys Med Biol*, 2018, 64:1, p. 015009. DOI: 10.1088/1361-6560/aaf5ac.

[67] Lourenço, A. et al. "Absolute dosimetry for FLASH proton pencil beam scanning radiotherapy". *Sci Rep*, 2023, 13:1, p. 2054. DOI: 10.1038/s41598-023-28192-0.

[68] Khan, A. U., Nelson, N. P., Culberson, W. S., and DeWerd, L. A. "On the perturbation effect and LET dependence of beam quality correction factors in carbon ion beams". *Med Phys*, 2023, 50:2, pp. 1105–1120. DOI: 10.1002/mp.16089.

[69] Khan, A. U., Simiele, E. A., and DeWerd, L. A. "Monte Carlo-derived ionization chamber correction factors in therapeutic carbon ion beams". *Phys Med Biol*, 2021, 66:19, p. 195003. DOI: 10.1088/1361-6560/ac226c.

[70] Urago, Y., Sakama, M., Sakata, D., Fukuda, S., Katayose, T., and Chang, W. "Monte Carlo-calculated beam quality and perturbation correction factors validated against experiments for Farmer and Markus type ionization chambers in therapeutic carbon-ion beams". *Phys Med Biol*, 2023, 68:18, p. 185013. DOI: 10.1088/1361-6560/acf024.

[71] Burigo, L. N. and Oborn, B. M. "Integrated MRI-guided proton therapy planning: Accounting for the full MRI field in a perpendicular system". *Med Phys*, 2022, 49:3, pp. 1853–1873. DOI: 10.1002/mp.15398.

[72] Gebauer, B., Baumann, K.-S., Fuchs, H., Georg, D., Oborn, B. M., Looe, H.-K., and Lühr, A. "Proton dosimetry in a magnetic field: Measurement and calculation of magnetic field correction factors for a plane-parallel ionization chamber". *Med Phys*, 2023, 61:3, pp. 2293–2305. DOI: 10.1002/mp.16797.

[73] Lee, E. et al. "Ultrahigh dose rate pencil beam scanning proton dosimetry using ion chambers and a calorimeter in support of first in-human FLASH clinical trial". *Med Phys*, 2022, 49:9, pp. 6171–6182. DOI: 10.1002/mp.15844.

[74] Villoing, D. et al. "Technical note: Proton beam dosimetry at ultra-high dose rates (FLASH): Evaluation of GAFchromic™ (EBT3, EBT-XD) and OrthoChromic (OC-1) film performances". *Med Phys*, 2022, 49:4, pp. 2732–2745. DOI: 10.1002/mp.15526.

[75] Palmans, H. "Perturbation factors for cylindrical ionization chambers in proton beams. Part I: corrections for gradients". *Phys Med Biol*, 2006, 51:14, pp. 3483–3501. DOI: 10.1088/0031-9155/51/14/014.

[76] Palmans, H. and Verhaegen, F. "On the effective point of measurement of cylindrical ionization chambers for proton beams and other heavy charged particle beams". *Phys Med Biol*, 2000, 45:8, pp. L20–L22. DOI: 10.1088/0031-9155/45/8/103.

[77] Barna, S., Resch, A. F., Puchalska, M., Georg, D., and Palmans, H. "Technical note: Experimental determination of the effective point of measurement of the PTW-31010 ionization chamber in proton and carbon ion beams". *Med Phys*, 2022, 49:1, pp. 675–681. DOI: 10.1002/mp.15377.

[78] Grevillot, L. et al. "Clinical implementation and commissioning of the MedAustron Particle Therapy Accelerator for non-isocentric scanned proton beam treatments". *Med Phys*, 2020, 47:2, pp. 380–392. DOI: 10.1002/mp.13928.

[79] Grevillot, L., Stock, M., Palmans, H., Osorio Moreno, J., Letellier, V., Dreindl, R., Elia, A., Fuchs, H., Carlino, A., and Vatnitsky, S. "Implementation of dosimetry equipment and phantoms at the MedAustron light ion beam therapy facility". *Med Phys*, 2018, 45:1, pp. 352–369. DOI: 10.1002/mp.12653.

[80] Arjomandy, B. et al. "AAPM task group 224: Comprehensive proton therapy machine quality assurance". *Med Phys*, 2019, 46:8, e678–e705. DOI: 10.1002/mp.13622.

[81] Vilches-Freixas, G., Unipan, M., Rinaldi, I., Martens, J., Roijen, E., Almeida, I. P., Decabooter, E., and Bosmans, G. "Beam commissioning of the first compact proton therapy system with spot scanning and dynamic field collimation". *BJR*, 2020, 93:1107, p. 20190598. DOI: 10.1259/bjr.20190598.

[82] Decabooter, E., Roijen, E., Martens, J., Unipan, M., Bosmans, G., and Vilches-Freixas, G. "Quality assurance of scanned proton beams at different gantry angles using an ionization chamber array in a rotational phantom". *Phys Med*, 2022, 104, pp. 67–74. DOI: 10.1016/j.ejmp.2022.10.014.

A

APPENDIX

Abbreviations

CoP	Code of Practice
EPOM	Effective point of measurement
FWHM	Full-width-at-half-maximum
MC	Monte Carlo
MRI	Magnetic resonance imaging
NTCP	Normal tissue complication probability
PBS	Pencil beam scanning
TCP	Tumor control probability
SOBP	Spread-out Bragg peak
WET	Water equivalent thickness
2D	Two-dimensional
3D	Three-dimensional

English summary

The outcome of a radiation therapy treatment is affected by the accuracy of the dose delivered to the tumor and the surrounding healthy tissues. Because small uncertainties in dose can lead to clinically relevant changes in the probability of normal tissue complications or tumor control, any uncertainty in the treatment process should be small. Dose measurements, also known as dosimetry, are used to set up the treatment machine and planning software, validate patient treatment plans, and calibrate the absolute dose output. To ensure that these steps are performed with high accuracy, the detectors used to perform the measurements must be well characterized, and detector specific corrections are required. While detectors in photon radiation fields have been investigated in many studies in the past, dosimetry in proton beams is associated with higher uncertainties and requires further research.

Therefore, this thesis investigates point detectors for measurements in proton beams to improve the accuracy of dosimetry in proton beam therapy. The investigation comprises measurements in reference and non-reference conditions, resulting in three main chapters 2, 3 and 4. Approximations in proton reference dosimetry are considered by Monte Carlo simulations of perturbation and beam quality correction factors for ionization chambers in monoenergetic proton fields. To provide more insight into potential point detector perturbations in proton measurements under non-reference conditions, several ionization chambers, a diode, and a diamond detector are characterized by determining their lateral dose response functions. Thereafter, the detector's impacts on lateral dose profile and output measurements are investigated for three different proton beam delivery techniques, and correction strategies to compensate for perturbations are presented.

Since perturbation factors for proton beams were approximated by unity in the available Codes of Practice at the time Chapter 2 was written, Monte Carlo simulations are conducted in **Chapter 2** to determine perturbation and beam quality correction factors for five cylindrical and four plane-parallel ionization chambers. Monoenergetic proton beam energies between 70 MeV and 250 MeV are considered. The simulations cover the determination of perturbations caused by individual chamber components, revealing the largest influences for the chamber wall and the chamber displacement perturbation for large cylindrical ionization chambers positioned with their reference point. Beam quality correction factors for cylindrical chambers are presented for two positioning approaches commonly used in proton reference dosimetry. The influence of the positioning method was found to be especially pronounced at low energies but also persisted at high energies, highlighting the importance of accurately positioning ionization chambers in proton reference dosimetry. The correction factors presented are

different from the recommendations in Codes of Practice available at the time of writing Chapter 2. Thereby, the results help to increase proton reference dosimetry accuracy.

Chapters 3 and 4 consider volume effect measurement perturbations from point detectors to reduce uncertainties in proton non-reference dosimetry. Detector-specific lateral dose-response functions can be used to estimate volume effects and to develop correction strategies for perturbed measurements. Hence, lateral dose response functions for three ionization chambers, a diode, and a diamond detector are determined experimentally and by Monte Carlo simulations in **Chapter 3**. The experimentally derived and simulated lateral dose response functions agree within 2.1% of the maximum value. An analysis of the response functions for various proton energies and depths in water revealed that the functions can be considered energy and depth independent in the investigated energy range. The contribution from individual detector components to the overall volume effect is examined for an ionization chamber and a diamond detector as an example. Compared to photon dosimetry, the density perturbation caused by the non-water equivalent materials is small in proton beams, and the main contribution to the volume effect is the result of volume-averaging from the extended sensitive volume of detectors. The derived response functions can be used within a convolution model to correct volume effect perturbations in proton dose distributions. In **Chapter 4**, the investigation has been extended to realistic clinical measurement conditions. The functions obtained in Chapter 3 are used within a convolution model to estimate volume effect perturbations in fields created with three different proton beam delivery techniques. Lateral dose profile and output measurements of fields delivered by pencil beam scanning, pencil beam scanning combined with collimators, and passive scattering with collimators are considered. Convolving the lateral dose response functions derived in Chapter 3 with high-resolution film measurements serving as reference allows quantifying perturbations from the detectors. While the lateral penumbra broadening from the investigated point detectors in pencil beam scanning fields was small with respect to the unperturbed reference, differences of up to 2.2 mm were found for fields created with collimators. Similarly, the signal reduction at the maximum was especially dominant in collimated fields where the investigated detectors led to signal reductions between 7.6% and 60.7% in a collimated 3 mm diameter field, depending on the detector. Output ratio measurements performed with an ionization chamber, a diode, and a diamond detector in passively scattered collimated fields are corrected by correction factors determined by their lateral dose response functions. While the uncorrected output ratios deviated by up to 9.7%, the corrected output ratio measurements agreed within 0.9%. The results can be used to estimate volume effect perturbations of investigated point detectors in various proton dose distributions.

The general discussion in Chapter 5 contextualizes the results of Chapters 2, 3, and 4, lists limitations, and indicates future research topics in dosimetry. The results presented in Chapter 2 contributed to the derivation of current best estimates for beam quality correction factors in proton beams, which were used in an update of a Code of Practice for proton reference dosimetry. Compared to an older version of the Code of Practice, the beam quality correction factors for proton beams recommended in the updated version are more accurate, and associated uncertainties were reduced from 2.1% to 1.4%. While this improves the accuracy of reference dosimetry in proton therapy, experimentally derived correction factors would be helpful to validate the data. Future research based on calorimetry seems most worthwhile for reducing the uncertainty associated with proton reference dosimetry. The investigation of lateral dose response functions and their application in different proton fields demonstrates that detector choice is crucial for accurate beam characterization and that very small fields require corrections for absolute dose measurements even if small volume detectors are used. To ensure high accuracy in beam characterization measurements, patient plan verifications, and quality assurance, the future development of a Code of Practice for non-reference proton dosimetry is important.

In conclusion, this thesis presents more accurate correction factors for reference dosimetry and provides methods to estimate or correct detector perturbations in proton fields under non-reference conditions. The results help to improve the accuracy of proton dosimetry, which is important because even small dose differences influence tumor control, healthy tissue complication probability, and hence the outcome of a patient's radiation therapy treatment.

Nederlanse Samenvatting

Het resultaat van een behandeling met radiotherapie hangt af van de nauwkeurigheid van de bepaling van de stralingsdosis in de tumor en de omringende gezonde weefsels. Omdat kleine onzekerheden in de dosis kunnen leiden tot klinisch relevante veranderingen in de kans op complicaties in normaal weefsel of in de tumor controle, moet elke onzekerheid in het behandelingsproces klein zijn. Dosismetingen, ook wel dosimetrie genoemd, worden gebruikt om het bestralingsapparaat en de planningssoftware in te stellen, om behandelplannen van patiënten te valideren en de afgegeven absolute dosis te kalibreren. Om te zorgen dat deze stappen met een hoge nauwkeurigheid worden uitgevoerd, moeten de detectoren die voor de metingen worden gebruikt goed gekarakteriseerd zijn en zijn detectorspecifieke correcties nodig. Hoewel de werking van veel detectoren in stralingsvelden van fotonen al uitgebreid is onderzocht, zijn de onzekerheden in dosimetrie in protonenvelden nog relatief groot.

Om de nauwkeurigheid van dosimetrie bij protonentherapie te verbeteren, richt het onderzoek in dit proefschrift zich op puntdetectoren voor metingen in protonenvelden. Het onderzoek omvat metingen in referentie- en niet-referentieomstandigheden waarvan de resultaten zijn beschreven in de drie kernhoofdstukken 2, 3 en 4. De invloed van benaderingen in referentiedosimetrie voor protonen is onderzocht via Monte Carlo simulaties van perturbatie- en bundelkwaliteitscorrectiefactoren voor ionisatiekamers in mono-energetische protonenvelden. Om meer inzicht te krijgen in mogelijke verstoringen tijdens metingen in protonenvelden onder niet-referentieomstandigheden, zijn verschillende ionisatiekamers, een diode en een diamantdetector gekarakteriseerd door hun laterale dosisresponsfuncties te bepalen. Vervolgens is het effect van iedere detector op het laterale dosisprofiel en de output factor onderzocht bij drie verschillende technieken voor afgifte van de protonendosis, en worden correctiestrategieën ter compensatie van de verstoringen voorgesteld.

Omdat tijdens het schrijven van hoofdstuk 2 in de geldende dosimetrierichtlijn de correctiefactoren voor verstoringen bij metingen in een protonenveld nog werden benaderd door één, zijn in **hoofdstuk 2**, via Monte Carlo simulaties, perturbatie- en bundelkwaliteitscorrectiefactoren in protonenvelden bepaald voor vijf cilindrische en vier planparallelle ionisatiekamers. Hierbij zijn mono-energetische protonenbundels met een energie tussen 70 MeV en 250 MeV onderzocht. De simulaties richten zich op de verstoringen door individuele onderdelen van de ionisatiekamers. Hieruit blijkt dat de grootste effecten veroorzaakt worden door de wand van de ionisatiekamer en door het verschil tussen effectieve en referentie positie van de grote cilindrische ionisatiekamers . De correctiefactoren voor stralingskwaliteit zijn bepaald voor cilindrische kamers voor

twee positioneringsmethoden die gangbaar zijn in de referentiedosimetrie voor protonen. De invloed van de positioneringsmethode was vooral belangrijk bij lage energieën, maar ook nog zichtbaar bij hoge energieën. Dit onderstreept het belang van nauwkeurige positionering van ionisatiekamers in referentiedosimetrie voor protonen. De gepresenteerde correctiefactoren wijken af van de aanbevelingen in de richtlijn die gangbaar was ten tijde van het bewerken van hoofdstuk 2. De resultaten dragen bij aan een hogere nauwkeurigheid van de referentiedosimetrie in protonenvelden.

Ten einde de onzekerheden in protonendosimetrie onder niet-referentieomstandigheden te verminderen zijn in hoofdstukken 3 en 4 de verstoringen onderzocht ten gevolge van het volume-effect op metingen met puntdetectoren. Detectorspecifieke laterale dosis responsfuncties kunnen worden gebruikt om een schatting te maken van deze volume-effecten en om strategieën te ontwikkelen ter correctie van verstoorde metingen. In **hoofdstuk 3** zijn laterale dosis responsfuncties bepaald, zowel experimenteel als door middel van Monte Carlo simulaties, voor drie ionisatiekamers, een diode en een diamant detector. De experimentele en gesimuleerde laterale dosisresponsfuncties komen binnen 2.1% van de maximale waarde overeen. Een analyse voor verschillende protonenergieën en diepten in water toont aan dat de functies in het onderzochte energiebereik als energie- en diepte-onafhankelijk kunnen worden beschouwd. De bijdrage van individuele detectorcomponenten aan het totale volume-effect is nader onderzocht voor een ionisatiekamer en een diamantdetector. Vergeleken met fotonendosimetrie is de verstoring door dichtheidsverschillen van de niet-waterequivalente materialen klein in protonenbundels, en de belangrijkste bijdrage aan het volume-effect is het gevolg van volumemiddeling over het uitgebreide detectie volume van de detectoren. De gevonden dosisreponsefuncties kunnen met behulp van een convolutiemodel worden gebruikt om verstoringen door volume-effecten in protonendosisverdelingen te corrigeren. In **hoofdstuk 4** is het onderzoek uitgebreid naar metingen onder realistische klinische omstandigheden. De dosis reponsefuncties die in hoofdstuk 3 zijn verkregen, zijn gebruikt in een convolutiemodel om volume-effectverstoringen te schatten in velden die zijn gecreëerd met drie verschillende afgiftetechnieken voor het protonenveld. Laterale dosisprofielen en output factoren zijn bepaald voor stralingsvelden die zijn gegenereerd door pencil beam scanning, pencil beam scanning gecombineerd met collimatoren, en passieve verstrooiing in combinatie met collimatoren. Door de in hoofdstuk 3 afgeleide laterale dosisresponsfuncties te convolueren met hoge-resolutie filmmetingen die als referentie dienen, kunnen de verstoringen van de detectoren worden gekwantificeerd. Hoewel de laterale penumbraverbreding van de onderzochte puntdetectoren in pencil beam scanningvelden klein is ten opzichte van de ongestoorde referentie, zijn er verschillen tot 2.2 mm gevonden voor velden die met collimatoren zijn gecreëerd. Evenzo is de maximale signaalreductie vooral belangrijk in gecollimeerde velden, waar afhankelijk

van de onderzochte detector, signaalreducties, gevonden zijn tussen 7.6% en 60.7% in een gecollimeerd veld met een diameter van 3 mm. Metingen van de relatieve outputfactor, uitgevoerd met een ionisatiekamer, een diode en een diamantdetector in passief verstrooide gecollimeerde velden, zijn gecorrigeerd met correctiefactoren die zijn bepaald door hun laterale dosisresponsfuncties. Terwijl de ongecorrigeerde relatieve outputfactoren tot 9.7% afwijken, komen de gecorrigeerde waarden binnen 0.9% overeen. Deze resultaten kunnen worden gebruikt om volume-effectverstoringen van de onderzochte puntdetectoren in verschillende protonendosisverdelingen te schatten.

De algemene discussie in hoofdstuk 5 verbindt de resultaten van hoofdstukken 2, 3 en 4, somt beperkingen op en geeft toekomstige onderzoeksonderwerpen in de dosimetrie aan. De resultaten gepresenteerd in hoofdstuk 2 hebben bijgedragen tot de huidige beste schattingen voor correctiefactoren voor de bundelkwaliteit in protonenbundels. Deze factoren zijn verwerkt in een update van de richtlijn voor protonenreferentiedosimetrie. Vergeleken met een oudere richtlijn zijn de in de bijgewerkte versie aanbevolen correctiefactoren voor de bundelkwaliteit voor protonenbundels nauwkeuriger en zijn de bijbehorende onzekerheden teruggebracht van 2.1% naar 1.4%. Hoewel dit de nauwkeurigheid van referentiedosimetrie bij protonentherapie verbetert, zouden aanvullende experimenteel afgeleide correctiefactoren nuttig kunnen zijn om de gegevens te valideren. Toekomstig onderzoek op basis van calorimetrie lijkt het meest geschikt om de onzekerheid die gepaard gaat met protonenreferentiedosimetrie te verminderen. Het onderzoek naar laterale dosisresponsfuncties en hun toepassing in verschillende protonenvelden toont aan dat de keuze van de detector cruciaal is voor nauwkeurige bundelkarakterisering en dat zeer kleine velden correcties vereisen voor absolute dosismetingen, zelfs bij gebruik van detectoren met een klein volume. Om een hoge nauwkeurigheid te garanderen bij bundelkarakteriseringsmetingen, verificaties van patiëntplannen en kwaliteitsborging, is de ontwikkeling van een richtlijn voor protonendosimetrie in niet-referentieomstandigheden belangrijk voor de toekomst.

Concluderend, in dit proefschrift worden nauwkeurigere correctiefactoren voor referentiedosimetrie in protonenvelden afgeleid en worden methoden aangereikt om detectorverstoringen in protonenvelden onder niet-referentieomstandigheden te schatten of te corrigeren. De resultaten dragen bij aan de verbetering van de nauwkeurigheid van protonendosimetrie. Dit is van belang omdat zelfs kleine dosisverschillen de tumorcontrole, de kans op complicaties in gezond weefsel en daarmee de uitkomst van een radiotherapiebehandeling van een patiënt kunnen beïnvloeden.

Deutsche Zusammenfassung

Die Wirkung einer strahlentherapeutischen Behandlung ist abhängig von der Genauigkeit der Dosis im Tumor und im umliegenden gesunden Gewebe. Da kleine Unsicherheiten in der Dosis die Wahrscheinlichkeit für klinisch relevante Normalgewebsreaktionen und für die Tumorkontrolle beeinflussen können, sollte jede Unsicherheit im Behandlungsprozess minimiert werden. Messungen der Dosis, auch bezeichnet als Dosimetrie, sind notwendig, um die Bestrahlungsgeräte und Planungs-Software korrekt einzurichten, um Patienten-Bestrahlungspläne zu validieren und den absoluten Dosis-Output zu kalibrieren. Um all diese Schritte mit hoher Genauigkeit durchführen zu können, ist es erforderlich, dass die genutzten Detektoren gut charakterisiert sind und detektorspezifische Korrekturfaktoren vorliegen. Während viele Studien Detektoren in Photonenstrahlungs-Feldern betrachtet haben, ist die Dosimetrie in Protonenstrahlungs-Feldern weniger untersucht und mit größeren Unsicherheiten verbunden.

Daher werden in dieser Arbeit Punktdetektoren für Messungen in Protonen-Feldern untersucht, um die Genauigkeit der Dosimetrie in der Protonenstrahlentherapie zu verbessern. Die Betrachtung umfasst Messungen unter Referenz- und Nicht-Referenzbedingungen und wird in den drei Hauptkapiteln 2, 3 und 4 zusammengefasst. Eine Überprüfung von Näherungen in der Protonenstrahl-Referenzdosimetrie erfolgt durch Monte-Carlo-Simulationen von Störungs- und Strahlqualitätskorrekturfaktoren für Ionisationskammern in monoenergetischen Protonen-Feldern. Um potenzielle Detektor-Störungseffekte bei Protonenmessungen unter Nicht-Referenzbedingungen zu untersuchen, werden mehrere Ionisationskammern, eine Diode und ein Diamantdetektor durch ihre lateralen Dosis-Ansprechfunktionen charakterisiert. Anschließend wird der individuelle Einfluss der Detektoren auf Messungen von lateralen Dosisprofilen und Output Faktoren unter Berücksichtigung von drei verschiedenen Protonen-Bestrahlungstechniken untersucht, sowie Korrekturstrategien zur Kompensation der Detektor-Störungseffekte vorgestellt.

Da Störungskorrekturfaktoren für Protonen-Felder zum Zeitpunkt der Arbeit für Kapitel 2 in den verfügbaren Dosimetrie-Richtlinien mit Eins abgeschätzt wurden, werden in **Kapitel 2** Monte-Carlo-Simulationen durchgeführt, um die Störungs- und Strahlungsqualitätskorrekturfaktoren für fünf zylindrische und vier planparallele Ionisationskammern zu bestimmen. Die Untersuchung umfasst monoenergetische Protonenenergien zwischen 70 MeV und 250 MeV. Unter anderem werden Störungskorrekturfaktoren einzelner Kammerkomponenten simuliert, mithilfe derer identifiziert wurde, dass der größte Störungseffekt durch die Ionisationskammerwand und die Kammerverschiebung von großen zylindrischen Ionisationskammern, die in ihrem Referenzpunkt positioniert

sind, hervorgerufen wird. Strahlungsqualitätskorrekturfaktoren für zylindrische Ionisationskammern werden für zwei Positionierungsmethoden, die üblicherweise in der Protonen-Referenzdosimetrie verwendet werden, bestimmt. Die Korrekturfaktoren der zwei Positionierungsmethoden zeigten besonders bei niedrigen Energien aber auch bei hohen Energien Abweichungen, was die Bedeutung einer genauen Positionierung von Ionisationskammern in der Protonen-Referenzdosimetrie unterstreicht. Die ermittelten Korrekturfaktoren weichen von den Empfehlungen in den zum Zeitpunkt der Erstellung von Kapitel 2 verfügbaren Dosimetrie-Richtlinien ab. Dadurch tragen die Ergebnisse zu einer verbesserten Genauigkeit in der Protonen-Referenzdosimetrie bei.

Um Unsicherheiten in der Protonen-Nicht-Referenzdosimetrie zu reduzieren, werden in Kapitel 3 und 4 Volumeneffekt-Störungen in Messungen von Punktdetektoren betrachtet. Detektorspezifische laterale Dosis-Ansprechfunktionen können genutzt werden, um Volumeneffekte abzuschätzen und Korrekturstrategien für gestörte Messungen zu entwickeln. Mit diesem Ziel werden in **Kapitel 3** laterale Dosis-Ansprechfunktionen für drei Ionisationskammern, eine Diode und einen Diamantdetektor experimentell und mit Hilfe von Monte-Carlo-Simulationen bestimmt. Die gemessenen und simulierten lateralen Dosis-Ansprechfunktionen stimmen innerhalb von 2.1% des Maximalwertes überein. Die Untersuchung der Funktionen in Abhängigkeit der Protonenenergie und Messtiefe zeigt, dass die Funktionen im untersuchten Energie- und Tiefenbereich als energie- und tiefenunabhängig angesehen werden können. Der Beitrag einzelner Detektorkomponenten zum Gesamtvolumeneffekt wurde am Beispiel einer Ionisationskammer und eines Diamantdetektors untersucht. Im Vergleich zur Photonenstrahl-Dosimetrie ist der Dichteeffekt, der durch die nicht-wasseräquivalenten Materialien verursacht wird, in Protonenstrahlen gering, und der Hauptbeitrag zum Volumeneffekt entsteht durch den Volumenmittelungseffekt durch das ausgedehnte sensitive Volumen der Detektoren. Die ermittelten Ansprechfunktionen können innerhalb eines Faltungsmodells verwendet werden, um Volumeneffekt-Störungen in Protonendosisverteilungen zu korrigieren. In **Kapitel 4** wird die Untersuchung auf realistische klinische Messbedingungen ausgeweitet. Die in Kapitel 3 bestimmten Ansprechfunktionen werden innerhalb eines Faltungsmodells verwendet, um Volumeneffekt-Störungen zu korrigieren oder abzuschätzen. Dabei werden die Funktionen in Strahlenfeldern genutzt, die mit drei verschiedenen Protonen-Bestrahlungstechniken erzeugt wurden. Betrachtet werden laterale Dosisprofile und Output-Faktoren von Feldern, die durch Pencil-Beam-Scanning-Verfahren, Pencil-Beam-Scanning-Verfahren in Kombination mit Kollimatoren und Passive-Scattering mit Kollimatoren erzeugt werden. Die Faltung der in Kapitel 3 ermittelten lateralen Dosis-Ansprechfunktionen mit hochaufgelösten Filmmessungen, die gleichzeitig als Referenz dienen, ermöglicht die Abschätzung der Störungen durch die Detektoren. Während die laterale Halbschattenverbreiterung durch die Nutzung der untersuchten Punktdetek-

toren in Pencil-Beam-Scanning-Feldern im Vergleich zur Referenz gering war, wurden für Felder bei denen Kollimatoren zum Einsatz kamen Unterschiede von bis zu 2.2 mm bestimmt. Zusätzlich, war die Signalreduktion im Maximum durch die untersuchten Detektoren in kollimierten Feldern besonders ausgeprägt und betrug je nach Detektor zwischen 7.6% und 60.7% in einem kollimierten Feld mit 3 mm Durchmesser. Output-Faktor-Verteilungen für kollimierte Passive-Scattering-Felder wurden mit einer Ionisationskammer, einer Diode und einem Diamantdetektor bestimmt und mithilfe von Korrekturfaktoren, die durch die detektorspezifischen lateralen Dosis-Ansprechfunktionen bestimmt wurden, korrigiert. Während die unkorrigierten relativen Output-Faktoren um bis zu 9.7% voneinander abwichen, stimmten die korrigierten relativen Output-Faktoren innerhalb von 0.9% überein. Die Ergebnisse können verwendet werden, um Volumeneffektstörungen durch die untersuchten Punktdetektoren in Feldern von verschiedenen Protonen-Bestrahlungstechniken abzuschätzen.

Die allgemeine Diskussion in Kapitel 5 stellt die Ergebnisse der Kapitel 2, 3 und 4 in einen Zusammenhang, listet Grenzen und zeigt zukünftige Forschungsthemen in der Dosimetrie auf. Die Ergebnisse aus Kapitel 2 wurden für eine derzeit best-mögliche Abschätzung von Strahlqualitätskorrekturfaktoren in Protonenstrahlen verwendet, welche zur Aktualisierung einer Dosimetrie-Richtlinie für die Protonen-Referenzdosimetrie verwendet wurde. Im Vergleich zu einer älteren Version der Dosimetrie-Richtlinie sind die empfohlenen Korrekturfaktoren für die Strahlqualitätskorrektur bei Protonenstrahlen in der aktualisierten Version genauer, und ermöglichten die Reduktion der zugehörigen Unsicherheit von 2.1% auf 1.4%. Obwohl dies die Genauigkeit der Referenzdosimetrie in der Protonentherapie verbessert, wären experimentell bestimmte Korrekturfaktoren hilfreich, um die Daten zu validieren. In Bezug auf zukünftige Forschungsthemen, erscheinen Kalorimetrie basierte Verfahren am vielversprechendsten, um die Unsicherheit in der Protonen-Referenzdosimetrie zu verringern. Die Untersuchung der lateralen Dosis-Ansprechfunktionen und ihrer Anwendung in Feldern von verschiedenen Protonen-Bestrahlungstechniken zeigt, dass die Wahl des Detektors entscheidend für die genaue Charakterisierung des Feldes ist und dass absolute Dosismessungen in sehr kleinen Feldern Korrekturen erfordern, auch wenn kleinvolumige Detektoren verwendet werden. Um eine hohe Genauigkeit bei der Einmessung von Protonenfeldern, bei Patientenplanverifikationen und bei Messungen in der Qualitätssicherung zu gewährleisten, ist die Entwicklung einer Richtlinie für die Nicht-Referenz-Protonendosimetrie notwendig.

Zusammenfassend präsentiert diese Arbeit genauere Korrekturfaktoren für die Referenzdosimetrie und Methoden zur Abschätzung oder Korrektur von Detektorstörungseffekten in Protonenfeldern unter Nicht-Referenz-Bedingungen. Die Ergebnisse tragen zu einer verbesserten Genauigkeit in der Protonen-Dosimetrie bei, was entscheidend ist, da selbst

kleine Dosisunterschiede Einfluss auf die Tumorkontrolle, auf die Wahrscheinlichkeit für Normalgewebsreaktionen und damit auf den Behandlungserfolg der Strahlentherapie einer Patientin oder eines Patienten haben.

Author's independence declaration

English version:
I declare that I completed this work independently and used only the indicated resources. I declare that the work submitted is my own work except for work which was part of a joint authored publication. Author contributions have been specified below. I confirm that I am aware of the guidelines for good scientific practice of the Carl von Ossietzky University Oldenburg and that I observed them. I declare that this dissertation has, neither as a whole, nor in part, been submitted for assessment in a doctoral procedure at another university than the University of Oldenburg and the University of Groningen for the Joint Doctoral Degree.

German version:
Ich versichere, dass ich die vorliegende Arbeit selbstständig verfasst und nur die angegebenen Hilfsmittel benutzt habe. Ich versichere, dass die eingereichte Arbeit mein eigenes Werk ist, es sei denn, die Arbeit war Teil einer gemeinsam verfassten Veröffentlichung. Die Beiträge der Autoren sind im Folgenden aufgeführt. Ich erkläre, dass mir die Leitlinien guter wissenschaftlicher Praxis der Carl von Ossietzky Universität Oldenburg bekannt sind und von mir befolgt wurden. Ich versichere, dass diese Dissertation weder in ihrer Gesamtheit noch in Teilen einer anderen wissenschaftlichen Hochschule zur Begutachtung in einem Promotionsverfahren vorgelegt wurde, als der Universität Oldenburg und der Universität Groningen im Rahmen des gemeinsamen Promotionsverfahrens.

Ort, Datum **Jana Kretschmer**

Statement on own contributions

I hereby confirm, that Jana Kretschmer contributed to the studies presented in this thesis as stated below:

Chapter 2

Publication: Kretschmer, J., Dulkys, A., Brodbek, L., Stelljes, T.S., Looe, H.K., and Poppe, B. "Monte Carlo simulated beam quality and perturbation correction factors for ionization chambers in monoenergetic proton beams." *Med Phys*, 2020, 47:11, pp. 5890-5905. DOI: `https://doi.org/10.1002/mp.14499`

Author contributions: J.K.: project conceptualization, planned and carried out the simulations, analysis of the data, interpretation of the data, figure preparations, manuscript writing and revision; A.D.: planned and carried out the simulations, analysis of the data, interpretation of the data, review and editing of the manuscript; L.B.: planned the simulations, interpretation of the data, review and editing of the manuscript; T.S.S.: project conceptualization, interpretation of the data, review and editing of the manuscript; H.K.L.: project conceptualization, planned the simulations, interpretation of the data, project supervision, review and editing of the manuscript; B.P.: project conceptualization, interpretation of the data, project supervision, review and editing of the manuscript

Chapter 3

Publication: Kretschmer, J., Brodbek, L., Looe, H.K., van der Graaf, E., van Goethem, M.J., Kiewiet, H., Olivari, F., Meyer, C., Poppe, B. and Brandenburg, S. "Investigating the lateral dose response functions of point detectors in proton beams." *Phys Med Biol*, 2022, 67:14, p. 145003. DOI: `doi:10.1088/1361-6560/ac783c`

Author contributions: J.K.: project conceptualization, planned and carried out the simulations, planned and carried out the experiments, analysis of the data, interpretation of the data, figure preparations, manuscript writing and revision; L.B.: project conceptualization, planned and carried out the experiments, interpretation of the data, review and editing of the manuscript; H.K.L.: project conceptualization, planned the simulations, planned the experiments, interpretation of the data, project supervision, review and editing of the manuscript; E.v.d.G.: project conceptualization, planned the simulations, planned and carried out the experiments, interpretation of the data, review and editing of the manuscript; M.J.v.G.: project conceptualization, planned and carried

out the experiments, interpretation of the data; H.K.: planned the experiments; F.O.: carried out the experiments, review and editing of the manuscript; C.M.: carried out the experiments; B.P.: project conceptualization, planned the simulations, planned the experiments, interpretation of the data, project supervision, review and editing of the manuscript; S.B.: project conceptualization, planned the simulations, planned the experiments, interpretation of the data, project supervision, review and editing of the manuscript

Chapter 4

Publication: Kretschmer, J., Brodbek, L., Behrends, C., Kugel, F., Koska, B., Bäumer, C., Wulff., J., Timmermann, B., Poppe, B. and Looe, H.K. "Comprehensive investigation of lateral dose profile and output factor measurements in small proton fields from different delivery techniques." *Med Phys*, 2023, 50:7, pp. 4546-4561. DOI: `https://doi.org/10.1002/mp.16357`

Author contributions: J.K.: project conceptualization, planned and carried out the experiments, analysis of the data, interpretation of the data, figure preparations, manuscript writing and revision; L.B.: planned and carried out the experiments, interpretation of the data, review and editing of the manuscript; C.B.: planned and carried out the experiments, interpretation of the data, review and editing of the manuscript; F.K.: planned and carried out the experiments, interpretation of the data, review and editing of the manuscript; B.K.: planned and carried out the experiments, interpretation of the data, review and editing of the manuscript; C.B.: project conceptualization, planned and carried out the experiments, interpretation of the data, review and editing of the manuscript; J.W.: project conceptualization, planned and carried out the experiments, interpretation of the data, review and editing of the manuscript; B.T.: project conceptualization, review and editing of the manuscript; B.P.: project conceptualization, planned the experiments, interpretation of the data, project supervision, review and editing of the manuscript; H.K.L.: project conceptualization, planned the experiments, interpretation of the data, project supervision, review and editing of the manuscript

Place, Date **Prof. Dr. Björn Poppe (Supervisor)**

Acknowledgements

I was not always sure I would actually reach this point. But here it is - my PhD thesis. I am grateful to have made it this far, and know that I could not have done it without all the people who contributed to this work. For this reason, I would like to sincerely thank everyone who supported me, in one way or another, in completing this thesis.

First, I would like to thank my supervisors **Prof. Dr. Sytze Brandenburg** and **Prof. Dr. Björn Poppe**, who made this thesis possible.

Dear **Sytze**, I am very happy to have had the chance to work with you and feel incredibly honored to be your last PhD student. Although I did not spend a longer period of time in Groningen, it did not feel like a long-distance supervision as you were always available for online meetings and quick with responses. Thank you for sharing your vast knowledge, for your guidance, and for providing me with critical feedback, which helped me improve my work. Thanks for all the time you invested, even after your retirement – thank you for your constant support, patience, and personal advice. I am very grateful to have you as my supervisor!

Dear **Björn**, thank you for allowing me to be part of your research group in Oldenburg. We have known each other for more than 11 years now, and I am highly grateful for the opportunity to work with you. I still remember talking to you in your office about whether I should apply for this PhD. This conversation was the reason for me to give it a try, and today I am glad that you encouraged me to do so. Throughout my PhD, I knew that your door was always open, and I appreciate how you always listened and came up with solutions when I came to talk to you. I would like to truly thank you for your support during my PhD.

I would also like to sincerely thank the members of the assessment committee **Prof. Georg**, **Prof. Verhaegen**, **Prof. van de Par** and **Prof. Schippers** for generously dedicating their time and expertise to reviewing my thesis.

Of course, I would also like to acknowledge everyone I got to meet in person and in online meetings at **KVI**, **UMCG** and **PARTREC** in **Groningen** – I always enjoyed the positive and supportive work atmosphere, and would have really liked to spend more time in person with your group in Groningen. Dear **Emiel**, I always enjoyed working with you and am grateful for your support during my PhD. I greatly appreciate your constructive feedback and your availability for questions. Thank you also for providing so much support in planning and preparing the experiments at PARTREC, for your help during the long night shifts, and for the nice conversations that kept me awake. Dear **Marc Jan**, thank you for

all your help with our experiments, for your input, and for providing the required tools or programming software. Thank you **Harry** for your support with the preparations of the experiments. Dear **Francesco**, **Christoph**, **Isabel**, **Marc-Jan**, **Emiel** and **Leonie**: I am thankful for your support during the experiments and for creating a pleasant work environment no matter how long the night shifts became. Thanks also to **Jospert** for the beamline model and to **Justin** for helping me with the formatting and printing of my thesis.

Many thanks also to my colleagues at the **Medical Radiation Physics working group** and **Pius Hospital** in **Oldenburg**. I am very grateful for the support of everyone who shared their knowledge and experience or helped me with my research. Dear **Hui Khee**, I can not express how grateful I am for all your help and certainly could not have finished this PhD without your support. I learned so much from you over the past years, and I truly appreciate how I could always count on you during all the ups and downs of my PhD. Thank you for sharing your impressive knowledge, supportive guidance, and feedback. I would also like to acknowledge that you showed me how much fun working in research is. I especially enjoyed our weekly or sometimes even daily discussions on new simulation results or evaluation progress, celebrating small and big achievements, and how our notes from brainstorming were sometimes written on napkins or hung on sheets all over the walls in our office. I admire your passion for research and your impressive ability to manage all kinds of projects simultaneously. Thank you for always making time for me, for your patience, and for the trust you put in me. Dear **Leonie**, I was so lucky to start this journey with you. I would like to thank you for your support with the experiments and research, for being there for me when I needed someone to talk about concerns, for all the memories we made during our conference and non-conference trips around Europe, and for the delicious food and recipes you introduced to my world. I am deeply grateful for having had you by my side as a friend during this intense time. Dear **Tenzin**, **Björn**, **Ilga**, **Hui Khee**, **Wolfgang**, **Ralf**, and **Björn**, thank you for everything you taught me during my time at the Pius Hospital. Dear **Tenzin**, **Björn**, **Hui Khee**, and **Ilga**, I learned so much from you and am immensely grateful for all the time you invested in my training and for your patience with me. Dear **Wolfgang** and **Ralf**, thank you for sharing your knowledge, for always being ready to help, and for your advice on holiday destinations. Many thanks to **Dr. Willborn** and all other members of the clinical radiation therapy department of the Pius Hospital – I am very thankful to have had the chance to work with you. Thanks as well to all the students I got to meet and work with during my time in Oldenburg and of course to my PhD colleagues - dear **Ann-Britt**, **Leonie**, **Tuba**, **Isabel**, **Lukas**, **Katrin**, **Henrik**, **Meisam**, **Christoph** and **Pascal**, thanks for your help and all the fun moments during lunch and coffee breaks - it was a pleasure to work with you and I wish you all the best for your future. Dear **Vanessa**, it was so nice to have

you back in our working group. I very much enjoyed all our mainly non-work-related conversations and want to thank you for your advice and emotional support, for the sometimes much-needed distractions from work, and for bringing Marie. Dear **Anna**, it has been a pleasure working with you during your Master's studies, and I want to thank you for your contribution and support with the Monte Carlo simulations. I admire your focused and determined way of working and am happy that we are colleagues now. Dear **Daniela**, thank you for sharing your comprehensive expertise, for inviting me to work with you, for personal advice, and for bringing us all together outside of work at conferences or when you are in Oldenburg. Dear **Vanessa**, **Sascha**, **Sebastian**, **Ann-Britt**, and **Leonie**, I am more than thankful to have worked with you and for becoming friends. I would like to thank you for all the times I cried laughing, for the fun moments in the office, during measurement sessions, but especially when we met for game nights, dinners, or different places around Europe. I am happy to have gotten to know you and thankful for the memories we made.

I would also like to thank all **co-authors** and **research collaborators** for their contributions to the Chapters of this thesis and making my PhD possible. I enjoyed working with you and greatly appreciate the support each of you provided. Thanks to **Jörg** and **Christian** for the fruitful discussions and for giving me the opportunity to work with your team in Essen. Thank you **Carina**, **Fabian** and **Benjamin** for helping me collect the data needed for our paper. Thanks **Kilian** for your constructive feedback on my articles and your advice.

Many thanks also to everyone I got to know in our PhD programme, the **Oldenburg-Groningen Joint Graduate Research Training Group**. I would like to acknowledge all my PhD colleagues: thanks for being in this experience with me, for inspiring me, and for sharing your struggles and advice during training or lunch breaks and dinners. Major thanks also to **Nina** and **Corinna** for your great support with the joint PhD and for organizing all the helpful workshops.

Additionally, I want to thank my current employer, the **Strahlentherapie Nord**, and **Friederike** and **Kristin** for helping me to complete this thesis by being incredibly supportive and providing me with a lot of flexibility. Many thanks to all my colleagues for listening, cheering me up, and being so understanding – I genuinely enjoy working with you!

Moreover, I would like to acknowledge my paranymphs **Ebba** and **Lukas** - thank you for supporting me in completing this chapter of my life.

Many thanks also to **Cerrin** for designing the cover of my thesis - I deeply appreciate all the time and thought you put into it.

Thank you **Hilbert** for proofreading chapters of this thesis. I know how busy you are and appreciate your remarks and time. Moreover, I am incredibly thankful to **Christa** and you for allowing me to write these words on the (in my eyes) most beautiful balcony and apartment in Oldenburg.

Finally, I would like to thank my family and friends – I am incredibly grateful to be surrounded by so many warmhearted people who fill my everyday life with happiness and joy. Liebe **Mama**, lieber **Papa**, danke für all eure Liebe, Unterstützung und euren Rückhalt. Ich weiß sehr zu schätzen, wie viel ihr dafür getan habt, dass ich die Freiheit hatte, so viele schöne Dinge ausprobieren und erleben zu dürfen - ich glaube, dass ihr mir dadurch den Mut geschenkt habt, auch andere Wege, als die mir und euch bisher bekannten, zu bestreiten. Ich möchte euch dafür und für alles andere, was ihr für mich getan habt, von Herzen Danke sagen! Liebe **Marieka**, du bist nicht nur meine jüngere große Schwester sondern auch meine längste Freundin und ich bin unendlich froh dich zu haben - du hast mir in den letzten Jahren zugehört, dich um mich gesorgt, warst für mich da, als ich dich brauchte und hast mich mit schönen Erlebnissen abgelenkt. Vielen Dank für deine liebevolle verständnisvolle Art und bedingungslose Unterstützung! Lieber **Mika**, du warst erst 12 Jahre alt, als ich mit meiner Promotion angefangen habe und ich bin froh, dass wir trotz unseres Altersunterschieds all die Jahre so eng miteinander waren. Ich hoffe, dass wir das immer bleiben werden und danke dir für unsere minutenlangen Lachanfälle, fürs Zuhören und deine klugen objektiven Ratschläge! Liebe **Alica**, du hast, glaube ich, jedes Up und Down meiner Promotion miterlebt. Ich bin dir sehr dankbar, dass du immer für mich da warst und mich mit deiner empathischen Art, Ratschläge zu geben und zu motivieren, immer wieder aufgefangen hast. Danke außerdem, für die Ablenkung und die vielen gemeinsamen Glücksmomente – unsere Gespräche bei Balkonabenden oder beim Laufen, unsere Erlebnisse, wenn wir zu zweit in Oldenburg unterwegs waren, oder während unserer stundenlangen Telefonate! Lieber **Henry**, ich bin so unfassbar froh dich zu haben und danke dir von Herzen für deine bedingungslose Unterstützung in der letzten Phase meiner Promotion – danke, dass du mir den Rücken freigehalten hast, mir zuhörst und mir immer und immer wieder meine Selbstzweifel nimmst und Fähigkeiten aufzeigst. Danke für deine liebevolle positive Art und die Leichtigkeit, die du in mein Leben bringst, für die vielen kleinen und großen Glücksmomente und dafür, dass du mich daran erinnerst, was wirklich wichtig ist! Liebe **Ebba**, **Anneke**, **Johanna**, **Cerrin**, **Max**, **Julia**, **Alea**, **Marieka**, **Lukas**, **Mika**, **Laura**, **Alica**, **Henry**, **Lena** und **Lars**, danke für die vielen Gespräche, die Lachanfälle, für euren Rat, eure Spontanität, Kreativität, Coffee-Dates, für die (Floh-)Marktbesuche, Bastelabende, Urlaube, Festivals, Konzerte und Ausflüge. Danke, dass ihr mein Leben und Herz mit so viel schönen Erinnerungen füllt und mich in den letzten Jahren immer unterstützt und an mich geglaubt habt!

Curriculum vitae

Academic Studies at the University of Groningen

since 10/2020	PhD candidate on the topic: *Improving patient dosimetry under non-reference conditions for proton beams*

Academic Studies at the University of Oldenburg

since 03/2018	PhD candidate on the topic: *Improving patient dosimetry under non-reference conditions for proton beams*
10/2015-02/2018	Master of Science in *Engineering Physics*, Thesis on: *Characterization of spatial and energetic response patterns of two-dimensional detector arrays*
10/2012-09/2015	Bachelor of Engineering in *Engineering Physics*, Thesis on: *Debiasing CILBO meteor observations and the mass accumulation of the earth*

Practical experiences

since 01/2024	Medical physicist at the radiation therapy of the *Strahlentherapie Nord* in Bremen and Westerstede with leading position in Westerstede
05/2022-12/2023	Medical physicist at the radiation therapy of the *Strahlentherapie Nord* in Bremen and Westerstede
03/2021-04/2022	Medical physicist at the radiation therapy of the *Pius Hospital* in Oldenburg
03/2018-03/2021	Medical physicist in training at the radiation therapy of the *Pius Hospital* in Oldenburg
07/2016-02/2018	Research assistant in radiation therapy at the *Pius Hospital* in Oldenburg

2015 In preparation of the Bachelor thesis: Two two-week visits at the research center of the *European Space Agency* (*ESA*), *ESTEC* in Noordwijk, the Netherlands

Year Abroad

08/2011-09/2012 Au Pair in Connecticut, USA, including participation in language courses

Awards

2016 *Zarm Förderpreis 2016* by the center of applied space technology and microgravity (Zarm) of the University of Bremen, promotion award

2015 *Bachelor thesis award* by the fifth department of the University of Oldenburg for the best thesis from the institute of physics in the summer semester 2015

Conference contributions

Kretschmer, J., Brodbek, L., Behrends, C., Kugel, F., Koska, B., Bäumer, C., Wulff, J., Timmermann, B., Looe, H.K. and Poppe, B. "PD-0814 Quantification and correction of volume effect perturbations from detectors in small proton fields." *Radiotherapy and Oncology, ESTRO Conference*, 2022, poster presentation.

Baumann, K. Gomà, C., Wulff, J., **Kretschmer, J.** and Zink, C. "PO-1553 A review of Monte Carlo calculated f_Q factors for ionization chambers in clinical proton beams." *Radiotherapy and Oncology, ESTRO Conference*, 2022, poster presentation.

Kretschmer, J., Brodbek, L., Looe, H.K., van der Graaf, E., van Goethem, M.J., Kiewiet, H., Meyer, C., Poppe, B. and Brandenburg, S. "V78 Experimental determination and Monte Carlo simulation of lateral dose response functions for point detectors in proton beams." *Abstractband, Joint Conference of the ÖGMP, DGMP and SGSMP, virtual*, 2021, oral presentation.

Brodbek, L., **Kretschmer**, J., Looe, H.K., Stelljes, T.S., Brandenburg, S. and Poppe, B., "V6 Dosimetric characterisation of liquid-filled ionisation chamber array OCTAVIUS detector 1600SRS." *Abstractband, Joint Conference of the ÖGMP, DGMP and SGSMP, virtual*, 2021, oral presentation.

Brodbek, L., **Kretschmer**, J., Looe, H.K., Poppe, B. and Poppinga, D. "eP36 Investigation of the RUBY head phantom and MultiMet insert for multiple-targets end-to-end testing." *Abstractband, Joint Conference of the ÖGMP, DGMP and SGSMP, virtual*, 2021, poster presentation.

Kretschmer, J., Brodbek, L., Looe, H.K., van der Graaf, E., van Goethem, M.J., Kiewiet, H., Meyer, C., Poppe, B. and Brandenburg, S. "PD-0898 Experimental determination of detector specific lateral dose response functions in proton beams." *Radiotherapy and Oncology, ESTRO Conference*, 2021, poster presentation.

Kretschmer, J., Dulkys, A., Brodbek, L., Stelljes, T.S., Looe, H.K. and Poppe, B. "Monte Carlo simulation of beam quality correction factors for ionisation chambers in monoenergetic proton beams." *51. Jahrestagung der DGMP*, 2020, oral presentation.

Kretschmer, J., Brodbek, L., Büsing, I., Olivari, F., van der Graaf, E., Looe, H.K. and Poppe, B. "Determination of k_{S} and k_{pol} for ionisation chambers in a 150 MeV proton beam." *51. Jahrestagung der DGMP*, 2020, poster presentation.

Kretschmer, J., Brodbek, L., Behrends, C., Kugel, F., Bäumer, C., Wulff, J., Timmermann, B., Looe, H.K. and Poppe, B. "Comparisons of experimental and calculated lateral profiles of collimated proton beams." *51. Jahrestagung der DGMP*, 2020, poster presentation.

Kugel, F., **Kretschmer, J.**, Behrends, C., Brodbek, L., Kern, A., Bäumer, C., Looe, H.K., Poppe, B., Wulff, J., Timmermann, B. "Dosimetrie kleiner Protonenfelder – Vergleich experimenteller Messungen mit der Vorhersage aus dem Planungssystem." *51. Jahrestagung der DGMP*, 2020, oral presentation.

Poppinga, D., **Kretschmer, J.**, Brodbek, L., Meyners, J., Poppe, B. and Looe, H.K. "Untersuchung eines neuen modularen Phantoms für die Qualitätssicherung in der Strahlentherapie." *51. Jahrestagung der DGMP*, 2020, poster presentation.

Brodbek, L., **Kretschmer, J.**, Meijers, A., Looe, H.K., Knopf, A.K. and Poppe, B. "Analysis on the error detection capability of different detector arrays in intensity modulated proton therapy." *51. Jahrestagung der DGMP*, 2020, poster presentation.

Kretschmer, J., Dulkys, A., Brodbek, L., Stelljes, T.S., Looe, H.K. and Poppe, B. "Monte Carlo simulations of ionization chamber perturbation correction factors in monoenergetic proton beams." *50. Jahrestagung der DGMP*, 2019, oral presentation, Abstractband, p.51; V21.

Kretschmer, J., Dulkys, A., Brodbek, L., Stelljes, T.S., Looe, H.K. and Poppe, B. "Investigation of ionization chamber responses to monoenergetic proton beams using Monte Carlo simulations." *AAPM*, 2019, poster presentation, AAPM ePoster Library; 269387; WE-C1030-GePD-F7-3.

Kretschmer, J., Dulkys, A., Brodbek, L., Stelljes, T.S., Willborn, K., Looe, H.K. and Poppe, B. "Monte Carlo simulations to improve the beam quality correction factors of ionization chambers in monoenergetic proton beams." *25. Jahrestagung der DEGRO*, 2019, poster presentation, Abstractband Strahlenther Onkol 195(Suppl 1):1, p.183; P27-3-jD, DOI: 10.1007/s00066-019-01465-2

Brodbek, L., **Kretschmer, J.**, Dulkys, A., Le, T.L.T., Espelage, T., Marmitt, G.G., Stelljes, T.S., Willborn, K., Looe, H.K., Langendijk, J.A., Knopf, A.K., Meijers, A. and Poppe, B. "A frequency analysis of scanned intensity modulated proton therapy treatment plans." *50. Jahrestagung der DGMP*, 2019, poster presentation, Abstractband; p.323; P91.

Dulkys, A., **Kretschmer, J.**, Brodbek, L., Stelljes, T.S., Willborn, K., Looe, H.K. and Poppe, B. "Monte Carlo simulations of ionization chamber perturbation correction factors in monoenergetic proton beams." *25. Jahrestagung der DEGRO*, 2019, poster presentation, Abstractband Strahlenther Onkol 195(Suppl 1):1, p.182; P27-2-jD, DOI: 10.1007/s00066-019-01465-2

Brodbek, L., **Kretschmer, J.**, Dulkys, A., Le, T.L.T., Espelage, T., Marmitt, G.G., Meijers, A., Willborn, K., Stelljes, T.S., Looe, H.K., Langendijk, J.A., Knopf, A.K. and Poppe, B. "IMPT verification with Gafchromic EBT3 films and the OCTAVIUS detector array 1500XDR." *25. Jahrestagung der DEGRO*, 2019, poster presentation, Abstractband Strahlenther Onkol 195(Suppl 1):1, p.183; P27-2-jD, DOI: 10.1007/s00066-019-01465-2

Kretschmer, J., Brodbek, L., Stelljes, T.S., Looe, H.K. and Poppe, B. "Star shot based absolute isocentre verification using the OCTAVIUS detector array 1000SRS." *49. Jahrestagung der DGMP*, 2018, oral presentation, Abstractband, p.22; V8.

Brodbek, L., **Kretschmer, J.**, Stelljes, T.S., Looe, H.K. and Poppe, B. "Estimating the variation of the non-reference condition correction factor for different detector

types used to measure intensity modulated dose distributions." *49. Jahrestagung der DGMP*, 2018, poster presentation, Abstractband, p.313; P44.

Kretschmer, J., Brodbek, L., Stelljes, T.S., Looe, H.K. and Poppe, B. "Position-dependent non-reference condition corrections for treatment plan verification using two-dimensional detector arrays." *Biomed. Eng.-Biomed. Tech.*, 2017, poster presentation, 62(s1) p.377.

Stelljes, T.S., Poppinga, D., **Kretschmer, J.**, Brodbek, L., Looe, H.K., Harder, D. and Poppe, B. "Comparison between differing fill factor definitions for two-dimensional detector arrays." *Biomed. Eng.-Biomed. Tech.*, 2017, poster presentation, 62(s1) p.373.

Brodbek, L., **Kretschmer, J.**, Stelljes, T.S., Looe, H.K., Loutfi-Krauss, B., Blanck, O. and Poppe, B. "Isocenter verification of a standard linear accelerator using the OCTAVIUS detector array 1000SRS." *Biomed. Eng.-Biomed. Tech.*, 2017, poster presentation, 62(s1) p.378.

List of publications

Kretschmer, J., Brodbek, L., Behrends, C., Kugel, F., Koska, B., Bäumer, C., Wulff., J., Timmermann, B., Poppe, B. and Looe, H.K. "Comprehensive investigation of lateral dose profile and output factor measurements in small proton fields from different delivery techniques." *Med Phys*, 2023, 50:7, pp. 4546-4561. DOI: https://doi.org/10.1002/mp.16357

Baumann, K.-S., Gomà, C., Wulff, J., **Kretschmer, J.**, and Zink, K. "Monte Carlo calculated ionization chamber correction factors in clinical proton beams – deriving uncertainties from published data." *Phys Med*, 2023, 113, p. 102655, DOI: https://doi.org/10.1016/j.ejmp.2023.102655

Kugel, F., Wulff, J., Bäumer, C., Janson, M., **Kretschmer, J.**, Brodbek, L., Behrends, C., Verbeek, N., Looe, H. K., Poppe, B. and Timmermann, B. "Validating a double Gaussian source model for small proton fields in a commercial Monte-Carlo dose calculation engine." *Z Med Phys*, 2023, 33:4, pp. 529-541. DOI: https://doi.org/10.1016/j.zemedi.2022.11.011

Kretschmer, J., Brodbek, L., Looe, H.K., van der Graaf, E., van Goethem, M.J., Kiewiet, H., Olivari, F., Meyer, C., Poppe, B. and Brandenburg, S. "Investigating the lateral dose response functions of point detectors in proton beams." *Phys Med Biol*, 2022, 67:14, p. 145003. DOI: doi:10.1088/1361-6560/ac783c

Brodbek, L., **Kretschmer, J.**, Büsing, K., Looe, H. K., Poppe, B. and Poppinga, D. "Systematic end-to-end testing of multiple target treatments using the modular RUBY phantom." *Biomed Phys Eng Express*, 2022, 8:1, p. 015018. DOI: https://doi.org/10.1088/2057-1976/ac3e37

Kretschmer, J., Dulkys, A., Brodbek, L., Stelljes, T.S., Looe, H.K. and Poppe, B. "Monte Carlo simulated beam quality and perturbation correction factors for ionization chambers in monoenergetic proton beams." *Med Phys*, 2020, 47:11, pp. 5890-5905. DOI: https://doi.org/10.1002/mp.14499

Poppinga, D., **Kretschmer, J.**, Brodbek, L., Meyners, J., Poppe, B. and Looe, H. K. "Evaluation of the RUBY modular QA phantom for planar and non-coplanar VMAT and stereotactic radiations", *J Appl Clin Med Phys*, 2020, 21, pp. 69–79, DOI: https://doi.org/10.1002/acm2.13006

Brodbek, L., **Kretschmer, J.**, Willborn, K., Meijers, A., Both, S., Langendijk, J.A., Knopf, A., Looe, H.K. and Poppe, B. "Analysis of the applicability of two-dimensional

detector arrays in terms of sampling rate and detector size to verify scanned intensity modulated proton therapy plans." *Med Phys*, 2020, 47:9, pp. 4589-4601. DOI: https://doi.org/10.1002/mp.14346

Stelljes, T.S., Poppinga, D., **Kretschmer, J.**, Brodbek, L., Looe, H.K. and Poppe, B. "Experimental determination of the “collimator monitoring fill factor” and its relation to the error detection capabilities of various 2D-arrays." *Med Phys*, 2019, 46:4, pp. 1863-1873. DOI: https://doi.org/10.1002/mp.13417

Drolshagen, G., Koschny, D., Drolshagen, S., **Kretschmer, J.** and Poppe, B. "Mass accumulation of earth from interplanetary dust, meteoroids, asteroids and comets." *Planetary and Space Science*, 2017, 143, pp. 21-27. DOI: https://doi.org/10.1016/j.pss.2016.12.010

Koschny, D., Drolshagen, E., Drolshagen, S., **Kretschmer, J.**, Ott, T., Drolshagen, G. and Poppe, B. "Flux densities of meteoroids derived from optical double-station observations." *Planetary and Space Science*, 2017, 143, pp. 230-237. DOI: https://doi.org/10.1016/j.pss.2016.12.007